

ISSN 0911-5730

UVSOR-49

August 2022

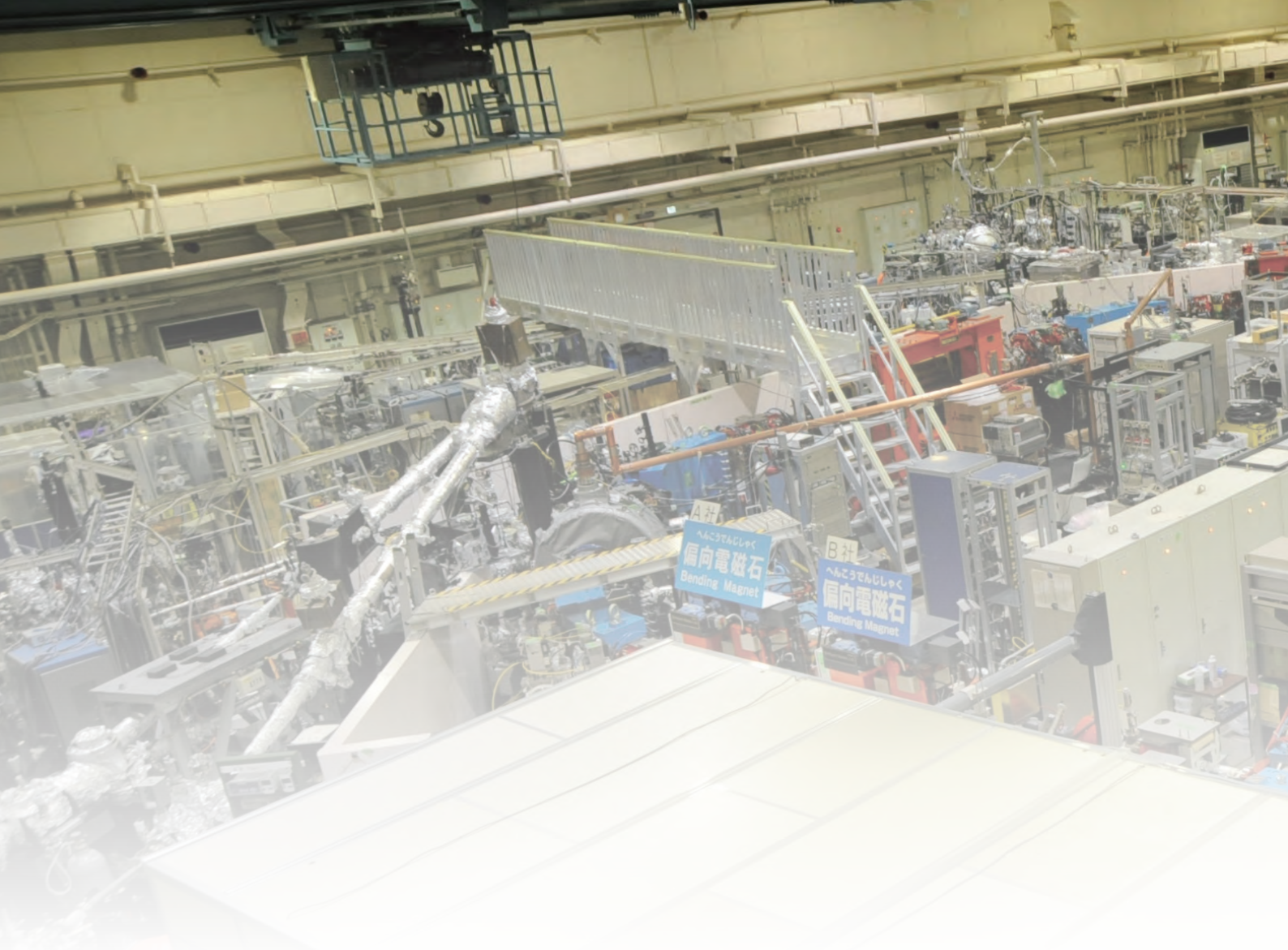
UVSOR ACTIVITY REPORT 2021

UVSOR Synchrotron Facility
Institute for Molecular Science
National Institutes of Natural Sciences



UVSOR II
since 2012

The logo features the text 'UVSOR II' in a stylized, blue, serif font. The 'U' and 'V' are connected, and the 'S' is a large, flowing script. Below it, 'since 2012' is written in a smaller, blue, sans-serif font. The logo is centered within a large, glowing blue circular graphic that resembles a synchrotron ring or a lens, with a bright white center and a ring of small white dots around the perimeter.



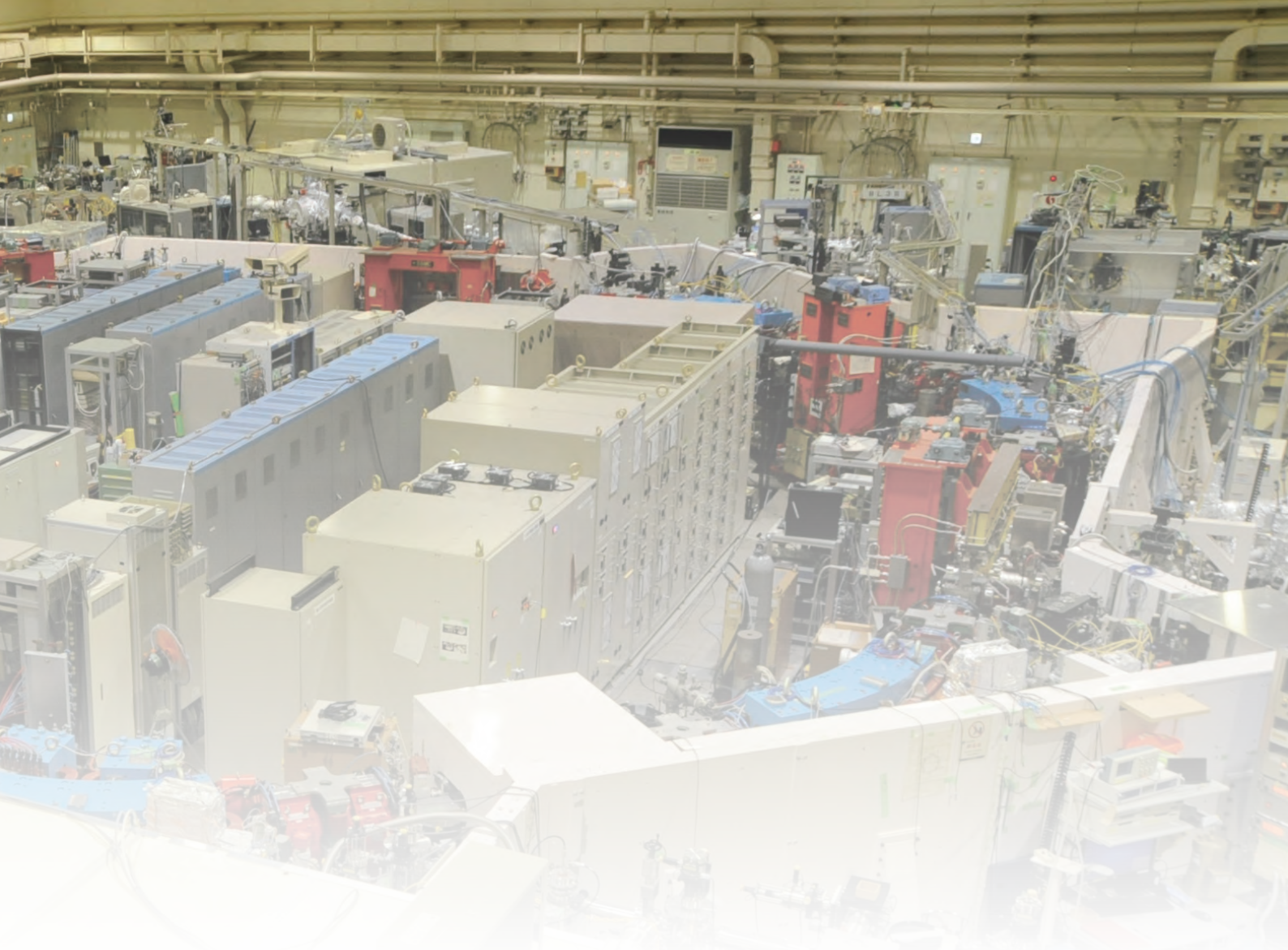
Preface



This Activity Report covers scientific and technological activities carried out using the UVSOR-III Synchrotron in FY2021 (April 2021 - March 2022). We present scientific examples of how the users study at the UVSOR Synchrotron Facility.

The present UVSOR-III Synchrotron is one of the most advanced low-energy SR facilities of the 3rd generation SR in the world and is now one of the critical resources to accelerate the investigation of molecular science. The UVSOR-III Synchrotron has a small electron storage ring but has powerful 6-undulator beamlines (3 VUV and 3 in-vacuum soft X-ray undulators) with 8-dipole beamlines. We continue improving and upgrading our micro- and nano-scale photoabsorption and photoemission approaches and in situ/operando measurements in the IR, VUV, and soft X-ray regions, based on our strategic international collaboration program in molecular science. We are grateful to all the people who use our facility and support our efforts.

UVSOR operates for 40 weeks/year (ca. 2,200 h user time), accepts ~230 proposals, about ~600 individual researchers counting total ~4,000 people*day/year. Most users stay for one or two weeks for experimenting. To continue high-level achievements in science and technology at the UVSOR-III Synchrotron, our in-house staff is constantly committed to maintaining and improving high-performance accelerators and beamlines. Research activity has been affected by COVID-19 worldwide, however, the daily life of scientists seems to be renovated. Of course, it has impacted overseas researchers who cannot travel to Japan. We support some of their research



by doing the experiment on their behalf.

In terms of personnel, Assistant professors, Takuji Ohigashi and Masaki Fujimoto left UVSOR. They will kindly support the beamlines by cross-appointment contract in FY2022. The support office staff, Hisayo Hagiwara retired, who has been dedicated as a secretary for a quite long time since the early days of UVSOR.

On the experimental side, technology development will not stop, hence we will make a progress on the imaging-related techniques to inspire advanced molecular science. We have started to construct the new endstation at the undulator-based soft X-ray beamline BL6U since 2020. The new instrumentation of the photoelectron momentum microscope is developing and you may see the final whole picture of the apparatus in FY2022, which consists of a double-hemispherical analyzer with spin detector. In the beamline BL1U, we have conducted in developing the novel light sources, including pulsed- γ ray and their use for the measurements. To optimize the high-power laser light to UVSOR-III for versatile use, we arranged the endstation layout of BL1U. In FY2022, we will test the new orbit trajectory for doing the γ -ray experiments daily to avoid affecting other beamlines. The advanced SR-related instrument will offer opportunities in characterizing the electronic structure of surface atomic sites, thin films, molecular adsorbates, bulk crystals, and so on.

We have discussed the possibility to construct the post-UVSOR-III as a long-term plan for sustainable development since 2019. We look forward to receiving your feedback and suggestions on the continuing evolution of the UVSOR Synchrotron Facility. And we hope many users will perform excellent work by fully utilizing the UVSOR-III Synchrotron as a unique international hub for the SR research in advanced molecular science.

April 2022

Satoshi Kera

Director of the UVSOR Synchrotron Facility

The Commendation for Science and Technology by the Minister of Education, Culture, Sports, Science and Technology (Outstanding Support for Research Award) Given to Mr. Eiken Nakamura

Mr. Eiken Nakamura, Chief Engineer in UVSOR Synchrotron Facility, received the Commendation for Science and Technology by the Minister of Education, Culture, Sports, Science and Technology (Outstanding Support for Research Award) for "Development of an L-shaped slit for synchrotron radiation and its contribution to a design for beamlines with insertion light sources." This award is given to persons who made outstanding achievements in research and development in science and technology in order to raise the level of science and technology in Japan.



The Outstanding Presentation Award of the 64th Annual Meeting of the Japanese Society of Radiation Chemistry Given to Dr. Yoshitaka Taira

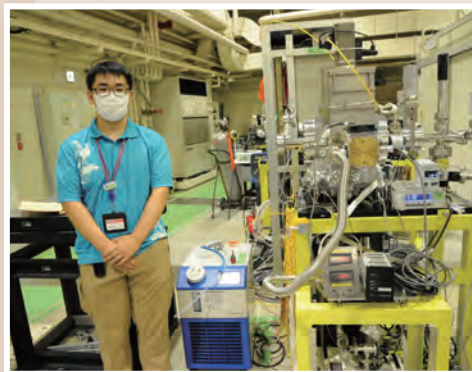
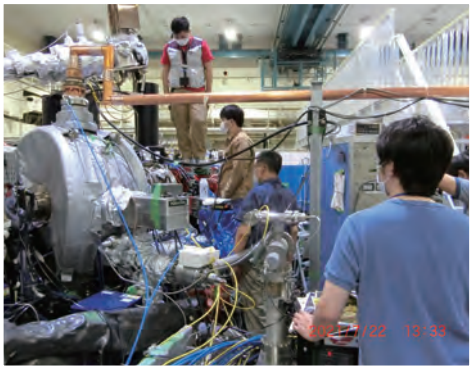
Dr. Yoshitaka Taira, Associate Professor in UVSOR Synchrotron Facility, received the Outstanding Presentation Award of the 64th Annual Meeting of the Japanese Society of Radiation Chemistry for his presentation entitled “Development of gamma-ray induced positron annihilation spectroscopy at UVSOR-III.” The gamma-ray induced positron annihilation spectroscopy enables defect analysis of the entire bulk sample with a thickness of several cm, which was difficult to measure with the conventional method using a positron radiation source.



The 2021 Young Presentation Award of the Young Researchers Association of the Japan Beam Physics Club given to Mr. Ryohei Yamamoto

Mr. Ryohei Yamamoto received the Young Presentation Award of the Young Researchers Association of the Japan Beam Physics Club 2021 for his presentation entitled “Development of gamma-ray-induced positron age-momentum correlation measurement method in UVSOR-III”. In UVSOR-III, gamma-ray induced positron annihilation spectroscopy by ultrashort pulse gamma rays is being developed.

Staff



UVSOR ACTIVITY REPORT 2021

Preface

S. Kera

News

I. Organization and Staff List 1

II. Current Status of Light Sources and Beamlines 7

Light Sources in 2021 (Y. Taira) 9

Beamlines in 2021 (F. Matsui) 12

III. Research Activities

III-1. Accelerators and Instruments 31



Improvement of Image Quality of Selective Isotope 3D-CT in UVSOR-BL1U [1U] 33
H. Ohgaki, K. Ali, H. Zen, T. Kii, T. Hayakawa, T. Shizuma, M. Fujimoto, Y. Taira and M. Katoh

Photon Counting Experiments of Young's Double-Slit Interference Using Undulator Vortex Radiation [1U] 34
S. Wada, H. Ohta, A. Mano, M. Fujimoto and M. Katoh



Development Mass Production Facilities of Nuclear Emulsion Films [Others] 35
I. Usuda, H. Rokujo and M. Nakamura

Laser Pulse Shaping and Transport at UVSOR-III [1U] 36
Y. Takashima, A. Mano, G. Jang, Y. Taira, M. Fujimoto, Y. Okano and M. Katoh

Revival of UVSOR-FEL and Gamma Ray Generation by Intra-cavity Laser Compton Scattering [1U] 37
H. Zen, J. Yamazaki, M. Fujimoto, K. Hayashi, H. Ohta, Y. Taira and M. Katoh

Evaluation of Analyzing Power of Gamma-ray Polarimeter [1U] 38
S. Endo, T. Shizuma, H. Zen, Y. Taira, K. Sugita, O. Mohamed, S. Kawamura, R. Abe, T. Okudaira, M. Kitaguchi and H. M. Shimizu


Development of Gamma ray Induced Positron Annihilation Spectroscopy [1U] 39
Y. Taira, K. Sugita, R. Yamamoto, Y. Okano and T. Hirade

Single Electron Storage at UVSOR-III [1U] R. Shinomiya, M. Shimada, H. Miyauchi, M. Fujimoto and M. Katoh	40
Exploring Novel Application of Undulator Radiation Based on Interferometric Technique [1U] K. Kato, M. Shimada, H. Miyauchi, A. Mano and M. Katoh	41
Calibration of CMOS Sensor with Reflective-type Flux Reduction System [2A] N. Narukage	42
Photon Energy Resolutions of BL3B Evaluated by Appearance Energy Measurements of Xe⁺ Ions [3B] H. Iwayama	43
BL4B Usage for Developing the Photoelectron Spectroscopy End-station for Organic Materials [4B] K. Fukutani, H. Iwayama, F. Matsui and S. Kera	44
Development of High Efficiency Liquid Cell in Total Electron Yield Using Atomically-thin Graphene [4B] I. Mitsuishi, K. Kashiwakura, Y. Niwa, T. Ogawa, Y. Tawara, R. Kitaura, P. Solís-Fernández, K. Kawahara, H. Ago, T. Taniguchi, K. Nomoto, H. Kodaka, T. Horigome, E. Nakamura, H. Iwayama, M. Nagasaka and K Tanaka	45
Development of a Fluorescence Polarimeter in Extreme Ultraviolet Region [5B] T. Kaneyasu, K. Hosaka and J. Adachi	46
Measurement of a Detection Efficiency of High-sensitivity Microchannel Plates with Tapered Pores [5B] S. Matoba, H. Iwayama and T. Kaneyasu	47
Study on the Source of Photon-Energy Drift of BL5B [5B] H. Zen, E. Nakamura, K. Hayashi and K. Tanaka	48
Complex Refractive Index Measurement by Reflectance Spectra in Different Polarization Configurations [7B] M. Horiba, K. Fukui, K. Yamamoto and T. Saito	49
III-2. Materials Sciences	51
 Study on Defects in Iron Formed under Hydrogen Embrittlement Environment Using In-Situ Measurement Technique of Gamma-Ray Induced Positron Annihilation Lifetime Spectroscopy [1U] A. Yabuuchi, T. Hirade, M. Fujinami, R. Awaji, N. Oshima, K. Takai, K. Sugita and Y. Taira	53
 Momentum Microscope Study of a Kagome Superconductor CsV₃Sb₅ [6U] T. Kato, K. Nakayama, Y. Li, Z. Wang, Y. Yao, F. Matsui, T. Takahashi and T. Sato	54

Probing Vacancy-type Defects in Ce:LuAG Scintillators by GiPALS Experiment and DFT Calculation [1U] M. Kitaura, Y. Taira and S. Watanabe	55
LCS-gamma Induced Positron Annihilation Study for the Dynamics of Defect Behavior in Bulk Materials [1U] F. Hori, S. Araki, K. Sugita and Y. Taira	56
Effect of the Particle Size on the Positron Annihilation Lifetime and Relative Intensity of CeO₂ Nanoparticles [1U] S. Dohshi, K. Maeda, Y. Taira, H. Toyokawa and T. Hirade	57
Mo LIII-Edge XANES Study of Highly Active MoC_x Species in Mo-V Modified H-MFI Catalysts for Methane Dehydroaromatization [2A] K. Kuramochi, R. Yamazaki, Y. Sonobe, Y. Uchimura and H. Aritani	58
Evaluation of the Electronic State of MgO by NEXAFS Spectroscopy [2A] E. Kobayashi, K. K. Okudaira, S. Yoshioka and A. Inoishi	59
Sintering Behavior of Mg-Doped Hydroxyapatite Nano Particles [2A] H. Murata, R. Kawanabe and A. Nakahira	60
Local Structure around Mg in Mg_{1-x}Ni_xAl₂O₄ [2A] S. Yoshioka, K. Yasuda, S. Matsumura, E. Kobayashi and K. Okudaira	61
Local Structure Investigations of Zn in ZnAl₂O₄ Induced on Swift Heavy Ion Irradiations [2A] S. Yoshioka, K. Yasuda, S. Matsumura, E. Kobayashi and K. Okudaira	62
UPS Spectroscopy of TFP Doped P3HT/PCBM Thin Films [2B] K. K. Okudaira and Y. Hoshi	63
Valence and In-gap states of a Polyethylene Model Oligomer, C₄₄H₉₀, Film Studied by Conventional and High-Sensitivity Photoelectron Spectroscopy [2B, 7U] R. Nakazawa, M. Yoshizawa, S. Kera and H. Ishii	64
Structure Analysis on Helical Nanofilament of B4 Phase of Bent-core Liquid Crystals Mixed with Rod-like Cholesteric Liquid Crystals by Resonant Soft X-ray Scattering (RSoXS) at UVSOR [3U] Y. Takanishi, F. Araoka and H. Iwayama	65
Evaluation of Fluorescence Lifetimes of Wavelength Shifting Fibers for High-energy Particle Experiments [3B] K. Shintate, R. Abe, R. Ishiyama, T. Naitou, S. Nakamura, S. Sakano, J. Ohashi, Y. Tajima and H. Y. Yoshida	66
Thermoluminescence of LuAG Thick Film Scintillators Prepared via Chemical Vapor Deposition Process [3B] S. Matsumoto, S. Kurosawa and A. Ito	67
Temperature Dependence of Photoluminescence Properties of Li₂HfF₆ [3B] C. Fujiwara, S. Kurosawa and A. Yamaji	68

Reflectivity Spectra of $\text{Sm}_{0.9}\text{Ca}_{0.1}\text{S}$ in Vacuum Ultra Violet Region [3B]	69
Y. Yokoyama, K. Kishida, F. Matsunaga, M. Kanou, K. Takano, Y. Okamoto, H. S. Suzuki, K. Takehana, Y. Imanaka and K. Takenaka	
Optical Investigation on Fluoro-olefins in Vacuum-Ultraviolet for New Refrigerant Gas Development [3B]	70
K. Yamanoi, Y. Sakata, H. Iwayama, Y. Hasumoto, O. Yamamoto and M. Noumi	
Absorption Bands of Tl^+ Centers in CsI-based Ternary Crystals [3B]	71
S. Ito and T. Kawai	
Photoluminescence Properties of Cs_2ZrI_6 [3B]	72
S. Kodama and S. Kurosawa	
Structural Analysis of Unvulcanized Rubber by Scanning Transmission X-ray Microscopy [4U]	73
T. Ohigashi, F. Kaneko, H. Yuzawa and H. Kishimoto	
C-K Edge Spectra of Bound-rubber Structure in SBR Materials with Filler and/or Reagents [4U]	74
T. Ejima and Y. Tamura	
Analysis of Materials for Secondary Batteries by STXM [4U]	75
E. Hosono, D. Asakura, H. Yuzawa and T. Ohigashi	
Probing the Electronic Structure of Ni-Co Binary Oxide/Graphene Nanocomposites as Supercapacitor Electrodes by Scanning Transmission X-ray Microscope [4U]	76
H. W. Chang, T. C. Huang, T. Ohigashi, C. H. Chuang, Y. C. Tsai, C. L. Dong and W. F. Pong	
Development of Reflection XMCD Measurement Setup for the Investigation of Inner Structures of Magnetic Thin Films at UVSOR BL4B [4B]	77
K. Yamamoto, H. Iwayama, O. Ishiyama and T. Yokoyama	
Dirac Fermions and Topological Phase Transition in XMg_2Bi_2 ($X = \text{Ba}$ and Sr) [5U]	78
D. Takane, Y. Kubota, K. Nakayama, T. Kawakami, S. Souma, K. Sugawara, S. Ideta, K. Tanaka, T. Takahashi, K. Segawa and T. Sato	
Band-structure Reconstruction of $\text{Ca}_3\text{Ru}_2\text{O}_7$ Induced by K Adsorption [5U]	79
M. Horio, T. Wada, V. Granata, R. Fittipaldi, A. Vecchione, K. Tanaka, I. Matsuda and J. Chang	
Quadrupole Electronic Structure in Mn_{3-x}Ga Studied by Angle-resolved Photoemission Spectroscopy [5U]	80
J. Okabayashi, Y. Miura, K. Tanaka, K. Z. Suzuki and S. Mizukami	
Change of the Fermi Surface of $\text{Bi}_2\text{Sr}_2\text{CaCu}_2\text{O}_{8+\delta}$ Observed by ARPES [5U]	81
Y. Tsubota, S. Kumar, Y. Miyai, K. Tanaka, S. Ishida, H. Eisaki, S. Nakagawa, T. Kashiwagi, M. Arita, K. Shimada and S. Ideta	

CDW-induced Electronic Reconstruction in a Kagome Metal KV_3Sb_5 [5U]	82
T. Kato, K. Nakayama, T. Kawakami, A. Moriya, Yongkai Li, Z. Wang, S. Ideta, K. Tanaka, T. Takahashi, Y. Yao and T. Sato	
Electronic Structure of VNb_3S_6: a Transition-metal Intercalated NbS_2 [5U]	83
M. Horio, T. Wada, S. Okazaki, K. Tanaka, T. Sasagawa and I. Matsuda	
Angle-resolved Photoemission Study of Zr_3SnC_2 [5U]	84
T. Ito, M. Mita, D. Pinek, M. Nakatake, K. Tanaka and T. Ouisse	
Fermi Surface Measurements of $TiSe_2$ with the CDW Transition [5U]	85
S. Tanaka, K. Ueno and K. Tanaka	
Temperature Dependence of Electronic Structure in Pb-doped $La(O,F)BiS_2$ Superconductor [5U]	86
N. Kataoka, L. Y. Jun, T. Setoguchi, S. Demura and T. Yokoya	
Evaluation of Self-Energy in Overdoped Bi2201 by Angle-Resolved Photoemission Spectroscopy [5U]	87
Y. Miyai, S. Kumar, T. Kurosawa, M. Oda, S. Ideta and K. Shimada	
Multi-atom Resonance Photoemission from the Valence Band of $TiSe_2$ [6U]	88
S. Tanaka, K. Ueno, K. Fukutani and F. Matsui	
Temperature-dependent Electronic Structure of η-Mo_4O_{11} Revealed by Photoelectron Momentum Microscopy [6U]	89
T. Kobayashi, E. Iwamoto, K. Sakamoto, F. Matsui and S. Suga	
Characterization of CVD Graphene on $Ir(111)/\alpha$-$Al_2O_3(0001)$ by Photoelectron Momentum Microscope [6U]	90
E. Hashimoto, K. Tamura, H. Yamaguchi, F. Matsui and S. Koh	
Vibrational Spectroscopy of Pentacene Single Crystals in the Mid to Far Infrared Region and its Temperature Dependence [6B]	91
J. Miyamoto, A. Sugiyama, K. Yamauchi and Y. Nakayama	
Spectral Evidence of Current-Induced Local-to-Nonlocal Transition of SmS [6B]	92
H. Watanabe, S. Tatsukawa, K. Imura, H. S. Suzuki, N. K. Sato and S. Kimura	
Structural Analysis of Fiber Biomaterials by Synchrotron-Radiation Infrared Microspectroscopy [6B]	93
T. Kawasaki, F. Teshima and K. Tanaka	
Low-energy ARPES Study of Iron-chalcogenide High-temperature Superconductors [7U]	94
K. Nakayama, T. Kato, A. Moriya, F. Nabeshima, N. Shikama, T. Ishikawa, Y. Sakishita, S. Ideta, K. Tanaka, T. Takahashi, A. Maeda and T. Sato	
Elucidations of Electronic Structure and the Many-body Interactions of Organic Molecular Materials [7U]	95
K. Fukutani, Y. Hasegawa, M. Murakami, D. Okaue, K. Fukui, H. Ishii, K. Tanaka and S. Kera	

Dirac-cone and Saddle-point Energy Bands in a Kagome Superconductor AV_3Sb_5 [7U]	96
K. Nakayama, T. Kato, Y. Li, Z. Wang, K. Tanaka, T. Takahashi, Y. Yao and T. Sato	
Angle-resolved Photoemission Study of TPP[FePc(CN)₂]₂ [7U]	97
T. Ito, T. Hoshina, K. Tanaka, M. Matsuda and N. Hanasaki	
Relationship between Chemical Pressure Effect and Electronic Structure in $R_{1-x}Ce_xOBiS_2$ ($R=Nd, La$) [7U]	98
N. Kataoka, T. Wakita, Y. Hanada, M. Nagao and T. Yokoya	
Photoluminescence Properties of Cs_2ZnCl_4 and Cs_3ZnCl_5 with Vacuum Ultraviolet Excitation [7B]	99
K. Takahashi, M. Koshimizu, Y. Fujimoto and K. Asai	
Investigation of Gamma-ray-irradiated Oxide Glasses for Deep Ultraviolet Detector with High Efficiency [7B]	100
T. Shimizu, K. Shinohara, D. Umeno, K. Yamanoi and N. Sarukura	
III-3. Chemistry	103
 Solvent-Induced Transition of Polymorphological Chiral Supermolecular Architectures in Bent-Core Liquid Crystal Dimer/Nematic Binary Mixtures as Studied by Resonant Soft X-ray Scattering (RSoXS) at UVSOR [3U]	105
F. Araoka, Y. Takanishi, K. V. Le and H. Iwayama	
Energy-Dependence of Photoelectron Circular Dichroism of Chiral Molecules [1U]	106
H. Kohguchi, Y. Hikosaka, T. Kaneyasu, S. Wada, H. Ohta, M. Fujimoto, M. Katoh and Y.-I. Suzuki	
Photoionization of Atoms by Double-pulsed Radiation from a Tandem-Undulator [1U]	107
T. Kaneyasu, Y. Hikosaka, S. Wada, M. Fujimoto, H. Ota, H. Iwayama and M. Katoh	
Electronic State Changes of Cu Nanoparticles on Rutile $TiO_2(110)$ by CO Exposure [2B]	108
K. Mitsuhashi, K. Ide, H. Takatani, Y. Hasegawa and M. Takizawa	
X-ray Absorption Spectra of Aqueous Cellobiose [3U]	109
T. Sasaki and D. Akazawa	
X-ray Absorption Spectroscopy Study of 4-MBA on Gold Surfaces [3U]	110
I. Sakaida, S. Ohno, M. Nagasaka	
Resonant Soft X-ray Scattering Equipment Evaluated by Chicken Leg's Collagens and 100-nm Silica Nanoparticles [3U]	111
H. Iwayama, F. Araoka and Y. Takanishi	
Oxygen K-edge X-ray Absorption Spectroscopy of Aqueous Dimethyl Sulfoxide Solutions at Different Concentrations [3U]	112
M. Nagasaka	

Carbon K-edge X-ray Absorption Spectroscopy of Aqueous Ethanol Solutions at Different Concentrations [3U] M. Nagasaka, M. Bouvier, H. Yuzawa and N. Kosugi	113
The C–Si Bond Length of Organosilicon Compounds in Organic Solvent Probed by Carbon K-edge X-ray Absorption Spectroscopy [3U] S. Okumura, M. Nagasaka, H. Takaya and Y. Uozumi	114
Direct Observation of a High Valent Oxo Species of a μ-Nitrido-Bridged Iron Phthalocyanine Dimer Deposited on a Graphite Surface in Aqueous Solution by Soft X-ray Absorption Spectroscopy [3U] Y. Yamada and M. Nagasaka	115
Soft X-ray Absorption of Photocatalysts for Artificial Photosynthesis: A Feasibility Study under Ultraviolet Light Irradiation [3U] H. Onishi, T. Hirai, N. Ichikuni and T. Yoshida	116
Variation of the Resonance Band of Water in Soft X-Ray Absorption Spectra of Aqueous Acetone Solutions [3U] K. Okada, C. Sugahara, H. Iwayama and M. Nagasaka	117
Oxygen K-edge X-ray Absorption Spectroscopy of Molecular Oxygen Adsorbed on Lipid Bilayers [3U] F. Kumaki, M. Nagasaka, Y. Kinjo, R. Tero, Y. Okano, M. Fujimoto and J. Adachi	118
Position-Sensitive Soft X-ray Absorption Spectroscopy of Carbon-based Catalysts for Redox Flow Battery [4U] E. Hosono, D. Asakura, H. Yuzawa, T. Ohigashi and A. Ohira	119
Investigating Electrochemical Reactivity on Ni(OH)₂ Electrocatalyst in Alkaline Electrolytes [4U] J. Kim T. Ohigashi and J. Lim	120
Quadruple Auger Decay of the Xe 3d_{5/2} Core-Hole State Investigated by Multielectron–Ion Coincidence Spectroscopy [4B] Y. Hikosaka	121
Ion Branching Ratio for the Xe 4p Auger Decay Studied by Photoelectron–Ion Coincidence Spectroscopy [4B] Y. Hikosaka	122
Electronic Structure Analysis of Ni Complex Bearing <i>N</i>-Heterocyclic Carbene Ligand Using Ni L_{2,3}-edge X-ray Absorption Spectroscopy [4B] Y. Uetake, Y. Yamauchi and Y. Hoshimoto	123
Evaluation of Absorption Stability of a Hydrogen Absorption Cell [5B] M. Taguchi, M. Kuwabara, T. Katsumata, M. Tateyama, K. Yoshioka, Y. Suzuki, K. Goda, K. Inoue, A. Tomioka and A. Yamazaki	124


Polarization-dependent Photoelectron Intensity in Ca-doped Graphene [5U]

S. Ichinokura, K. Tokuda, K. Tanaka and T. Hirahara

127

Elucidation of the Function of Adsorbed Anions on the Surface of Cobalt Catalysts by Operando Observation [3U]

K. Harada, S. Tsunekawa, A. Sakai, M. Nagasaka and M. Yoshida

128

Evaluation of Interface Between Sapphire Substrate and UV Emitting Zinc Aluminate Phosphor Thin Films [3B]

H. Kominami, M. Endo, T. Kawashima, N. Sonoda, K. Inoue, N. Uesugi, K. Nie, A. Adachi, R. Ishihara, Y. Kamoi, A. Dorokhina and S. Kurosawa

129

Application of Atomically-thin Graphene to X-ray Astronomy: Soft X-ray Transmission Measurements [4U]

I. Mitsuishi, K. Kashiwakura, Y. Niwa, T. Ogawa, M. Hirota, Y. Tawara, R. Kitaura, P. Solís-Fernández, K. Kawahara, H. Ago, T. Taniguchi, K. Nomoto, H. Kodaka, T. Ohigashi, H. Yuzawa and K. Tanaka

130

Annealing Effect on the Vacuum Ultraviolet Transmission Spectrum of Amorphous Selenium [4B]

K. Hayashi

131

Magnetic Properties of CoPc/ γ' -Fe₄N Organic-inorganic Hybrid Interface [4B]

T. Miyamachi, H. Ono, Y. Umeda, K. Yamamoto, O. Ishiyama, T. Yokoyama and M. Mizuguchi

132

Enhancement of the Perpendicular Magnetic Anisotropy in N-surfactant Assisted FeCo Ordered Alloy Thin Films [4B]

T. Miyamachi, Y. Umeda, H. Ono, K. Yamamoto, O. Ishiyama, T. Yokoyama and M. Mizuguchi

133

ARPES from Si{111} Facet Surfaces on Three-dimensional Lined Structures on Si(001) Substrates [5U]

K. Hattori, L. N. Pamasí, Y. Sakai, H. Yang, T. Shimizu, Y. Ida, W. Imayama, S. Tanaka, A. N. Hattori, S. Suga and K. Tanaka

134

Electronic Structure of K Adsorbed SmS Surface [5U]

T. Nakamura, T. Nakaya, H. Sugihara, K. Tanaka, K. Imura, H. S. Suzuki, N. K. Sato and S. Kimura

135

Explorations for Spontaneously Formed Excitons in Narrow-gap Semiconductors and Semimetals [5U]

K. Fukutani, M. Murakami, C.I. Kwon, J. S. Kim, K. Tanaka and S. Kera

136

X-ray Absorption Spectroscopy Measurements of Au/Fe/MgO Sandwich Structure Sample for Study of Soft X-ray Second Harmonic Generation [5B]

T. Sumi, M. Horio, X. Zhang, T. Kato and I. Matsuda

137

Bromine Doping to Perylene Monolayer on Au(110): Photoelectron Momentum Microscopy [6U]

O. Endo, F. Matsui, S. Kera, W. -J. Chun, M. Nakamura, K. Amemiya and H. Ozaki

138

High-resolution Photoelectron Momentum Microscope Study on the Electronic Structure of Charge-density-wave Material [6U] K. Fukutani, S. Tanaka, F. Matsui and S. Kera	139
Twin-domain Boundary and Monoatomic Step of Graphite Surface Imaged by Photoelectron Momentum Microscopy [6U] F. Matsui, Y. Okano, H. Matsuda, T. Yano, E. Nakamura, S. Kera and S. Suga	140
Development of the Fabrication System for the μm-scale Ultra-thin Film at BL6U [6U] T. Nakamura, F. Matsui and S. Kimura	141
High-resolution Angle-resolved Photoemission Study on $\text{MnBi}_2\text{Se}_4/\text{Bi}_2\text{Se}_3/\text{MnBi}_2\text{Se}_4$ Sandwich Structure [7U] R. Fukushima, S. Ichinokura, K. Tanaka and T. Hirahara	142
Observation of Electronic Structure of $\text{YbCu}_2/\text{Cu}(111)$ Surface Alloy [7U] H. Sugihara, T. Nakamura, Y. Chen, K. Tanaka and S. Kimura	143
Electrochemical Attenuated Total Reflectance Ultraviolet (EC-ATR-UV) Spectroscopy Applied for Organic Semiconductor / Ionic Liquids Interface [7B] I. Tanabe, Y. Hanamori and K. Fukui	144
III-5. Life, Earth and Planetary Sciences	147
 Hayabusa2 Returned Samples: Unique and Pristine Record of Solar System Materials from Asteroid Ryugu [4U] M. Ito, N. Tomioka, M. Uesugi, A. Yamaguchi, N. Imae, N. Shirai, T. Ohigashi, M. Kimura, M-C. Liu, R. C. Greenwood, K. Uesugi, A. Nakato, K. Yogata, H. Yuzawa, Y. Kodama, A. Tsuchiyama, M. Yasutake, R. Findlay, I. A. Franchi, J. A. Malley, K. A. McCain, N. Matsuda, K. D. McKeegan, K. Hirahara, A. Takeuchi, S. Sekimoto, I. Sakurai, I. Okada, Y. Karouji, T. Yada, M. Abe, T. Usui, S. Watanabe and Y. Tsuda	149
Study of Pygmy Dipole Resonance using Linearly Polarized Photon Beam [1U] T. Shizuma, M. Omer, T. Hayakawa, K. Ali, H. Zen, H. Ohgaki, S. Miyamoto, K. Sugita and Y. Taira	150
X-ray Absorption Spectra of Lipid Bilayer Membranes in Aqueous Solutions [3U] R. Tero, Yu Kinjo and M. Nagasaka	151
Evaluation of Exposure-Effects on Biomolecules for the Molecular Mapping of Biological Specimens Using STXM [4U] A. Ito, K. Shinohara, A. Matsuura, S. Toné, M. Torigata, K. Tohya, H. Yuzawa and T. Ohigashi	152
Physicochemically Characterization of Dust/Salt Mixtures Originating from the Source of East Asian Dust Storms [4U] J. Li, W. Liu, L. Li, T. Ohigashi, M. Hallquist, S. Wang and X. Kong	153

Development of Multilayer-coated Mirrors for the Next Generation of the Inner Magnetospheric Imaging [5B] K. Inoue, A. Tomioka, J. Yang, H. Lin, K. Yoshioka and I. Yoshikawa	154
Performance Evaluation of an Optical Filter Aiming for Observation of Atmosphere of Comets [5B] Y. Sasaki, Y. Suzuki, K. Yoshioka, M. Taguchi, M. Kuwabara, H. Akadama, T. Kosugi, H. Lin and J. Yang	155
Performance Evaluation of UV Absorption Filter Onboard Spacecraft [5B] Y. Suzuki, M. Kuwabara, M. Taguchi, K. Yoshioka, T. Katsumata, M. Tateyama, K. Goda, A. Yamazaki, K. Inoue and A. Tomioka	156
The Effect of Space Weathering on The PAH Wavelength of Interstellar Dust Organic Matter [7B] J. Yang, H. Lin, K. Inoue, A. Tomioka, K. Yoshioka and I. Yoshikawa	157
A study on Space weathering of Carbonaceous Meteorites by Far-ultraviolet Spectroscopy [7B] H. Akadama, Y. Suzuki, J. Yang and K. Yoshioka	158
IV. List of Publications	159
V. Workshops	165
UVSOR Symposium 2021	167
The 4th workshop on prospects and construction plan of the next generation synchrotron radiation facility	170
2021 IMS Open House Event	172

I

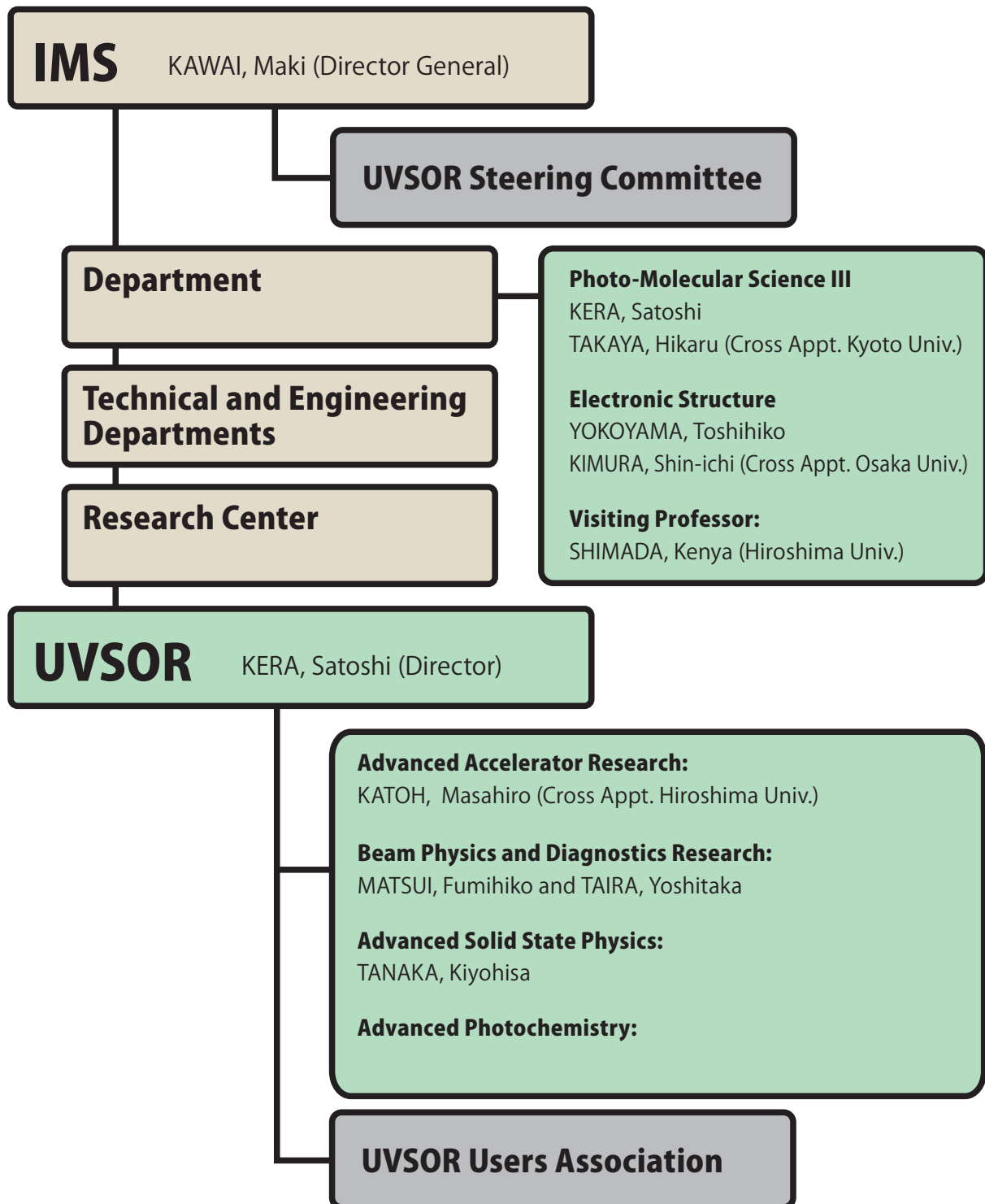
Organization and Staff List



UVSOR Synchrotron Facility Organization

Mar. 2022

I



Staff List

Mar. 2022

UVSOR Staff

Director

KERA, Satoshi	Professor	kera@ims.ac.jp
---------------	-----------	----------------

Division of Advanced Accelerator Research

KATOH, Masahiro	Project Professor (Cross Appt. Hiroshima Univ.)	mkatoh@ims.ac.jp	
FUJIMOTO, Masaki	Assistant Professor	mfmoto@ims.ac.jp	(until Mar. 2022)
SALEHI, Elham	Project Research Staff	elham@ims.ac.jp	

Division of Beam Physics and Diagnostics Research

MATSUI, Fumihiko	Professor	matui@ims.ac.jp
TAIRA, Yoshitaka	Associate Professor	yostaira@ims.ac.jp
OHIGASHI, Takuji	Associate Professor (Cross Appt. KEK)	ohigashi@ims.ac.jp
SUGITA, Kento	Assistant Professor	ksugita@ims.ac.jp
MATSUDA, Hiroyuki	Project Research Staff	hmatsuda@ims.ac.jp

Division of Advanced Solid State Physics

TANAKA, Kiyohisa	Associate Professor	k-tanaka@ims.ac.jp
------------------	---------------------	--------------------

Division of Advanced Photochemistry

IWAYAMA, Hiroshi	Assistant Professor	iwayama@ims.ac.jp
------------------	---------------------	-------------------

Technical Staff

HAYASHI, Kenji	Engineer (Unit Leader)
NAKAMURA, Eiken	Chief Engineer
MAKITA, Seiji	Engineer
YAMAZAKI, Jun-ichiro	Chief Technician
SAKAI, Masahiro	Chief Technician
YANO, Takayuki	Chief Technician
OKANO, Yasuaki	Chief Technician
TESHIMA, Fumitsuna	Chief Technician
KONDO, Naonori	Chief Technician
YUZAWA, Hayato	Technician
OTA, Hiroshi	Technician
HORIGOME, Toshio	Technical Fellow

I

OKUDA, Taichi	Hiroshima Univ.	(until Mar. 2022)
KUMIGASHIRA, Hiroshi	Tohoku Univ.	(until Mar. 2022)
HATSUI, Takaki	RIKEN	(until Mar. 2022)
KANEMITSU, Yoshihiko	Kyoto Univ,	
KIMURA, Shin-ichi	Osaka Univ.	
HARADA, Yoshihisa	Univ. of Tokyo	
FUKUSHIMA, Takanori	Tokyo Institute of Technology	
KAWAI, Maki	IMS, Director General	(until Mar. 2022)
AKIYAMA, Shuji	IMS	(until Mar. 2022)
KUSAMOTO, Tetsuro	IMS	(until Mar. 2022)
YAMAMOTO, Hiroshi	IMS	(until Mar. 2022)
YOKOYAMA, Toshihiko	IMS	
SHIGEMASA, Eiji	IMS	
HAYASHI, Kenji	IMS	
NAKAMURA, Toshikazu	IMS	

UVSOR Users Association (* Chair)

KIMURA, Shin-ichi *	Osaka Univ.	(until Mar. 2022)
KITaura, Mamoru	Yamagata Univ.	
OKABAYASHI, Jun	Univ. of Tokyo	(until Mar. 2022)
YAMANE, Hiroyuki	PhoSIC	(until Mar. 2022)
HIKOSAKA, Yasumasa	Toyama Univ.	

The background is a vibrant teal color with a complex geometric design. It features several overlapping circular patterns, some with dashed lines and others with small dots. Diagonal lines and light rays emanate from the top left, creating a sense of depth and movement. The overall aesthetic is modern and technical.

II

Current Status of Light Sources and Beamlines

Light Source in 2021

Yoshitaka Taira

UVSOR Synchrotron Facility, Institute for Molecular Science, Okazaki 444-8585, Japan

In FY2021, UVSOR-III was scheduled to operate for 36 weeks from end of May 2021 to March 2022 for users. However, the user operation time was cut by two weeks due to a vacuum leak incident and its restoration work. Finally, the 300 mA multi-bunch top-up mode was operated for 32 weeks and the 35 mA single-bunch top-up mode for 2 weeks. Monthly statistics of operation time and integrated beam current are shown in Figure 1.

From April 1 to May 7 was a shutdown period, during which periodic inspections and replacement of sextupole coils were conducted. The details of the replacement of sextupole coils are described in last year's activity report [1]. The replacement of the sextupole coils was conducted over a multi-year period, and all replacements were completed during this period. The two weeks following the shutdown were allocated to the adjustment of the accelerator and beamlines.

The vacuum leak accident over the entire circumference of the storage ring was occurred in July 2021 and was caused by water leaking from the cooling water pipe of the four-quadrant slit used to cut out the synchrotron radiation, which is located between the manual valve and the fast-acting valve immediately after the bending magnet. It took a total of five weeks for baking, photobaking, and adjustment of the accelerator and beamlines before user operation resumed.

Minor machine problems including the failure of the beam position monitor module due to an instantaneous voltage drop and the failure of the RF-frequency signal oscillator, both of which were addressed by replacing them with alternatives or repairing them.

The weekly operation schedule is as follows. Mondays are assigned to machine studies from 9:00 AM to 9:00 PM. User operation is assigned Tuesday through Friday, with Tuesday and Wednesday operating from 9:00 AM to 9:00 PM, and Thursday from 9:00 AM to 9:00 PM on Friday for 36 continuous hours. Thus, the user's beam time per week is 60 hours.

We started a design study for the future plan of UVSOR-IV. As a first step, we have analyzed the present magnetic lattice, seeking a possibility to reduce the emittance more [2]. Although, we did not find a solution to drastically reduce emittance, we have found a few interesting solutions that achieved lower emittance than the current situation. As the second step, we have started designing a totally new storage ring, which is close to the diffraction limit in the VUV range.

The light source development and utilization beamline BL1U, constructed under the support of Quantum Beam Technology Program by MEXT/JST,

continue to develop new light source technologies and their applications such as free electron laser, coherent harmonic generation, coherent synchrotron radiation, coherent control [3], laser Compton scattered gamma rays [4], and optical vortices.

In particular, in April 2021, a new vacuum duct for laser injection was installed in the storage ring, shown in Figure 2. To solve the space constraint, a manual valve and injection windows were integrated. By using this injection windows, the gamma ray intensity was increased by a factor of 10 or more.

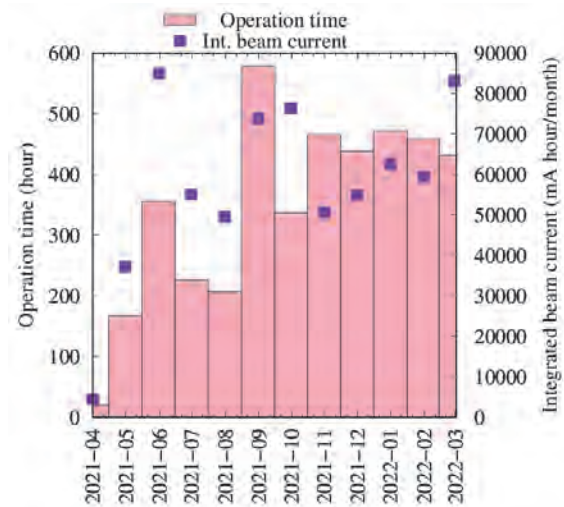


Fig. 1. Monthly statistics in FY2021.

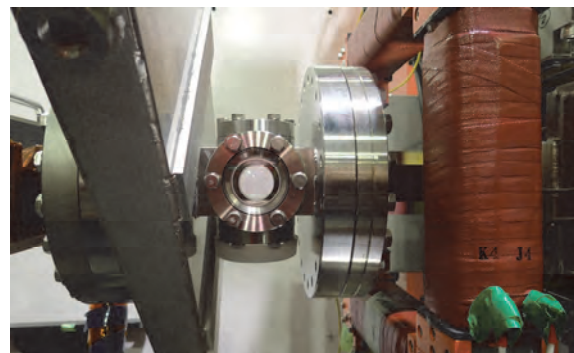


Fig. 2. Laser injection vacuum duct installed in April 2021.

- [1] M. Katoh, UVSOR Activity Report (2021).
- [2] E. Salehi and M. Katoh, Proceedings of IPAC2021 (2021) 3970.
- [3] T. Kaneyasu *et al.*, Phys. Rev. Lett. **126** (2021) 113202.
- [4] K. Ali *et al.*, Appl. Sci. **11** (2021) 3415.

UVSOR Accelerator Complex

Injection Linear Accelerator

Energy	15 MeV
Length	2.5 m
Frequency	2856 MHz
Accelerating RF Field	$2\pi/3$ Traveling Wave
Klystron Power	1.8 MW
Energy Spread	~ 1.6 MeV
Repetition Rate	2.6 Hz

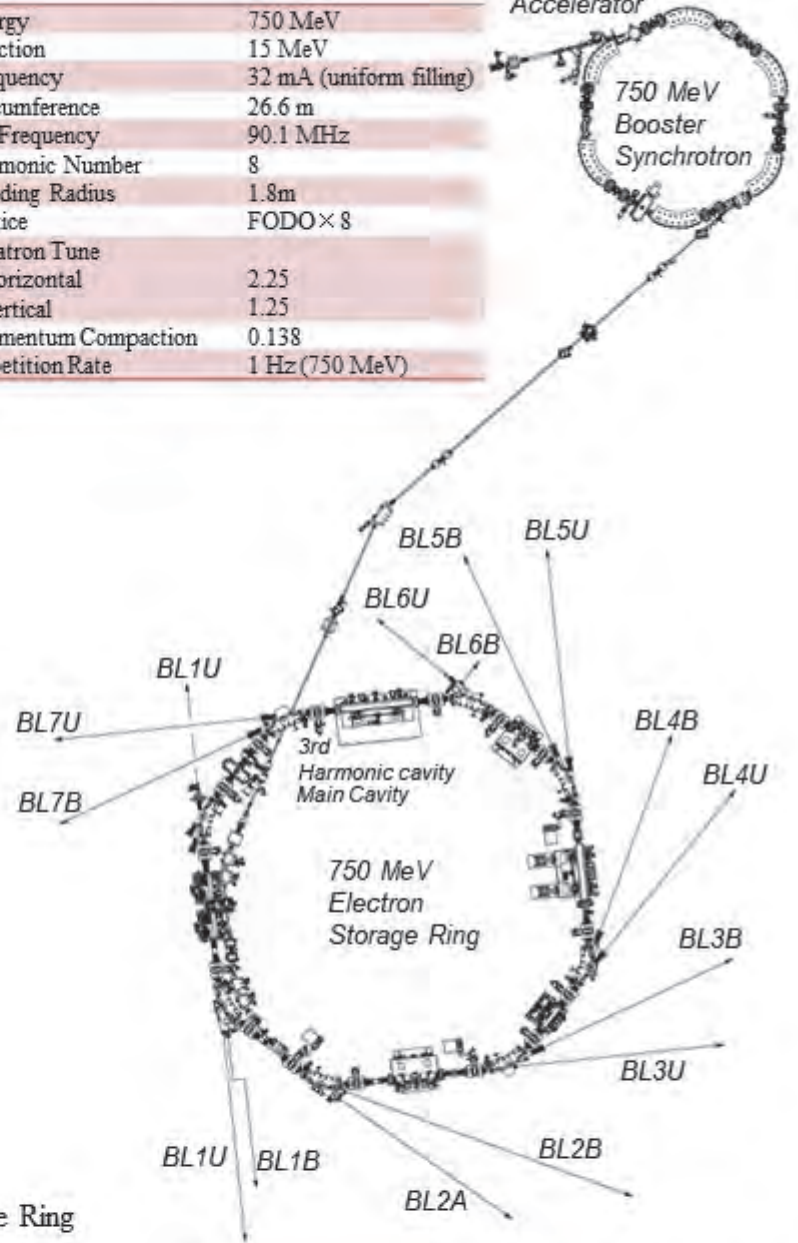
UVSOR-III Storage-Ring

Energy	750 MeV
Injection Energy	750 MeV
Maximum Storage Current	500 mA (multi bunch) 100 mA (single bunch)
Normal operation current (Top-up mode)	300 mA (multi bunch) 50 mA (single bunch)
Natural Emittance	17.5 nm-rad
Circumference	53.2 m
RF Frequency	90.1 MHz
Harmonic Number	16
Bending Radius	2.2 m
Lattice	Extended DBA $\times 4$
Straight Section	$(4\text{ m} \times 4) + (1.5\text{ m} \times 4)$
RF Voltage	120 kV
Betatron Tune	
Horizontal	3.75
Vertical	3.20
Momentum Compaction	0.030
Natural Chromaticity	
Horizontal	-8.1
Vertical	-7.3
Energy Spread	5.26×10^{-4}
Coupling Ratio	1%
Natural Bunch Length	128 ps

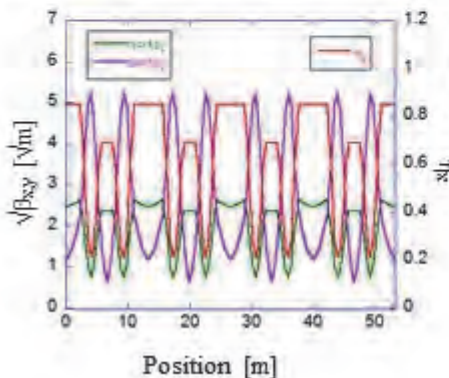
Booster Synchrotron

Energy	750 MeV
Injection	15 MeV
Frequency	32 mA (uniform filling)
Circumference	26.6 m
RF Frequency	90.1 MHz
Harmonic Number	8
Bending Radius	1.8m
Lattice	FODO $\times 8$
Betatron Tune	
Horizontal	2.25
Vertical	1.25
Momentum Compaction	0.138
Repetition Rate	1 Hz (750 MeV)

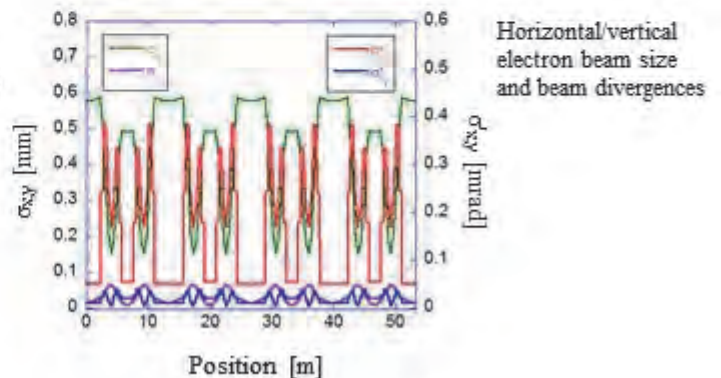
15 MeV
Linear
Accelerator



Electron Beam Optics of UVSOR-III Storage Ring



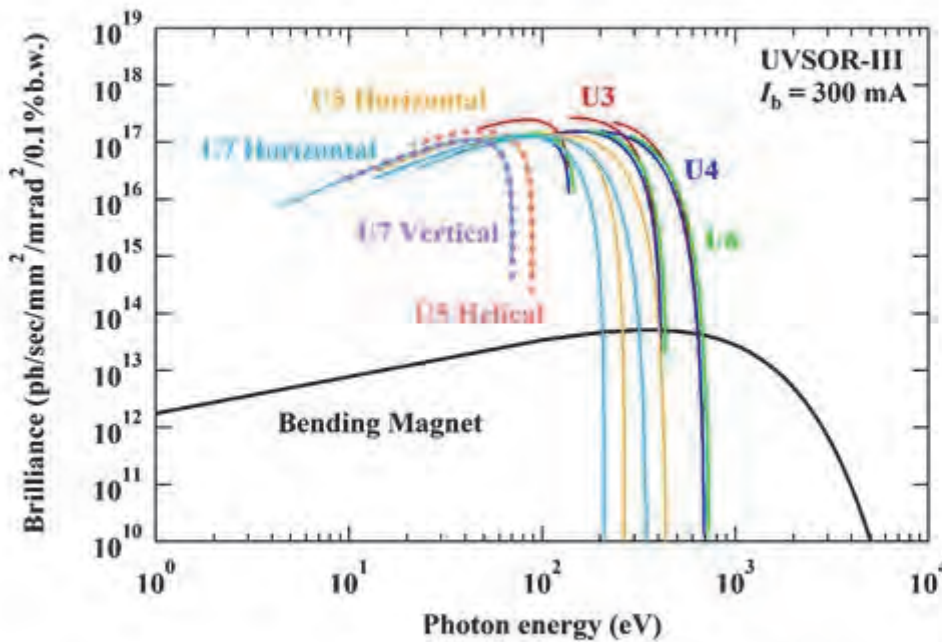
Horizontal/vertical betatron functions and dispersion function



Horizontal/vertical electron beam size and beam divergences

Insertion Device

II



Brilliance of radiation from the insertion devices (U3, U4, U5, U6 and U7) and a bending magnet of UVSOR-III

U1 Apple-II Undulator /

Optical Klystron

Number of Periods	10+10
Period length	88 mm
Pole Length	0.968 m + 0.968 m
Pole Gap	24-200 mm
Deflection Parameter	7.36 (Max. Horizontal) 4.93 (Max. Vertical) 4.06 (Max. Helical)

U3 In-vacuum Undulator

Number of Periods	50
Period length	38 mm
Pole Length	1.9 m
Pole Gap	16.5-40 mm
Deflection Parameter	1.8-0.24

U4 In-vacuum Undulator

Number of Periods	26
Period length	38 mm
Pole Length	0.99 m
Pole Gap	13-40 mm
Deflection Parameter	2.4-0.19

U5 Apple-II

Variable Polarization Undulator

Number of Periods	38
Period length	60 mm
Pole Length	2.28 m
Pole Gap	24-190 mm
Deflection Parameter	3.4 (Max. Horizontal) 2.1 (Max. Vertical) 1.8 (Max. Helical)

U6 In-vacuum Undulator

Number of Periods	26
Period length	36 mm
Pole Length	0.94 m
Pole Gap	13-40 mm
Deflection Parameter	1.78 - 0.19

U7 Apple-II

Variable Polarization Undulator

Number of Periods	40
Period length	76 mm
Pole Length	3.04 m
Pole Gap	24-200 mm
Deflection Parameter	5.4 (Max. Horizontal) 3.6 (Max. Vertical) 3.0 (Max. Helical)

Bending Magnets

Bending Radius	2.2 m
Critical Energy	425 eV

Beamlines in 2021

Fumihiko Matsui

UVSOR synchrotron Facility, Institute for Molecular Science

II

UVSOR is one of the highest-brilliance light sources in the extreme-ultraviolet region among the synchrotron radiation facilities with electron energies of less than 1 GeV. The low natural emittance of the UVSOR-III storage ring, 17.5 nm-rad, was accomplished after the successful completion of the storage ring upgrade project (the UVSOR-III project) in 2012. Eight bending magnets and six insertion devices are available as synchrotron light sources at UVSOR. There are a total of fourteen operational beamlines. Twelve of them are the so-called “Public beamlines”, which are open to scientists from universities and research institutes belonging to the government, public organizations, private enterprises and also those from foreign countries. The beamline BL6U is the “In-house beamlines”, and are dedicated to the use of research groups within Institute for Molecular Science (IMS). The beamline BL1U is a partially “Public” and partially “In-house” beamline. There is one tender X-ray (TX) station equipped with a double-crystal monochromator, seven extreme ultraviolet (EUV) and soft X-ray (SX) stations with grazing incidence monochromators, three vacuum ultraviolet (VUV) stations with normal incidence monochromators, two infrared (IR) stations equipped with Fourier Transform interferometers, and one direct radiation station located after two tandem undulators, as shown in the appended table (next page) for all available beamlines at UVSOR in 2021. The details of the updates for undulator beamlines are the followings.

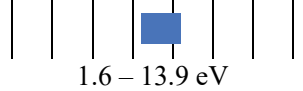
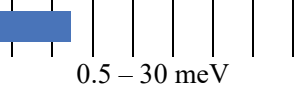
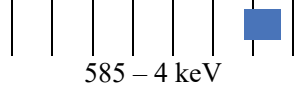


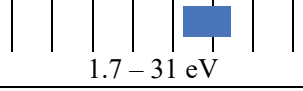
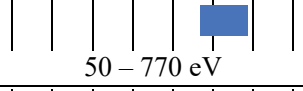
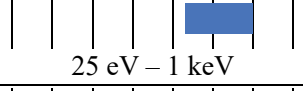
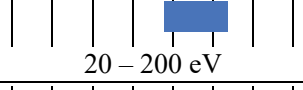
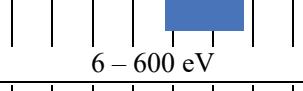

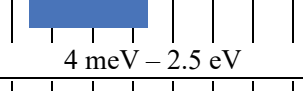
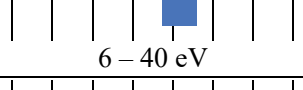
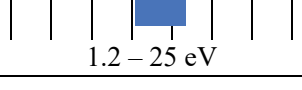
- In **BL1U**, the development of a new light source and the utilization of gamma-rays are being carried out. Users are provided with gamma-ray induced positron annihilation spectroscopy that can analyze nanometer-order defects in bulk materials. To increase the counting rate of annihilation gamma rays, an array detector with eight BaF₂ scintillators was developed. The measurement can be completed in a few hours for metal samples.
- In **BL3U**, the ultrathin-liquid cell for low-energy XAS has been developed. The studies of local structures of several aqueous solutions and various chemical processes in solution such as catalytic and electrochemical reactions, and laminar flows in microfluidics by using operando XAS in C, N, and O K-edges were demonstrated. Moreover, we have established an argon gas window that is effective from 60 to 240 eV with the removal of high-order X-rays, which will develop chemical research since it includes K-edges of Li and B and L-edges of Si, P, S, and Cl. Resonant soft X-ray scattering for soft materials is also applicable.
- **BL4U**, which is equipped with a scanning transmission soft X-ray microscope (STXM), is actively used not only by academic users but also by many industrial users. In FY2020, it became possible to image the lithium K-edge with a spatial resolution of 72 nm. Final adjustments for the airtight sample transport system and the sample transport container were carried out for the organic substance analysis of the Hayabusa2 returned samples for the summer of FY2021.
- In **BL5U**, high energy resolution angle-resolved photoemission spectroscopy (ARPES) is available. Users can now use so-called “deflector mapping” for all kinetic energies and lens modes by using the latest version of ARPES analyzer. An alkali-metal deposition system has been installed. Potassium for example can be deposited while the sample is still mounted on the manipulator at low temperatures. As part of the development of spin-resolved ARPES, a two-dimensional image of the spin-resolved spectrum of the Rashba splitting of Au(111) surface has been successfully obtained.
- At **BL6U**, one of the In-house beamlines, photoelectron momentum microscope (PMM), which is a new-concept multi-modal electronic structure analysis system with high resolution in real space and momentum space, has been installed and is in operation. Experiments such as valence band photoelectron spectroscopy on the micrometer scale and resonance photoelectron diffraction by soft X-ray excitation are performed. In FY2021, valence band study on graphenes, high-temperature superconductors, dichalcogenides, and organic molecular adsorbates were conducted in collaboration with several groups. In FY2022, we plan to further expand PMM's capabilities by introducing an additional 2D spin filter.
- At **BL7U**, high-energy resolution ARPES is available with extremely low energy of photons (6 eV~) using the low-temperature 6-axis manipulator with a sample temperature 4.5-350 K. In FY2022, the deflector-type detector for the hemispherical analyzer was installed to realize an effective 2D measurement with the automated manipulator control. Users can perform the measurement of the bulk sensitive electronic structure of solids and the high-throughput measurement for molecular materials using high-photoionization cross-section using low-excitation photon energy.

Those wishing to use the open and in-house beamlines are recommended to contact the appropriate beamline contact persons (see next page). Applications can be submitted at NOUS ([https:// nous.nins.jp/user/signin](https://nous.nins.jp/user/signin)). All users are required to refer to the beamline

manuals and the UVSOR guidebook, on the occasion of conducting the actual experimental procedures. For

updated information on UVSOR, please see <http://www.uvsor.ims.ac.jp>.

Beamlines at UVSOR

Beamline	Monochromator / Spectrometer	Energy Range	Targets	Techniques	Contact
BL1U	Free electron laser	 1.6 – 13.9 eV		(Irradiation)	Y. Taira yostaira@ims.ac.jp
BL1B	Martin-Puplett FT-FIR	 0.5 – 30 meV	Solid	Reflection Absorption	K. Tanaka k-tanaka@ims.ac.jp
BL2A	Double crystal	 585 – 4 keV	Solid	Reflection Absorption	F. Matsui matui@ims.ac.jp
BL2B	18-m spherical grating (Dragon)	 23 – 205 eV	Solid	Photoemission	S. Kera kera@ims.ac.jp
BL3U	Varied-line-spacing plane grating (Monk-Gillieson)	 40 – 800 eV	Gas Liquid Solid	Absorption Photoemission Photon-emission	H. Iwayama iwayama@ims.ac.jp
BL3B	2.5-m off-plane Eagle	 1.7 – 31 eV	Solid	Reflection Absorption Photon-emission	F. Matsui matui@ims.ac.jp
BL4U	Varied-line-spacing plane grating (Monk-Gillieson)	 50 – 770 eV	Gas Liquid Solid	Absorption (Microscopy)	T. Ohigashi ohigashi@ims.ac.jp
BL4B	Varied-line-spacing plane grating (Monk-Gillieson)	 25 eV – 1 keV	Gas Solid	Photoionization Photodissociation Photoemission	H. Iwayama iwayama@ims.ac.jp
BL5U	Spherical grating (SGM-TRAIN [†])	 20 – 200 eV	Solid	Photoemission	K. Tanaka k-tanaka@ims.ac.jp
BL5B	Plane grating	 6 – 600 eV	Solid	Calibration Absorption	K. Tanaka k-tanaka@ims.ac.jp
BL6U*	Variable-included-angle varied-line-spacing plane grating	 40 – 500 eV	Gas Solid	Photoionization Photodissociation Photoemission	F. Matsui matui@ims.ac.jp
BL6B	Michelson FT-IR	 4 meV – 2.5 eV	Solid	Reflection Absorption IR microscope	K. Tanaka k-tanaka@ims.ac.jp
BL7U	10-m normal incidence (modified Wadsworth)	 6 – 40 eV	Solid	Photoemission	K. Tanaka k-tanaka@ims.ac.jp
BL7B	3-m normal incidence	 1.2 – 25 eV	Solid	Reflection Absorption Photon-emission	F. Matsui matui@ims.ac.jp

Yellow columns represent undulator beamlines.

* In-house beamline.

BL1U

Light Source Development Station

▼ Description

BL1U is dedicated for developments and applications of novel light sources. This beamline is equipped with a dedicated tandem undulator for variable polarization with a buncher section, which can be used for free electron laser in the range from visible to deep UV, VUV coherent harmonic generation (CHG), and generation of spatiotemporal structured light such as an optical vortex beam, a vector beam and double-pulse wave packets. It is also equipped with a femto-second laser system synchronized with the accelerator, which is used for the generation of CHG, laser Compton scattered gamma-rays, and coherent THz radiation. Nowadays, material analysis by positron annihilation spectroscopy using laser Compton scattered gamma rays is actively used.

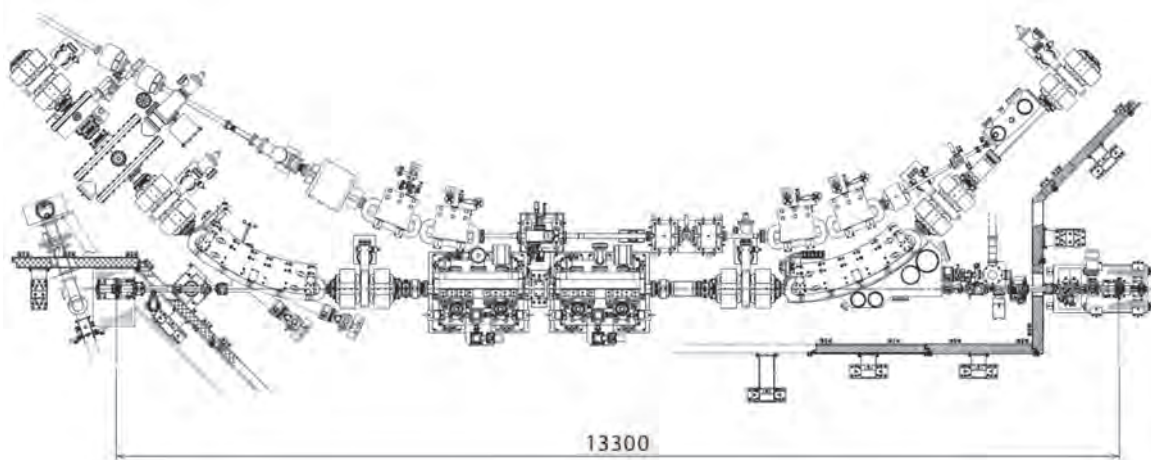


Fig. 1. Configuration of the free electron laser

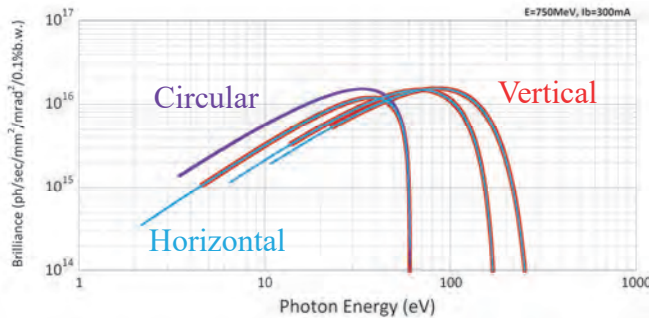


Fig. 2. Brilliance of BL1U Apple-II Undulator

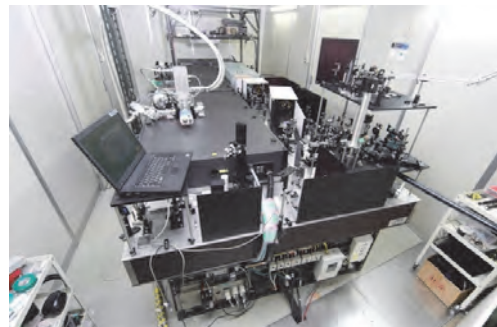


Fig. 3. Accelerator Synchronized Laser System

▼ Technical Data of FEL

Wave Length	199-800 nm
Spectral Band Width	~10 ⁻⁴
Polarization	Circular/Linear
Pulse Rate	11.26 MHz
Max. Ave. Power	~1 W

▼ Technical Data of Ti:Sa Laser

Wave Length	800 nm
Pulse Length	130 fsec
Oscillator	90.1 MHz
Pulse Energy	2.5 mJ 10 mJ 50 mJ
Repetition Rate	1 kHz 1 kHz 10 Hz

BL1B

Terahertz Spectroscopy Using Coherent Synchrotron Radiation

II

▼ Description

Coherent synchrotron radiation (CSR) is a powerful light source in the terahertz (THz) region. This beamline has been constructed for basic studies on the properties of THz-CSR. However, it can be also used for measurements of reflectivity and transmission spectra of solids using conventional synchrotron radiation.

The emitted THz light is collected by a three-dimensional magic mirror (3D-MM, M0) of the same type as those already successfully installed at BL43IR in SPring-8 and BL6B in UVSOR-II. The 3D-MM was installed in bending-magnet chamber #1 and is controlled by a 5-axis pulse motor stage (x , z translation; θ_x , θ_y , θ_z rotation). The acceptance angle was set at 17.5-34 degrees (total 288 mrad) in the horizontal direction. The vertical angle was set at ± 40 mrad to collect the widely expanded THz-CSR.

The beamline is equipped with a Martin-Puplett type interferometer (JASCO FARIS-1) to cover the THz spectral region from 4 to 240 cm^{-1} ($h\nu = 500 \mu\text{eV}$ -30 meV). There is a reflection/absorption spectroscopy (RAS) end-station for large samples (\sim several mm). At the RAS end-station, a liquid-helium-flow type cryostat with a minimum temperature of 4 K is installed.

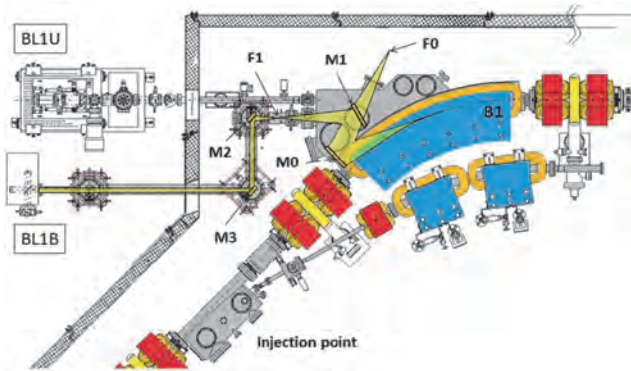


Fig. 1. Schematic top view of the beam extraction part of the THz-CSR beamline, BL1B. The three-dimensional magic mirror (3D-MM, M0) and a plane mirror (M1) are located in the bending-magnet chamber. A parabolic mirror (M2) is installed to form a parallel beam. The straight section (BL1U) is used for coherent harmonic generation (CHG) in the VUV region.

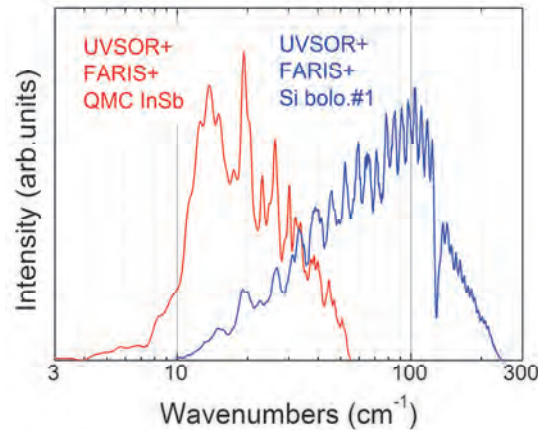


Fig. 2. Obtained intensity spectra with the combination of a light source (UVSOR), interferometer (FARIS-1), and detectors (Si bolometer and InSb hot-electron bolometer).

▼ Technical Data

Interferometer	Martin-Puplett (JASCO FARIS-1)
Wavenumber range (Energy range)	4-240 cm^{-1} (500 μeV -30 meV)
Resolution in cm^{-1}	0.25 cm^{-1}
Experiments	Reflection/transmission spectroscopy
Miscellaneous	Users can use their experimental system in this beamline.

BL2A

Soft X-Ray Beamline for Photoabsorption Spectroscopy

▼ Description

BL2A is a soft X-ray beamline for photoabsorption spectroscopy. The beamline is equipped with a pre-focusing mirror and a double-crystal monochromator [1]. The monochromator serves soft X-rays in the energy region from 585 to 4000 eV using several types of single crystals, such as beryl, KTP (KTiOPO₄), and InSb. The throughput spectra measured using a Si photodiode (AXUV-100, IRD Inc.) are shown in Fig. 1. The typical energy resolution ($E / \Delta E$) of the monochromator is approximately 1500 for beryl and InSb.

There is a small vacuum chamber equipped with an electron multiplier (EM) detector. Photoabsorption spectra for powdery samples are usually measured in total electron yield mode, with the use of the EM detector. In addition, a hemispherical electron analyzer for photoelectron spectroscopy is equipped.

Recently, a new omnidirectional photoelectron acceptance lens (OPAL) has been developed aiming to realize 2π -steradian photoelectron spectroscopy and photoelectron holography [2]. By combining OPAL and the existing hemispherical electron analyzer, a photoelectron spectrometer with high energy resolution can be realized, and a full range ($\pm 90^\circ$) 1D angular distribution can be measured at once. This upgrade is currently in the commissioning phase.

[1] Hiraya *et al.*, Rev. Sci. Instrum. **63** (1992) 1264.

[2] H. Matsuda and F. Matsui, Jpn. J. Appl. Phys. **59** (2020) 046503.

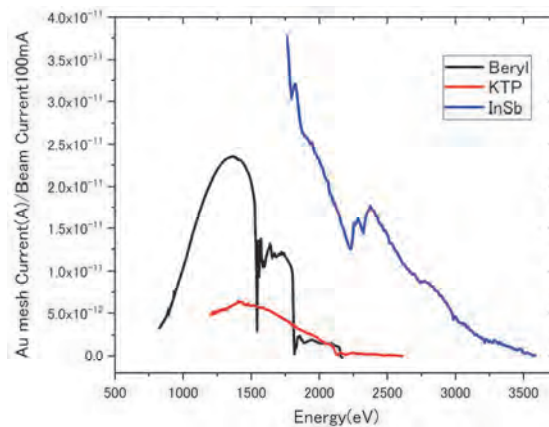


Fig. 1. Throughput spectra of the double-crystal monochromator at BL2A.

▼ Technical Data

Monochromator	Double crystal monochromator
Monochromator crystals: (2d value, energy range)	beryl (15.965 Å, 826–2271 eV), KTP (10.95 Å, 1205–3310 eV), InSb (7.481 Å, 1764–4000 eV), Ge (6.532 Å, 2094–4000 eV)
Resolution	$E/\Delta E = 1500$ for beryl and InSb
Experiments	Photoabsorption spectroscopy (total electron yield using EM and partial fluorescence yield using SDD)

BL2B

Photoelectron spectroscopy of molecular solids

II

▼ Description

This beamline previously dedicated for experiments in the field of gas phase photoionization and reaction dynamics. Then, the beamline has been reconstructed for photoelectron spectroscopy of molecular solids with a new end station, and experiments can be performed from May 2014. The monochromator is a spherical grating Dragon type with 18-m focal length. High throughput (1×10^{10} photons s^{-1}) and high resolution ($E/\Delta E = 2000 - 8000$) are achieved simultaneously under the condition of the ring current of 100 mA [1]. The optical system consists of two pre-focusing mirrors, an entrance slit, three spherical gratings (G1 - G3), two folding mirrors, a movable exit slit, and a refocusing mirror [2]. The monochromator is designed to cover the energy range of 23–205 eV with the three gratings: G1 (2400 lines mm^{-1} , $R = 18$ m) at 80–205 eV; G2 (1200 lines mm^{-1} , $R = 18$ m) at 40–100 eV; G3 (2400 lines mm^{-1} , $R = 9.25$ m) at 23–50 eV. The percentage of the second-order light contamination at $h\nu = 45.6$ eV is 23 % for G2 or 7 % for G3.

A UHV chamber is placed downstream of the refocusing mirror chamber and equipped silicon photodiode, sapphire plate Au mesh and filters for absolute photon flux measurement, monitor the photon-beam position, relative photon flux measurements and attenuate higher order light, respectively.

The new end station consists of a main chamber with a hemispherical analyzer (SCIENTA R3000) and a liquid-He-cooled cryostat (temperature range of 15-400 K) with 5-axis stage, a sample preparation chamber with a fast-entry load-lock chamber and a cleaning chamber with LEED, ion gun for sputtering and IR heating unit.

[1] M. Ono, H. Yoshida, H. Hattori and K. Mitsuke, Nucl. Instrum. Meth. Phys. Res. A **467-468** (2001) 577.

[2] H. Yoshida and K. Mitsuke, J. Synchrotron Radiation **5** (1998) 774.

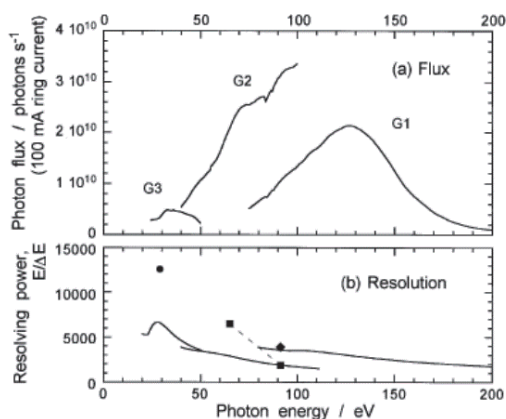


Fig. 1. Throughput from Dragon monochromator.

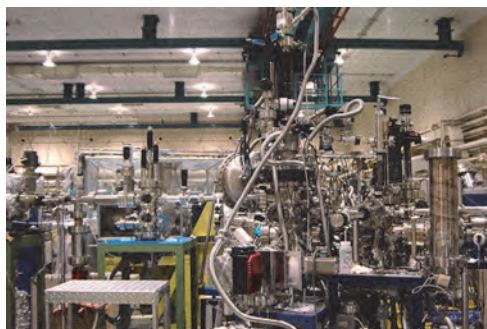


Fig. 2. End station of BL2B for photoelectron spectroscopy of molecular solids.

▼ Technical Data

Monochromator	18 m spherical grating Dragon-type
Wavelength Range	23-205 eV
Resolution	2000–8000 depending on the gratings
Experiments	Angle-resolved ultraviolet photoelectron spectroscopy

BL3U

Varied-Line-Spacing Plane Grating Monochromator for Molecular Soft X-Ray Spectroscopy

▼ Description

The beamline BL3U is equipped with an in-vacuum undulator composed of 50 periods of 3.8 cm period length. The emitted photons are monochromatized by the varied-line-spacing plane grating monochromator (VLS-PGM) designed for various spectroscopic investigations in the soft X-ray range. Three holographically ruled laminar profile plane gratings are designed to cover the photon energy range from 40 to 800 eV. The beamline has liquid cells for soft X-ray absorption spectroscopy (XAS) in transmission mode as shown in Fig. 1. The liquid cell is in the atmospheric helium condition, which is separated by a 100 nm thick Si_3N_4 membrane with the window size of $0.2 \times 0.2 \text{ mm}^2$ from the beamline in an ultrahigh vacuum condition. The thin liquid layer is assembled by using two 100 nm thick Si_3N_4 membranes. The thickness of the liquid layer is controllable from 20 to 2000 nm by adjusting the helium pressures around the liquid cell in order to transmit soft X-rays. Liquid samples are exchangeable *in situ* by using a tubing pump. The liquid cell has two types of windows: one is the liquid part to obtain the soft X-ray transmission of liquid (I), and the other is the blank part to obtain the transmission without liquid (I_0). We can obtain the reliable XAS spectra based on the Lambert-Beer law $\ln(I_0/I)$. Since the liquid cell is in the atmospheric condition, we can measure XAS of liquid samples in the real environment. *Operando* XAS observation of several chemical reactions such as catalytic, electrochemical reactions are also possible by using our liquid cells developed for these purposes.

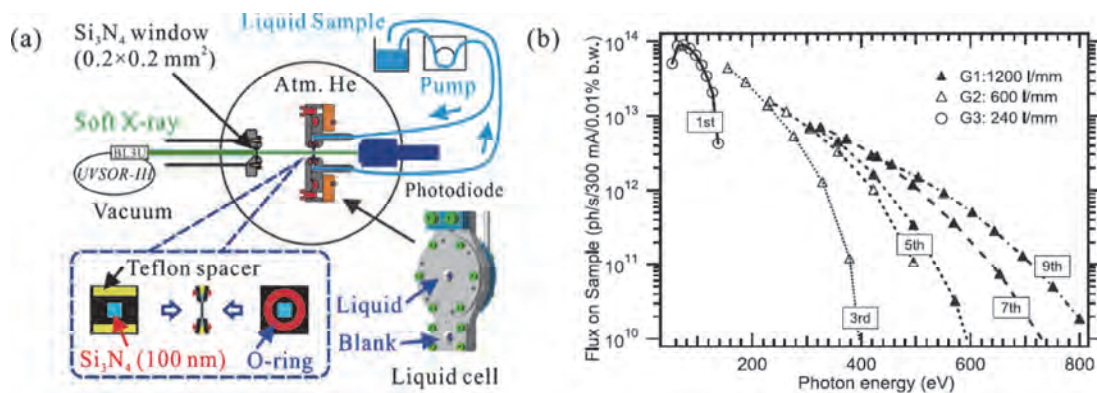


Fig. 1. (a) Schematics of a liquid cell for XAS in transmission mode settled in BL3U. The blowup shows a thin liquid layer assembled by two Si_3N_4 membranes with the thickness of 100 nm. (b) Flux at the sample position with the resolving power of $\lambda/\Delta\lambda=10^4$.

▼ Technical Data

Monochromator	Varied-line-spacing plane grating monochromator
Energy Range	40-800 eV
Resolution	$E / \Delta E > 10\ 000$
Experiments	Soft X-ray absorption spectroscopy of liquid in transmission mode

BL3B (HOTRLU)

VIS-VUV Photoluminescence and Reflection/Absorption Spectroscopy

▼ Description

BL3B has been constructed to study photoluminescence (PL) in the visible (VIS) to vacuum ultraviolet (VUV) region. This beamline consists of a 2.5 m off-plane Eagle type normal-incidence monochromator, which covers the VUV, UV, and VIS regions, i.e., the energy (wavelength) region of 1.7-31 eV (40-730 nm), with three spherical gratings having constant grooving densities of 1200, 600, and 300 l/mm optimized at the photon energies of ~ 20 , ~ 16 , and ~ 6 eV, respectively. The schematic side view and top view layouts are shown in Figs. 1(a) and 1(b), respectively. The FWHM of the beam spot at the sample position is 0.25 mm (V) \times 0.75 mm (H). Low energy pass filters (LiF, quartz, WG32, OG53) can be inserted automatically to maintain the optical purity in the G3 (300 l/mm) grating region (1.7 \sim 11.8 eV). Figure 2 shows the throughput spectra (photon numbers at a beam current of 300 mA) for each grating with entrance and exit slit openings of 0.1 mm (resolving power $E / \Delta E$ of ~ 2000 (G3, ~ 6.8 eV)). Since both slits can be opened up to 0.5 mm, a monochromatized photon flux of 10^{10} photons/s or higher is available for PL measurements in the whole energy region.

The end station is equipped with a liquid-helium-flow type cryostat for sample cooling and two detectors; one of which is a photomultiplier with sodium salicylate and the other a Si photodiode for reflection/absorption measurement. For the PL measurements in the wide energy region from VIS to VUV, two PL monochromators, comprising not only a conventional VIS monochromator but also a VUV monochromator with a CCD detector, are installed at the end station.

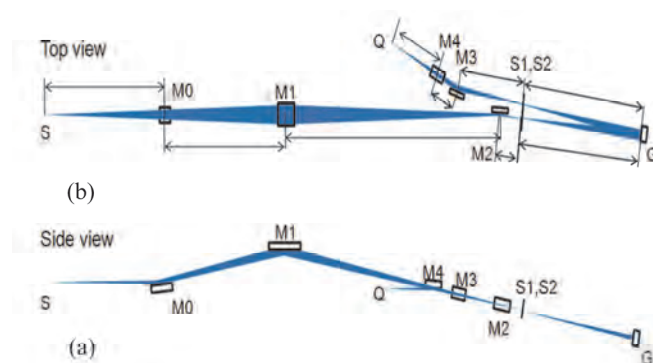


Fig. 1. Schematic layout of the BL3B (a) side view and (b) top view.

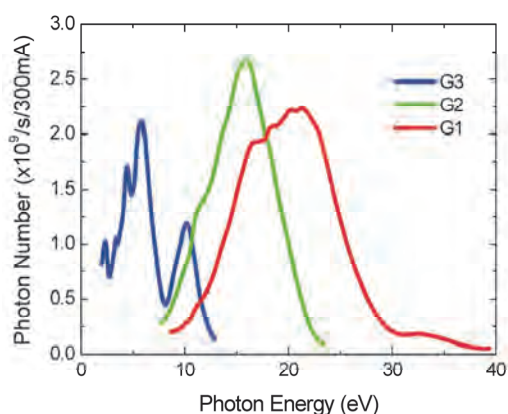


Fig. 2. Throughput spectra for each grating (G1:1200 l/mm, G2:600 l/mm and G3:300 l/mm) with $S1 = S2 = 0.1$ mm.

▼ Technical Data

Monochromator	-2.5 m normal-incidence monochromator
Energy range	1.7-31 eV (40~730 nm)
Resolution ($\Delta h\nu / h\nu$)	≥ 12000 (at ~ 6.9 eV, 0.02 mm slits, G1 (1200 l/mm))
Experiments	Photoluminescence, reflection, and absorption spectroscopy, mainly for solids

BL4U

Scanning Transmission X-ray Microscopy in the Soft X-ray Region

▼ Description

In the soft x-ray region, there are several absorption edges of light elements and transition metals. The near edge X-ray absorption fine structure (NEXAFS) brings detailed information about the chemical state of target elements. A scanning transmission X-ray microscope (STXM) in the soft X-ray region is a kind of extended technique of the NEXAFS with high spatial resolution. The STXM has a capability of several additional options, for example, in-situ observations, 3-dimensional observation by computed tomography and ptychography, by utilizing the characteristics of the X-rays. The STXM can be applied to several sciences, such as polymer science, material science, cell biology, environmental science, and so on.

This beamline equips an in-vacuum undulator, a varied-line-spacing plane grating monochromator and a fixed exit slit. The soft X-ray energy range from 50 to 770 eV with the resolving power ($E/\Delta E$) of 6,000 is available. The aperture size of the fixed exit slit determines not only the resolving power but also the size of a microprobe. A Fresnel zone plate is used as a focusing optical device through an order select aperture and its focal spot size of ~ 30 nm is available at minimum. An image is acquired by detecting intensities of the transmitted X-rays by a photomultiplier tube with scintillator with scanning a sample 2-dimensionally. By changing the energy of the incident beam, each 2-dimensional NEXAFS image is stacked. A main chamber of STXM is separated from the beamline optics by a silicon nitride membrane of 50-nm thickness; therefore, sample folders can be handled in vacuum or in helium.

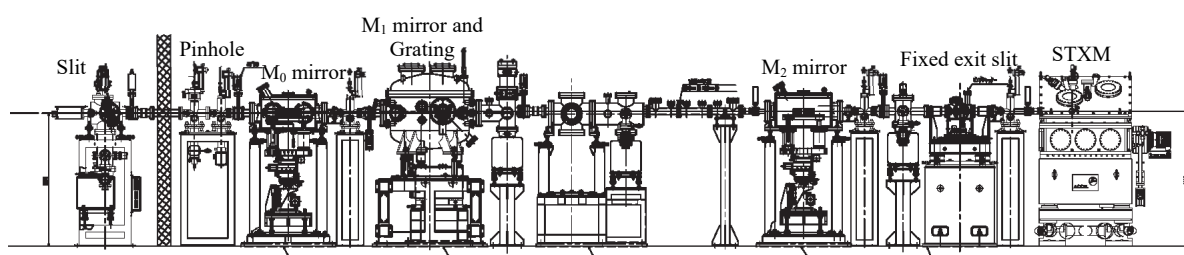


Fig. 1. Schematic image of BL4U

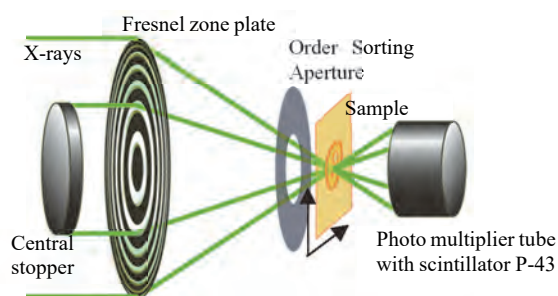


Fig. 2. Schematic image of STXM

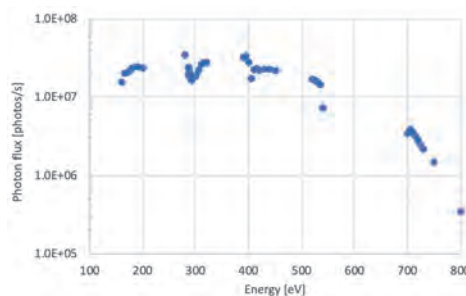


Fig. 3. Photon flux at the sample

▼ Technical Data

Energy range (E)	50 -770 eV
Resolving power ($E/\Delta E$)	$\sim 6,000$
Photon flux on a sample (photons/s)	$\sim 2 \times 10^7$ @400 eV
Focusing optical element	Fresnel zone plate
Spatial resolution	~ 30 nm
Experiments	2-dimensional absorption spectroscopy
Measurement environment	standard sample folder in vacuum or in helium, specially designed sample cell in ambient condition

BL4B

Varied-Line-Spacing Plane Grating Monochromator for Molecular Soft X-Ray Spectroscopy

▼ Description

The beamline BL4B equipped with a varied-line-spacing plane grating monochromator (VLS-PGM) was constructed for various spectroscopic investigations in a gas phase and/or on solids in the soft X-ray range. Three holographically ruled laminar profile plane gratings with SiO₂ substrates are designed to cover the photon energy range from 25 to 800 eV. The gratings with groove densities of 100, 267, and 800 l/mm cover the spectral ranges of 25–100, 60–300, and 200–1000 eV, respectively, and are interchangeable without breaking the vacuum. Figure 1 shows the absolute photon flux for each grating measured using a Si photodiode (IRD Inc.), with the entrance- and exit-slit openings set at 50 and 50 μm, respectively. The maximum resolving power ($E/\Delta E$) achieved for each grating exceeds 5000.

There is no fixed endstation on this beamline. A small vacuum chamber equipped with an electron multiplier (EM) detector is available. Soft X-ray absorption spectra of solid samples are usually measured by means of the total electron yield method using EM, and the partial fluorescence yield method using a silicon drift detector (SDD).

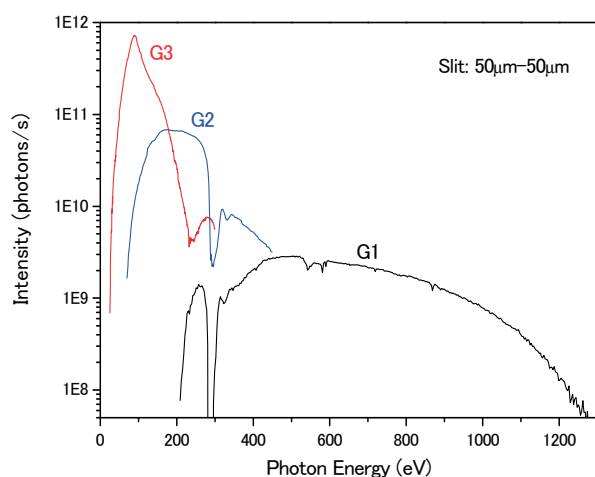


Fig. 1. Throughput from the VLS-PGM monochromator on BL4B.



Fig. 2. Photo of BL4B.

▼ Technical Data

Monochromator	Varied-line-spacing Plane Grating Monochromator
Energy range	25-1000 eV
Resolution	$E / \Delta E > 5000$ (at maximum)
Experiments	Soft X-ray spectroscopy (mainly, photoabsorption spectroscopy for solid targets by means of total electron yield method using EM and partial fluorescence yield method using SDD)

BL5U

Photoemission Spectroscopy of Solids and Surfaces

▼ Description

Since the monochromator of BL5U was an old-style spherical grating type SGMTRAIN constructed in 1990s and the throughput intensity and energy resolution were poor, the whole beamline has been replaced to state-of-the-art monochromator and end station. The new beamline has been opened to users from FY2016 as high-energy resolution ARPES beamline. Samples can be cooled down to 3.8 K with newly developed 5-axis manipulator to perform high energy resolution measurements. Users can also obtain spatial-dependence of the electronic structure of solids using micro-focused beam ($\sim 50 \mu\text{m}$). The new electron lens system makes it possible to obtain ARPES spectra without moving samples. This beamline will also have new capability to perform high-efficient spin-resolved ARPES in the future.

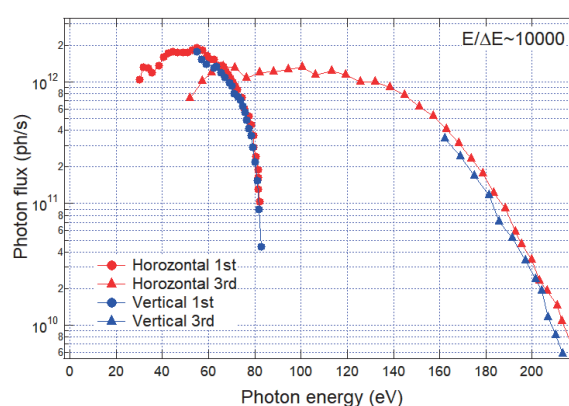


Fig. 1. Picture and photon flux of BL5U.

▼ Technical Data (Expected Performance)

Light source	APPLE-II type undulator ($\lambda_u = 60 \text{ mm}$, $N = 38$) vertical/horizontal, right/left circular (depending on $h\nu$)
Monochromator	Monk-Gillieson VLS-PGM
Energy Range	20-200 eV
Resolution	$h\nu / \Delta E > 10,000$ for $< 10 \mu\text{m}$ slits
Experiment	ARPES, Space-resolved ARPES, Spin-resolved ARPES
Flux	$< 10^{12}$ photons/s for $< 10 \mu\text{m}$ slits (at the sample position)
Beam spot size	23 (H) x 40 (V) μm
Main Instruments	Hemispherical photoelectron analyzer with deflector scan (MBS A-1 Lens#4), Liq-He flow cryostat with 5-axis manipulator (3.8 K-350 K)

BL5B

Calibration Apparatus for Optical Elements and Detectors

II

▼ Description

BL5B has been constructed to perform calibration measurements for optical elements and detectors. This beamline is composed of a plane grating monochromator (PGM) and three endstations in tandem. The most upstream station is used for the calibration measurements of optical elements, the middle one for optical measurements for solids, and the last for photo-stimulated desorption experiments. The experimental chamber at the most downstream station is sometimes changed to a chamber for photoemission spectroscopy. The calibration chamber shown in Fig. 2 is equipped with a goniometer for the characterization of optical elements, which has six degrees of freedom, X-Y translation of a sample, and interchanging of samples and filters. These are driven by pulse motors in vacuum. Because the polarization of synchrotron radiation is essential for such measurements, the rotation axis can be made in either the horizontal or vertical direction (s- or p-polarization).

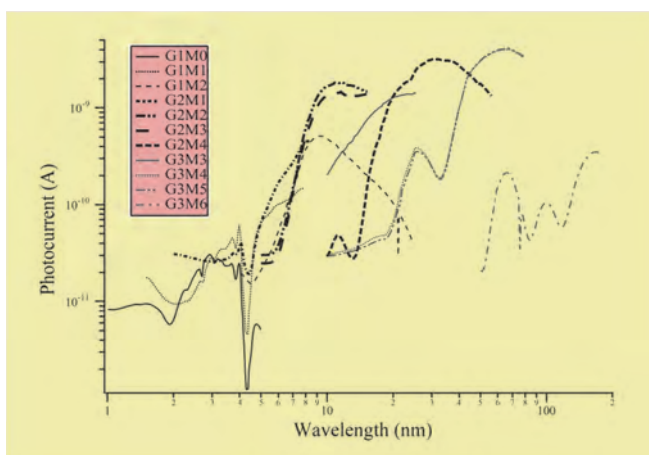


Fig. 1. Throughput spectra for possible combinations of gratings and mirrors at BL5B measured by a gold mesh.

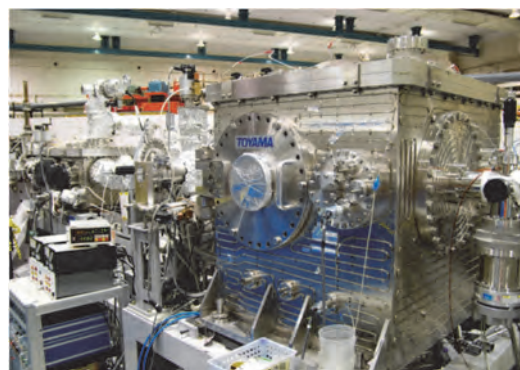


Fig. 2. A side view of the experimental chamber for calibration measurements.

▼ Technical Data

Monochromator	Plane Grating Monochromator
Energy range	6-600 eV (2-200 nm)
Resolution	$E / \Delta E \sim 500$
Experiments	Calibration of optical elements, reflection and absorption spectroscopy mainly for solids

BL6U

Variable-Included-Angle / Variable-Line-Spacing Plane Grating Monochromator for Soft X-Ray photoelectron Spectroscopy

▼ Description

The beamline BL6U equipped with a variable-included-angle Monk-Gillieson mounting monochromator with a varied-line-spacing plane grating was constructed for various spectroscopic investigations requiring high-brilliance soft X-rays on solid surfaces. Through a combination of undulator radiation and sophisticated monochromator design (entrance slit-less configuration and variable-included-angle mechanism), using a single grating, the monochromator can cover the photon energy ranging from 40 to 500 eV, with resolving power of greater than 10000 and photon flux of more than 10^{10} photons/s. Figure 1 shows an example of the monochromator throughput spectra measured using a Si photodiode, with the exit-slit opening set at 30 μm , which corresponds to the theoretical resolving power of 10000 at 80 eV.

A new Momentum Microscope experimental station for photoelectron spectroscopy resolved in 3D momentum space with a microscopic field of view has been built at BL6U (SPECS KREIOS 150 MM). A momentum resolution of 0.01 \AA^{-1} in k_x/k_y , as well as k_z is achieved. A spatial resolution of 50 nm, an energy resolution of 20 meV at 9 K, and a field of view of 2 μm for ARPES are successfully demonstrated. This experimental station specializes in characterizing the electronic structure of surface atomic sites, thin films, molecular adsorbates, and bulk crystals. This method opens the door to direct observation of the Fermi surface of μm -sized crystals, which was difficult with conventional ARPES-type hemispherical analyzers.

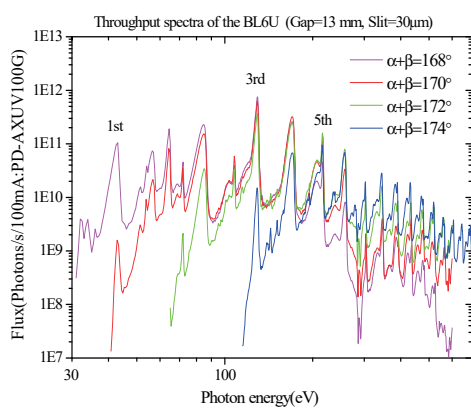


Fig. 1. Throughput spectra of the BL6U monochromator at various included angles.

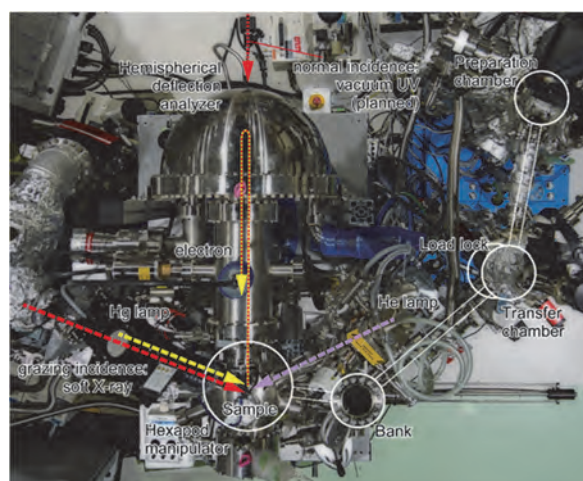


Fig. 2. Photograph of BL6U end station

▼ Technical Data

Monochromator	Variable-included-angle Varied-line-spacing Plane Grating Monochromator
Energy range	40-500 eV(practical)
Resolution	$E / \Delta E > 10000$ (at maximum)
Experiments	High-resolution soft X-ray spectroscopy (photoelectron spectroscopy for solid surfaces)

BL6B

Infrared and Terahertz Spectroscopy of Solids

II

▼ Description

Synchrotron radiation (SR) has good performance (high brilliance and high flux) not only in the VUV and soft X-ray (SX) regions but also in the infrared (IR) and THz regions. BL6B covers the IR and THz regions. The previous beamline, BL6A1, which was constructed in 1985, was the pioneer in IRSR research. The beamline was deactivated at the end of FY2003 and a new IR/THz beamline, BL6B (IR), was constructed in FY2004. The front-end part including bending duct #6 was replaced with a new part having a higher acceptance angle ($215 \text{ (H)} \times 80 \text{ (V)} \text{ mrad}^2$) using a magic mirror, as shown in Fig. 1.

There are two Michelson type interferometers in this endstation; with first one (Bruker Vertex70v), which covers a wide spectral region from 30 to 20,000 cm^{-1} ($h\nu = 4 \text{ meV} - 2.5 \text{ eV}$), reflection/absorption spectroscopy measurements of large samples (up to several mm) and IR/THz microscopy measurements of tiny samples (up to several tens of μm) can be performed. For reflection/absorption spectroscopy measurements, a liquid-helium-flow type cryostat with a minimum temperature of 4 K is installed. The other interferometer (Jasco FT/IR-6100), which covers 350 to 15,000 cm^{-1} ($h\nu = 45 \text{ meV} - 1.8 \text{ eV}$), has been available for IR microscopy imaging measurements from FY2014. One can also perform ATR measurements using diamond ATR prism.

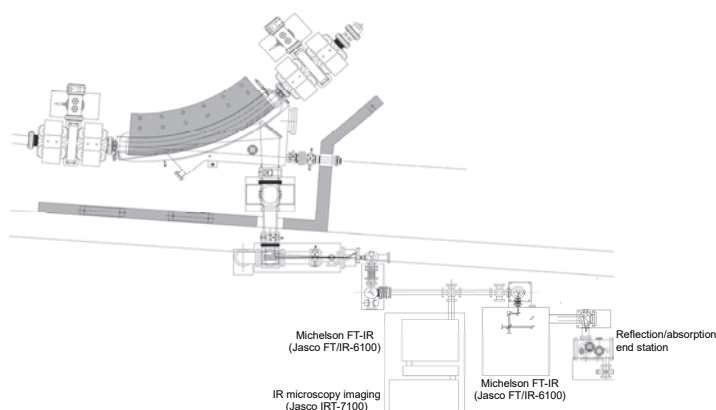


Fig. 1. Schematic top view of BL6B.

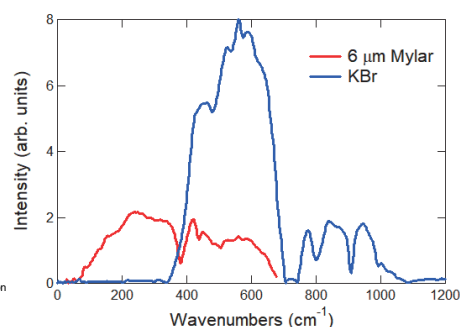


Fig. 2. Obtained intensity spectra with the combination of a light source (UVSOR), detector (Si bolometer), and interferometer (Bruker Vertex70v) with different beamsplitters (6 μm Mylar and KBr). (Only low energy side is shown).

▼ Technical Data

Interferometer	Michelson (Bruker Vertex70v)	Michelson (Jasco FT/IR-6100)
Wavenumber Range (Energy range)	30-20,000 cm^{-1} (4 meV-2.5 eV)	350-15,000 cm^{-1} (45 meV-1.8 eV)
Resolution in cm^{-1}	0.1 cm^{-1}	0.5 cm^{-1}
Experiments	Reflectivity and transmission spectroscopy THz Microspectroscopy	IR microscopy imaging (JASCO IRT-7000) ATR spectroscopy

BL7U (SAMRAI)

Angle-Resolved Photoemission of Solids in the VUV Region

▼ Description

Beamline 7U, named the Symmetry- And Momentum-Resolved electronic structure Analysis Instrument (SAMRAI) for functional materials, was constructed to provide a photon flux with high energy resolution and high flux mainly for high-resolution angle-resolved photoemission spectroscopy, so-called “ARPES”, of solids [1]. An APPLE-II-type variable-polarization undulator is installed as the light source. The undulator can produce intense VUV light with horizontal/vertical linear and right/left circular polarization. The undulator light is monochromatized by a modified Wadsworth type monochromator with three gratings (10 m radius; 1200, 2400, and 3600 lines/mm optimized at $h\nu = 10, 20,$ and 33 eV). The energy resolution of the light ($h\nu/\Delta h\nu$) is more than 10^4 with a photon flux of 10^{11} - 10^{12} ph/s or higher on samples in the entire energy region. The beamline has a photoemission end-station equipped with a 200 mm-radius hemispherical photoelectron analyzer (MB Scientific AB, A-1 analyzer) with a wide-angle electron lens and a liquid-helium-cooled cryostat with 6-axis pulse motor control. The main function of the beamline is to determine the electronic structure of solids and its temperature dependence in order to reveal the origin of their physical properties.

[1] S. Kimura, T. Ito, M. Sakai, E. Nakamura, N. Kondo, K. Hayashi, T. Horigome, M. Hosaka, M. Katoh, T. Goto, T. Ejima and K. Soda, Rev. Sci. Instrum. **81** (2010) 053104.

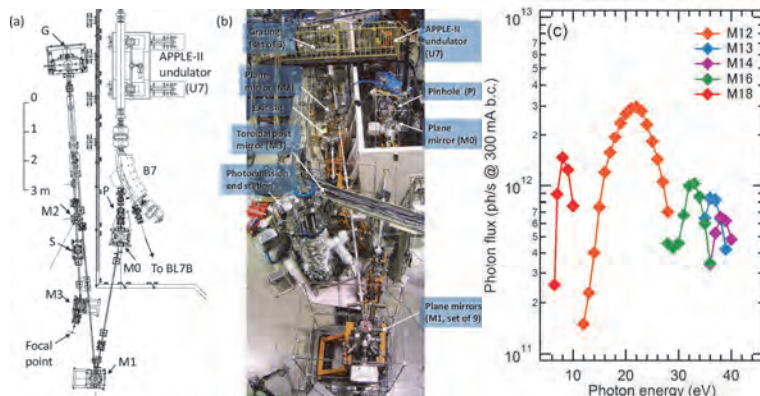


Fig. 1. SAMRAI beamline [(a), (b)] consisting of an APPLE-II type undulator (U7), a modified Wadsworth type monochromator (M0-S), and a high-resolution photoemission analyzer at the focal point. The monochromator has five major optical components: two plane mirrors (M0 and M1) with water cooling, one set of three spherical gratings (G), an exit slit (S), and one toroidal refocusing mirror (M3). (c) Example of flux intensity *versus* photon energy [1]

▼ Technical Data

Light source	APPLE-II type undulator ($\lambda_u = 76$ mm, $N = 36$) vertical/horizontal, right/left circular (depending on $h\nu$)
Monochromator	10 m normal-incidence monochromator (modified Wadsworth type)
Photon energy range	6 – 40 eV ($\lambda = 30 - 200$ nm)
Resolution ($h\nu/\Delta h\nu$)	$E / \Delta E > 10000$ - 50000
Photon flux on sample	$\geq 10^{11}$ - 10^{12} ph/s (depending on $h\nu$)
Beam size on sample	200 (H) \times 50 (V) μm^2
Experiments	Angle-resolved photoemission of solids (MV Scientific A-1 analyzer, acceptance angle: ± 18 deg)

BL7B

3 m Normal-Incidence Monochromator for Solid-State Spectroscopy

II

▼ Description

BL7B has been constructed to provide sufficiently high resolution for conventional solid-state spectroscopy, sufficient intensity for luminescence measurements, wide wavelength coverage for Kramers–Kronig analyses, and minimum deformation to the polarization characteristic of incident synchrotron radiation. This beamline consists of a 3-m normal incidence monochromator, which covers the vacuum ultraviolet, ultraviolet, visible, and infrared, i.e., the wavelength region of 50–1000 nm, with three gratings (1200, 600, and 300 l/mm). Two interchangeable refocusing mirrors provide two different focusing positions. For the mirror with the longer focal length, an LiF or a MgF₂ window valve can be installed between the end valve of the beamline and the focusing position. Figure 1 shows the absolute photon intensity for each grating with the entrance and exit slit openings of 0.5 mm. A silicon photodiode (AXUV-100, IRD Inc.) was utilized to measure the photon intensity and the absolute photon flux was estimated, taking the quantum efficiency of the photodiode into account.

The cooling system for the pre-focusing mirror has been removed, resulting in longer beam settling times. Currently, BL7B is opened during single bunch mode, but limited use is possible during multi bunch mode.

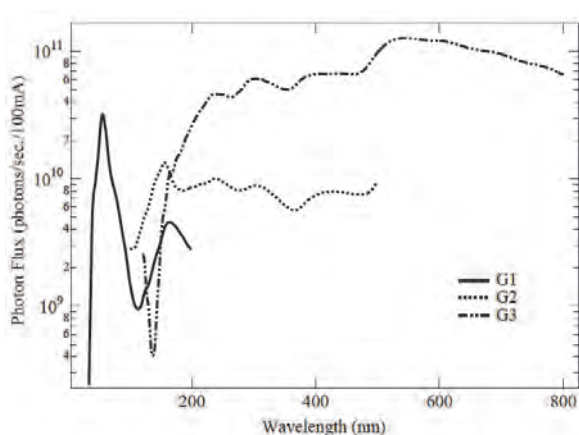


Fig. 1. Throughput spectra of BL7B measured using a silicon photodiode.

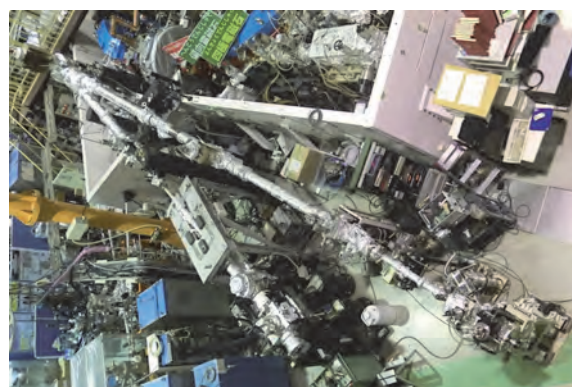
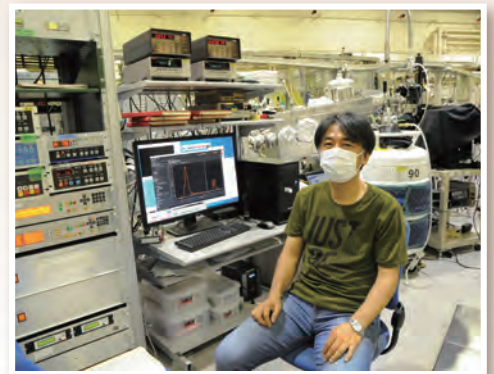
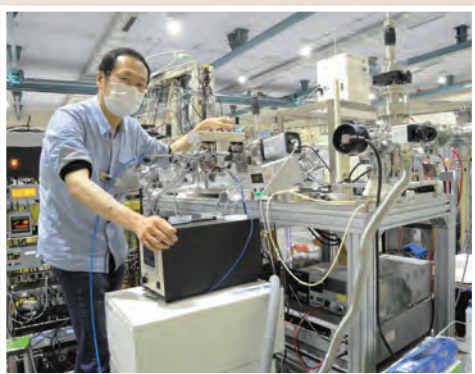
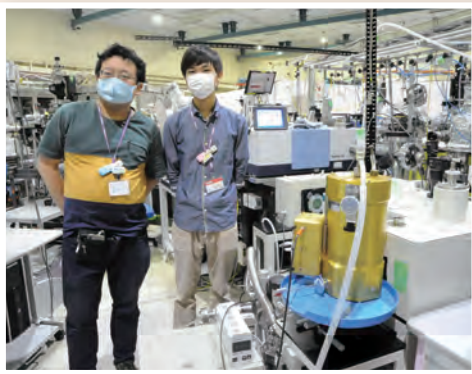
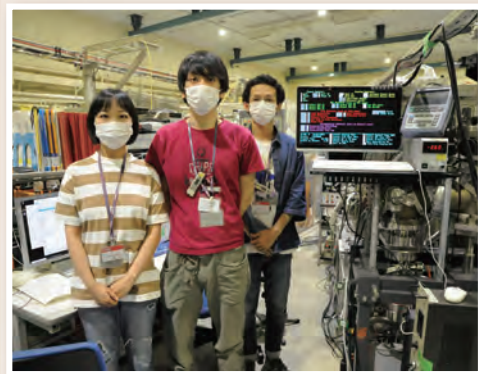
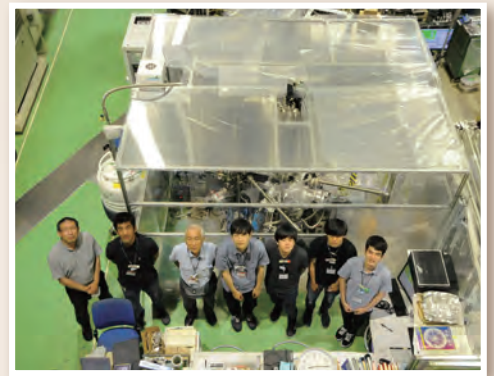
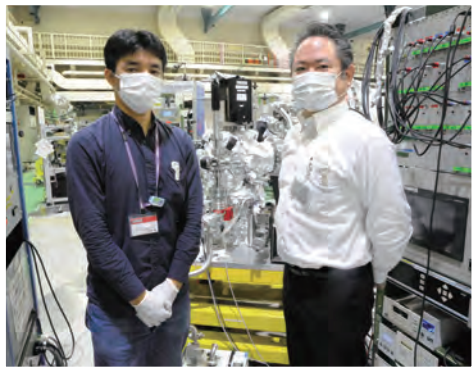


Fig. 2. Photo of BL7B.

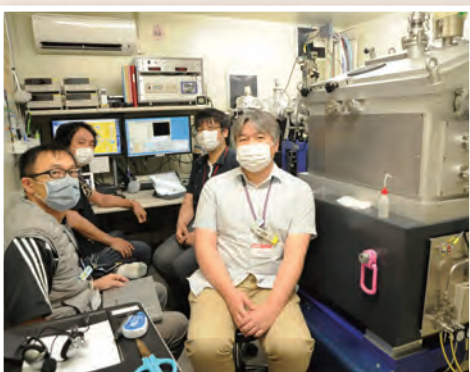
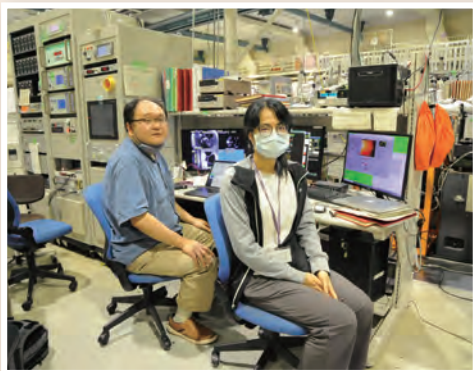
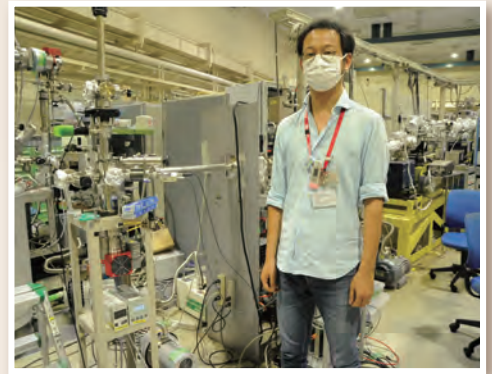
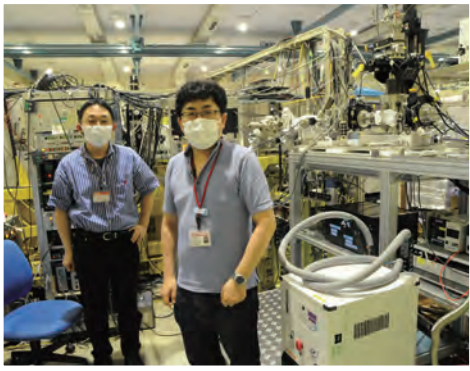
▼ Technical Data

Monochromator	3 m Normal-Incidence Monochromator
Wavelength Range	50-1000 nm (1.2-25 eV)
Resolution	$E / \Delta E = 4000-8000$ for 0.01 mm slits
Experiments	Absorption, reflection, and fluorescence spectroscopy, mainly for solids

UVSOR User 1



UVSOR User 2



III-1

Accelerators and
Instruments

BL1U

Improvement of Image Quality of Selective Isotope 3D-CT in UVSOR-BL1U

H. Ohgaki¹, K. Ali¹, H. Zen¹, T. Kii¹, T. Hayakawa², T. Shizuma², M. Fujimoto³, Y. Taira³ and M. Katoh^{3,4}

¹Institute of Advanced Energy, Kyoto University, Kyoto 611-0011, Japan

²Tokai Quantum Beam Science Center, National Institutes for Quantum and Radiological Science and Technology, Ibaraki 319-1106, Japan

³UVSOR Synchrotron Facility, Institute for Molecular Science, Okazaki 444-8585, Japan

⁴Hiroshima University, Higashi-Hiroshima 739-8511, Japan

Nuclear Resonance Fluorescence (NRF) is a powerful tool to identify the specific isotope, especially in combination with a Laser Compton Backscattering (LCS) gamma-ray beam which provides quasi-monochromatic and energy variable gamma-rays. We have been developed an NRF-CT technique by using the LCS gamma-ray beam available at the beamline BL1U in UVSOR and demonstrated a three-dimensional (3D) isotope-selective CT image of the enriched lead isotope distribution of ²⁰⁸Pb in a cylindrical holder (Fig. 1), so far [1]. However, we needed 48 h beam time to obtain a CT image with a 4 mm/pixel in the horizontal plane and 8 mm/pixel in the vertical plane using the LCS gamma-ray beam with a beam size of 2 mm and a flux density of 10 photons/s/eV.

To overcome this problem, we proposed a fusion visualization (FV) technique by combining the NRF-CT image which provides a rough distribution of targeting isotope with a gamma-ray CT image which can be obtained by the same measurement system with NRF-CT but can provide better pixel resolution with a short measurement time (5 hours) [2]. We measured a 3D gamma-CT image of the same CT target [1] with the 3D NRF-CT in BL1U. The obtained 3D gamma-CT image (Fig. 2) has a 1 mm/pixel resolution with an LCS gamma-ray beam size of 1 mm and a flux density of 0.7 photons/s/eV. The target consists of two enriched lead isotopes (^{206,208}Pb), iron, and aluminum. As shown in Fig. 2, two enriched lead isotopes can be obtained but we cannot identify which one is the target isotope ²⁰⁸Pb.

After a few FV methods were applied to construct an FV image between NRF-CT and gamma-ray CT images, the post-multiply FV method which can keep the quantitative information of NRF interaction was selected. Figure 3 shows the 3D isotope-selective fused CT image. Consequently, we can improve the image quality of 3D NRF-CT of ²⁰⁸Pb rods embedded in the aluminum cylinder with ²⁰⁶Pb rod as well as iron rods with keeping quantitative information of NRF interaction.

[1] K. Ali *et al.*, “Three-Dimensional Nondestructive Isotope-Selective Tomographic Imaging of ²⁰⁸Pb Distribution via Nuclear Resonance Fluorescence.” *Appl. Sci.* **11** (2021) 3415. <https://doi.org/10.3390/app11083415>.

[2] K. Ali, *et al.*, “Fusion Visualization TecFighnique to Improve a Three-Dimensional Isotope-Selective CT Image Based on Nuclear Resonance Fluorescence with a Gamma-CT Image”, *Appl. Sci.* **11** (2021) 11866. <https://doi.org/10.3390/app112411866>.

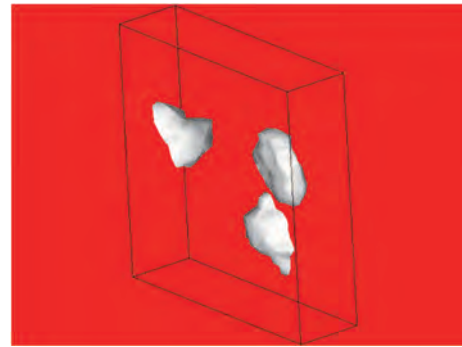


Fig. 1. 3D NRF-CT image measured in BL1U.

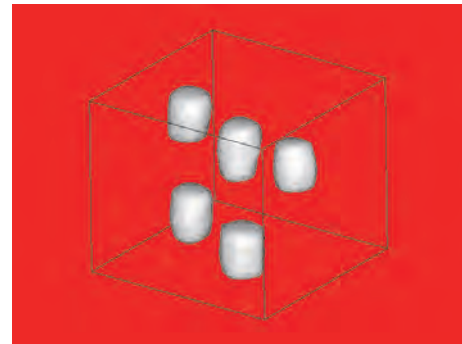


Fig. 2. 3D Gamma-ray CT image measured in BL1U.

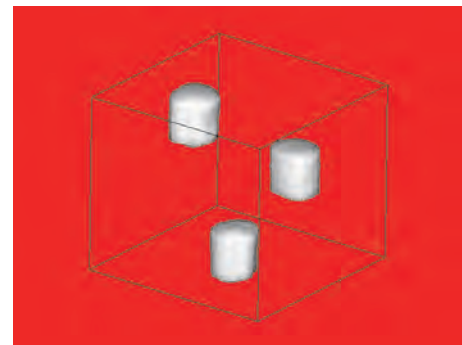


Fig. 3. 3D FV NRF-CT image

BL1U

Photon Counting Experiments of Young's Double-Slit Interference Using Undulator Vortex Radiation

S. Wada^{1,2}, H. Ohta², A. Mano³, M. Fujimoto^{4,3} and M. Katoh^{5,2,4}¹Graduate School of Advanced Science and Engineering, Hiroshima University, Higashi-Hiroshima 739-8526, Japan²Faculty of Science, Hiroshima University, Higashi-Hiroshima 739-8526, Japan³Synchrotron Radiation Research Center, Nagoya University, Nagoya 464-8603, Japan⁴UVSOR Synchrotron Facility, Institute for Molecular Science, Okazaki 444-8585, Japan⁵Hiroshima Synchrotron Radiation Center, Hiroshima University, Higashi-Hiroshima 739-0046, Japan

Recent theoretical and experimental progresses in the synchrotron radiation technology reveal that high harmonics emitted from a helical undulator possesses helical wave-front structure [1,2]. The undulator beamline BL1U at UVSOR can produce fundamental and its harmonics of circularly polarized radiation in visible and UV regions. Therefore, leading experiments using vortex radiation from the undulator have been conducted [3,4]. Especially, Young's double-slit interference experiments demonstrated the characteristic nature of vortex radiation as a singularity in the middle of the interference pattern arising from helical wave-front structure. This phenomenon is quite interesting from the view point whether a single photon spontaneously emitted from a high-energy electron can also possess such a characteristic or not. In this study, we demonstrated Young's double-slit experiments under photon-counting condition in order to confirm the above nature of vortex radiation from a helical undulator [5].

Experiments were performed at UVSOR BL1U under quite low-current mode (less than 1 mA). Circularly polarized radiation centered at 355 nm of second harmonics was extracted from a vacuum beamline to atmosphere via a quartz window, passed through an iris and an interference filter (Alluxa 7057) in order to extract center part and remove fundamental 710 nm light from the undulator radiation, and then irradiated onto a double-slit (0.1 mm width and 1 mm separation). By using as few optics as possible mentioned above, we could achieve very low simultaneous detection of two photons, that is single-photon counting condition in keeping helical wave-front structure. Single photons after interference were detected by a gated ICCD camera system (Hamamatsu Photonics, M7971-01 and ORCA-05G) 1 m far from the double-slits.

After confirming the double-slit interference in this experimental setup under multiphoton detection mode using a normal CCD camera, we could measure interference pattern even by photon counting detection as shown in Fig. 1(a). The figure was obtained by integrating 5000 shots of images with an exposure time of 200 μ s, and about 150 photons were randomly detected in each image. As clearly shown in the figure, we can find stripes due to interference by the double-slit and the singularity, that is mismatch of stripes at the dark middle region. The result obviously demonstrates that the interference patterns of circularly polarized

radiation from a helical undulator exhibit characteristics of optical vortex even under single-photon counting condition. The nature of vortex radiation from the undulator in the photon-counting condition is also confirmed by removing the double-slit as shown in Fig. 1(b), indicating the integrated beam profile like donut-shaped with the center missing. This is characteristic of vortex radiation with no light intensity due to a phase singularity.

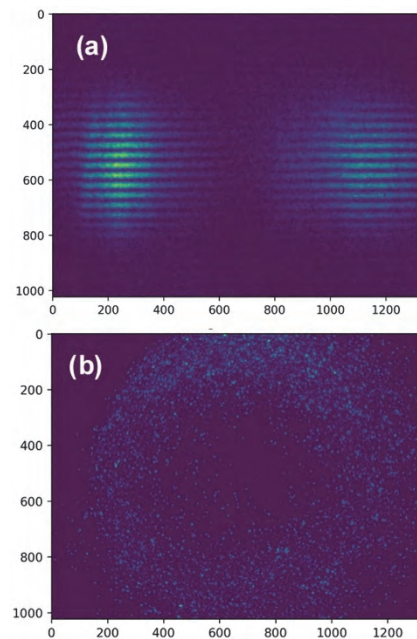


Fig. 1. (a) Young's double-slit interference pattern of vortex radiation measured at BL1U under photon-counting condition. (b) Integrated beam profile without the double-slit.

[1] S. Sasaki and I. McNulty, *Phys. Rev. Lett.* **100** (2008) 124801.

[2] J. Bahrtdt *et al.*, *Phys. Rev. Lett.* **111** (2013) 034801.

[3] M. Katoh *et al.*, *Sci. Rep.* **7** (2017) 6130.

[4] T. Kaneyasu *et al.*, *J. Synchrotron Rad.* **24** (2017) 934.

[5] H. Ohta, B.Sc. Thesis, Hiroshima University (2021).

Others

Development Mass Production Facilities of Nuclear Emulsion Films

I. Usuda, H. Rokujo and M. Nakamura

Graduate School of Science, Nagoya University, Nagoya 464-8602, Japan

Nuclear emulsion is a kind of photographic films that have sensitivity for ionizing radiation. The films record tracks of charged particle with high angular resolution.

In Nagoya University, we have developed gel production machine and developed several types of emulsion by ourselves. We are planning some experiments (e.g., gamma ray telescope, neutrino interaction research, muon radiography) using more than 500 m² nuclear emulsion films.

Nuclear emulsion is made by coating emulsion gel on plastic base. Previously, it was difficult to make large amount of films because we have coated emulsion gel by hand.

We have developed roll-to-roll coating machine in Nagoya University (Fig. 1). For mechanical coating, we have tried to add new chemicals to nuclear emulsion gel and optimize the gel's viscosity. We were the first in the world to succeed in the mechanical coating of over 60 μm thickness of nuclear emulsion films. We also introduced new gel production machine that can make 30 times amount of nuclear emulsion gel compared with conventional machine.

Now, we can make about 100 m² nuclear emulsion films per month.

We checked the performance of new emulsion gel and films. The index of sensitivity is Grain Density (GD) which is number of silver grains in the tracks of minimum ionized particle. The index of noise rate is Fog Density (FD) which is number of randomly generated silver grains unrelated to tracks. After we exposed electron beam to emulsion films at UVSOR (Fig. 2), we evaluated GD and FD.

We checked that GD and FD of nuclear emulsion gel and films which made by mass production facilities are comparable to that of conventional products. And the performance is stable for repeated operation. (Fig. 3, 4)

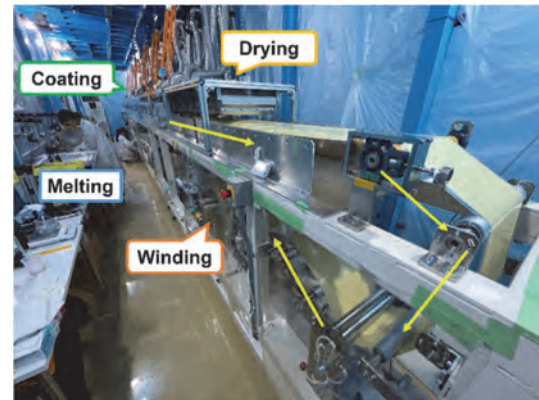


Fig. 1. Overview of roll-to-roll coating machine in Nagoya University.



Fig. 2. Optical microscopic image of electron beam (several tens of MeV) track. The electron beam was exposed at UVSOR.

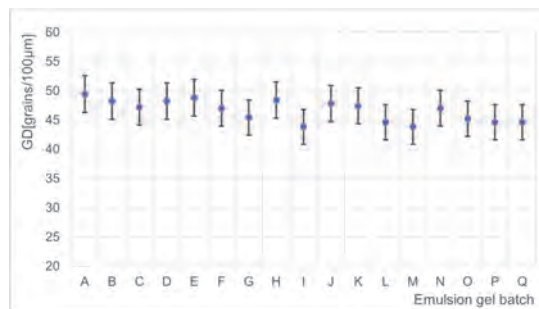


Fig. 3. Difference of Grain Density (GD) by emulsion gel batch.

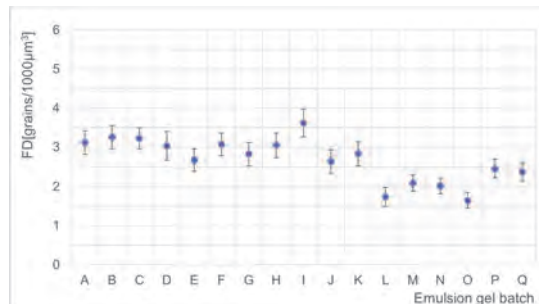


Fig. 4. Difference of Fog Density (FD) by emulsion gel batch.

BL1U

Laser Pulse Shaping and Transport at UVSOR-III

Y. Takashima^{1,2}, A. Mano¹, G. Jang², Y. Taira³, M. Fujimoto³, Y. Okano³ and M. Katoh^{4,3}

¹Synchrotron Radiation Research Center, Nagoya University, Nagoya 464-8603, Japan

²School of Engineering, Nagoya University, Nagoya 464-8603, Japan

³UVSOR Synchrotron Facility, Institute for Molecular Science, Okazaki 444-8585, Japan

⁴HiSOR, Hiroshima University, Higashi-Hiroshima 739-0046, Japan

We constructed the compact optics to shape a laser pulse to develop advanced Laser-Compton scattering gamma-ray source or sophisticated laser-synchrotron radiation combination experiment. The optics is a kind of Michelson interferometer [1]. As the first step, we tried to generate two temporally consecutive laser pulses (double pulse) from one original laser pulse. We confirmed generating double pulses.

Figure 1 shows the optics for the generation of the double pulse of the short-pulse laser. The original laser pulse is injected from the direction of arrow 1 in Fig. 1. The laser pulse is divided into the orthogonal direction "A" and "B" by the beam splitter in Figure 1; the laser pulses are reflected by the mirror 1 and 2. Mirror 2 is mounted on the movable stage so that the path length of the laser pulse along to "B" can be changed. The reflected pulses are mixed in the beam splitter and go through the direction "C", and then reflected the mirror 3 and exit to the direction "D".

We used an autocorrelator to measure the pulse width and the interval of the double pulses. The autocorrelator is installed downstream of the direction "D". According to the measurement using the autocorrelator, when we interrupt the laser pulse reflected on mirror 1, the FWHM of the pulse width of the laser of the single pulse is about 5.0 ps. Figure 2 showed the output signal from the autocorrelator when

we arranged the difference of the path length appropriately by moving the stage of mirror 2. We obtained the interval of the double pulse of about 3.0 ps. Fig. 3. shows the spectrum of the double pulse laser.

We successfully transported the laser pulse onto the circulating electron beam in the UVSOR-III storage ring by using the existing laser transport line for the Laser-Compton scattering.

III -1

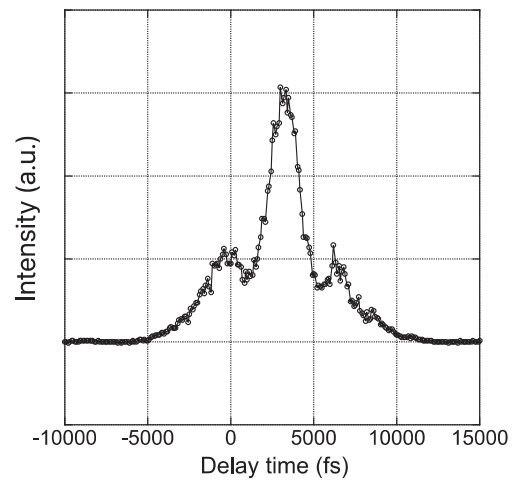


Fig. 2. The output signal of the autocorrelator.

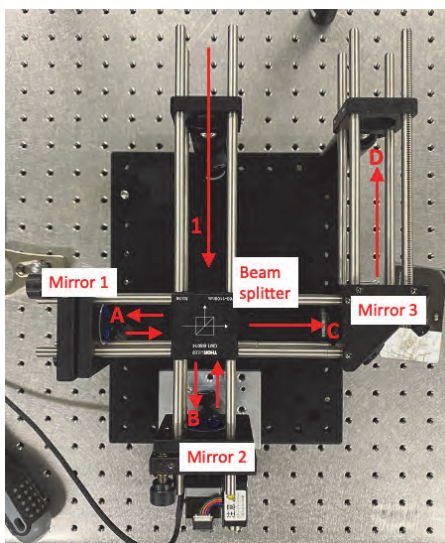


Fig. 1. Optics for the generation of the double pulse.

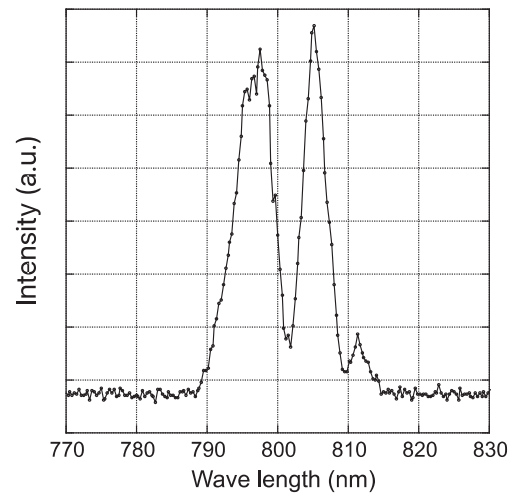


Fig. 3. The spectrum of the double pulse laser.

[1] G. Jang, Graduation thesis of School of Engineering, Nagoya University (2021)

BL1U

Revival of UVSOR-FEL and Gamma Ray Generation by Intra-cavity Laser Compton Scattering

H. Zen¹, J. Yamazaki², M. Fujimoto^{2,3}, K. Hayashi², H. Ohta², Y. Taira^{2,3} and M. Katoh^{2,4}

¹*Institute of Advanced Energy, Kyoto University, Uji 611-0011, Japan*

²*UVSOR Synchrotron Facility, Institute for Molecular Science, Okazaki 444-8585, Japan*

³*The Graduate University for Advanced Studies (SOKENDAI), Okazaki 444-8585, Japan*

⁴*Hiroshima Synchrotron Radiation Center, Hiroshima University, Higashi-Hiroshima 739-0046, Japan*

The lasing of Free Electron Laser (FEL) at S5 section was firstly achieved in 1992. The research activity related to FEL had been continued until the end of FY2011. Then the straight section used for activities of FEL and coherent light source developments was changed to S1, which has been newly created by moving the injection point. Two APPLE-II type undulators with an electromagnetic buncher magnet have been installed in the S1 section. The optical cavity used for FEL lasing was removed from S5 section at the end of FY2010 and reconstructed at the beginning of FY2015. In FY2017, we tried to have a first lasing of FEL at S1 section. At that time, we could achieve storage of undulator radiation in the optical cavity [1] but could not achieve FEL lasing due to a mismatch between the optical cavity length and the electron bunch interval. In the April-2021 shutdown of UVSOR, the position of the downstream mirror chamber was shifted to make the roundtrip frequency of the optical cavity the same as the electron bunch interval. In February 2022, a commissioning experiment of optical cavity and FEL was conducted to confirm the FEL lasing at S1 section.

The commissioning experiment of FEL was performed with an FEL cavity mirror pair which has high reflectivity around 520 nm. At first, the gap and the phase of the APPLE-II undulators are adjusted to have the center wavelength of 520 nm with the electron beam energy of 600 MeV. Next, the angles of the optical cavity mirrors were adjusted to store the undulator radiation in the optical cavity. Then the length of the optical cavity was scanned for finding the matching condition between the roundtrip frequency of the optical cavity and the electron bunch interval. This adjustment was performed with two bunch equidistant filling mode. The pulse duration of the stored light is strongly depending on the cavity length. The cavity length condition giving the shortest pulse duration of the stored light should be corresponding with the matched condition. After finding the matched condition of the cavity length, the electron beam current was increased up to 20 mA/2 bunch and the excitation current of the buncher magnet was increased up to 20 A. With a slight adjustment of the angle of the optical cavity mirror, lasing of the FEL can be achieved. Figure 1 shows the photograph of the FEL beam and its wavelength spectrum. The bright green spot in the photograph was the FEL beam having a central wavelength of 524.5 nm.

One of the interesting applications of UVSOR-FEL is the gamma-ray generation by the intra-cavity laser

Compton scattering [2]. In this study, two small current electron bunches were injected into 3 buckets behind the main bunches for generating gamma-ray by colliding with intra-cavity FEL beams. The spectrum of the generated gamma-ray measured by a NaI scintillator is shown in Fig. 2. The maximum gamma-ray energy was evaluated as 13 MeV. In this measurement, the optical cavity length was slightly detuned to avoid the pile-up events in the scintillator.

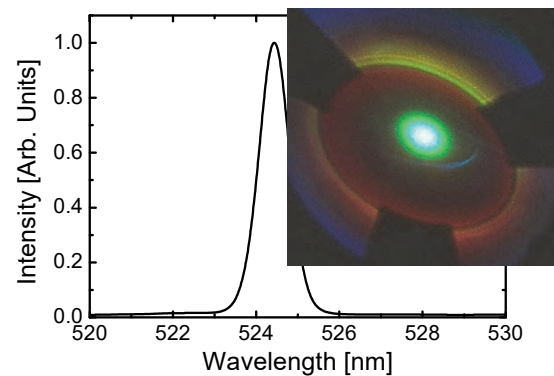


Fig. 1. Wavelength Spectrum and beam profile of FEL observed at the downstream of the optical cavity.

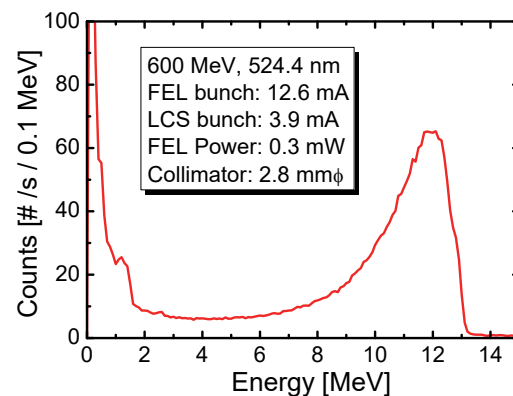


Fig. 2. The spectrum of the generated gamma-ray measured by a NaI scintillator.

[1] H. Zen *et al.*, UVSOR Activity Report 2017 **45** (2018) 31.

[2] M. Hosaka *et al.*, Nucl. Instrum. Meth. A **393** (1997) 525.

BL1U

Evaluation of Analyzing Power of Gamma-ray Polarimeter

S. Endo^{1,2}, T. Shizuma³, H. Zen⁴, Y. Taira⁵, K. Sugita⁵, O. Mohamed¹, S. Kawamura²,
R. Abe², T. Okudaira², M. Kitaguchi² and H. M. Shimizu²

¹Japan Atomic Energy Agency, Tokai 319-1195, Japan

²Nagoya University, Nagoya 464-8062, Japan

³National Institute for Quantum Science and Technology, Tokai 319-1195, Japan

⁴Kyoto University, Uji 611-0011, Japan

⁵Institute for Molecular Science, Okazaki 444-8585, Japan

A measurement of a circular polarization ratio of the gamma-rays emitted from an un-polarized neutron capture reaction of nuclei leads to the study for the compound nuclei [1]. Furthermore, the total angular momentum of neutron resonances can be determined by measuring the circular polarization ratio of gamma-rays from a polarized-neutron capture reaction [2]. We are aiming to conduct these measurements at J-PARC/MLF. The degree of the circular polarization of gamma-rays can be determined by measuring the transmission ratio of the magnet, called a gamma-ray polarimeter, because the cross-section of the Compton scattering depends on the direction of the electron polarization in the magnetized material and the gamma-ray helicity, i.e., circular polarization [3]. We developed a gamma-ray polarimeter and evaluated its analyzing power using a circularly polarized gamma-ray beam generated by the inverse Thomson scattering in the UVSOR BL1U [4].

The analyzing power is defined as

$$P_a = \frac{N^r - N^l}{N^r + N^l},$$

where N^r and N^l are the transmission ratio of the polarimeter for right- and left-circularly polarized gamma-rays, respectively. Figure 1 shows the schematic of the experiment. The beam flux was monitored by detecting gamma-rays scattered from brass with a LaBr detector. Gamma-rays transmitting the polarimeter were detected using a Ge detector. Figure 2 shows the gamma-ray energy spectrum taken by the Ge detector. Background measurement was performed with the laser off. Therefore, it includes the environmental radiation and backgrounds derived from the Bremsstrahlung. The pile-up effect was corrected, and the transmission ratio was obtained from the number of events for the LaBr and Ge detectors.

Since the analyzing power depends on the magnetic field, it depends on the current flowing the polarimeter. Figure 3 shows the obtained analyzing power for each current for 100% circularly polarized gamma-rays. The current up and down mean whether the current was increased or decreased, respectively, reflecting the effect of magnetic hysteresis. The analyzing power was obtained as $P_a = 2.12 \pm 0.04\%$ above 2 A.

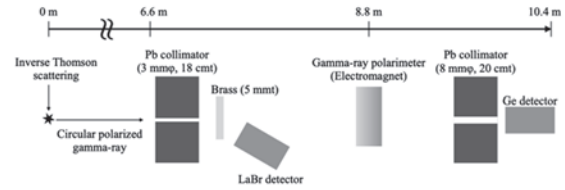


Fig. 1. Schematic of experimental setup.

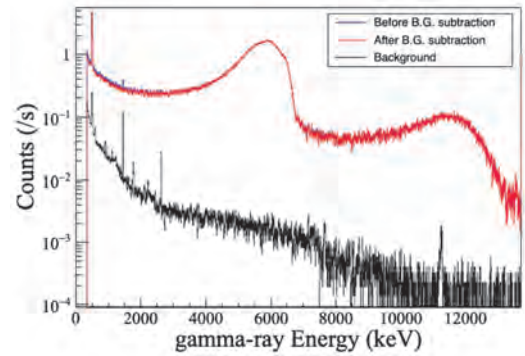


Fig. 2. Gamma-ray energy spectrum taken by the Ge detector.

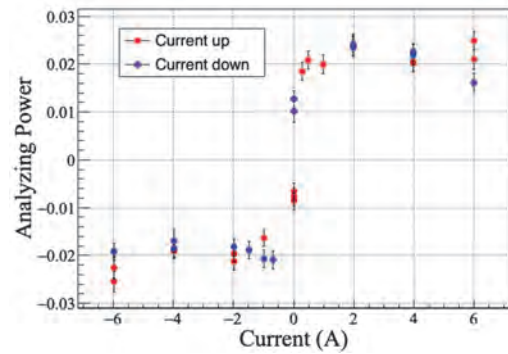


Fig. 3. Analyzing power for each current.

[1] V.V. Flambaum and O.P. Sushkov, Nucl. Phys. A **435** (1985) 352.

[2] L.C. Bindenham *et al.*, Phys. Rev. **83** (1951) 683.

[3] H.A. Tolhoek, Rev. Mod. Phys. **28** (1956) 277.

[4] Y. Taira *et al.*, Nucl. Instrum. Meth. Phys. Res. A **637** (2011) 116.

BL1U

Development of Gamma ray Induced Positron Annihilation Spectroscopy

Y. Taira^{1,2}, K. Sugita^{1,2}, R. Yamamoto³, Y. Okano¹ and T. Hirade⁴

¹UVSOR Synchrotron Facility, Institute for Molecular Science, Okazaki 444-8585, Japan

²School of Physical Sciences, The Graduate University for Advanced Studies (SOKENDAI), Okazaki 444-8585, Japan

³Graduate School of Engineering, Nagoya University, Nagoya, 464-8603, Japan

⁴Nuclear Science and Engineering Center, Japan Atomic Energy Agency, Tokai, 316-8511, Japan

Positron annihilation spectroscopy (PAS) is an excellent method to detect lattice defects in solids such as vacancies, dislocations, and clusters and free volumes in polymers [1]. Conventional β^+ radioisotopes such as ^{22}Na , a positron beam generated from an electron accelerator, and a high energy gamma ray [2,3] are used for PAS. PAS using a high energy gamma ray, which is called gamma ray induced PAS (GiPAS), has several advantages compared with PAS using conventional radioisotopes. (i) It enables defect analysis of a thick material in a few centimeters because positrons are created throughout a bulk material via pair production by irradiation with gamma rays having high penetration into the material. (ii) Source contribution of positrons annihilated in the covering material is negligible. In conventional radioisotopes, about 10 % ~ 15 % of positrons annihilate in the source. This distorts the positron lifetime spectra and complicates the data analysis.

Inverse Thomson/Compton scattering is a scattering process between high energy electrons and a laser, which can produce high energy gamma rays. A MeV gamma ray can be generated by the scattering between a 1 GeV electron and a 1 eV photon. The generated gamma rays possess features such as quasi-monochromatic and tunable energy, highly polarized, low divergence angle, and low background. Inverse Thomson/Compton scattered gamma rays have been generated at several electron accelerator facilities in the world. We have developed ultra-short pulsed gamma rays by inverse Thomson scattering at UVSOR-III [4]. They are generated via inverse Thomson scattering with 90 degree collisions between a 750-MeV electron beam and a Ti:Sa laser pulse. The maximum energy is 6.6 MeV and the pulse width is calculated to be sub-ps to ps ranges.

We are currently developing GiPAS using the ultra-short pulsed gamma ray [5]. Gamma ray induced positron annihilation lifetime spectroscopy (GiPALS), which is a technique to measure positron lifetime and evaluate type of defects at the nanometer scale and their concentrations inside material, is currently available for users. The measured positron lifetime spectrum of stainless steel distributed by National Metrology Institute of Japan (NMIJ) as reference material for positron lifetime is shown in Fig. 1. The positron lifetime spectrum was analyzed using LT9 program.

In addition to GiPALS, we have developed gamma

ray induced age-momentum correlation (GiAMOC), which is a technique to measure time resolved momentum distribution of an electron which is the annihilation counterpart of a positron. The measured AMOC spectrum of the NMIJ stainless steel is shown in Fig. 2.

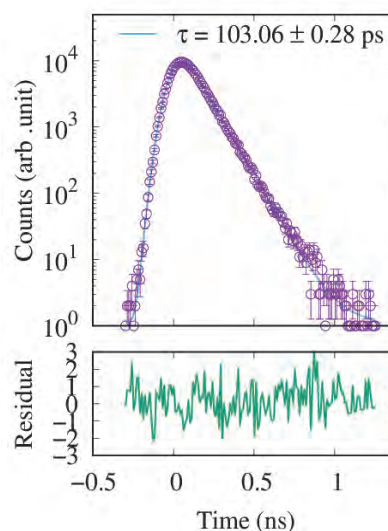


Fig. 1. Measured positron lifetime spectrum of NMIJ stainless steel. Time resolution is 138 ps in full width at half maximum.

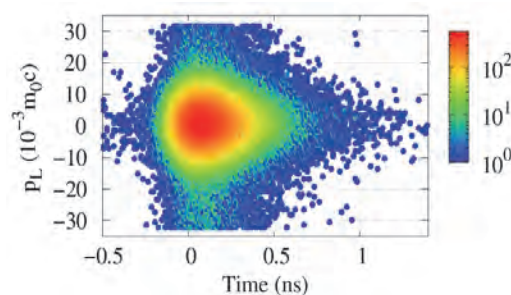


Fig. 2. GiAMOC spectrum of NMIJ stainless steel.

- [1] J. Cizek, *J. Mat. Sci. Tech.* **34** (2018) 577.
- [2] F. A. Selim, *Acta Phys. Pol. A* **132** (2017) 1450.
- [3] M. Butterling *et al.*, *Nucl. Instr. Meth. Phys. Res. B*, **269** (2011) 2623.
- [4] Y. Taira *et al.*, *Nucl. Instr. Meth. A* **652** (2011) 696.
- [5] Y. Taira *et al.*, *Rev. Sci. Instr.* **84** (2013) 053305.

BL1U

Single Electron Storage at UVSOR-III

R. Shinomiya¹, M. Shimada^{2,3}, H. Miyauchi^{2,3}, M. Fujimoto⁴ and M. Katoh^{3,1,4,2}

¹*School of Science, Hiroshima University, Higashi-hiroshima 739-8526, Japan*

²*High Energy Accelerator Research Organization (KEK), Tsukuba 305-0801, Japan*

³*Hiroshima Synchrotron Radiation Research Center, Hiroshima University, Higashi-hiroshima 739-0046, Japan*

⁴*UVSOR Synchrotron Facility, Institute for Molecular Science, Okazaki 444-8585, Japan*

Single electron storage in an electron synchrotron (electron storage ring) has been achieved at several facilities, aiming to investigate electron dynamics in a synchrotron [1,2], to investigate electromagnetic radiation from an electron [3,4], or to utilize the radiation as a primary standard [5,6]. However, in Japan, as far as we know, there is no report on such studies.

We have tried the single electron storage at UVSOR-III aiming to establish accelerator techniques for this special operation mode toward novel experiments in future.

The experimental procedure is as follows. First, we accumulate an electron beam with relatively low current, typically around 1 mA. Then, we reduce the beam current by using a device called beam scraper, which is a movable copper rod installed on the beam pipe at a straight section. We can insert the rod into the beam pipe close to the beam from the vertical direction. When we make the distance between the rod and the beam around 1 mm, the beam lifetime becomes several minutes, which is much shorter than the normal one, typically several hours. We observe the beam current by using DCCT until around 0.1 mA. Below this beam current, the DCCT cannot give reliable data. Then, we use a photomultiplier tube (PMT) to measure the synchrotron radiation intensity at BL1U, where ultraviolet radiation can be produced from an undulator. The wavelength of the fundamental radiation from the undulator was set to be 355 nm. The PMT was set at a small dark room surrounded by black curtains, where the undulator radiation was extracted from the ultra-high vacuum chamber of the beamline to the air through a sapphire window. The signal from the PMT was analyzed with a counting unit and was recorded by a PC. We tried to apply various bandpass filters to improve the signal to noise ratio. We found that a bandpass filter which had a moderately large bandwidth of about 60 nm and passed almost all the fundamental component of the undulator radiation gave the best result.

We mounted four ND filters with OD 2.0 on the PMT at the start of the measurement. As decreasing the beam current, we removed them one by one as keeping the counting rate of PMT lower than the limit of the processing rate of the counting unit. After removing all the ND filters, we successfully observed step-function-like jumps in the time history of the counting rate as shown in Fig. 1, which indicated the loss of the electrons one by one. The background rate is much smaller than the step of the counting rate, which corresponds to the

radiation intensity emitted from one electron. The observed counting rate from one electron was consistent with a preliminary evaluation of the photon flux based on an analytic formula.

We do not describe the details here, but we also succeeded in observing which RF bucket the last electron existed in. Moreover, after confirming that only one electron is circulating, we pulled out the beam scraper and observed that the last electron was stored for more than 2 hours, which is sufficiently long to carry out the experiments with single electron.

In conclusion, we successfully demonstrated the single electron operation at UVSOR-III and establish the basic techniques for this special operating mode. We are going to start novel researches utilizing this new mode.

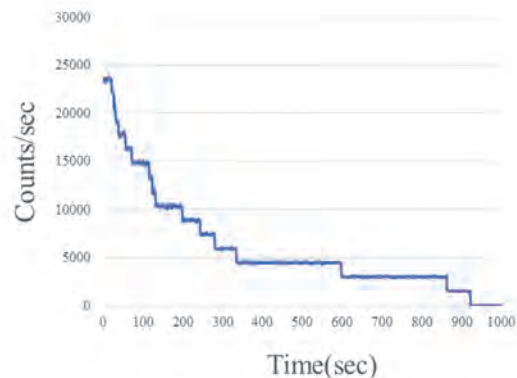


Fig. 1. Synchrotron radiation intensity at BL1U.

- [1] A. N. Aleshaev *et al.*, NIM A **359** (1995) 80.
- [2] I. V. Pinayev *et al.*, NIM A **375** (1996) 71.
- [3] I. V. Pinayev *et al.*, NIM A **341** (1994) 17.
- [4] A. Romanov *et al.*, JINST **16** (2021) P12009.
- [5] R. Klein *et al.*, Phys. Rev. STAB **11** (2008) 110701.
- [6] R. Klein *et al.*, Metrologia **47** (2010) R33.

BL1U

Exploring Novel Application of Undulator Radiation Based on Interferometric Technique

K. Kato¹, M. Shimada^{2,3}, H. Miyauchi^{2,3}, A. Mano⁴ and M. Katoh^{3,1,5,2,4}

¹*School of Science, Hiroshima University, Higashi-hiroshima 739-8526, Japan*

²*High Energy Accelerator Research Organization (KEK), Tsukuba 305-0801, Japan*

³*Hiroshima Synchrotron Radiation Research Center, Hiroshima University, Higashi-hiroshima 739-0046, Japan*

⁴*Synchrotron Radiation Research Center, Nagoya University, Nagoya 464-8603, Japan*

⁵*UVSOR Synchrotron Facility, Institute for Molecular Science, Okazaki 444-8585, Japan*

The classical electromagnetic theory indicates that radiation from a relativistic electron running in an undulator forms a wave packet whose number of cycles is exactly same as the number of magnetic periods of the undulator. In case of the undulator at BL1U, the number of the magnetic period is 10. If we set the wavelength of the fundamental radiation at 355 nm, then the wave packet has a length of 3.5 micron which corresponds to about 10 femtosecond. This “ultrafast” property of synchrotron radiation has merely been considered useful for any applications except for only a few previous works [1]. However, recently, at UVSOR, interesting applications of this property has been demonstrated successfully [2,3,4].

Following these successes, we continue exploring other possible applications. We were inspired by a previous study using interferometer, in which the undulator radiation showed a clear interferogram [5]. We started considering an application to the tomographic imaging. In the optics technology field, a technology called optical coherence tomography has been successfully demonstrated and are widely used particularly in the medical field [6]. Its principle may be described as follows. A low coherence light beam splits into two by means of a beam splitter. Two beams are reflected by mirrors and come back to the beam splitter and merge. When the path lengths are exactly same, interference fringe is observed in the merged beam. If a sample material is inserted on a path, because of the refractive index of the sample, the path length which gives the interference changes. Moreover, if multi-reflection takes place in the sample, interference is observed at several different path lengths. From such observation, one can get information on the inner structure and its optical property of the sample. We have carried out a proof of principle experiment on such a tomography method using undulator radiation at BL1U [7]. Some preliminary results are presented here.

The wavelength of the undulator radiation was selected at 355 nm, which is compatible with the wavelength range of the Mach–Zehnder interferometer, which was constructed in a previous study [5]. We utilized the existing interferometer to observe the change of the interferogram as putting samples on its light paths. We tried two configurations, transmitting and reflecting ones. To minimize the modification of the interferometer, in the former configuration, we just

placed the sample on the one of the path after the beam splitter, and, in the latter, we placed the sample at the reflecting mirror.

We carried out the interferogram measurements on some thin materials such as glass plates or films and several stimulated samples which has multilayer structure. One example of the interference fringe is shown in Fig. 1. In this measurement, a thin film is placed in a transmitting configuration. The sample covered a half of the light path. By adjusting the optical path length, we could observe interference fringe only for the half area where the film existed. More details will be presented in future papers.

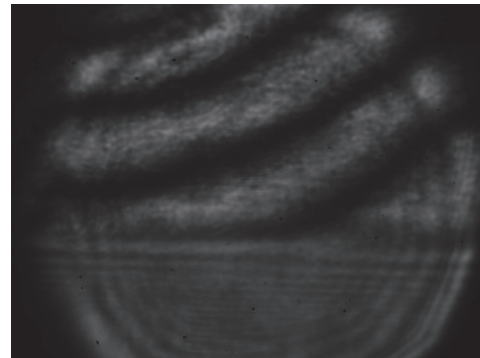


Fig. 1. Interference fringe observed for 25 micron OPP film as a sample. In the upper side, the OPP film is placed and in the lower none.

[1] S. Nakanishi *et al.*, *J. Synchrotron Rad.* **5** (1998) 1702.

[2] T. Kaneyasu *et al.*, *Phys. Rev. Lett.* **123** (2019) 233401.

[3] Y. Hikosaka *et al.*, *Nature Comm.* **10** (2019) 4988.

[4] T. Kaneyasu *et al.*, *Phys. Rev. Lett.* **126** (2021) 113202.

[5] *e.g.* D. Huang *et al.*, *Science* **254** (1991) 1178

[6] A. Mano *et al.* UVSOR Activity Report 2020 **48** (2021) 38.

[7] K. Kato *et al.*, presented at JSR 2022 (2022).

BL2A

Calibration of CMOS Sensor with Reflective-type Flux Reduction System

N. Narukage

National Astronomical Observatory of Japan, Mitaka 181-8588, Japan

The solar corona is full of dynamic phenomena such as solar flares. The understandings of these phenomena have been progressing step-by-step with the evolution of the observation technology in EUV and X-rays from the space. But there are fundamental questions remain unanswered or haven't even addressed so far. Our scientific objective is to understand underlying physics of the dynamic phenomena in the solar corona, covering some of the long-standing questions in solar physics such as particle acceleration in flares and coronal heating. To achieve this objective, we identify the imaging spectroscopy (the observations with spatial, temporal and energy resolutions) in the soft X-ray range (from ~ 0.5 keV to ~ 10 keV) is a powerful approach for the detection and analysis of energetic events [1]. This energy range contains many lines emitted from below 1 MK to beyond 10 MK plasmas plus continuum component that reflects the electron temperature.

The soft X-ray imaging spectroscopy is realized with the following method. We take images with a short enough exposure to detect only single X-ray photon in an isolated pixel area with a fine pixel Silicon sensor. So, we can measure the energy of the X-ray photons one by one with spatial and temporal resolutions. When we use a high-speed soft X-ray camera that can perform the continuous exposure with a rate of more than several hundred times per second, we can count the photon energy with a rate of several 10 photons / pixel / second. This high-speed exposure is enough to track the time evolution of spectra generated by dynamic phenomena in the solar corona, whose lifetimes are about form several ten seconds to several minutes. For the first imaging spectroscopic observation of the solar corona in soft X-ray range, we launched a NASA's sounding rocket (FOXSI-3) on September 7th, 2018 and successfully obtained the unprecedented data [2] using a high-speed X-ray camera [3] with a back-illuminated CMOS sensor [4].

Calibration of CMOS detectors is essential for scientific data analysis. For this purpose, a completely monochromatic X-ray light source is needed. In addition, the flux must be adjusted so that individual X-ray photons can be isolated. Therefore, so far, we have controlled (reduced) the flux by adjusting the material and thickness of metal filters. However, in this case, the lower energy was preferentially attenuated, so the contamination of higher-order (2nd, 3rd and 4th order) components could not be removed, resulting in incomplete data for calibration.

In this time, we developed a mirror-based reflective-type flux reduction system (see Fig. 1). In this system, two flat mirrors aligned in parallel are mounted on a rotating stage, and by changing the angle of incidence, the reflectance, i.e., attenuation rate, can be flexibly

adjusted. The system worked well as expected and successfully produced the completely monochromatic light with the appropriate flux. As a result, the response of the CMOS detector used in the FOXSI-3 sounding rocket project could be completely calibrated in the energy range of 830 eV to 4500 eV in 50 eV intervals (see Fig. 2).

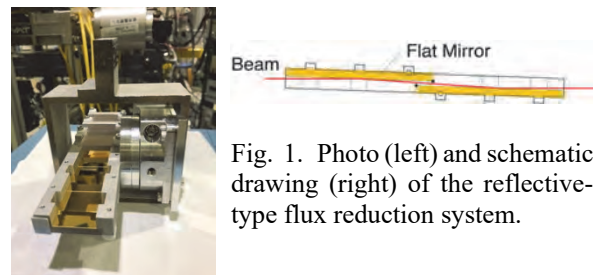


Fig. 1. Photo (left) and schematic drawing (right) of the reflective-type flux reduction system.

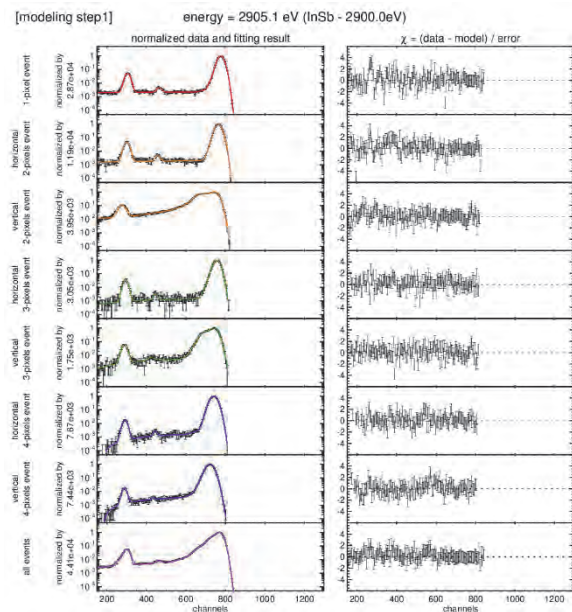


Fig. 2. Measured (black data points) and modeled (colored lines) response of the CMOS sensor to the monochromatic X-rays (at 2905.1 eV in this case).

[1] N. Narukage *et al.*, White paper of the “soft X-ray imaging spectroscopy”, arXiv:1706.04536 (2017).

[2] N. Narukage and S. Ishikawa, UVSOR Activity Report 2018 **46** (2019) 36.

[3] S. Ishikawa *et al.*, Nuclear Instruments and Methods in Physics Research Section A, **912** (2018) 191-194.

[4] N. Narukage *et al.*, Nuclear Instruments and Methods in Physics Research Section A, **950** (2020) 162974.

BL3B

Photon Energy Resolutions of BL3B Evaluated by Appearance Energy Measurements of Xe⁺ Ions

 H. Iwayama^{1,2}
¹UVSOR Synchrotron Facility, Institute for Molecular Science, Okazaki 444-8585, Japan

²School of Physical Sciences, The Graduate University for Advanced Studies (SOKENDAI), Okazaki 444-8585, Japan

A beamline in a synchrotron facility generally works as a monochromator and focus system. A photon energy resolution of the beamline is one of the most important parameters for various measurements. To maintain the performance of the beamlines, it is desirable to check the actual photon energy resolution regularly.

The beamline BL3B can provide monochromatic light in the range from visible to extreme ultraviolet region. Previously the photon energy resolution of BL3B was evaluated by vibration-rotation spectra of oxygen molecules [1], which are significantly complex. In this work, we estimate photon energy resolutions of BL3B from appearance energy spectra, which have step functional structure at an ionization threshold.

The photoelectron-photoion coincidence (PEPICO) measurements for an ion time-of-flight mass spectrum were performed at UVSOR BL3B. A schematic view of PEPICO measurements is described in the previous report [2]. Sample gas is xenon, whose ionization threshold is 12.130 eV [3]. The ion mass spectra were recorded at photon energies ranging from 12.100 eV to 12.200 eV in 0.001 eV-increments. We used G1 grating of BL3B. We estimate photon energy resolutions for three slit configurations of (entrance slit, exit slit) = (500 μm , 500 μm), (300 μm , 300 μm) and (100 μm , 100 μm).

Figure 1 shows a typical mass spectrum of Xe ions. The peak structure results from an isotope distribution of Xe atoms. The corresponding mass resolution $m/\Delta m$ is 400.

Figure 2 shows Xe ions yield spectra for three slit configurations. We find steep rises at the ionization threshold of 12.130 eV. With narrowing slit sizes, steps of Xe ion yield spectra become steeper. This shows that photon energy resolution become better. From three spectra, we estimate photon energy resolutions for three slit configurations and summarize Table 1. In future, we also perform estimations of photon energy resolutions for G2 and G3 gratings.

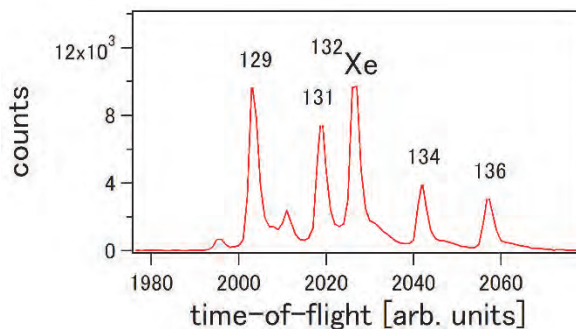


Fig. 1. Typical time-of-flight mass spectrum of Xe ions.

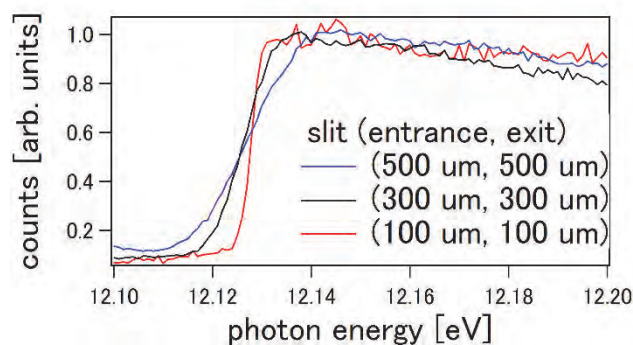


Fig. 2. Xe ion yield spectra around the ionization energy of 12.130 eV for three slit configurations.

Table 1. Photon energy resolutions for G1 grating

Slit size	ΔE @ $h\nu=12\text{eV}$	$E / \Delta E$
(500 μm , 500 μm)	20 meV	600
(300 μm , 300 μm)	11 meV	1000
(100 μm , 100 μm)	4.2 meV	3000

[1] K. Fukui, *et al.*, J. Synchrotron Rad. **21** (2014) 452.

[2] H. Iwayama and T. Horigome, UVSOR Activity Report 2020 **48** (2021) 41.

[3] https://physics.nist.gov/PhysRefData/ASD/levels_form.html.

BL4B

BL4B Usage for Developing the Photoelectron Spectroscopy End-station for Organic Materials

K. Fukutani, H. Iwayama, F. Matsui and S. Kera
Institute for Molecular Science, Okazaki 444-8585, Japan

The field of organic electronics has been prolific in the last couple of years. However, the study of the molecular function and property using the synchrotron light sources has been limited so far due to difficulty in the measurements for irradiation sensitive materials and lack of the suitable environment for the comprehensive experiments.

The soft X-ray beamline BL4B, monochromator was designed to cover the energy range of 35 – 800 eV and used for XMCD and XAS by setting the user apparatus. To achieve the fundamental understanding of charge transport properties, adsorption properties, interface energetics, chemical reactivity and so on, we placed the end-station with the acceptance-cone-tunable electron spectrometer (ACTES) for the highly efficient constant-energy photoelectron mapping based on the ARPES system equipped with a hemispherical analyzer (MBS A-1 Lens4) [1].

In the initial process, we tested the figure of merit for a typical experimental procedure, that is core-level photoelectron spectroscopy, valence band energy-band dispersion measurement, low-energy secondary electron cut-off measurement with bias voltage, and near-edge X-ray absorption fine structure (NEXAFS) spectroscopy. The samples of Au(111) and molecular films of OV-phthalocyanine (OVPC) are prepared.

The photon flux is moderate at BL4B, however it is still high enough to make some troubles on the sample of organic films, like an irradiation damage. We have checked a typical measurement condition of photon flux and analyzer parameters with energy resolution and spectral intensity for optimizing the molecular systems. The beam-spot size was set at 0.68 x 0.52 mm at photon energy ($h\nu$) of 60 eV with a resolution power ($E/\Delta E$) of 5,000. Effective low- $h\nu$ range could start from 30 eV, and it would be very hard to obtain the results at 25 eV for ARPES experiments. The high- $h\nu$ range could be useful up to 1,200 eV for XPS experiments, though the monochromator covers up to 1,500 eV. The contribution of the second-order light is estimated less than 1 % for $h\nu = 250$ eV at the $E/\Delta E$ of 2,000 for grating G1.

XAS was demonstrated for C-, N-, and O- K edges. A large photon-flux dropping due to a mirror contamination is observed for C-K edge region, and the NEXAFS experiments for bulk samples could be reasonable by changing the irradiating position slightly for recording the data by using a relatively clean area of the gratings, however we request to clean up the mirror systems. Moreover, the reference data of Au mesh must be clarified to obtain the data for thin-film interfaces.

The beam stabilities of the photon energy and flux

have been carefully checked by repeatedly measuring the binding energy and intensity of Au 4f and Fermi edge. The result confirms that the light will be stabilized after about 1 hour. The continuous scanning for accumulating the data long time under the low-photon flux should be confirmed again.

The beam damage on the molecular film sample is checked for the annealed monolayer of OVPC/Au(111) with $h\nu = 60$ eV at the $E/\Delta E$ of 2,000, which gives the sample current (I_s) of 5.2 nA (corresponding to the Au mesh current (I_0) of 167 pA). We observed discernible broadening of the HOMO spectral feature over the 2 h irradiation as shown in Fig. 1. We find the irradiation effects are settled by reducing the photon flux to the $I_s = 0.55$ nA to give no remarkable change in the features over 40 min. The impact will depend on the $h\nu$ range, hence the molecular film survived for 60 min. in XPS for $h\nu = 500$ eV at the $E/\Delta E$ of 2,000, giving the $I_s = 0.28$ nA ($I_0 = 32$ pA), but not suitable for a higher-photon flux of $I_s = 0.77$ nA ($I_0 = 85$ pA) as an example.

The detailed experiments upon cooling the sample will be continued in FY2022.

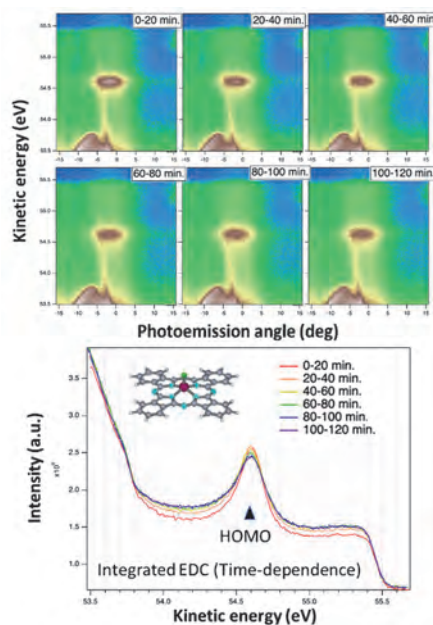


Fig. 1. Impacts of irradiation time on the ARPES of a monolayer of OVPC/Au(111) surface taken at 295 K and $h\nu = 60$ eV.

[1] H. Yamane *et al.*, *Rev. Sci. Instrum.* **90** (2019) 093102.

BL4B

Development of High Efficiency Liquid Cell in Total Electron Yield Using Atomically-thin Graphene

I. Mitsuishi¹, K. Kashiwakura¹, Y. Niwa¹, T. Ogawa¹, Y. Tawara¹, R. Kitaura², P. Solís-Fernández³, K. Kawahara³, H. Ago³, T. Taniguchi⁴, K. Nomoto⁴, H. Kodaka⁴, T. Horigome⁵, E. Nakamura⁵, H. Iwayama⁵, M. Nagasaka⁵ and K Tanaka⁵

¹ Graduate School of Science, Division of Particle and Astrophysical Science, Nagoya University, Nagoya 464-8602, Japan

² Department of Chemistry, Nagoya University, Nagoya 464-8602, Japan

³ Global Innovation Center, Kyushu University, Kasuga 816-8580, Japan

⁴ Optical Measurement Technology Development Department, R&D Division, USHIO INC., Yokohama 225-0004, Japan

⁵ UVSOR Synchrotron Facility, Institute for Molecular Science, Okazaki 444-8585, Japan

X-rays are a powerful probe to investigate material properties through, e.g., X-ray absorption spectroscopy (XAS) which can reveal local atomic and electronic states of oxygen, carbon, etc.. Among the XAS methods for liquid, total electron yield is preferably utilized in some cases because short electron escape depth in this method makes it possible to examine atomic and electron states of liquid surface and solid-liquid interfaces. In order to realize high efficiency measurements through the total electron yield method, high efficiency films with high electron transmission are a key and therefore have been strongly desired.

To construct our original device for the total electron yield measurements, we propose to utilize graphene which is atomically thin and has high electron transmission [1]. As a first step, we tried to establish our original experimental setup to verify our idea as shown in Fig. 1. As a preliminary experiment, liquid water was sandwiched by a silicon nitride window and free-standing 5-layer graphene on a quartz substrate with apertures of 0.5 x 0.5 mm. A high voltage system was also prepared between the entrance window of the sample and the X-ray source to reduce the contamination of electrons produced by the surface of the substrate and sample holder. We obtained the spectra around the O K-edge structure as shown in Fig. 2 and confirmed the O K-edge absorption by the liquid water. However, photoelectrons of oxygen were also detected in background spectra without the sample. Thus, to reduce the contamination, voltages of 200, 400, 600, and 800 eV were applied and the reduction of the commination was confirmed successfully as shown in Fig. 2. Although the high-voltage system worked well and the contamination level went down significantly, we could not conclude that there is no significant contribution to the observed photoelectrons with the sample. Thus, to evaluate the sensitivity of our liquid cell, optimizations of our experimental setup based on simulations are necessary.

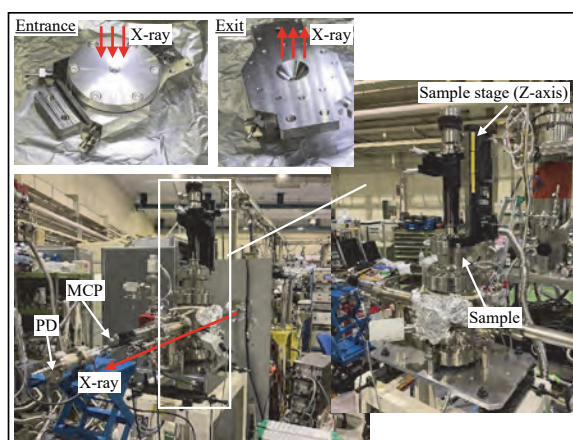


Fig. 1 Experimental setup and an overview of the sample holder.

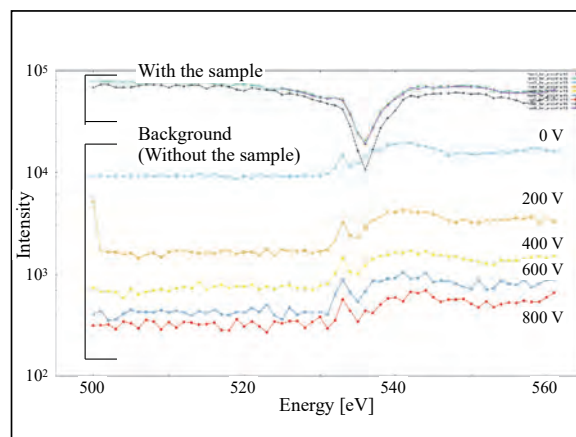


Fig. 2 Examples of observed MCP spectra around the O K-edge structure with / without the sample. The spectra with voltages of 200, 400, 600, 800 eV are also shown for comparison.

[1] G. Hassink, R. Wanke, I. Rastegar, W. Braun, C. Stephanos, P. Herlinger, J. H. Smet and J. Mannhart, *APL Materials* **3** (2015) 076106.

BL5B

Development of a Fluorescence Polarimeter in Extreme Ultraviolet Region

T. Kaneyasu¹, K. Hosaka² and J. Adachi³¹SAGA Light Source, Tosu 841-0005, Japan²National Institutes for Quantum Science and Technology, Takasaki 370-1292, Japan³Institute of Materials Structure Science, KEK, Tsukuba 305-0801, Japan

Polarization is one of the most important characteristics of synchrotron radiation. In addition to the use of horizontal linear polarization in the bending magnet radiation, the recent advent of insertion devices allows us to use arbitrarily polarized light in a wide spectral range from vacuum ultraviolet to x-ray. For accurate measurements using the polarization properties of synchrotron radiation, it is essential to evaluate the polarization state of light at a sample point. Here, we present a polarization measurement of synchrotron radiation in the extreme ultraviolet (XUV) wavelength region using a fluorescence polarimeter. This method is based on the conversion of the XUV radiation to visible radiation on the atomic resonance [1-3]. The fluorescence preserves the polarization state of the excitation light when it is observed along the light propagation axis. Comparing with the optical polarimeters [3], this method has advantages in its simple apparatus and easy operation.

The experiment was performed at the bending magnet beamline BL5B in UVSOR synchrotron. Figure 1 shows the experimental layout of the present study. The monochromatized synchrotron radiation interacted with helium atoms provided by an effusive beam. The pressure of the interaction chamber was around 1×10^{-3} Pa during the measurement. The excitation wavelength was 51.56 nm, corresponding to the 1s5p resonance of helium atom. We observed 361-nm-wavelength fluorescence photons emitted in decays from 1s5p to 1s2s state of a helium atom. The fluorescence photons emitted parallel to the light propagation axis (z-axis) were detected by a photomultiplier tube equipped with a polarizer and a bandpass filter. To evaluate the polarization state of XUV radiation, we measured fluorescence intensity as a function of the rotation angle of the polarizer.

Figure 2 shows the fluorescence intensity measured as a function of the polarizer angle which is defined by the angle of the polarization axis with respect to the horizontal axis (x-axis). The fluorescence intensity shows a sinusoidal modulation reflecting the polarization state of the XUV radiation. Assuming an elliptical polarization, the experimental data points are fitted by a theoretical curve. The linear polarization degree of light is evaluated to be 0.74 which is somewhat smaller than the ideal value of 0.84 [4]. This disagreement is probably due to the detection solid angle for the fluorescence photons, and it is expected that this instrumental effect can be improved by reducing the detection solid angle.

The present work shows the capability of a fluorescence polarimeter to evaluate the polarization state of XUV radiation. Although we evaluated the degree of linear polarization only, this method has the potential to determine Stokes parameters [3] by just introducing a quarter waveplate in the detector system.

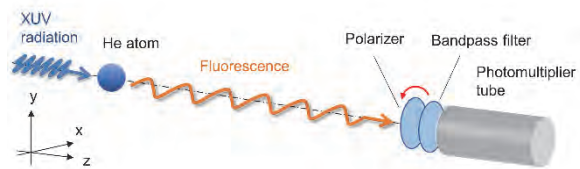


Fig. 1. Experimental layout of the present study. The fluorescence photon emitted along the light propagation axis was detected.

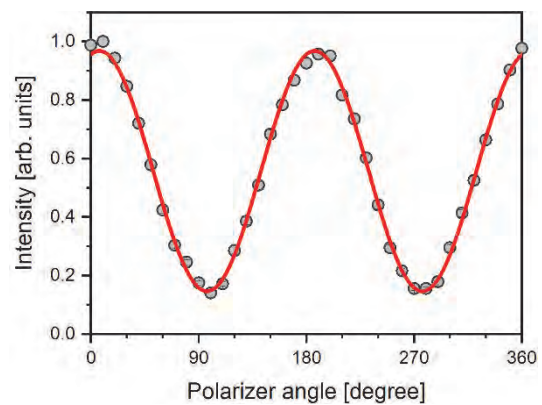


Fig. 2. Fluorescence intensity measured as a function of the polarizer angle. The experimental data points are fitted by a theoretical curve.

- [1] V. Bobahev and O. S. Vasyutinkii, *Rev. Sci. Instrum.* **63** (1992) 1509.
- [2] C. J. Latimer et al., *J. Electron Spectroscopy Relat. Phenom.* **101-103** (1999) 875.
- [3] E. Allaria et al., *Phys. Rev. X* **4** (2014) 041040.
- [4] Y. Hikosaka et al., *J. Synchrotron Rad.* **27** (2020) 675.

BL5B

Measurement of a Detection Efficiency of High-sensitivity Microchannel Plates with Tapered Pores

S. Matoba¹, H. Iwayama^{2,3} and T. Kaneyasu⁴¹*Institute of Materials Structure Science, KEK, Tsukuba 305-0801, Japan*²*Editorial Board, UVSOR Synchrotron Facility, Institute for Molecular Science, Okazaki 444-8585, Japan*³*School of Physical Sciences, The Graduate University for Advanced Studies (SOKENDAI), Okazaki 444-8585, Japan*⁴*SAGA Light Source, Tosu 841-0005, Japan*

A microchannel plate (MCP) is a lead glass detector with a two-dimensional array of electron-multiplying pores of about 10 μm in diameter. When charged particles or short-wavelength photons collide with the inner wall of the pore, secondary electrons are generated and amplified in the pore to be detected as electron pulses. MCPs are used in a very wide range of fields from basic research to industry because of their large area, high spatial resolution, and high-speed detection capability. The maximum detection efficiency of an MCP is at the upper limit of its open-area-ratio, and typical MCPs have a detection efficiency of 50-60%. This causes a problem of reduced detection efficiency when used in coincidence measurement experiments. For example, if an MCP with a detection efficiency of 60% is used in a triple coincidence experiment, the total detection efficiency drops to about 20%. We have developed a tapered MCP with an effective aperture of 89% by applying a tapered aperture to the incident area, based on the idea that the detection efficiency can be increased by increasing the aperture. The maximum detection efficiency of the tapered MCP for monatomic ions was improved to 90%, comparable to the open-area-ratio, demonstrating for the first time the effectiveness of tapered processing in the detection of monatomic ions [1]. MCPs are also used as UV and X-ray detectors, and are employed as imaging elements for planetary atmosphere observation from satellites and spacecraft. It is known that a CsI coating on the surface of an MCP improves the detection efficiency by several tens of times in the wavelength region above 100 nm, but below 100 nm, where emission lines from helium and oxygen ions, which are major components of many astronomical atmospheres, are concentrated, the improvement is only 1.2 times [2]. Therefore, it is not a decisive observation method for understanding the dynamic picture of celestial atmospheres. In this experiment, the detection efficiency of EUV is measured using a tapered MCP to verify its usefulness. The wavelength range of about 32-190 nm was used for the measurement. Spectrified EUV passes through a pinhole with a diameter of 1 mm and is injected into the MCP. Since the counting rate of the MCP saturates at high intensity, a molybdenum mesh and a Kapton thin film were used to attenuate the light. A 300-nm-thick aluminum foil was inserted to attenuate higher-order light. The MCP used for the measurement is a custom-made type divided into four regions: normal type,

tapered type, CsI-coated normal type, and CsI-coated tapered type.

Figure 1 shows the intensity ratios of the measured count rates of tapered MCP (T-MCP), CsI-coated MCP (CsI-MCP), and tapered CsI-coated MCP (TCsI-MCP) to normal-type MCP (N-MCP). The detection efficiency of the tapered MCP is higher than that of the normal MCP in all the measured wavelength ranges. In the short wavelength range, the tapered MCP has a higher detection efficiency than the CsI-coated MCP. The synergistic effect of tapered MCP and CsI coating on the detection efficiency of MCP was confirmed. These results demonstrate that tapered MCP is a powerful tool for UV detection.

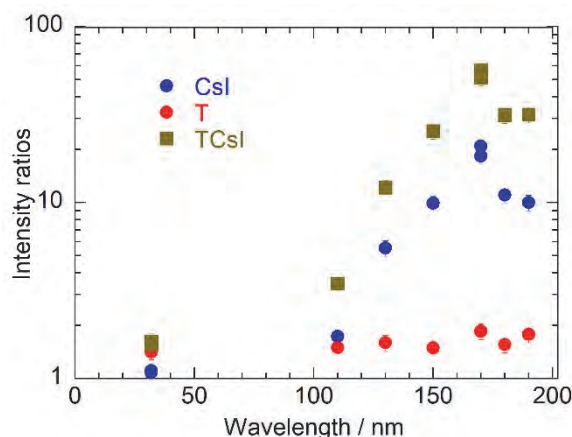


Fig. 1. intensity ratio of measured count rates of tapered MCP (T), CsI-coated MCP (CsI) and tapered CsI-coated MCP (TCsI) to normal type MCP (N-MCP).

[1] S. Matoba *et al.*, *Jpn. J. Appl. Phys.* **50** (2011) 112201.

[2] K. Yoshioka *et al.*, *Rev. Sci. Instrum.* **83** (2012) 083117.

BL5B

Study on the Source of Photon-Energy Drift of BL5B

H. Zen¹, E. Nakamura², K. Hayashi² and K. Tanaka^{2,3}

¹*Institute of Advanced Energy, Kyoto University, Uji 611-0011, Japan*

²*UVSOR Synchrotron Facility, Institute for Molecular Science, Okazaki 444-8585, Japan*

³*School of Physical Sciences, The Graduate University for Advanced Studies (SOKENDAI) Okazaki 444-8585, Japan*

The stability of the photon beam properties, such as beam position, beam intensity, photon energy, and so on, during user operation in beamlines, are very important for the advanced application of synchrotron radiation (SR) facilities. A photon-energy drift at BL5B has been observed during user experiments [1]. We started the study on the source of this photon-energy drift in 2019. Although we have tried several countermeasures to suppress the photon-energy drift [2], no significant improvement has been achieved.

In the study performed FY2020, we found a clear correlation between the temperature of the M1 mirror holder and the photon energy [3]. Therefore, in this FY, a heater attached directly to the M1 mirror holder was introduced to control the temperature of the M1 mirror holder. By using the heater, the temperature of the M1 mirror holder can be stabilized as shown in Fig. 1 (a) black line. However, even with the stabilized M1 temperature, the wavelength of the SR exit the monochromator continuously changes as shown in Fig. 1 (c) black line and red line.

To find the origin of the photon-energy drift, several trials were made; 1: Turn off and on the heater on M1 holder, 2: Remove M1 mask to increase the M1 holder temperature, 3: decrease mirror temperature by reducing SR amount on M1 and successive optics. By trial 1, we could confirm the correlation between M1 holder temperature and the photon energy. By trial 2, we found that the temperature variation of the M1 holder has no significant influence on the trend of photon-energy drift. By trial 3, we found that the variation of SR amount has a significant influence on the photon energy drift. After reducing the SR amount, the temperature of the M1 mirror gets stable within 3 hours (see Fig. 1 (b) red line) but the photon-energy drift last for longer than 6 hours (see Fig. 1 (c) red line). These results imply that the significant source of the photon-energy drift should exist after the M1 mirror.

We checked our results obtained in FY2019. In FY2019, grating #3 and mirror #23 (configuration of G3M3) were used and roughly 0.1 eV photon-energy drift was observed from 12 to 21 o'clock. In this FY, roughly 0.24 eV photon-energy drift was observed from 12 to 21 o'clock with grating #2 and mirror #24 (G2M4). The sensitivity of the photon energy to the angular variation for the G2M4 configuration is approximately 1.2 times higher than that of the G3M3 configuration. The observed difference of photon-energy variation was much larger than the difference of sensitivity. From this result, grating and its holding

mechanics are considered to be a significant source of the photon-energy drift of BL5B. Further study should be conducted to clarify whether the grating and its holding mechanics are the significant sources of the photon-energy drift or not.

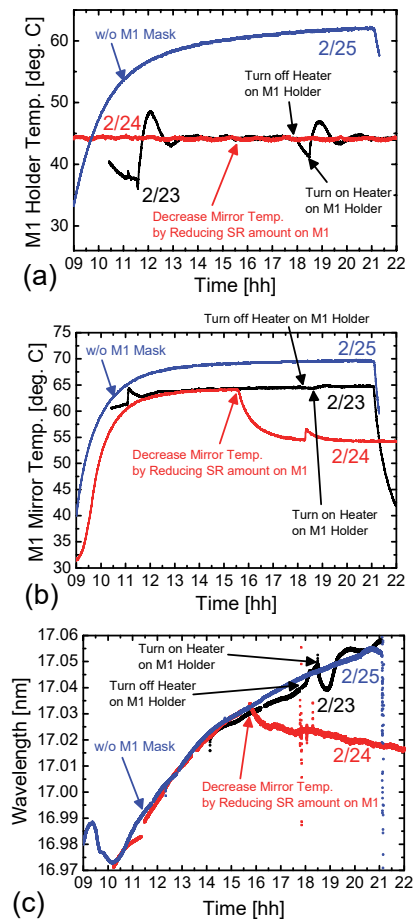


Fig. 1. Trend of (a) temperature of M1 mirror holder, (b) temperature of M1 mirror, and (c) wavelength of SR light exit monochromator of BL5B.

[1] K. Hayashi, UVSOR Activity Report 2011 **39** (2012) 121.

[2] H. Zen *et al.*, UVSOR Activity Report 2019 **47** (2020) 42.

[3] H. Zen *et al.*, UVSOR Activity Report 2020 **48** (2021) 47.

BL7B

Complex Refractive Index Measurement by Reflectance Spectra in Different Polarization Configurations

M. Horiba¹, K. Fukui¹, K. Yamamoto¹ and T. Saito²¹Department of Electrical and Electronics Engineering, University of Fukui, Fukui 910-8507, Japan²Department of Electrical and Electronic Engineering, Tohoku Institute of Technology, Sendai 982-8577, Japan

Based on the basic design of the instrument by the AIST group [1], we have been developing a complex type refractive index spectrum measurement device (CRIMS-VUV) [2], which can continuously measure not only in the visible region but also in the ultraviolet and vacuum ultraviolet regions. CRIMS-VUV can perform spectroscopic ellipsometry measurements and reflection spectrum measurements under the same environment.

The spectroscopic ellipsometry measurement mode of CRIS-VUV has the advantage of measuring the complex refractive index with high accuracy. However, this mode has the disadvantage that, due to its measurement principle, it takes time to measure at each measurement point (photon energy), making it difficult to measure a continuous spectrum. In this respect, reflection spectrum measurement mode is suitable for measuring continuous spectrum. The well-known Kramers - Kronig analysis method is used to determine the complex refractive index spectrum from the reflectance spectrum. However, Kramers - Kronig analysis method requires appropriate approximations on both sides of the measured photon energy range, since Kramers - Kronig analysis method uses the integral of reflectance at photon energy from 0 to infinity to obtain complex refractive index at each photon energy. Therefore, this method is useful, for example, for obtaining qualitative complex refractive index spectrum for limited photon energy region around the absorption edge, but is not well suited for obtaining quantitative complex refractive index spectrum over a wide photon energy region. Unlike the Kramers - Kronig analysis method, there are two methods to obtain the complex refractive index at each photon energy from reflectance measurements under different measurement conditions, one with reflectance measurements at different incident angles and the other with different polarization configurations. Therefore, we decided to use a method of measuring reflectance with *p*- and *s*-polarization configurations (PS method) to obtain the complex refractive index for each photon energy, since CRIMS-VUV has a mechanism that automatically changes the polarization configuration as desired. In this report, we show the trial results of PS method measurements on an Au mirror as a sample.

PS method measurements were carried out with CRIMS-VUV installed at BL7B. The photon energy range was 2 to 20 eV. Since output light of BL7B (input light of CRIMS-VUV) is highly linearly polarized

(Stokes parameter $S_1/S_0 \sim 0.8$), reflectance measured in the horizontal and the vertical configuration are almost equal to the reflectance of *p*- and *s*-polarization, respectively.

The reliability of complex refractive index derived from experimental values is directly related to the magnitude of the difference in reflectance in *p*- and *s*-polarization configuration. Therefore, the angle of incidence should be close to Brewster's angle, and experiments have confirmed that the difference in reflectance spectra between the *p*- and *s*-polarization configuration increases in the order of 8°, 45°, and 67° angle of incidence. Therefore, results for 45° and 67° are used for analysis. Figure 1 shows the photon energy dependence spectra of complex refractive index of Au mirror. The curves represent refractive index *n* and extinction coefficient *k* derived from PS method, and symbols from spectroscopic ellipsometry measurement mode. The overall trend of *n* and *k* spectra from PS method are in good agreement with those from spectroscopic ellipsometry measurement mode. However, a marked difference in absolute values remains an issue to be solved.

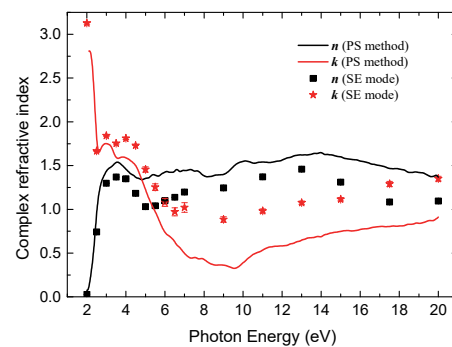
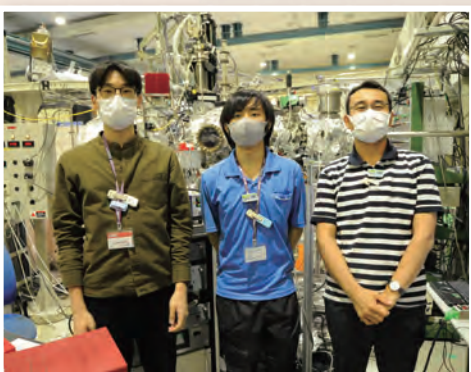
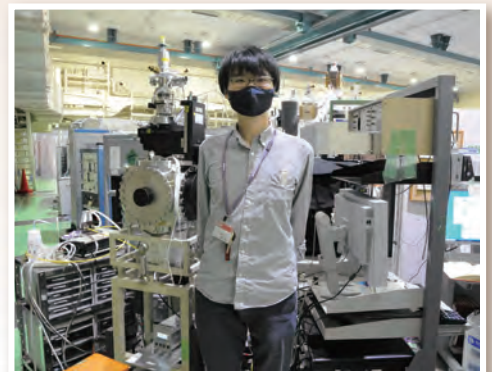
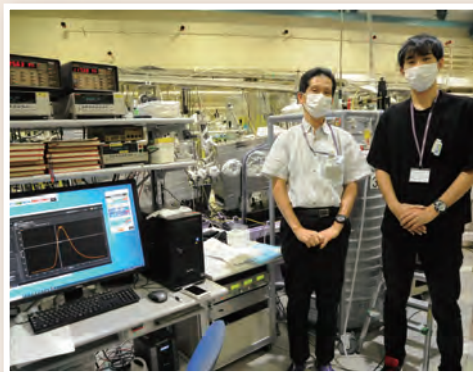
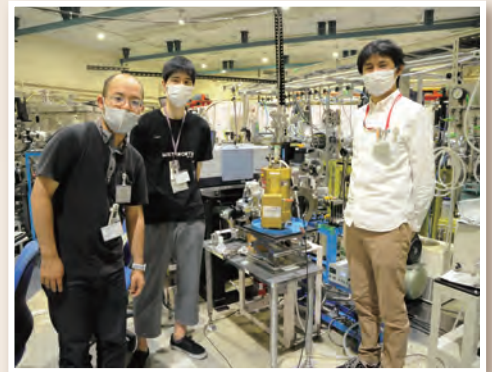
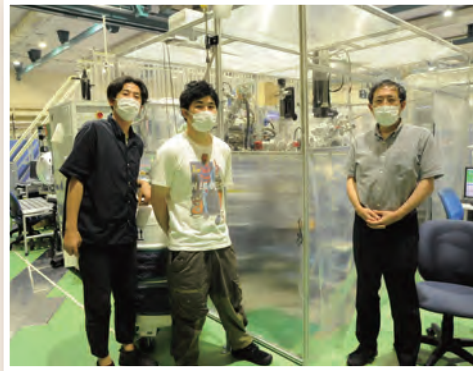


Fig. 1. Complex refractive index of Au mirror

- [1] T. Saito, M. Yuri and H. Onuki, Rev. Sci. Instrum. **66** (1995) 1570.
 [2] D. Imai *et al.*, UVSOR Activity Report 2018 **46** (2019) 39.

UVSOR User 3



III-2

Materials Sciences

BLIU

Study on Defects in Iron Formed under Hydrogen Embrittlement Environment Using In-Situ Measurement Technique of Gamma-Ray Induced Positron Annihilation Lifetime Spectroscopy

A. Yabuuchi¹, T. Hirade², M. Fujinami³, R. Awaji³, N. Oshima⁴, K. Takai⁵, K. Sugita⁶ and Y. Taira⁶

¹Institute for Integrated Radiation and Nuclear Science, Kyoto University, Kumatori 590-0494, Japan

²Nuclear Science and Engineering Center, Japan Atomic Energy Agency, Tokai 319-1195, Japan

³Department of Applied Chemistry and Biotechnology, Chiba University, Chiba 263-8522, Japan

⁴National Institute of Advanced Industrial Science and Technology, Tsukuba 305-8568, Japan

⁵Department of Engineering and Applied Sciences, Sophia University, Tokyo 102-8554, Japan

⁶UVSOR Synchrotron Facility, Institute for Molecular Science, Okazaki 444-8585, Japan

The incorporation of hydrogen into metals such as steel is known to cause embrittlement of the metal. In a previous study, vacancy clusters have been detected near the hydrogen embrittlement fracture surface by positron annihilation lifetime spectroscopy. However, conventional positron annihilation lifetime spectroscopy requires measurements after hydrogen charging, and therefore, in-situ positron annihilation lifetime measurements were desired to understand defect behavior during hydrogen charging. In this study, we irradiated pure iron samples with high-energy pulsed gamma-rays obtained from UVSOR and measured the positron lifetimes in-situ during hydrogen embrittlement tests or tensile tests using positrons induced inside the samples.

Well-annealed pure iron tensile test pieces (10 mm in width and 2 mm in thickness) were either (1) mounted in a 0.1 N NaOH aqueous solution containing 5 g/L NH₄SCN and charged with cathodic hydrogen by applying a current density of 50 A/m², or (2) mounted in a tensile testing apparatus and stretched to a nominal strain of 8% and held under a constant load. The samples (1) and (2) were irradiated with a pulsed gamma-ray beam for in-situ positron annihilation lifetime measurements.

Figure 1 shows positron annihilation lifetime spectrum obtained from a hydrogen-charged pure iron sample mounted in NaOH aqueous solution. A lifetime component of ~2 ns, corresponding to the annihilation of positrons in the aqueous solution, was observed with non-negligible intensity, indicating that further refinement of the measurement technique is needed. Figure 2 shows positron annihilation lifetime spectra obtained from a pure iron tensile-test piece under no load and under the load required for stretching to a nominal strain of 8%. The spectral shape clearly changed by applying the load, indicating the appearance of a defect component. Furthermore, focusing on the change in positron lifetime over time may reveal more than what can be obtained by conventional positron annihilation lifetime spectroscopy. A more detailed analysis of the obtained spectra is currently underway.

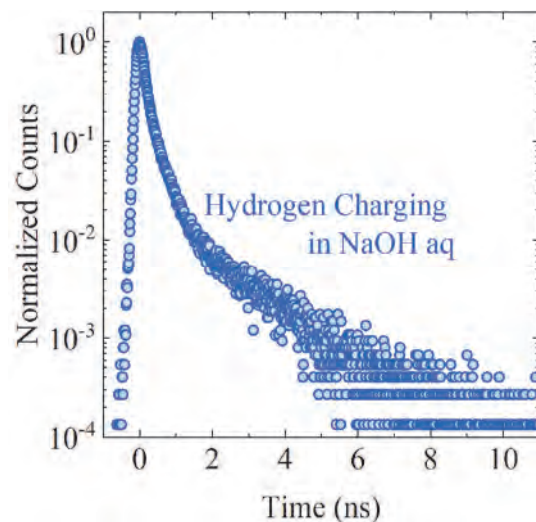


Fig. 1. Positron annihilation lifetime spectrum obtained from a hydrogen-charged pure iron sample mounted in NaOH aqueous solution.

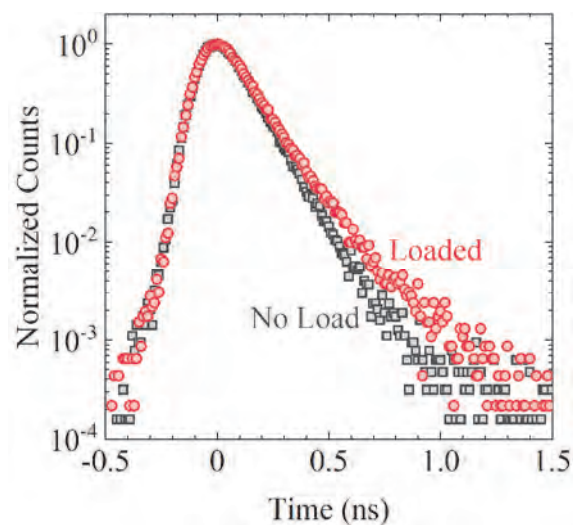


Fig. 2. Positron annihilation lifetime spectra obtained from a pure iron tensile-test piece under no load (open squares) and under the load required for stretching to a nominal strain of 8% (open circles).

BL6U

Momentum Microscope Study of a Kagome Superconductor CsV₃Sb₅

T. Kato¹, K. Nakayama^{1,2}, Y. Li^{3,4}, Z. Wang^{3,4}, Y. Yao^{3,4}, F. Matsui⁵, T. Takahashi^{1,6,7}
and T. Sato^{1,6,7}

¹Department of Physics, Graduate School of Science, Tohoku University, Sendai 980-8578, Japan

²Precursory Research for Embryonic Science and Technology (PRESTO), Japan Science and Technology Agency (JST), Tokyo 102-0076, Japan

³Centre for Quantum Physics, Key Laboratory of Advanced Optoelectronic Quantum Architecture and Measurement (MOE), School of Physics, Beijing Institute of Technology, Beijing 100081, China

⁴Beijing Key Lab of Nanophotonics and Ultrafine Optoelectronic Systems, Beijing Institute of Technology, Beijing 100081, China

⁵UVSOR Synchrotron Facility, Institute for Molecular Science, Okazaki 444-8585, Japan

⁶Center for Spintronics Research Network, Tohoku University, Sendai 980-8577, Japan

⁷Advanced Institute for Materials Research (WPI-AIMR), Tohoku University, Sendai 980-8577, Japan

The kagome lattice, consisting of a two-dimensional network of corner-sharing triangles with 3d transition metal ions, offers a fertile ground to explore exotic quantum phenomena originating from electron correlation and non-trivial band topology. Band structure of a simple kagome lattice is composed of a flat band, a Dirac cone, and a saddle point. Owing to such a unique band structure, the kagome lattice shows various interesting physical properties depending on the position of the Fermi level (E_F).

Recently, a new family of kagome metals AV_3Sb_5 ($A = K, Rb, Cs$) with a V kagome network has been discovered. AV_3Sb_5 commonly exhibits superconductivity below $T_c = 0.9$ -2.5 K and charge-density wave (CDW) below $T_{CDW} = 78$ -103 K. To clarify the interplay among superconductivity, CDW, and electronic states, we have performed ARPES measurements of CsV₃Sb₅ ($T_c = 2.5$ K, $T_{CDW} = 91$ K) by using momentum microscope at BL6U in UVSOR [1].

Single crystals of CsV₃Sb₅ were synthesized with the self-flux method. ARPES measurements were performed using KREIOS 150 MM (SPECS) [2]. The energy resolution was set to be 35 meV.

Figure 1 shows the plot of ARPES intensity at E_F as a function of k_x and k_y at $T = 120$ K (above T_{CDW}) measured with 106-eV photons corresponding to the $k_z \sim 0$ plane [3,4]. Photoelectrons in this wide momentum window were simultaneously collected by using a momentum microscope. One can recognize three types of Fermi surfaces, a circular pocket and a large hexagonal pocket centered at the Γ point and a small triangular pocket at the K point. The circular pocket at the Γ point originates from an electron band with the Sb 5p_z orbital. On the other hand, the hexagonal pocket originates from linearly dispersive bands with the dominant V 3d_{xz/yz} orbital character. The triangular pocket at the K point is associated with the Dirac-cone band with the Dirac point at $E_B \sim 0.3$ eV. This band is attributed to the V 3d_{xy/x²-y²} orbital, and forms the saddle point slightly above E_F . Our high-resolution measurements below T_{CDW} (not shown) reveal the largest CDW-gap opening on this saddle-point band. Therefore, the

saddle point plays a crucial role in stabilizing CDW in AV_3Sb_5 .

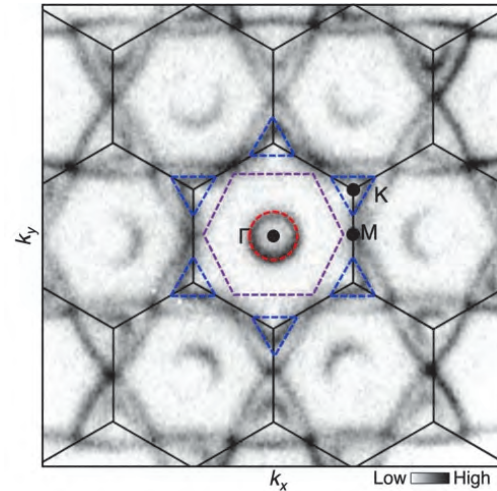


Fig. 1. ARPES-intensity map at E_F plotted as a function of k_x and k_y , measured at $T = 120$ K in CsV₃Sb₅. Red, purple, and blue dashed lines are guides for the eyes to trace the experimental Fermi surfaces.

[1] T. Kato *et al.*, submitted.

[2] F. Matsui *et al.*, Jpn. J. Appl. Phys. **59** (2020) 067001.

[3] K. Nakayama *et al.*, Phys. Rev. B **104** (2021) L161112.

[4] K. Nakayama *et al.*, Phys. Rev. X **12** (2022) 011001.

BL1U

Probing Vacancy-type Defects in Ce:LuAG Scintillators by GiPALS Experiment and DFT Calculation

 M. Kitaura¹, Y. Taira^{2,3} and S. Watanabe⁴
¹Faculty of Science, Yamagata University, Yamagata 990-8560, Japan

²UVSOR Synchrotron Facility, Institute for Molecular Science, Okazaki 444-8585, Japan

³School of Physical Sciences, The Graduate University for Advanced Studies, Okazaki 444-8585, Japan

⁴Institute of Innovative Research, Tokyo Institute of Technology, Tokyo 152-8550, Japan

Positron annihilation lifetime spectroscopy (PALS) is a unique experimental technique that can visualize the existence of vacancy-type defects in solids. Taira et al., one of the authors, have developed gamma-ray induced PALS (GiPALS) using ultrashort pulsed gamma-rays generated by 90-degree inverse Thomson scattering [1]. We applied this method to the visualization of negatively charged cation vacancies, which trigger the formation of photocarrier traps associated with defect complexes of cation antisites and oxygen vacancies in Ce:Gd₃Al₂Ga₃O₁₂ (Ce:GAGG) crystals [2].

In the present study, GiPALS experiment has been performed at 300 K for Ce-doped Lu₃Al₅O₁₂ (Ce:LuAG) crystals, which have the same crystal structure as Ce:GAGG. GiPALS spectra were analyzed according to the two-state trapping model of bulk and defect states. The lifetimes and relative intensities were determined by the least-square fitting using two exponential decay functions. Using these parameters, bulk- and defect-lifetimes were calculated, and were compared to those obtained from the theoretical calculation based on two-component density functional theory (TC-DFT).

Figure 1 shows the GiPALS spectrum of a Ce:LuAG crystals. The data were obtained at 300 K. The GiPALS spectra are reproduced by the sum of two exponential decay functions drawn by blue broken lines. The positron annihilation lifetime becomes longer at the negatively charged vacancy site, compared to the bulk state free from vacancy-type defects. Therefore, the short and long lifetime components are attributed to the positron annihilation at the bulk and defect states, respectively. The lifetimes τ_i and relative intensities I_i were analyzed by the least square fitting of experimental data. The values of τ_i and I_i are listed in Table I. The bulk lifetime τ_B and trapping rate κ were estimated to be 166 ± 2 ps and $(1.53 \pm 0.07) \times 10^9$ s⁻¹, respectively. Table II lists bulk τ_B and defect lifetimes τ_{24c} , τ_{16a} and τ_{24d} , obtained by the present TC-DFT calculation. The subscripts indicate the Wyckoff positions of the lattice sites introducing cation monovacancies in the TC-DFT calculation. The experimental value of τ_B is almost agreement with the calculated one. This result indicates the validity of our experiment and analysis.

In Table I, the value of τ_2 corresponds to the vacancy-related lifetime. This value is similar to those of τ_{24d} , and τ_{16a} in Table II. Thus, it is more likely that Al monovacancies are introduced at $16a$ and $24d$ sites. The

existence of Al vacancies was suggested in Y₃Al₅O₁₂ (YAG) [3].

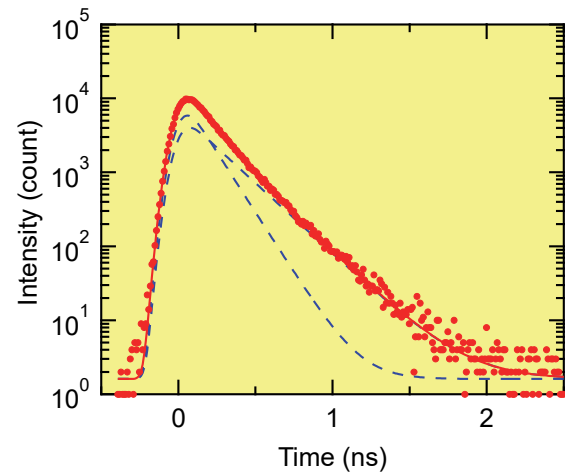


Fig. 1. GiPALS spectrum of a Ce:LuAG crystal measured at room temperature. Broken lines indicate the components due to positron annihilation at bulk and vacancy-related defect sites. The sum of them also was indicated by a red line.

Table I. Lifetimes τ_i , and relative intensities I_i for GiPALS spectra of Ce:LuAG, analyzed using the two-state trapping model.

	τ_1 (ps)	I_1 (%)	τ_2 (ps)	I_2 (%)
Ce:LuAG	132 ± 14	51.0 ± 0.8	226 ± 1	49.0 ± 0.8

Table II. Bulk τ_B and defect lifetimes τ_{24c} , τ_{16a} and τ_{24d} , obtained by the present TC-DFT calculation. The subscripts indicate the Wyckoff positions of the lattice sites introducing cation monovacancies in the TC-DFT calculation.

	τ_B (ps)	τ_{24c} (ps)	τ_{16a} (ps)	τ_{24d} (ps)
Lifetimes	162	274	239	233

[1] Y. Taira *et al.*, Rev. Sci. Instrum. **84** (2013) 053305.

[2] K. Fujimori *et al.*, Appl. Phys. Express **13** (2020) 085505.

[3] F. A. Selim *et al.*, Results Phys. **5** (2015) 28.

BL1U

LCS-gamma Induced Positron Annihilation Study for the Dynamics of Defect Behavior in Bulk Materials

F. Hori¹, S. Araki¹, K. Sugita² and Y. Taira²¹ Department of Quantum and Radiation Engineering, Osaka Prefecture University, Sakai 599-8531, Japan² UVSOR Synchrotron Facility, Institute for Molecular Science, Okazaki 444-8585, Japan

The behavior of hydrogen atoms is attracting attention in a wide range of research fields such as high-strength structural materials and hydrogen storage materials. In such materials, hydrogen atom diffuses and has various interaction with defects and surface, consequently it is possible to make change the serious characteristic features. In particular, in the corrosion process of high-strength materials under high pressure and chemically harsh environment, the presence or absence of defects in the material is considered to have a great influence on the intrusion of hydrogen and oxygen and the interaction with constituent atoms in the material. It has been almost impossible to directly observe the atomic-level defects behavior that occurs inside the material during processes such as corrosion. This has been hampered by the need for high-energy acceleration of charged particles such as electrons, which are probes in various analytical methods used for detecting defects at the atomic level, and high-energy X-rays. On the other hand, positron annihilation methods are used defects research in materials powerfully. In normal defects research, a radioisotope (RI) and an accelerated slow positron beam are generally used for positron annihilation experiments. The maximum energy of positron emitted from most standard positron source of ²²Na is about 540 keV and almost positron beam is the order of 100 keV so that possible research area is near surface of materials. In order to investigate the dynamics of the internal defect behavior which is not possible to detect without destructing the material, mega electron volts accelerated fast positron is needed or positron production in target materials is useful. By utilizing high-energy gamma rays generated by injecting a laser beam from the outside into the electrons of the UVSOR synchrotron radiation storage ring, positron experiments for detecting defect behavior in bulk materials such as the latter become possible. We have developed positron annihilation Doppler broadening system using LCS gamma-beam at NewSUBARU synchrotron facility and successfully measured defects in bulk materials [1]. However, that beam line was closed at 2020. In this study, we have developed a device of in-situ measurement of positron annihilation lifetime while applying stress to bulk a sample at UVSOR beam line BL1U as shown in Fig. 1. In this system, initial stress is applied for the sample and left as it was. Stress is measured as a voltage from the load cell connected to the sample.

Fe sample, which is well annealed at 1073 K for 1 h to remove residual defects, was mounted on this

apparatus for tensile test. Figure 2 shows the results of positron lifetime and voltage change after stress applied. The initial drastic change in stress is due to elastic deformation at a moment of stress apply, and the subsequent slow increase is thought to be due to the introduction of dislocations and hardening due to plastic deformation. After applying stress, positron lifetime increased slightly but almost constant. This change corresponds to defect formation such as dislocations and vacancies. However, that change did not exactly match the stress change. Considering that the positron lifetime analysis is an average value, it is necessary to do multi component defects analysis on the positron data.

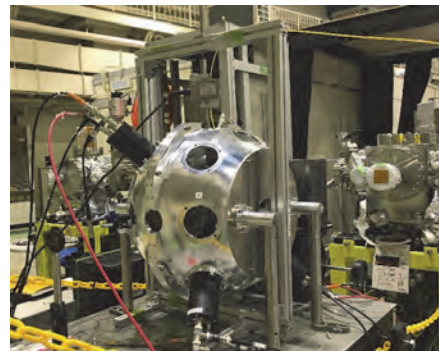


Fig. 1. Newly developed stress applying positron lifetime in-situ measurement apparatus at BL1U.

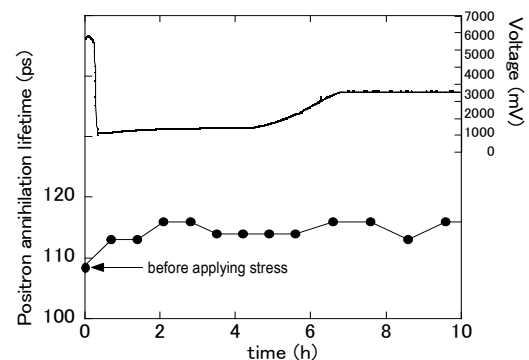


Fig. 2. Stress and positron lifetime change as a function of time.

[1] K. Sugita, S. Miyamoto, M. Terasawa, A. Iwase, K. Umezawa and F. Hori, AIP Conf. Proc. **2182** (2019) 040007.

BLIU

Effect of the Particle Size on the Positron Annihilation Lifetime and Relative Intensity of CeO₂ Nanoparticles

S. Dohshi¹, K. Maeda¹, Y. Taira², H. Toyokawa³ and T. Hirade⁴¹Osaka Research Institute of Industrial Science and Technology, Izumi 594-1157, Japan²UVSOR Synchrotron Facility, Institute for Molecular Science, Okazaki 444-8585, Japan³National Institute of Advanced Industrial Science and Technology, Tsukuba 305-8568, Japan⁴Japan Atomic Energy Agency, Tokai 319-1195, Japan

Recently, it has been reported that the presence of oxygen vacancies in CeO₂ catalysts affect their catalytic activity such as automotive exhaust gas purification, particulate matter and/or volatile organic compound oxidation [1]. Therefore, it becomes more and more important to analyze the presence and the concentration of oxygen vacancies in CeO₂ with high sensitivity.

Positron annihilation lifetime measurement is a powerful tool for the detection of lattice defects such as oxygen vacancies with high sensitivity. It was previously reported that two lifetime components were observed for CeO₂ catalysts: shorter lifetime component of 170–200 ps and longer lifetime component of ca. 400 ps [1]. Moreover, theoretical studies have estimated a positron annihilation lifetime of ca. 170 ps for the bulk of CeO₂ without oxygen vacancies [2]. This lifetime is in good agreement with the experimentally observed shorter lifetime component. However, there is no theoretical studies about the longer lifetime component (ca. 400 ps), and various arguments such as annihilation in oxygen vacancy clusters or at the surface have been experimentally made about this lifetime component.

In this study, positron annihilation lifetimes of CeO₂ catalysts with different primary particle sizes were measured to discuss the longer lifetime component in the positron annihilation for CeO₂ catalysts.

The particle sizes, which calculated from XRD analysis, of CeO₂ nanoparticles used in this experiment were 2.3 nm, 9.3 nm, 18.3 nm, and 26.7 nm, respectively. We have set up a gamma-ray spectroscopy system at the laser-Compton scattering (LCS) beamline of BLIU at UVSOR-III [3], and measured the lifetime of the annihilation gamma-rays at room temperature using BaF₂ scintillation detector. We used the software Lifetime9 (LT9) to analyze the spectra.

Figure 1 shows the positron annihilation lifetime spectrum of CeO₂ nanoparticle with a particle size of 2.3 nm. As shown in Fig. 1, this spectrum could be fitted with two lifetime components; ca. 155 ps (τ_1) and ca. 390 ps (τ_2). The positron annihilation lifetimes (τ_1 and τ_2) and relative intensities (I_1 and I_2 ; $I_2 = 100 - I_1$) analyzed using LT9 for CeO₂ nanoparticles with different particle sizes are listed in Table 1. Two lifetime components of ca. 170 ps and 390 ps were observed for all CeO₂ nanoparticles. The shorter lifetime component of ca. 170 ps is considered to be annihilation in the bulk of the CeO₂ nanoparticles, as

previously reported. Furthermore, as the particle size decreases, the relative intensity of the longer lifetime component (I_2) of ca. 390 ps increases. The longer lifetime component for CeO₂ nanoparticles with a particle size of 2.3 nm is found to be more than 90%. As particle size decreases, the ratio of surface to bulk increases. The longer lifetime component of ca. 390 ps observed in this experiment is dependent on the particle size, suggesting the annihilation at the CeO₂ surface. Theoretical calculations on the positron annihilation lifetime at CeO₂ surface will be performed in the future.

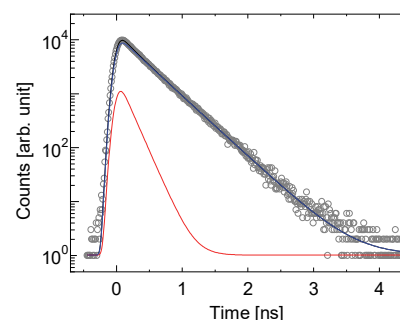


Fig. 1 Positron annihilation lifetime spectra of CeO₂ nanoparticles with a particle size of 2.3 nm.

Table 1 Positron annihilation lifetime and relative intensity of CeO₂ with different particle size.

particle size	τ_1 [ps]	τ_2 [ps]	I_2 [%]
2.3 nm	155.0 ± 17	388.2 ± 1.5	93.5 ± 0.7
9.3 nm	188.0 ± 30	408.0 ± 21	85.1 ± 5.9
18.3 nm	174.7 ± 4.6	386.3 ± 3.1	66.3 ± 1.1
26.7 nm	176.7 ± 7.8	388.0 ± 30	53.6 ± 4.0

[1] X. Liu *et al.*, J. Am. Chem. Soc. **131** (2009) 3140.

[2] B. Barbiellini *et al.*, Phys. Rev. Lett. **114** (2015) 147401.

[3] Y. Taira *et al.*, Rev. Sci. Instr. **84** (2013) 053305.

BL2A

Mo L_{III}-Edge XANES Study of Highly Active MoC_x Species in Mo-V Modified H-MFI Catalysts for Methane Dehydroaromatization

K. Kuramochi¹, R. Yamazaki¹, Y. Sonobe³, Y. Uchimura² and H. Aritani^{2,3}

¹Advanced Science Research Laboratory, Saitama Institute of Technology, Fukaya 369-0293 Japan

²Graduate School of Engineering, Saitama Institute of Technology, Fukaya 369-0293 Japan

³Faculty of Engineering, Saitama Institute of Technology, Fukaya 369-0293 Japan

For direct conversion from natural gases to useful petroleum compounds, innovative GTL (Gas To Liquid) catalysts are called for. A molybdenum- modified H-MFI zeolite (Mo/H-MFI) catalyst is a typical MTB (Methane To Benzene; $6\text{CH}_4 \rightarrow \text{C}_6\text{H}_6 + 9\text{H}_2$) catalyst with high activity for methane dehydroaromatization, which is a noted GTL process. Over the Mo/H-MFI catalysts, definite deactivation due to coke deposition has been a serious problem for enhancement of MTB reactivity, and thus, clarification of the deactivation process over the catalysts is one of the important points. A cause of the deactivation strongly depends on both coke deposition onto strong acid sites over H-MFI and structural deactivation of carbonized Mo species. One of the most important subjects for catalytically high and durable activity is the elucidation of active Mo-carbide sites. In this study, Mo L_{III}-edge XANES is applied to characterize the active MoC_x species on Mo/H-MFI and Mo-V co-modified H-MFI.[1]

Mo(5 wt%)/H-MFI (Si/Al₂=23) and Mo-V/H-MFI (Mo/V=10-40) catalysts were prepared as described in the previous paper.[2] The methane dehydroaromatization reactivity was evaluated at 1023 K. Mo L_{III}-edge XANES spectra were obtained in BL2A of UVSOR-IMS in a total-electron yield mode using InSb double-crystal monochromator. A REX-2000 (Rigaku) software was used for normalization of each XANES spectra.

At Mo/V=40, maximum durability for catalytic MTB reactivity was shown at 1023 K. For L_{III}-edge XANES spectra over Mo-V/H-MFI catalysts as shown in Fig. 1, deeply carbonized Mo species due to MoC_x ($x > 0.5$) are formed. On the time course of the MTB reaction over Mo-V/H-MFI (Mo/V=40), decrease of edge energy due to rapid carburization of Mo ions is revealed in the initial step. At 60 min., the catalytic MTB reactivity was shown. After 105 min., the energy value relatively approached the α -Mo₂C. Because deactivation of MTB was shown after 60 min., the structural change due to formation of α -Mo₂C like species can be assigned the decrease of active MoC_x sites. The rate of deactivation reduced by V co-modification, and thus, inhibition of excess carbonization by V co-modification is proposed. The result is likely to relate to a suppression effect of deactivation. For stabilize the active MoC_x species, V co-modification is effective on Mo/H-MFI catalysts.

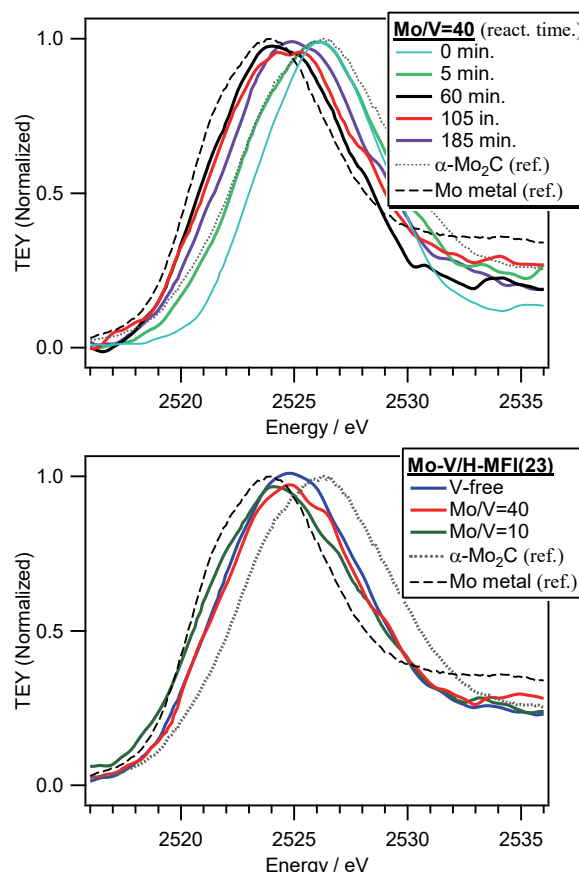


Fig. 1. Mo L_{III}-edge XANES spectra of Mo-V/H-MFI (Si/Al₂=23) [top] and the Mo/V=40 on the time course of MTB reaction [bottom] at 1023 K. The references, α -Mo₂C and Mo metal, are also shown in each figure.

Table 1. Edge energy values obtained by 1st derivatives of L_{III}-edge XANES (shown in Fig. 1).

Mo-V/H-MFI (React. 185 min.)		Mo-V/H-MFI (Mo/V=40)	
Catalyst	Edge Energy / eV	Time on Stream / min.	Edge Energy / eV
V-free	2520.9	0	2522.0
Mo/V=10	2520.7	5	2520.7
Mo/V=40	2520.9	60	2520.6
α -Mo ₂ C	2521.0	105	2520.9
Mo Metal	2520.2	185	2520.9

[1] H. Aritani *et al.*, UVSOR Activity Report 2020 **48** (2021) 57.; H. Aritani *et al.*, UVSOR Activity Report 2019 **47** (2020) 50.

[2] H. Aritani *et al.*, J. Environm. Sci. **21** (2009) 736.

BL2A

Evaluation of the Electronic State of MgO by NEXAFS Spectroscopy

E. Kobayashi¹, K. K. Okudaira², S. Yoshioka³ and A. Inoishi⁴

¹Kyushu Synchrotron Light Research Center, Tosu 841-0005, Japan

²Chiba University, Chiba 263-8522, Japan

³Graduate School of Engineering, Kyushu University, Fukuoka 819-0395 Japan

⁴Institute for Materials Chemistry and Engineering, Kyushu University, Kasuga 816-8580, Japan

Magnesium oxide (MgO) is used in various fields such as catalysts, electrical insulator and heat-resistant materials. In the development of organic solar cells, the introduction of a metal oxide layer improved functionality and efficiency [1]. For example, an MgO nanolayer is used as the electrode [1-3]. Therefore, it is important to evaluate the electronic state of the produced metal oxide.

We have been studying using Near-edge X-ray absorption fine structure (NEXAFS) spectroscopy as a method for evaluating electronic states. Usually, the spectrum is carried out by the electron yield (EY) method and the fluorescence yield (FY) method. The EY method is a surface-sensitive method, and the FY method is a bulk-sensitive method.

In this paper, we investigated how the presence of defects changes the electronic states of the metal oxide surface and bulk.

The sample is MgO powder. Samples with defects were prepared by mechanically crushing. NEXAFS spectra of the MgO powders were measured at the beamline 2A of the UVSOR in the Institute of Molecular Science. For TEY, the drain current from the sample was measured. For PFY fluorescence X-rays were collected using an energy dispersible silicon drift detector (SDD). All experiments were performed at room temperature.

Figure 1 shows the Mg K-edge NEXAFS spectra of MgO powder obtained from TEY. The black line is the untreated sample and the red line is the defective sample. The overall shape of the NEXAFS spectrum is very similar. The inset is an enlargement of the rising edge of the spectrum. The rise of the spectrum of defect MgO shifted to the low energy side. This is due to the presence of reduced MgO.

Figure 2 shows the Mg K-edge NEXAFS spectra of MgO powder obtained from PFY. The black line is the untreated sample and the red line is the defective sample. The overall shape of the NEXAFS spectrum is very similar, but distorted by defects. The rising edge of the spectrum is shifted to the low energy side due to the defect, but it is smaller than that obtained by TEY.

The NEXAFS results obtained by the TEY method showed little difference between the untreated and crashed samples. On the other hand, the NEXAFS results obtained by the PFY method differed significantly. Since the mechanical crashing was done in the atmosphere, the defects formed on the surface are

chemically unstable and quenched. On the other hand, the defects inside the powder are retained.

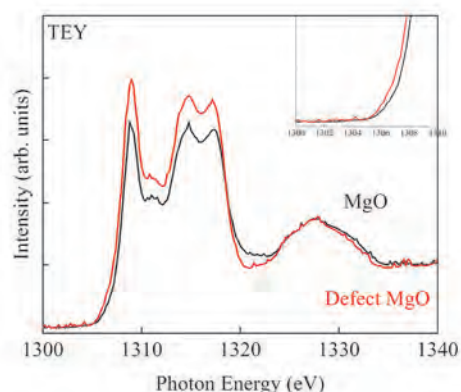


Fig. 1. Mg K-edge NEXAFS spectra of MgO by using TEY.

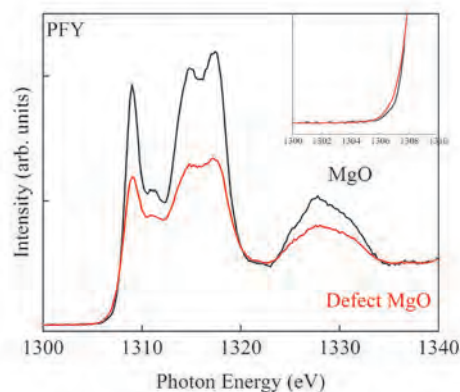


Fig. 2. Mg K-edge NEXAFS spectra of MgO by using PFY.

[1] H. J. Bolink, H. Brine, E. Coronado, and M. Sessolo, *J. Mater. Chem.* **20** (2010) 4047.

[2] J. Ma, G. Yang, M. Qin, X. Zheng, H. Lei, C. Chen, Z. Chen, Y. Guo, H. Han, X. Zhao, and G. Fang, *Adv. Sci.* **4** (2017) 1700031.

[3] I. Ierides, I. Squires, G. Lucarelli, T. M. Brown, and F. Cacialli, *J. Mater. Chem. C* **9** (2021) 3901.

BL2A

Sintering Behavior of Mg-Doped Hydroxyapatite Nano Particles

H. Murata, R. Kawanabe and A. Nakahira

Department of Materials Science, Osaka Prefecture University, Sakai 599-8531, Japan

Hydroxyapatite (HAp) is a main inorganic component of human bones and teeth. It has good biocompatibility and thus it is used as materials for artificial bones and teeth. HAp in human bodies is not pure but contains various kinds of impurities. They affect properties of HAp such as solubility in water, mechanical strength and so on.

Artificial HAp was commercially available in various forms, powders, granules, pastes and sintered bodies. Doping into HAp have been attempted to control properties of HAp. However, some dopants induce Ca deficiency [1], which cause high-temperature instability. In this study, local environment of Mg in hydroxyapatite were investigated by X-ray absorption near edge structure (XANES) to reveal their effects to sintering.

Mg-doped HAp (Mg-HAp) samples were prepared by the solution-precipitation method. Starting materials were 0.10 mol/L of $\text{Ca}(\text{NO}_3)_2$ and $(\text{NH}_4)_2\text{HPO}_4$ aqueous solutions. The initial Ca/P molar ratio were set to 2.0, which is larger than that of stoichiometric HAp, to prevent formation of Ca vacancies. The $(\text{NH}_4)_2\text{HPO}_4$ aqueous solution was dropped into the $\text{Ca}(\text{NO}_3)_2$ aqueous solution under Ar atmosphere. Then, the solution was sealed in a PFA bottle and it was matured at 37 °C in a water bath for 72 h. After maturing, samples were washed by ion-exchanged water, filtrated and dried at 50 °C. A parts of samples were pressed into pellets and sintered at 1000 °C for 6 h.

Samples were characterized by powder X-ray diffraction (XRD), inductively coupled plasma optical emission spectrometry (ICP-OES) and XANES. Mg-K XANES were collected at BL2A in UVSOR by the partial fluorescence yield method using a silicon drift detector. [2] Samples were mounted on a metal plate using carbon tapes.

The XRD pattern of as-dried samples can be assigned to that of hydroxyapatite. Although stoichiometric HAp were obtained in the present condition, (Ca+Mg)/P molar ratio of Mg-doped samples was smaller than that of HAp, 1.67. This indicated that Mg^{2+} in HAp are also associated with Ca vacancies and excess H [1].

Figure 1 shows Mg-K XANES of the samples. The spectrum of the sintered Mg-HAp has different features from that of as-dried Mg-HAp. The peak A and C shows formation of MgO. The shoulder D can be assigned to Mg-doped β -TCP. Therefore, Present Mg-HAp were partially decomposed to MgO and β -TCP during sintering. Since non-stoichiometric HAp are partially decomposed to CaO or β -TCP at 1000 °C [3], the low (Ca+Mg)/P molar ratio of the samples also cause the decomposition. Therefore, Mg-HAp and CaCO_3 were mixed to compensate lack of (Ca+Mg)/P molar ratio

and they were sintered. However, its Mg-K XANES spectrum has the same features to that of MgO. This result means Mg^{2+} are ejected from HAp during sintering. High-temperature instability of Mg-HAp are not due to low (Ca+Mg)/P molar ratio but fundamental character.

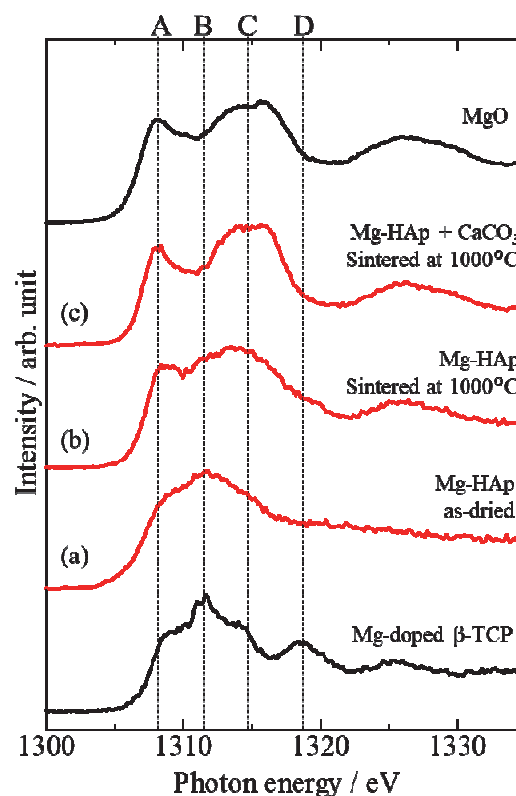


Fig. 1. Mg-K XANES of (a) as-dried and (b) sintered Mg-HAp and (c) Sintered samples of mixture Mg-HAp and CaCO_3 , respectively. Spectra of MgO and Mg-doped β -TCP were also shown as references.

[1] K. Matsunaga *et al.*, *Acta Biomater.* **6** (2010) 2289.

[2] H. Murata, T. Taniguchi and T. Yamamoto, *UVSOR Activity Report 2013* **41** (2014) 56.

[3] K. Shitara *et al.*, *J. Asian Ceram. Soc.* **2** (2014) 64.

BL2A

Local Structure around Mg in $\text{Mg}_{1-x}\text{Ni}_x\text{Al}_2\text{O}_4$

S. Yoshioka¹, K. Yasuda¹, S. Matsumura¹, E. Kobayashi² and K. Okudaira³

¹Department of Applied Quantum Physics and Nuclear Engineering, Kyushu University, Fukuoka 819-0395, Japan

²Kyushu Synchrotron Light Research Center, Tosu 841-0005, Japan

³Graduate school of Advanced Integration Science, Chiba University, Chiba 263-8522, Japan

Spinel oxides with the general formula AB_2O_4 can be formed with various kinds of divalent A and trivalent B cations. Owing to their unique mechanical, electronic, and magnetic properties, the spinel oxides have gained considerable attention not only from the fundamental research fields but also from the industrial application point of view. Some spinel compounds accommodate a large degree of cationic disorder. The cationic disordering naturally affects the structural properties of the spinels. For example, magnesium aluminate (MgAl_2O_4) and nickel aluminate (NiAl_2O_4) spinels are generally known as normal and inverse spinel structures, respectively. However, their inversion degrees for synthetic specimens were also reported to be fluctuating between 0 and 1, respectively, due to the cationic disordering. Recently, the structure of $\text{Mg}_{1-x}\text{Ni}_x\text{Al}_2\text{O}_4$ was reported using neutron total scattering to understand the cationic disordering process [1]. X-ray absorption spectroscopy (XAS) is a powerful structure characterization method that uses an X-ray probe to reveal local atomic coordination and electronic structures. In this study, we focus on the local structures in MgAl_2O_4 – NiAl_2O_4 solid solutions, particularly cationic-disordered structures.

The polycrystalline samples of $\text{Mg}_{1-x}\text{Ni}_x\text{Al}_2\text{O}_4$ ($x = 0.0, 0.05, 0.2, 0.5, 0.8, 1.0$) were synthesized by a solid-state reaction. They were sintered in air at 1300 °C for 10 h followed by furnace. Mg and Al *K*-edge XANES measurements were performed on BL2A beamline at UVSOR Synchrotron Facility, Okazaki, Japan, using the partial fluorescence yield method. A KTiPO_4 double-crystal monochromator gives Mg and Al *K*-absorption edges in the energy regions 1290–1340 eV and 1540–1610 eV, respectively. The measurements of Mg and Al *K*-edge XANES spectra were carried out in vacuum at a pressure and temperature of 1×10^{-4} Pa and 20 °C, respectively. Fluorescence X-rays of Mg K_α and Al K_α were collected utilizing an energy-dispersible silicon drift detector.

The Mg *K*-edge XANES spectra for $\text{Mg}_{1-x}\text{Ni}_x\text{Al}_2\text{O}_4$ are shown in Fig. 1 with the composition values $x = 0, 0.05, 0.2, 0.5,$ and 0.8 . The intensity of each spectrum was normalized to a value of 1 at the photon energy of 1335 eV after the removal of the background intensity. All the Mg *K*-edge XANESs show similar spectra and no significant energy shifts or relative intensity changes at the major peaks are observed. It suggests that the local structure of Mg remains unchanged for the whole composition range of $\text{Mg}_{1-x}\text{Ni}_x\text{Al}_2\text{O}_4$, whereas the Mg concentration changes with respect to x .

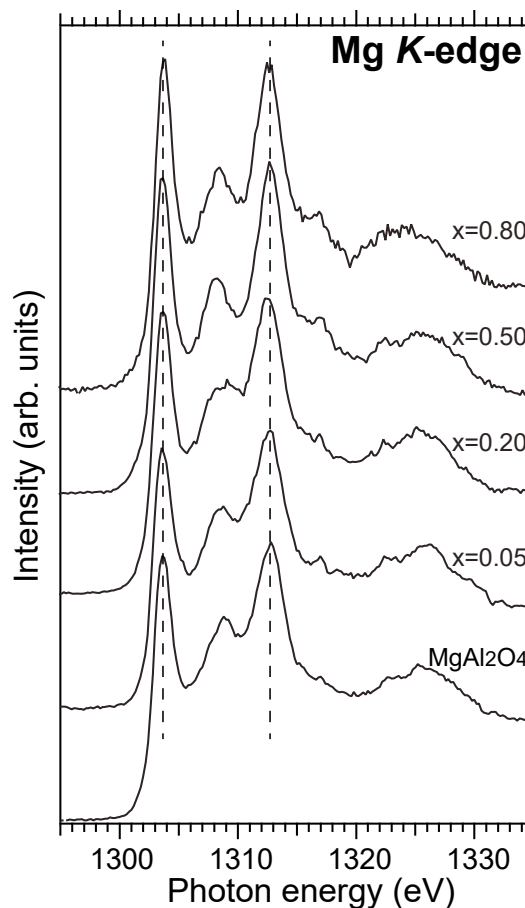


Fig. 1. Mg *K*-edge XANES spectra of $\text{Mg}_{1-x}\text{Ni}_x\text{Al}_2\text{O}_4$.

[1] E. O'Quinn *et al.*, *J. Am. Chem. Soc.* **139** (2017) 10395.

BL2A

Local Structure Investigations of Zn in ZnAl₂O₄ Induced on Swift Heavy Ion Irradiations

S. Yoshioka¹, K. Yasuda¹, S. Matsumura¹, E. Kobayashi² and K. Okudaira³

¹Department of Applied Quantum Physics and Nuclear Engineering Kyushu University, Fukuoka 819-0395, Japan

²Kyushu Synchrotron Light Research Center (SAGA-LS), Tosu 841-0005, Japan

³Graduate School of Advanced Integration Science, Chiba University, Chiba 263-8522, Japan

Zinc aluminate oxide (ZnAl₂O₄) is one of the common spinel compounds. Since it shows a variety of interesting physical and chemical properties, its microstructure has been extensively investigated. A cationic disordered ZnAl₂O₄ spinel is represented by the formula of [Zn_{1-x}Al_x](Zn_xAl_{2-x})O₄, where the square brackets and the parentheses denote the tetrahedral and octahedral sites, respectively. The variable *x* is called the inversion parameter, which quantifies the cation disorder. Radiation with swift heavy ions (SHIs) interacts with materials and causes the structural change. It is therefore applied to material processing, modifications, etc. SHI irradiation provides high energy deposition through electronic stopping to the materials. SHIs in insulating solid materials are known to leave trails of damage along the ion path with a diameter of several nanometers. Structural change related to the cationic disorder has been also observed in ZnAl₂O₄ with SHI irradiation using transmission electron microscopy observation. In this study, we clarify local coordination of each cation element, on which we conducted synchrotron radiation-based X-ray analysis.

Sintered ZnAl₂O₄ samples with the shape of 10 × 4 × 0.5 mm were used in this study. These specimens were irradiated with 340 MeV Au ions to fluences of 1 × 10¹² cm⁻² at the H1 beamline of the tandem ion accelerator facility in the Japan Atomic Energy Agency (JAEA)-Tokai. At the beginning of each paragraph, two space characters should be inserted as an indent. Zn L_{2,3}-edge and Al K-edge XANES measurements were performed at the BL2A beamline of UVSOR Okazaki, Japan, using the partial fluorescence yield method (PFY). A Be₃Al₂Si₆O₁₈ (beryl) double-crystal monochromator gives Zn L₃-edge in energy regions 1000–1070 eV. In the cases of Al K-absorption edges, a KTiOPO₄ double-crystal monochromator scanned the energy region 1540–1610 eV. The samples were set with their surface perpendicular to the incident X-ray beam. Fluorescence X-rays of Zn L_α and Al K_α were collected using an energy dispersible silicon drift detector (SDD). All measurements of XANES spectra were carried out in vacuum of 1 × 10⁻⁵ Pa at room temperature.

The XANES spectra with the Zn L₃-edge are shown in Fig. 1 for the ZnAl₂O₄ samples before and after irradiation with 340 MeV Au ions at fluences ranging from 1 × 10¹¹ to 1 × 10¹² cm⁻². The intensities of spectra were normalized to a value of 1 at 1055 eV for Zn L₃-edge, after the removal of background intensities. As

shown in Fig. 1, Zn L₃-edge XANES of the pristine ZnAl₂O₄ sample shows fine structures such as peaks A to H. The Zn L₃-edge XANES of the ZnAl₂O₄ samples have not changed drastically from that of the pristine sample even with high fluence irradiation. However, the intensities at the peak B were decreased and spectral shape between the peaks F and G as indicated an arrow were slightly changed with increasing of the ion fluences.

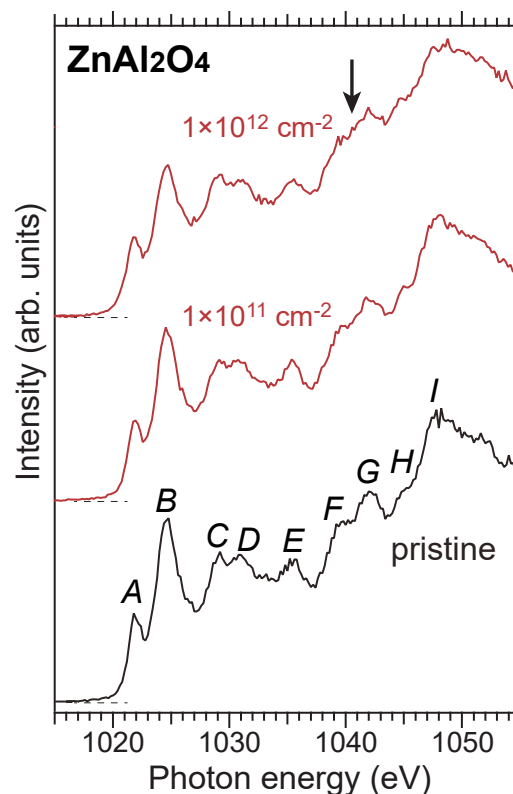


Fig. 1. Zn L₃-edge XANES spectra of pristine and irradiated ZnAl₂O₄ with 340 MeV Au ions to fluences of 1 × 10¹² cm⁻².

BL2B

UPS Spectroscopy of TFP Doped P3HT/PCBM Thin Films

K. K. Okudaira and Y. Hoshi
Chiba University, Chiba 263-8522, Japan

Organic solar cells (OSC) based on blends of polymers and fullerene derivatives are promising candidates for new renewable resource. However, the power conversion efficiency of OSC is low for commercial use. A bulk hetero-junction structure composed of poly (3-hexylthiophene (P3HT) and dphenyl-C61 -butyric-acid-methyl ester (PCBM) showed an improvement of the efficiency. To achieve higher efficiency, it is necessary to improve the excitation/charge transport. Recently, it was reported that by incorporating additives (i.e. doping) such as tetrafluorophthalnitrile (TFP), P3HT/PCBM system obtain high conversion efficiency [1]. In this study we observed photon- energy dependent photoemission of TFP doped P3HT/PCBM thin film to estimate the change of the electronic structure.

Photoemission measurements were performed at the beam line BL2B of the UVSOR storage ring at the Institute for Molecular Science. Incident photon energies of 28 eV, 40 eV, and 90 eV were used. Incident angle of photon and take-off angle of photoelectron are 60° and 0° with respect to surface normal, respectively. At first RR-P3HT (Mn \sim 40000) was dissolved with 0.1wt% in chlorobenzene, followed PCBM adding with weight ratio of 1:0.9 to P3HT. TFP with 5 wt% and 7 wt% were then added to the P3HT/PCBM solution, followed by stirring for 30 min. at 50°C . The solution consisting of P3HT/PCBM with or without TFP was spin-cast on the cleaned ITO substrate.

Figures 1 (a) and (b) show the measured UPS spectra of the secondary electron cutoff and valence top region, respectively. By TFP doping valence band top is shifted to E_f about 0.2 eV. It is expected that the gap states develop due to polaron and/or bipolaron on polythiophene chains of P3HT by TFP doping [2]. Figure 2 shows the measured UPS spectra at $h\nu = 28$ eV, 40 eV and 90 eV. In the UPS at $h\nu = 90$ eV, the relative intensity of the peak at binding energy (EB) of 6.5 eV is larger than those at $h\nu = 40$ eV and 28 eV. By considering the photoionization cross-section of S 3p and C 2s and 2p [3], the peak at EB of 6.5 eV can be assigned to the π state included S 3p orbital in thiophene ring. The photon-energy dependent photoemission can provide the precise information on the electronic structure.

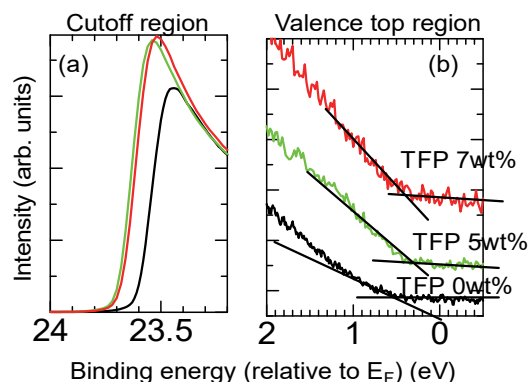


Fig. 1. UPS of secondary electron cutoff (a) and valence top (b) region at $h\nu = 28$ eV for P3HT/PCBM thin film with various TFP doping level.

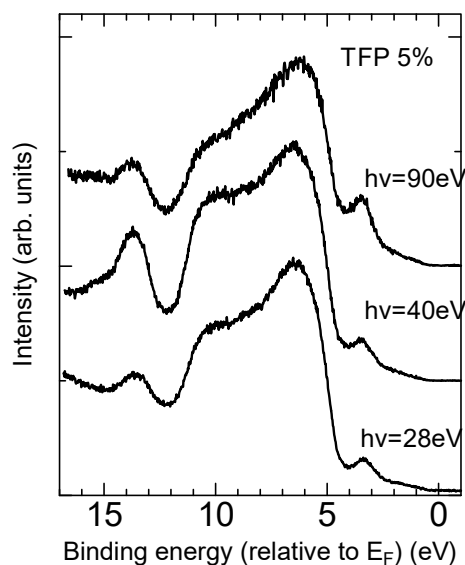


Fig. 2. photon-energy dependent photoemission of P3HT/PCBM thin film with 5 wt% TFP doping level.

[1] S. Jeong *et al.*, J. Nanosci. Nanotechnol. **14** (2014) 9219.

[2] M. Lögdlund *et al.*, Phys. Rev. Lett. **23** (1989) 1841.

[3] J.-J. YEH, Atomic Calculation of Photoionization Cross-sections and Asymmetry Parameters, (Gordon and Breach Science Publishers) (1993).

BL2B, BL7U

Valence and In-gap states of a Polyethylene Model Oligomer, C₄₄H₉₀, Film Studied by Conventional and High-Sensitivity Photoelectron Spectroscopy

R. Nakazawa¹, M. Yoshizawa¹, S. Kera² and H. Ishii^{1,3,4}¹Graduate School of Science and Engineering, Chiba University, Chiba 263-8522, Japan²Institute for Molecular Science, Okazaki 444-8585, Japan,³CFS, Chiba University, Chiba 263-8522, Japan⁴MCRC, Chiba University, Chiba 263-8522, Japan

The electronic structures of materials are a key to understand and control the nature of materials. Not only their highest occupied molecular orbital (HOMO) but also weak density-of-states (DOS) in the energy gap has been focused to discuss the practical electric properties. Our research group has been developing high-sensitivity photoelectron spectroscopy (HS-UPS) which enables to directly probe such in-gap states of organic materials [1,2]. Recently, we have applied constant final state photoelectron yield spectroscopy (CFS-YS) to organic and inorganic materials, and a very weak in-gap states whose density is less than 10⁻⁶ of HOMO [3]. The observed in-gap states are believed to be in relation to defect and disorder of the films. However, the origin of in-gap states is still open question. To qualify the nature of the wave function of the in-gap states, photoelectron spectroscopy using synchrotron radiation (SR) is suited because of photon energy tenability and polarizability of light, although conventional SR light includes stray photons to increase background intensity, leading to low sensitivity. BL7U has a unique advantage that high-sensitivity measurement is enable for less than 10 eV photon energy. We can expect that photon energy dependence and angular dependence of photo electron could give a hint to identify the wave function of in-gap states. In this study, a model compound of polyethylene, tetratetarcontane (TTC, C₄₄H₉₀) was investigated to clarify the valence and in-gap states by using BL2B (conventional UPS), BL7U(HS-UPS), and CFS-YS at Chiba University. Polyethylene is a basic polymer and applied to various products mainly as insulator. It is also interesting in relation to triboelectricity. The clarification of in-gap states is useful to understand its insulating nature.

TTC film was prepared by vacuum vapor deposition on an ITO-coated glass substrate, and the film thickness was 20 nm. The CFS-YS measurement was performed at Chiba University. SR measurements were performed at BL2B and 7U at UVSOR.

Figure 1 shows the UPS of TTC films for $h\nu=120$ eV@BL2B and 21.2 eV@Chiba U. The horizontal axis is the ionization energy relative to the vacuum level. The onset in 21.2 eV spectrum locates around 9 eV, which is consistent with the reported value of 8.9 eV [4]. The onset region is enhanced for 120 eV spectrum because of $h\nu$ dependence of photo-ionization cross-section of the HOMO, giving the onset around 7.5 eV, consistent with our CFS-YS results in the inset of Fig. 1. This result suggests that the reported ionization

energy should be updated.

Figure 2 shows the results of HS-UPS at BL7U for TTC film with and without anneal. The valence top region in the figure exhibited the intensity difference. Blue spectrum gives more intensity than red one, suggesting that the in-gap states seems to be reduced by decreasing the degree of disorder due to annealing. The obtained spectrum is compared with our CFS-YS result as shown in the inset. The both spectra are very similar, demonstrating the feasibility of high-sensitivity measurement at BL7U. The angular dependence of the photoelectrons from the in-gap states (1 to 3 eV in the binding energy in Fig. 2) were isotropic. Now we are going to check the photon energy dependence to squeeze the information about the wave function nature of the in-gap states.

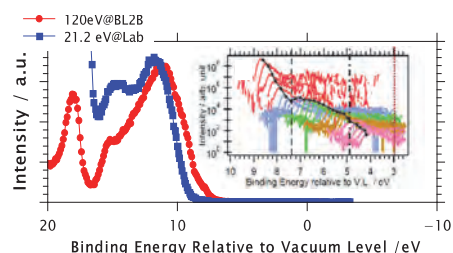


Fig. 1. UPS spectra of the TTC film for $h\nu=21.2$ and 120 eV. The inset shows CFS-YS curve (black dots).

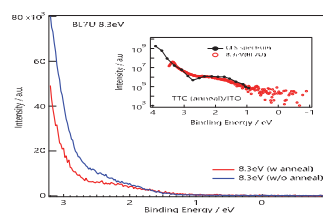


Fig. 2 HS-UPS spectra of TTC film with and without anneal. (The inset: CFS-YS result)

- [1] F. Bussolotti, J. Elect. Spec. Relat. Phenom. **204** (2015) 29.
- [2] T. Sato *et al.*, Appl. Phys. Express **10** (2016) 011602.
- [3] R. Nakazawa *et al.*, Appl Phys Express **14** (2021) 071004.
- [4] K. Seki *et al.*, Chem. Phys. **105** (1986) 247.

BL3U

Structure Analysis on Helical Nanofilament of B4 Phase of Bent-core Liquid Crystals Mixed with Rod-like Cholesteric Liquid Crystals by Resonant Soft X-ray Scattering (RSoXS) at UVSOR

Y. Takanishi¹, F. Araoka² and H. Iwayama^{3,4}¹Faculty of Science, Kyoto University, Kyoto, 606-8502, Japan²RIKEN Center for Emergent Matter Science, Wako 351-0198, Japan³UVSOR Synchrotron Facility, Institute for Molecular Science, Okazaki 444-8585, Japan⁴School of Physical Sciences, The Graduate University for Advanced Studies (SOKENDAI), Okazaki 444-8585, Japan

Due to the new intermolecular interactions, frustration and competition, soft matter is expected to have a new structure and new functionality. Liquid crystal is typical one of soft matter, and it exhibits various mesophases due to such an effect. For example, bent-core molecules show unique liquid crystalline phases called B1~B8. The B4 phase was the lowest temperature phase observed in the bent-core liquid crystals, and it shows spontaneously chiral separated domains despite of achiral molecules. After various experimental results, it is found that this phase forms a nano-helical structure.

Recently one of authors (YT) studied the binary system between a rod-like cholesteric liquid crystal (CLC) mixture and a bent-core liquid crystal showing a B4 phase [1]. The structure of the binary system composed of rod-like cholesteric liquid crystal mixture and bent-core molecules was analyzed in order to confirm whether nano-scale phase separation as observed in the 5CB–P-8OPIMB binary system is formed. As a summary, a new smectic structure that does not appear in only constituent molecules with wide temperature range was unexpectedly discovered. This structure seems to be fundamentally composed of rich concentration of rod-like molecules. On the other hand, there remains an open question with respect to the effect of the nano-helical filament of B4 phase formed by the bent-core liquid crystal.

In resonant X-ray scattering, using X-ray whose energy is coincident with a certain atom absorption edge, the structure factor becomes a tensor instead of the scalar in conventional X-ray diffraction. Recently, carbon K-edge resonant scattering has been applied to study, and successful in obtaining the precise structures of polymer blends, block copolymer, and liquid crystals. In this study, we report the local nano-structure analysis of B4 nano-helical filament using resonant soft-X-ray scattering (RSoXS) technique. Concentration dependence of rod-like molecules and temperature dependence were measured, and the mixing effect on the helicity and correlation of B4 nano-helical filament are discussed.

The experiment was performed at BL3U of UVSOR. For the measurement, a new vacuum chamber for small angle measurement was fabricated. Used achiral bent-core liquid crystal was P-8OPIMB, and a rod-like cholesteric liquid crystal (CLC) mixture was composed

of a nematic mixture (ZLI-2293, Merck) doped with a chiral rod molecule (MLC-6248, Merck). Samples used were filled in the isotropic phase between two pieces of 100 nm-thick Si₃N₄ membranes (NTT-AT). The scattering was detected by CCD (ANDOR DO940P-BN). Incident X-ray beam was tuned between 270~300 eV. Typical RSoXS image was shown in Fig.1, and in this compound, carbon K-edge energy was 285.5 eV.

Figure 2(a) shows chirality concentration dependence of helical half pitch of B4 phase. By mixing CLC mixture, half pitch of nano-helical filament decreases from ca.120 nm to ca.80 nm, but pitch is independent of chirality. Figure 2(b) shows correlation length as a function of chirality concentration of CLC. Correlation length of mixtures is about three times longer than that of pure P-8OPIMB, and slightly increases with increasing the chiral dopant concentration. It suggests that helical pitch of the nano filament of bent-core molecules rich region is spatially homogeneous due to the influence of the rod-like molecule rich region.

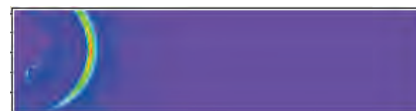


Fig. 1. Typical 2D RSoXS image from the helical nano-filament of the B4 phase.

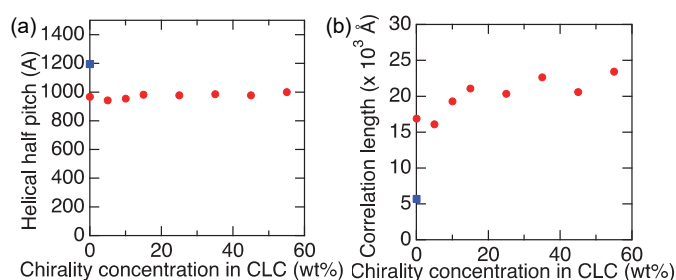


Fig. 2. half pitch (a) and its correlation length (b) as a function of chiral dopant concentration.

[1] Y. Takanishi, *Soft Matter* **17** (2021) 563.

BL3B

Evaluation of Fluorescence Lifetimes of Wavelength Shifting Fibers for High-energy Particle Experiments

K. Shintate, R. Abe, R. Ishiyama, T. Naitou, S. Nakamura, S. Sakano, J. Ohashi, Y. Tajima and H. Y. Yoshida

Department of Physics, Yamagata University, Yamagata 990-8560, Japan

Recently, operation of particle detectors at higher counting rates has been required in a high-energy physics experiment. To satisfy this requirement, scintillators used in particle detectors need to have a short fluorescence lifetime to allow fast time response. For this purpose, we measured fluorescence spectra and decay curves of newly developed wavelength shifting fibers for the future project of neutral kaon rare decay experiment [1]. The fluorescence decay curves were measured by using light pulses from visible to near ultraviolet under single bunch operation, which enables a time-correlated single-photon counting.

Figure 1 shows the decay curve of a wavelength shifting fiber Y-11 for the 500 nm band under excitation at 424 nm at room temperature. The blue lines indicate experimental data. The lifetime was analyzed by using the data analysis framework ROOT [2].

We assumed that the obtained decay curves are fitted with the formula

$$I(t) = \int_{-\infty}^{\infty} P(t')\theta(t' - T_0)G(t - t') dt',$$

where

$$P(t) = \sum_{i=1}^n A_i \exp\left(-\frac{t}{\tau_i}\right),$$

($n = 1, 2, 3$ and $A_1 = 1$)

and

$$G(t - t') = \sum_{i=1}^m C_i \exp\left(-\frac{(t - t' - \mu_i)^2}{2\sigma_i^2}\right).$$

($m = 1, 2$)

$I(t)$ represents the observed decay curve, and $P(t)$ represents the true fluorescence decay curve. If the true decay curve is composed of multiple components, it is described as the linear combination of exponential decay functions with the parameters of lifetime τ_i and initial intensity A_i . $\theta(t' - T_0)$ is a step function to decide the time origin T_0 . $G(t - t')$ represents the resolution of the measurement system, the time structure of the beam, and so on, and is given by a single gaussian or a sum of two gaussians. The red line is the fitting curve which reproduce the experimental data.

The lifetime analyses of wavelength shifting fiber YS4 and YS6 [3] were carried out by using the same analysis method. The top of Fig. 2 shows the decay curve of YS4 for the 500 nm band under excitation at 416 nm. The fitting curve reproduce the experimental

data. The fluorescence lifetimes of Y-11, YS4 and YS6, determined from our analyses, are summarized in Table 1.

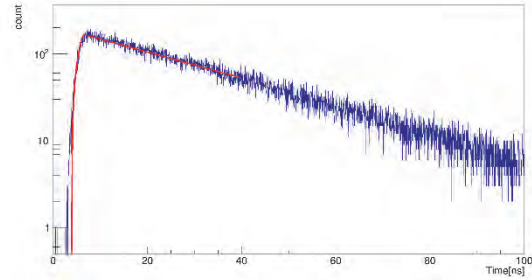


Fig. 1. Decay curve of Y-11 measured at room temperature under excitation at 424 nm obtained for the 500 nm photoluminescence band.

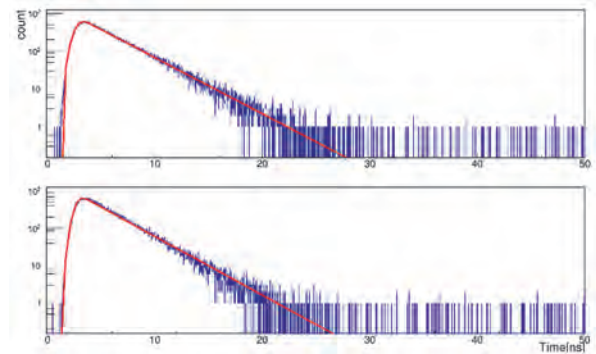


Fig. 2. Decay curves of YS4 (top) and YS6 (bottom) measured at room temperature under excitation at 416 nm and 418 nm. The former and latter are obtained for the 500 and 492 nm photoluminescence band.

Table 1. Fluorescence lifetimes of Y-11, YS4 and YS6, determined from data analyses.

Sample	λ_{EX} [nm]	λ_{EM} [nm]	τ [ns] (Ratio)
Y-11	424	500	6.44±0.00
YS4	416	500	1.37±0.00
YS6	418	492	1.27±0.00

[1] J. Comfort *et al.*, Proposal for $K_L \rightarrow \pi^0 \nu \bar{\nu}$ Experiment at J-PARC (2006).

[2] R. Brun and F. Rademakers, Nucl. Instrum. Methods Phys. Res. **A389** (1997) 81.

[3] H. Nakamura *et al.*, Europhys. Lett. **95** (2011) 22001.

BL3B

Thermoluminescence of LuAG Thick Film Scintillators Prepared via Chemical Vapor Deposition Process

S. Matsumoto¹, S. Kurosawa^{2,3} and A. Ito¹

¹Graduate School of Environmental and Information Sciences, Yokohama National University, Yokohama, 240-8501, Japan

²Institute for Materials Research, Tohoku University, Sendai 980-8577, Japan

³New Industry Creation Hatchery Center (NICHe), Sendai 980-8579, Japan

Scintillators are phosphor materials with conversion ability from radiation such as X-rays, γ -rays, and α -particles into UV-visible photons [1]. Scintillators have been used as radiation imaging systems coupled with photon detectors such as position-sensitive CCD. Recently, radiation imaging systems have been used in fields including non-destructive testing, nuclear medical imaging, and geological surveying [2–4]. Scintillator screens with excellent luminescence and emission wavelengths compatible with photon detectors are required for radiation imaging. Tl^+ doped CsI films and Tb^{3+} -doped Gd_2O_2S (GOS) powder phosphors are used as scintillator screens because of their high luminescence yield and well-matched emission band (500–800 nm) with CCD detectors [5]. Columnar and pixelated scintillators have been utilized to improve light yield and spatial resolution. Furthermore, thin scintillator screens of 10 μm or less can prevent light dispersion and are expected to be used in microtomography techniques [6].

$Lu_3Al_5O_{12}$ (LuAG)-based scintillator shows a high stopping power for radiation, excellent light yield, and a fast scintillation decay. Because of the excellent hardness of LuAG, LuAG thick film with less than 10 μm was hardly obtained via mechanical polishing. Crystal growth from the vapor phase is a promising process for the preparation of LuAG thick films. However, the vapor-grown LuAG thick film was only reported using the pulse laser deposition method, the resultant film was only 140 nm. In the previous work, we have demonstrated the preparation of 5 μm -thick Ce^{3+} :LuAG films via a chemical vapor deposition process at a high deposition rate [7]. The thick film showed an excellent light yield and a fast decay time compared with the Ce^{3+} :LuAG grown single-crystal by the melting-growth process. The reason for these excellent scintillation properties is not well known. Defect information is useful to explain the variation in scintillation properties of crystals grown by different methods. In this report, we have demonstrated the thermoluminescence (TL) properties for the sake of obtaining the defects in the vapor-grown Ce^{3+} :LuAG thick film.

In BL3B of UVSOR facilities, we measured TL properties from 18 K to 300 K (room temperature) for vapor-grown Ce^{3+} :LuAG film and melting-grown Ce^{3+} :LuAG single crystal. The crystals were irradiated at 165 nm for 10 minutes at a low temperature of 14–18

K. After the irradiation, the sample temperature was slowly raised and luminescence intensity was measured with a CCD detector.

The TL emission spectrum for the Ce^{3+} :LuAG thick film at 220 K was similar to that for the Ce^{3+} :LuAG single crystal at 140 K as shown in Fig. 1 (a). These emission peaks were originating from 5d–4f transition of Ce^{3+} ions. The TL glow curves of the thick film and single crystal are shown in Fig. 1 (b). The curve for the single crystal had continuous emissions up to room temperature while one peak was found at 140–150 K. In contrast, the thick film had two bands at ~80 and 220 K in the curve. These TL results suggested that types and amounts of defects existed in the single crystal scintillator were more and larger than those in the film scintillator.

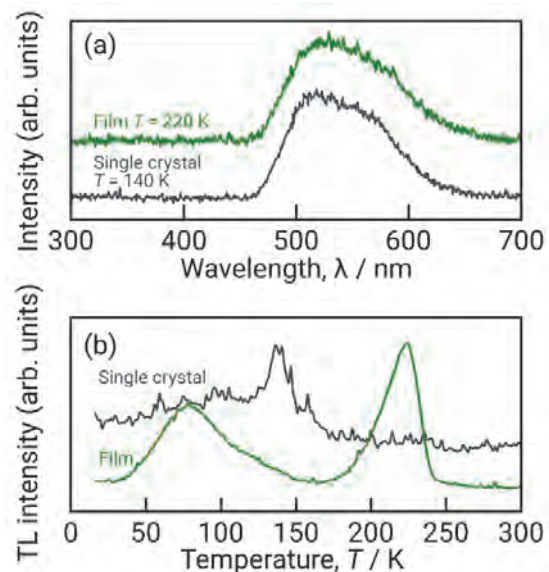


Fig. 1. (a) TL spectra and (b) glow curve of LuAG thick film and LuAG single crystal.

- [1] C.W.E. van Eijk, *Phys. Med. Biol.* **47** (2002) R85.
- [2] D.R. Schaart *et al.*, *Phys. Med. Biol.* **54** (2009) 3501.
- [3] J. Glodo *et al.*, *Phys. Procedia.* **90** (2017) 285.
- [4] S. Yamamoto *et al.*, *Radiat. Meas.* **115** (2018) 13.
- [5] T. Yanagida *et al.*, *Radiat. Meas.* **55** (2013) 99.
- [6] T. Martin *et al.*, *J. Synch. Radiat.* **13** (2006) 180.
- [7] S. Matsumoto, A. Minamino, A. Ito, *Sens. Mater.* **33** (2021) 2209.

BL3B

Temperature Dependence of Photoluminescence Properties of Li_2HfF_6

C. Fujiwara¹, S. Kurosawa^{1,2} and A. Yamaji¹¹Institute for Materials Research, Tohoku University, Sendai 980-8577, Japan²New Industry Creation Hatchery Center, Tohoku University, Sendai 980-8579, Japan

We have developed Cs_2HfF_6 (CHI) scintillator [1] for radiation monitoring in the Fukushima Daiichi Nuclear Power Plant. CHI has an emission wavelength of approximately 700 nm and light yield of 60,000 photons/MeV. Such a red emitting scintillator can be attached to an optical fiber for use in remote radiation monitoring [2]. However, CHI has low neutron sensitivity, and neutron muttering is also required due to nuclear debris including [3].

Most conventional neutron scintillators have an emission wavelength of 500 nm or less, and these scintillation materials are not suitable for the remote monitoring system with the optical fiber. We have developed a neutron scintillator with red and infrared emission by replacing Cs in CHI with Li. Here, ^6Li has a large neutron capture cross section. In this study, we measured the temperature dependence of the luminescence properties to estimate the band gap energy (E_{gap}) and to discuss the luminescence mechanism.

A Li_2HfF_6 crystal specimen was synthesized by the vertical Bridgman growth method in our laboratory using 99.9 %-pure LiI powders and 99 %-pure HfF_4 powders. We measured the photoluminescence excitation and emission spectra at 15, 50, 100, 150, 200, 250, 300 and 350 K. Multi-Gaussian fit was operated on the obtained spectra to analyze emission bands.

Figure 1 show the photoluminescence excitation and emission spectra of Li_2HfF_6 . At 15K, Li_2HfF_6 had an emission band of ~660 nm. The photoluminescence band stably existed from 15 K to 50 K. This emission bands can be originating from charge transfer emission or self-trapped exciton.

On the Other hands, Li_2HfF_6 had two emission bands from 100 K to 250 K. The one band located at ~550 nm was observed excited by ~305-nm photons. The other band had the broad red emission peak at ~660 nm. At The emission intensity of such bands gradually decreased as temperature increase. No luminescence was observed at room temperature due to thermal quenching.

To determine the emission mechanism exactly, we measure the temperature dependence of decay time in the future.

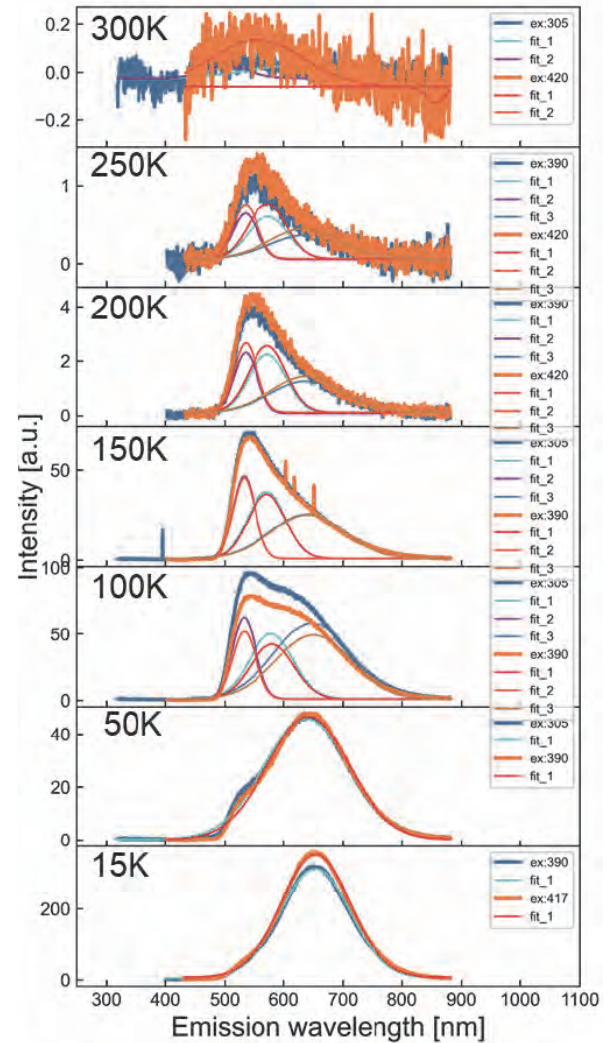


Fig. 1. Temperature dependence of photo-luminescence spectra of Li_2HfF_6 .

[1] S. Kodama, S. Kurosawa *et al.*, *Journal of Crystal Growth*, **492** (2018) 1.

[2] <https://fukushima.jaea.go.jp/en/pamphlet/topics/pdf/topics-fukushima070e.pdf>.

[3] https://www.hitachi-hgne.co.jp/download/2017/2017news17_17-11-1a.pdf

BL3B

Reflectivity Spectra of $\text{Sm}_{0.9}\text{Ca}_{0.1}\text{S}$ in Vacuum Ultra Violet Region

Y. Yokoyama¹, K. Kishida¹, F. Matsunaga¹, M. Kanou¹, K. Takano¹, Y. Okamoto¹,
H. S. Suzuki², K. Takehana³, Y. Imanaka³ and K. Takenaka¹

¹Department of Applied Physics, Nagoya University, Nagoya 464-8603, Japan

²The Institute of Solid State Physics, The University of Tokyo, Kashiwa 277-8581, Japan

³National Institute for Materials Science (NIMS), Tsukuba 305-0003, Japan

Samarium monosulfide (SmS), in which two electronic configurations (insulator $(4f)^6$ and metal $(4f)^5(5d)^1$) of Sm energetically compete, is known as valence fluctuation materials. The electronic state of Sm undergoes the transition to $(4f)^5(5d)^1$ from the $(4f)^6$ state by applying pressure and chemical doping, while the $(4f)^6$ state is stable under ordinary pressure and temperature condition [1]. It is promising to be applied to materials for negative thermal expansion (NTE) and actuators by controlling these electronic states [2] since this phenomenon is accompanied by a large volume change up to 10 %. To study changes in the electronic states due to the valence transition, we conducted systematic optical reflectivity measurements of $\text{Sm}_{1-x}\text{Y}_x\text{S}$ single crystalline samples, covering wide energy and compositional region [3]. It is clarified that a characteristic structure, which showed the changes in electronic states induced by the valence transition, became appeared in the optical spectra at Y composition of 0.28 [3]. For the application of the electric-field-driven actuator, the changes in the electronic state during the valence transition induced by the application of the electric field must be studied. It is also necessary that SmS can be applied electric field enough to induce the valence transition.

In this work, we prepared a $\text{Sm}_{0.9}\text{Ca}_{0.1}\text{S}$ single-crystalline sample to enhance the insulation, and conducted the optical reflectivity spectral measurements at room temperature at no electric field first. Normal incident reflectivity spectra were collected at 295 K by using a Fourier-type interferometer (0.005–1.6 eV) and a grating spectrometer (1–3 eV) installed with a microscope. For the measurements from visible to the vacuum-UV region (2–30 eV), we used synchrotron radiation at BL3B of UVSOR, Institute for Molecular Science.

Figure 1 shows the electrical resistivity of $\text{Sm}_{0.9}\text{Ca}_{0.1}\text{S}$ single crystal. By comparing to the non-doped SmS , it is clearly shown that the electrical resistivity significantly increased by more than two orders of magnitude. We succeeded in the valence transition to the metallic phase of this sample by applying the electric field of 300 V/cm at the liquid nitrogen temperature (data not shown). The optical reflectivity spectra of $\text{Sm}_{0.9}\text{Ca}_{0.1}\text{S}$ are shown in Fig. 2. The spectra in the lower energy region (Fig. 2(a)) show that both Ca-doped and non-doped SmS are characteristic of the insulator, in terms of low reflectivity in the far-IR region except for phonon peak. The reflectivity

spectrum of $\text{Sm}_{0.9}\text{Ca}_{0.1}\text{S}$ also demonstrated an appearance of the reflectivity dip around 40 meV, strongly suggesting further insulation by the Ca doping. On the other hand, for the reflectivity spectra in the higher energy region (Fig. 2(b)), problems in the data consistency remain. The reflectivity data above 5 eV must be reconsidered for precise discussion on the changes in the electric state due to the Ca doping, whereas fine structures below 5 eV are reliable. To elucidate the changes in the electronic states by the valence transition induced by the electric field, it is necessary to construct a measuring system that the reflectivity spectra in the wide energy region can be collected at the liquid nitrogen temperature and under the electric field in the future.

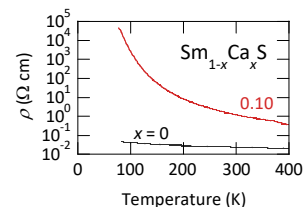


Fig. 1. Electrical resistivity of $\text{Sm}_{1-x}\text{Ca}_x\text{S}$ single crystals.

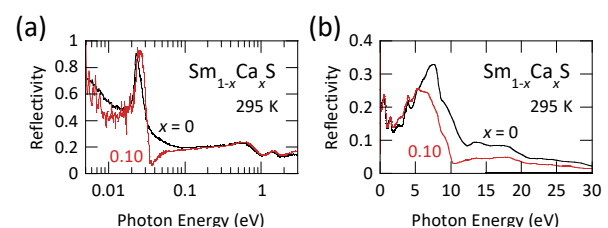


Fig. 2. Optical reflectivity spectra of $\text{Sm}_{1-x}\text{Ca}_x\text{S}$ at 295 K: (a) from far-IR to visible and (b) from visible to vacuum-UV regions.

- [1] A. Jayaraman *et al.*, Phys. Rev. B **11** (1975) 2783.
[2] K. Takenaka *et al.*, Sci. Rep. **9** (2019) 122.
[3] Y. Yokoyama *et al.*, Phys. Rev. B **100** (2019) 245143.

BL3B

Optical Investigation on Fluoro-olefins in Vacuum-Ultraviolet for New Refrigerant Gas Development

K. Yamanoi^{1,2}, Y. Sakata¹, H. Iwayama³, Y. Hasumoto^{1,2}, O. Yamamoto^{1,2} and M. Noumi^{1,2}

¹Osaka university, Suita 565-0871, Japan

²DAIKIN Industries Ltd, Settsu 566-8585, Japan

³UVSOR Synchrotron Facility, Institute for Molecular Science, Okazaki 444-8585, Japan

Chlorofluorocarbon (CFC), hydrochlorofluorocarbon (HCFC), and hydrofluorocarbon (HFC) have been used as a refrigerant. These gases have high global warming potential (GWP) over 100. Recently, the hydrofluoroolefin (HFO) gases are expected as new low environmental load refrigerant due to its low GWPs since olefin gas is unstable and easily decompose by ultraviolet light in nature. In order to put HFO into practical use as a refrigerant, it is necessary to clarify the physical characteristics of HFO such as UV absorption and decomposition process. In this study, we measured the vacuum ultraviolet (VUV) light induced decomposition of HFO.

The decomposition spectra measurements were carried out in BL3B in UVSOR facility. Trans-C₂H₂F₂ gas was flowed into vacuum chamber through the capillary tube. The pressure in vacuum chamber was kept less than 3×10^{-4} Pa. The VUV light from 8 to 30 eV was irradiated on sample gas and the ionized molecular fragments were detected TOF-mass spectrometer shown in Fig. 1.

Figure 2 shows the decomposition spectra of C₂H₂F₂. We could clearly observe the ionization energies of each fragments. The decomposition from C₂H₂F₂ to CH₂F₂ and HF arise with 14.9 eV. With higher energy about 18 eV, the C₂H₂F₂ dissociate to CHF and CHF. From our previous results, the trans-C₂H₂F₂ has the absorption from 135 nm (9.2 eV) to 190 nm (6.5 eV) as shown in Fig. 3. The absorption at 145 nm is attributed to the stretching and twisting of carbon double band and the 190 nm is the transition from π to π^* in C=C bonds, respectively [1]. However the ionization and decomposition threshold is quite higher than these absorption. These results show that the higher photon energy over 14 eV is needed for trans-C₂H₂F₂ to be decomposed in the air. However, we notice that other components exist such as oxygen and nitrogen which react with fluorocarbon in real case.

In conclusion, we could observe the optical properties and ionization energy of decomposition process of C₂H₂F₂ in VUV region. The results let us know the UV- or VUV-induced decomposition dynamics of fluoro-olefins as refrigerant in next-generation.

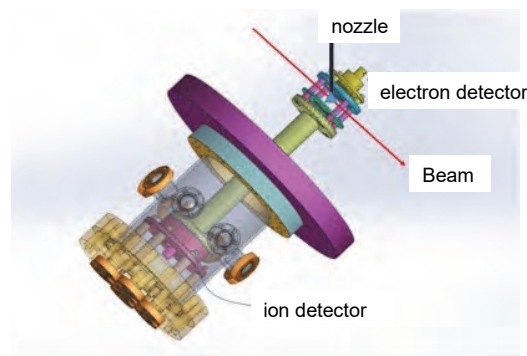


Fig. 1. Schematic image of the experimental setup in BL3B.

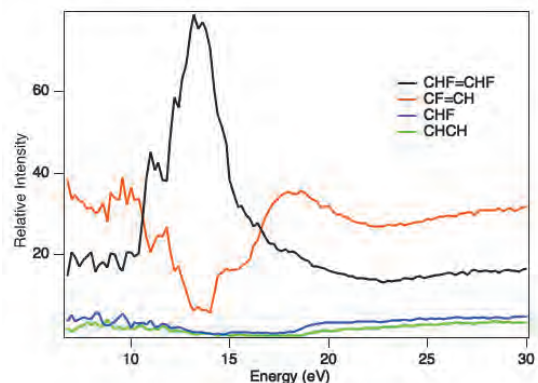


Fig. 2. Decomposition spectra of trans-C₂H₂F₂.

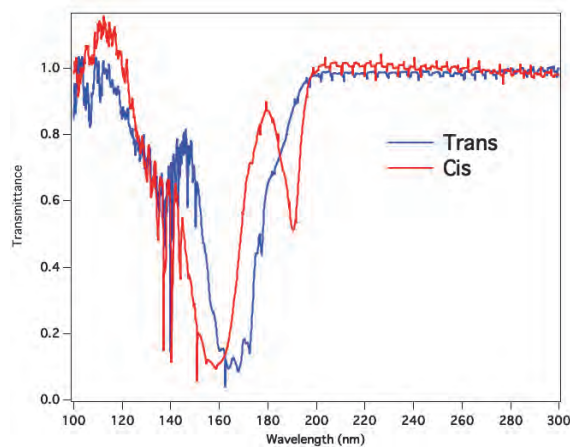


Fig. 3 Absorption spectrum of C₂H₂F₂.

[1] G. Belange *et al.*, J. Chem. Phys. **55** (1971) 2055.

BL3B

Absorption Bands of Tl^+ Centers in CsI-based Ternary Crystals

S. Ito and T. Kawai

Graduate School of science, Osaka Prefecture University, Sakai 599-8531, Japan

The optical properties of the Tl^+ centers in alkali halide crystals have been extensively investigated [1]. The Tl^+ centers in alkali halide crystals with the NaCl-type crystal structure exhibit the typical A, B, and C absorption bands. On the other hand, the Tl^+ centers in cesium halide crystals with the CsCl-type crystal structure have absorption bands different from the typical A, B, and C bands; in particular, the appearance of absorption bands in CsI: Tl^+ is unusual [2,3]. It has been regarded that the unusual absorption spectra of the Tl^+ centers in cesium halide crystals originate from the different ionic configurations around the Tl^+ ion in the NaCl- and CsCl-type crystal structures [2]. To provide a better understanding of these observations, we investigated absorption bands of CsCaI₃: Tl^+ , CsBa₂I₅: Tl^+ , Cs₄CaI₆: Tl^+ , and Cs₄SrI₆: Tl^+ crystals, which were prepared by a cell method [4].

Figure 1 shows the absorption spectra of CsCaI₃: Tl^+ , CsBa₂I₅: Tl^+ , Cs₄CaI₆: Tl^+ , and Cs₄SrI₆: Tl^+ crystals at 10 K. For reference, the absorption spectrum of CsI: Tl^+ is also demonstrated in the top of Fig. 1. In CsCaI₃: Tl^+ , the absorption bands having no extremely different absorption intensity are observed at 4.54, 5.14, and 5.55 eV. A absorption band is observed at 4.32 eV for CsBa₂I₅: Tl^+ . In Cs₄CaI₆: Tl^+ and Cs₄SrI₆: Tl^+ , the absorption band with a doublet structure is observed at about 4.23 eV and the band with the largest absorption intensity is observed at 4.94 eV. In addition, the weak absorption bands are observed at about 5.18 and 5.33 eV. The 4.23 eV band with a doublet structure and the 4.94 eV band in Cs₄CaI₆: Tl^+ and Cs₄SrI₆: Tl^+ may be assigned to the A and C bands of the Tl^+ centers, respectively, from the intensity ratio between them. On the other hand, it is hard to assign the absorption bands of CsCaI₃: Tl^+ and CsBa₂I₅: Tl^+ to the A, B, and C bands, just like the absorption bands in CsI: Tl^+ .

The CsI-based ternary crystals above have various crystal structures; orthorhombic (CsCaI₃) [5], monoclinic (CsBa₂I₅) [6], and trigonal (Cs₄CaI₆ and Cs₄SrI₆) [7] structures. In the host lattice, the Tl^+ ions which replace the Cs⁺ ion, have various coordinations of the I⁻ ions. That is to say, the Tl^+ ions in the ternary iodide crystals have different coordination of the I⁻ ions from the Tl^+ ion in the CsI crystal. Despite the difference of the coordination, the absorption bands of CsI: Tl^+ seem to appear at the energy positions which the absorption bands of the Tl^+ centers in the ternary iodides are observed. For example, the lowest absorption band of CsI: Tl^+ is located at 4.27 eV, which is close to the lowest bands of Cs₄CaI₆: Tl^+ and Cs₄SrI₆: Tl^+ in the energy position. The 4.52 eV absorption band of CsI: Tl^+ is located at the energy position close to the lowest 4.54 eV band of CsCaI₃: Tl^+ . The energy positions of the

absorption bands in CsI: Tl^+ may be related to the coordination states around the Tl^+ ion.

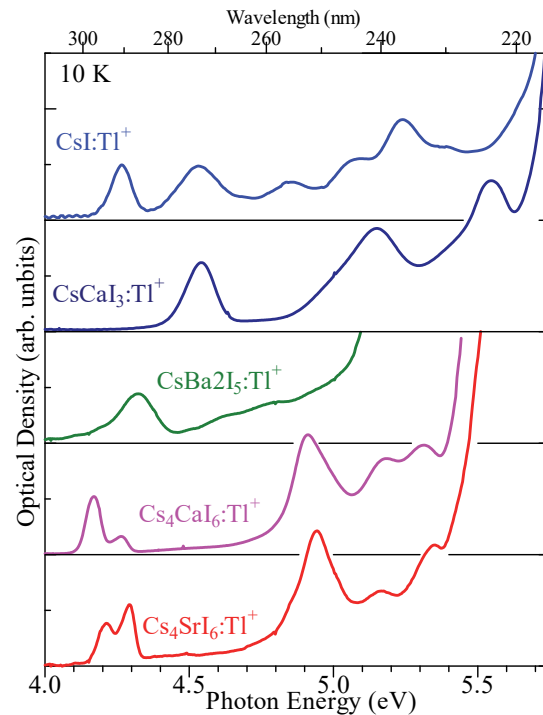


Fig. 1. Absorption spectra of CsI: Tl^+ , CsCaI₃: Tl^+ , CsBa₂I₅: Tl^+ , Cs₄CaI₆: Tl^+ , and Cs₄SrI₆: Tl^+ crystals at 10 K.

- [1] P. W. M. Jacobs, *J. Phys. Chem. Solids* **52** (1991) 35.
- [2] S. Masunaga and M. Ishiguro, *J. Phys. Soc. Jpn.* **25** (1968) 1337.
- [3] T. Kawai, *et al.*, *Phys. Status Solidi B* **227** (2001) 587.
- [4] S. Hashimoto and M. Itoh, *Jpn. J. Appl. Phys.* **27** (1988) 726.
- [5] J. Grimm, *et al.*, *Inorg. Chem.* **45** (2006) 10905.
- [6] B. Kang, *et al.*, *J. Phys. D: Appl. Phys.* **49** (2016) 395103.
- [7] L. Stand, *et al.*, *J. Cryst. Growth* **486** (2018) 162.

BL3B

Photoluminescence Properties of Cs₂ZrI₆

S. Kodama¹ and S. Kurosawa²¹Saitama University, Saitama 338-8570, Japan²New Industry Creation Hatchery Center, Tohoku University, Sendai 980-8579, Japan

The intrinsic luminescent scintillators with the chemical formula of A_2BX_6 (A : monovalent cation, B : tetravalent cation, X : halogen ion) are attracting large attention due to their high light outputs and high energy resolutions. We reported Cs₂HfI₆ and Rb₂HfI₆ as the novel red-emitting scintillators with the high light output over 40,000 photons/MeV [1-5]. While the candidate compositions of A_2BX_6 scintillators are actively studied, the detailed mechanism of intrinsic luminescence is still unclear. We have studied the photoluminescence properties of A_2BX_6 scintillators to understand the basic luminescence behaviors and compare them with the that of conventional phosphors using the beamline of BL3B, UVSOR.

In the UVSOR activity report 2020, we reported the low-temperature photoluminescence properties of Cs₂HfI₆. Cs₂HfI₆ showed two photoluminescence bands at 10K. The origin of each band was unclear. In order to compare the effect of B cation on the photoluminescence properties, we grew Cs₂ZrI₆ crystal and evaluated the temperature dependence of photoluminescence emission spectra. A single crystalline Cs₂ZrI₆ specimen was obtained by the vertical Bridgman growth method in our laboratory from 99.95 %-pure ZrI₄ and 99.999 %-pure CsI powders.

Figure 1 shows the measured spectra of Cs₂ZrI₆. The emission wavelength of Cs₂ZrI₆ was ~630 nm at 300 K, and shifted towards shorter wavelength as cooled down reaching ~720 nm at 10K. Cs₂ZrI₆ had only one photoluminescence band at all temperature, while Cs₂HfI₆ had two bands at 10K. Therefore, the numbers of photoluminescence bands of Cs₂BI₆ were determined to be two when B is Hf and to be one when B is Zr. The tetravalent cation B might play the important roll in the luminescence phenomena of A_2BX_6 scintillators. For future study, we would continue to study A_2BX_6 compounds to reveal the rolls of A , B and X ions.

[1] S. Kodama *et al.*, IEEE Trans. Nucl. Sci. **67** (2020) 1055.

[2] S. Kodama *et al.*, Appl. Phys. Express **13** (2020) 047002.

[3] S. Kodama *et al.*, UVSOR Activity Report 2019 **47** (2020) 60.

[4] S. Kodama *et al.*, UVSOR Activity Report 2020 **48** (2021) 65.

[5] S. Kodama *et al.*, Rad. Meas. **124** (2019) 54.

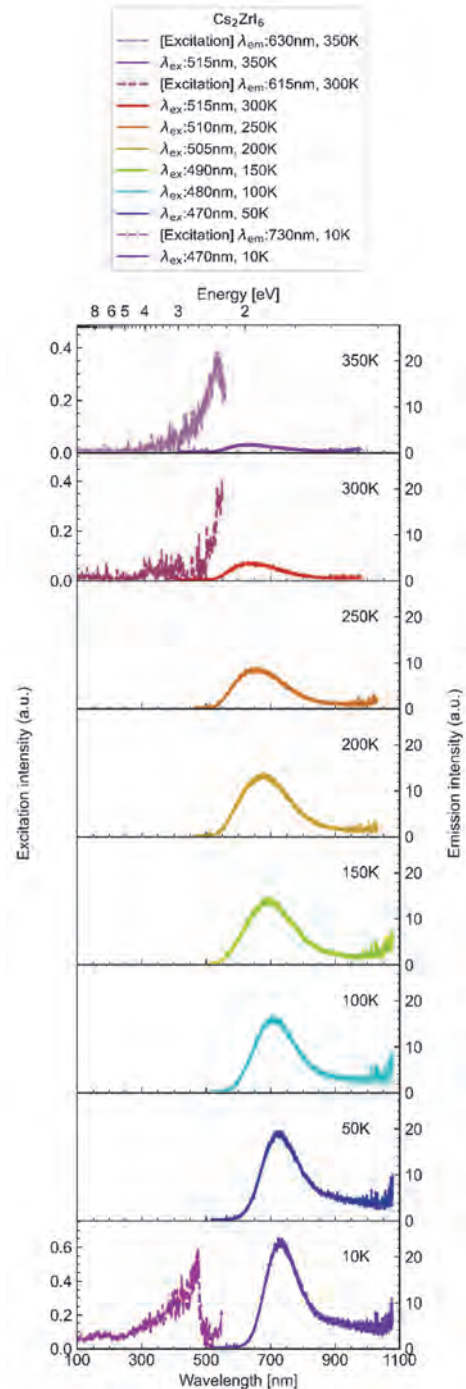


Fig. 1. Temperature dependence of photoluminescence excitation and emission spectra of Cs₂ZrI₆ at 10, 50, 100, 150, 200, 250, 300 and 350 K.

BL4U

Structural Analysis of Unvulcanized Rubber by Scanning Transmission X-ray Microscopy

T. Ohigashi^{1,2,3}, F. Kaneko⁴, H. Yuzawa¹ and H. Kishimoto⁴

¹UVSOR Synchrotron Facility, Institute for Molecular Science, Okazaki 444-8585, Japan

²Institute of Material Structure Science, High Energy Accelerator Research Organization, Tsukuba 305-0801, Japan

³School of Physical Sciences, The Graduate University for Advanced Studies (SOKENDAI), Okazaki 444-8585, Japan

⁴Sumitomo Rubber Industries Ltd., Kobe 651-0071, Japan

Reduction of consumption of limited resources is nowadays a critical issue to maintain our daily life. Rubber is one of the important resources and its demand is assumed to increase especially according to growth of car industries. Therefore, further improvement in wear- and destruction-resistant of rubber is necessary to reduce its consumption. Then, control of crosslinking of sulfur in rubber is a key technology. Heterogeneity of network of crosslinking in rubber has been confirmed by small-angle neutron scattering [1]. This heterogeneity causes destruction of rubber because it gathers internal stress under deformation. Therefore, dispersion of a crosslinking reagent in the rubber is important to make the crosslinking network homogeneous.

To achieve the above goal, it is important to measure the relationship between the dispersion and various parameters of synthesis. Thus, this dispersion has been conventionally tried to depict by using electron microscopy. However, its observation was not easy because the rubber contains only small amount of the crosslinking agent. Moreover, the crosslinking agent is consisted of light elements and is easily damaged by electron beam. Then, scanning transmission X-ray microscopy (STXM) can be an alternative approach. STXM can probe the crosslinking agent by using near-edge X-ray absorption fine structure (NEXAFS). The advantages of STXM are high spatial resolution around 30 nm and much lower radiation damage than the electron microscopy. In this report, the distribution of crosslinking agent in unvulcanized rubber is investigated by STXM.

An ultra-thin section of the unvulcanized rubber of 250 nm thick was prepared as a sample by a cryo ultramicrotome. In the case of STXM observation, the sample was cooled down to ~ -90 degree with cryo-cooling setup to suppress the radiation damage [2].

Figure 1(a) shows an X-ray fluorescence image at N-K α line by using transmission electron microscopy with an energy dispersive detector. Since signal intensity of N-K α line is low, the image is noisy and does not have any structures. Even though the detection of the X-ray fluorescence brings high sensitivity to the analytical system, the crosslinking agent could not be detected. We assumed that the crosslinking agent was damaged by irradiation of the electron beam.

The STXM image acquired at the X-ray energy of 401 eV is shown in Fig. 1(b). The observed image

shows many dark domains with high absorption. X-ray absorption spectra of these dark domains (Fig. 2(a)) are compared with references of the crosslinking agent "A" and "B" by comparing with the reference spectra (Fig. 2(b)). Matrix of the rubber has quite lower nitrogen signals than the dark domains, which implies heterogeneity of the distribution of the crosslinking agent. As a result of linear combination fitting, these dark domains are consisted of the crosslinking agent "A" and "B".

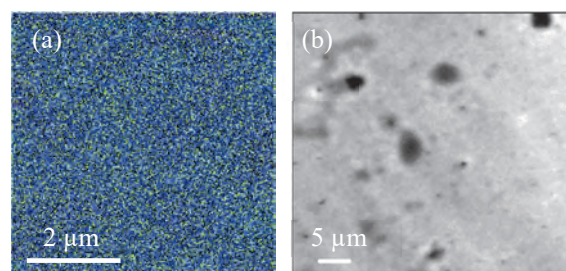


Fig. 1. (a) Images of unvulcanized rubber acquired by transmission electron microscopy with an energy dispersive detector acquired at N-K α line and (b) that by STXM at N-K edge (401 eV).

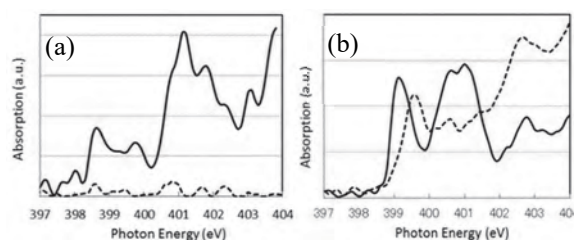


Fig. 2. (a) X-ray absorption spectra of the unvulcanized rubber in the dark domain (solid line) and matrix (dashed line) in Fig.1(b) around N-K edge and (b) those of the crosslinking agents for "A" (solid line) and "B" (dashed line).

[1] Y. Ikeda, N. Higashitani, K. Hijikata, Y. Kokubo and Y. Morita, *Macromolecules* **42** (2009) 2741.

[2] T. Ohigashi, F. Kaneko, Y. Inagaki, T. Yano, H. Kishimoto and N. Kosugi, *UVSOR Activity Report* **2017 45** (2018) 34.

BL4U

C-K Edge Spectra of Bound-rubber Structure in SBR Materials with Filler and/or Reagents

T. Ejima^{1,2} and Y. Tamura^{2,3,*}¹SRIS, Tohoku University Sendai 980-8577, Japan²IMRAM, Tohoku University, Sendai 980-8577, Japan³JSR Corporation, Yokkaichi 510-8552, Japan

Adding filler materials such as carbon black to elastomer materials such as synthetic rubber can significantly change mechanical properties: stress properties, tensile strength, and abrasion resistance [1]. The factors that cause the changes in mechanical properties are not well understood, and the type and the amount of filler materials added to obtain the desired mechanical properties are known empirically. In addition, it is known that the structure of an elastomer material differs at each scale and exhibits a hierarchical structure [2-4]. Among the hierarchical structure, we presume that the chemical state and the 3D structure of the bound-rubber structure formed between filler particles at the nm scale determine the overall mechanical properties. In the study, we will add filler materials and/or reagents to elastomer materials that the mechanical properties are known, then the chemical states of the bound rubber structure and its spatial distribution will be measured using the STXM in BL4U. We believe that this process will clarify the origin of the mechanical properties.

In the measurement, compounds were prepared from an elastomer material with a filler material and various reagents, and styrene-butadiene rubber (SBR) and modified SBR are used as the elastomer materials. The fabricated compounds were cut into sections and used in the STXM measurements. The measurement was performed with a spatial resolution of 100 nm and an exposure time of 2 msec per point. The obtained soft X-ray images clearly distinguish the position of the added filler material. Based on the preliminary NEXAFS results, spectral measurements were performed focusing on the difference between the π^* - and the σ^* - structures of the C-K absorption edge. The obtained nanoscopic spectra around bound-rubber structures in a same compound showed a similar spectral shape with a change in peak intensity depending on the presence or the absence of the filler and/or reagents. Different spectral shape was observed around a bound-rubber structure according to a modification of the SBR. An example of the spectral change in shape is shown in Fig. 1. By the energy positions of the peaks, we estimate the origins of peaks as that: peak A is a transition from C1s orbital to π^* orbital due to the C=C bond, peak B is a transition to C-H* orbital, and peaks C and C' are transitions to σ^* orbital [5].

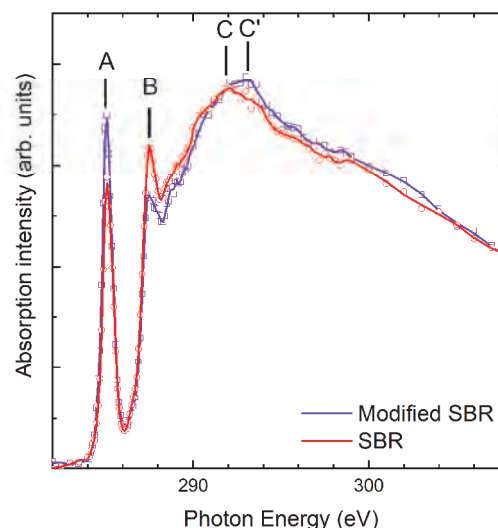


Fig. 1. C-K edge spectra of SBR and modified SBR with same filler and reagents. Curves are smoothing results for guide to see.

[1] M. Ashida *et al.*, J.Soc. Rubber Science and Technology, Japan **49** (1976) 821.

[2] K. Nakajima, *et al.*, Rub. Chem. Technol. **90** (2017) 272.

[3] J. Kikuma, *et al.*, J. Surf. Anal. **25**, (2018) 34.

[4] Z. Martin, I. Jimenez, M.A. Gomez-Fatou, M. West and A. P. Hitchcock, Macromolecules **44** (2011) 2179.

[5] J. Stoehr, "NEXAFS Spectroscopy", Springer-Verlag, Berlin Heiderberg GmbH (1992), Chap. 7 and 8.

*Present Address: ENEOS Materials Corporation, Yokkaichi, Mie 510-0871, Japan

BL4U

Analysis of Materials for Secondary Batteries by STXM

E. Hosono^{1,2,3}, D. Asakura^{1,2,3}, H. Yuzawa⁴ and T. Ohigashi^{4,5}

¹Global Zero Emission Research Center, National Institute of Advanced Industrial Science (AIST), Tsukuba 305-8569, Japan

²Research Institute for Energy Conservation, AIST, Tsukuba 305-8565, Japan

³AIST-UTokyo Advanced Operando Measurement Technology Open Innovation Laboratory (Operando-OIL), Kashiwa 277-8565, Japan

⁴UVSOR Synchrotron Facility, Institute for Molecular Science, Okazaki 444-8585, Japan

⁵School of Physical Sciences, The Graduate University for Advanced Studies (SOKENDAI), Okazaki 444-8585, Japan

In order to improve the performance of secondary batteries such as lithium-ion batteries (LIB) and develop innovative electrode materials, investigation on the electronic state of electrode materials under charge/discharge condition is required. This is because the electronic state determined by redox conditions is one of the critical factors for the energy density such as charge/discharge capacity and operating voltage of battery. Since soft X-ray absorption spectroscopy (XAS) is sensitive to the change of local electronic state, it is suitable analytical method for electrode materials [1,2].

In addition, study of facet is also important to control of the stability of the interface between the electrode active material and the electrolyte. To elucidate the behavior of the facet, analysis for spatial distribution of electronic state at interface is required.

For spatially selective analysis, various techniques of electron microscopes have been developed. For example, TEM-EELS and TEM-EDS are widely used as elemental analysis with a high spatial resolution. However, in order to understand the electronic state of the active materials, synchrotron radiation soft X-ray spectroscopy is advantageous in terms of the energy resolution and lower beam (X-ray) damage than the damage by electron beams in electron microscopes. Moreover, the scanning transmission soft X-ray microscopy (STXM) with a spatial resolution of several tens of nm is highly effective for analyzing the electronic-state distribution in one particle of the electrode material because the particle size is in the order of several micrometers.

So far, we have mainly focused on cathode materials like transition-metal oxides, but now we apply STXM analysis to 2D carbon materials used for the anode as well. Figure 1 shows the STXM image of 2D carbon nanosheets at 320 eV and the C *K*-edge XAS spectrum of selected area. Graphite-like π^* and σ^* peaks are observed. We believe that STXM is important for carbon materials as well because it enables analysis for the distribution of local electronic structure to discuss the stability of the material.

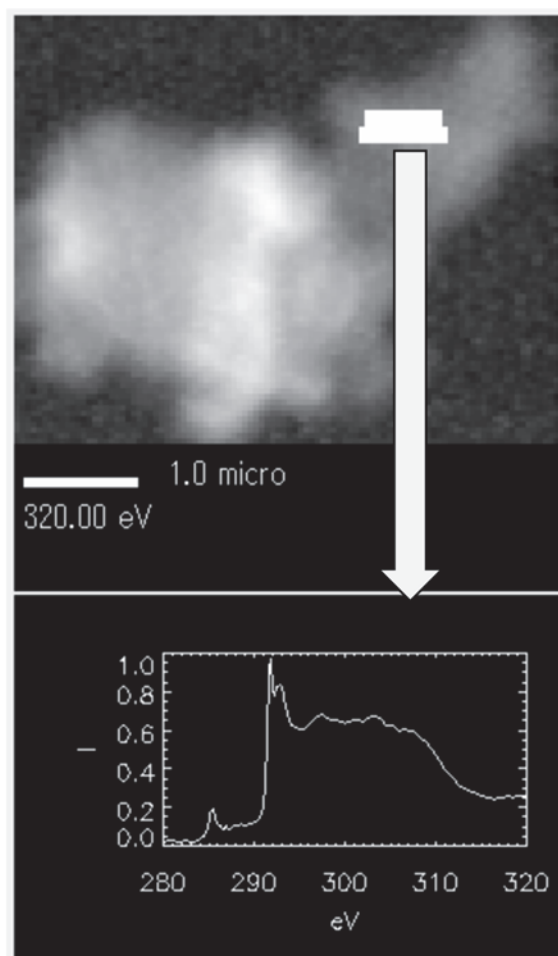


Fig. 1. STXM image and spectrum of selected area.

[1] Y. Nanba *et al.*, Chem. Mater. **28** (2016) 1058.

[2] D. Asakura *et al.*, ChemPhysChem. **17** (2016) 4110.

BL4U

Probing the Electronic Structure of Ni-Co Binary Oxide/Graphene Nanocomposites as Supercapacitor Electrodes by Scanning Transmission X-ray Microscope

H. W. Chang^{1,2}, T. C. Huang², T. Ohgashi³, C. H. Chuang¹, Y. C. Tsai⁴, C. L. Dong¹ and W. F. Pong¹¹Department of Physics, Tamkang University, Tamsui 251, Taiwan²Department of Chemical Engineering, National United University, Miaoli 360302, Taiwan³UVSOR Synchrotron Facility, Institute for Molecular Science, Okazaki 444-8585, Japan⁴Department of Chemical Engineering, National Chung Hsing University, Taichung 40227, Taiwan

Nickel and cobalt-based oxide are considered as promising materials for supercapacitors owing to the multiple oxidation states and excellent electrochemical redox activity. The conductive carbon materials (such as graphite, carbon nanotubes, and graphene) serve as a conductive component can create the possibility to form the conducting interconnection between carbon materials and transition metal oxides, allowing fast ions and electrons transport inside interior space of transition metal oxide pore/channel structure, thus dramatically enhanced the electrocatalytic activity. In this study, Ni-Co binary oxide were synthesized on the graphene to obtain Ni-Co binary oxide/graphene (NCG) nanocomposites as supercapacitor electrodes. NCG nanocomposites were tested with the applied voltage of 0.3 and -0.1 V to evaluate pseudocapacitive behavior toward studying the change of the local chemical environment of a selected element using STXM. Figure 1 show the optical density images of NCG at C K-edge and O K-edge under applied voltage of 0.3V and -0.1V. The C K-edge XANES spectra has several distinct features (G_a , G_b , and G_c). Features G_a and G_c at 284.6 and 290.9–291.9 eV are associated with the transitions from C 1s to the unoccupied π^* and σ^* orbitals, respectively, reflecting the bonding perpendicular to the ring plane and within the ring plane. Features G_b consist of three peaks G_{b1} (286.3 eV), G_{b2} (287.5 eV), and G_{b3} (288.5 eV) correspond to C–O π^* (hydroxyl or ether), C=O π^* (carbonyl groups), and O=C–O π^* (anhydride, lactone, or carboxylic acids). The O K-edge XANES spectra reveals H_a and H_b features at 532.8 and 540.0–545.0 eV. These features are associated with C=O π^* states of carbonyl groups and the O–H σ^* , C–O σ^* and C=O σ^* symmetry states from carbonyl, carboxylic acid, and hydroxyl groups. The spectral profile in Figs. 1(g) and (h) changes with the bias potential applied from selected regions of the edges (yellow) and the center (red) that indicate favorable structural and chemical reversibility during the charge/discharge process, suggesting that the oxygen-containing functional groups provide pseudocapacitance through Faradaic reactions that occur near the surface of the graphene-based materials: $>C-OH \leftrightarrow C=O + H^+ + e^-$, $-COOH \leftrightarrow -COO + H^+ + e^-$, and $>C=O + e^- \leftrightarrow >C-O^-$ [1-3]. Further studies at Ni and Co L-edge are expected to provide detail information of the energy storage mechanisms.

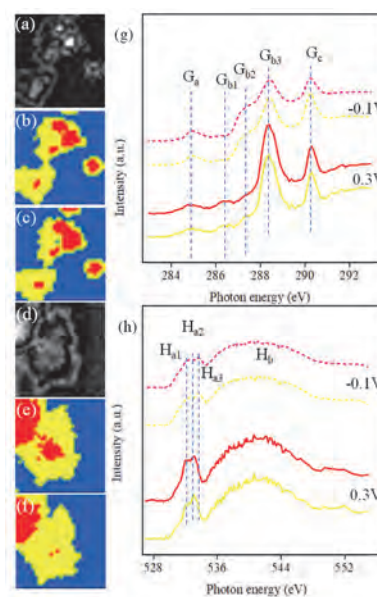


Fig. 1. Optical density images of NCG under (a) 0.3 V and (d) -0.1 V. (b,e) C K-edge and (c,f) O K-edge STXM. (g) C K- and (h) O K-edge STXM-XANES of NCG from different regions (yellow and red).

[1] Han *et al.*, Nat. Commun. **11** (2020) 1.

[2] Gandhiraman *et al.*, J. Phys. Chem. C **118** (2014) 18706.

[3] Chang *et al.*, J. Phys. Chem. C **120** (2016) 22.

BL4B

Development of Reflection XMCD Measurement Setup for the Investigation of Inner Structures of Magnetic Thin Films at UVSOR BL4B

K. Yamamoto, H. Iwayama, O. Ishiyama and T. Yokoyama
Institute for Molecular Science, Okazaki 444-8585, Japan

Magnetic thin films/multilayers with complex depth structures exhibit a wide variety of magnetic phenomena due to the interactions between layers [1]. Furthermore, multilayer structures have been used to realize useful properties in recording media, which is an important application of magnetic materials. Direct observation of the magnetic distribution in the depth direction of such magnetic multilayers has been used to elucidate the mechanism of evolution of magnetic structures in thin films

We installed an experimental setup for reflectance x-ray magnetic circular dichroism (XMCD) method [2] in the soft X-ray region at BL4B and experiments were performed on test samples as shown in Fig. 1.

The sample and the detector can be rotated independently to obtain reflectivity. X-rays were detected by a photodiode (AXUV100G, Optodiode inc.). The magnetic field was about 0.35T, and measurements were made at room temperature. The magnetic field was applied by two pairs of Nd magnets disposed oppositely. The magnets can be rotated and the relative positional relationship between the magnetic field and the sample was kept constant. The setup is schematically depicted in Fig. 2.

We used off-axis components of x-rays from the bending magnet to obtain circularly polarized light. The x-rays are elliptically polarized. XMCD intensity was measured by changing the direction of magnetic field.

The sample was CoFeB and an oscillating structure was observed due to the interference of the cap layer and the underlying layers. We observed the difference corresponding to XMCD by changing the direction of magnetic field, which is consistent with the simulation results. The same measurements were made around the absorption edges and spectroscopic information was extracted. These results can be reproduced by the simulation based on the full matrix algorithm and the magneto-optical effects of the elliptically polarized x-rays were treated explicitly. Although there have been previous studies using XMCD of reflectance, there are few studies that extends this method to obtain spectroscopic information. We also conducted spectroscopic measurements and obtained photon energy and reflection angle dependence to analyze the depth-resolved magnetization information.

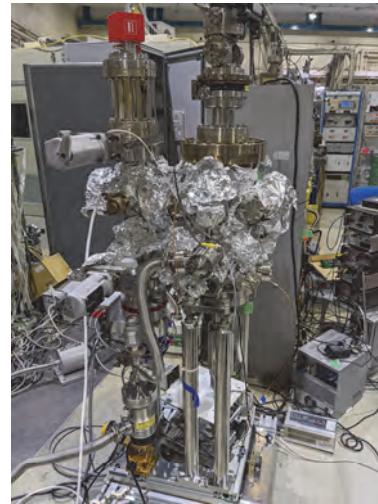


Fig. 1. The experimental setup installed at BL4B.

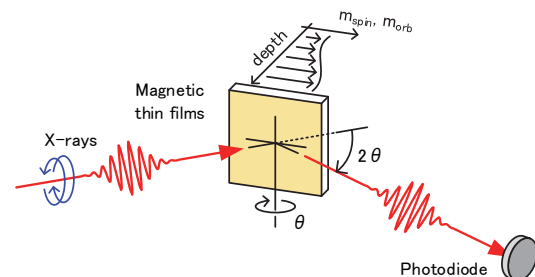


Fig. 2 The illustration for the XMCD reflectivity measurements.

[1] F. Hellman *et al.*, *Rev. Mod. Phys.* **89** (2017) 025006.

[2] S. Macke and E. Goering, *J. Phys. Condens. Matter.* **26** (2014) 363201.

BL5U

Dirac Fermions and Topological Phase Transition in XMg_2Bi_2 ($X = \text{Ba}$ and Sr)

D. Takane¹, Y. Kubota¹, K. Nakayama^{1,2}, T. Kawakami¹, S. Souma^{3,4}, K. Sugawara^{1,2,3,4}, S. Ideta^{5,6}, K. Tanaka^{5,6}, T. Takahashi^{1,3,4}, K. Segawa⁷ and T. Sato^{1,3,4}

¹Department of Physics, Graduate School of Science, Tohoku University, Sendai 980-8578, Japan

²Precursory Research for Embryonic Science and Technology (PRESTO), Japan Science and Technology Agency (JST), Tokyo 102-0076, Japan

³Center for Spintronics Research Network, Tohoku University, Sendai 980-8577, Japan

⁴Advanced Institute for Materials Research (WPI-AIMR), Tohoku University, Sendai 980-8577, Japan

⁵UVSOR Synchrotron Facility, Institute for Molecular Science, Okazaki 444-8585, Japan

⁶School of Physical Sciences, The Graduate University for Advanced Studies (SOKENDAI), Okazaki 444-8585, Japan

⁷Department of Physics, Kyoto Sangyo University, Kyoto 603-8555, Japan

The search for novel fermions is recently becoming an exciting challenge in condensed-matter physics, as highlighted by the discovery of two-dimensional (2D) Dirac fermions in graphene and helical 2D Dirac fermions at the surface of three-dimensional (3D) topological insulators. The recent discovery of 3D Dirac fermions in topological Dirac semimetals (TDSs) further enriches the category of exotic fermions. TDSs show exotic quantum phenomena such as high carrier mobility and giant linear magnetoresistance governed by the linearly dispersive Dirac-cone energy band. Also, TDSs provide a fertile playground for realizing a variety of topological phases, e.g., by breaking the time-reversal/crystalline symmetry or by chemical substitution. However, despite many theoretical predictions for TDS candidates, TDSs that have been experimentally verified are still rare. Moreover, topological phase transition from TDSs has been scarcely realized partly because of the difficulty in substituting constituent elements of known TDSs. Thus, it is highly desired to explore new TDS materials that overcome such difficulties.

Here we demonstrate that ternary compound BaMg_2Bi_2 is a new TDS and serves as a useful platform to study topological phase transition [1].

High-quality single crystals of XMg_2Bi_2 ($X = \text{Ba}$ and Sr) were synthesized by the self-flux method. ARPES measurements were performed with micro-focused VUV synchrotron light at BL5U. Prior to the ARPES measurements, samples were cleaved in an ultrahigh vacuum.

Figure 1(a) shows the ARPES intensity near E_F measured along a momentum (k) cut crossing the Γ point. One can see linearly dispersive bulk valence band (VB) which crosses E_F . To search for a possible band touching of VB and conduction band (CB) predicted in the calculation, we deposited K atoms onto the surface in an ultrahigh vacuum. One can clearly see in Fig. 1(b) that the hole bands in K-deposited BaMg_2Bi_2 are shifted downward due to the electron doping to the surface. Intriguingly, VB in the negative k region appears to almost continuously disperse across $k = 0$ and cross E_F at positive k , without losing its intensity at $k = 0$, indicative of the formation of Dirac-cone dispersion. In contrast to the case of K-deposited BaMg_2Bi_2 , the spectral weight

associated with the CB is absent and no Fermi-edge cut-off is observed in K-deposited SrMg_2Bi_2 [Fig. 1(c)]. This observation demonstrates that an intrinsic band gap opens in SrMg_2Bi_2 , suggesting the occurrence of topological phase transition from the TDS state to the ordinary insulator phase upon replacing Ba with Sr [Fig. 1(d)].

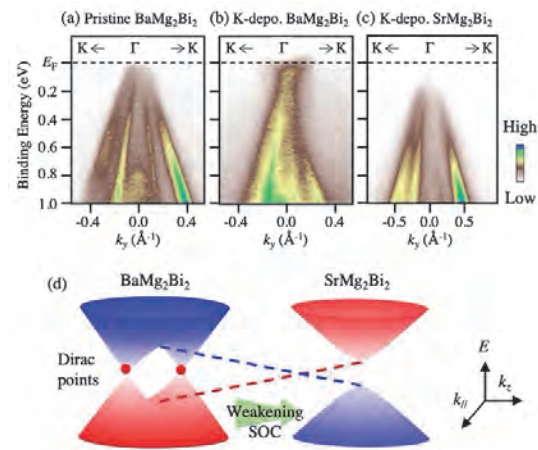


Fig. 1. (a)-(c) ARPES intensity plot near E_F in BaMg_2Bi_2 , K-dosed BaMg_2Bi_2 , and K-dosed SrMg_2Bi_2 . (d) Schematic band diagram of XMg_2Bi_2 .

[1] D. Takane *et al.*, Sci. Rep. **11** (2021) 21937.

BL5U

Band-structure Reconstruction of $\text{Ca}_3\text{Ru}_2\text{O}_7$ Induced by K Adsorption

M. Horio^{1,2}, T. Wada¹, V. Granata³, R. Fittipaldi³, A. Vecchione³, K. Tanaka⁴,
I. Matsuda¹ and J. Chang²

¹Institute for Solid State Physics, The University of Tokyo, Kashiwa 277-8581, Japan

²Physik-Institut, Universität Zürich, Winterthurerstrasse 190, CH-8057 Zürich, Switzerland

³CNR-SPIN, I-84084 Fisciano, Salerno, Italy

⁴UVSOR Synchrotron Facility, Institute for Molecular Science, Okazaki 444-8585, Japan

Application of external perturbations to Mott insulators often leads to dramatic changes in the electronic structure. For example, the Mott insulator Ca_2RuO_4 can be metallized by chemical substitutions [1,2], physical pressure [3], and electric current [4]. Changing the number of the RuO_2 layer in the unit cell from one (Ca_2RuO_4) to two ($\text{Ca}_3\text{Ru}_2\text{O}_7$), the system can also become metallic down to low temperatures [5]. Instead, $\text{Ca}_3\text{Ru}_2\text{O}_7$ exhibit a first-order phase transition at $T = 48$ K that involves lattice and spin degrees of freedom [6]. At 48 K, antiferromagnetically ordered spins change their orientation from the a to b crystalline axis and the lattice undergoes slight compression along the c axis. This phase transition makes a significant influence on the transport properties such as resistivity, Hall effect, and Seebeck effect [7], suggesting dramatic changes in the band structure near the Fermi level. Indeed, our recent angle-resolved photoemission spectroscopy (ARPES) study [8] has revealed a clear band-structure reconstruction into a Dirac-semimetallic state upon cooling across 48 K.

Recently, alkali-metal adsorption is being recognized as an efficient way to dope a solid surface with electrons. This methodology has been applied to Mott insulators such as iridates [9] and cuprates [10] and the occurrence of metal-insulator transition has successfully been demonstrated through *in-situ* ARPES measurements. With this technique, electrons can be doped at the surface even in the case where bulk electron doping by chemical substitutions is impossible. $\text{Ca}_3\text{Ru}_2\text{O}_7$ is one such case where electron doping has never been realized.

We have dosed K on $\text{Ca}_3\text{Ru}_2\text{O}_7$ and carried out ARPES measurements at BL5U at $T = 10$ K. Figure 1 shows energy distribution curves in a wide energy range. As K is adsorbed on the surface, a peak at the binding energy of ~ 1.7 eV, which is a remnant of the lower Hubbard band, loses its intensity and instead a spectral weight accumulates at the Fermi level. This spectral-weight re-distribution suggests that the electronic state changes away from the Mott insulating state. The change is even more clearly seen in the ARPES spectra in Fig. 2. Notably, the hole-like dispersion around the Γ point expands, which is opposite to what is expected from electron doping. It is therefore likely that the effect of adsorbed K atoms goes beyond simple electron doping to cause the observed band structure reconstruction.

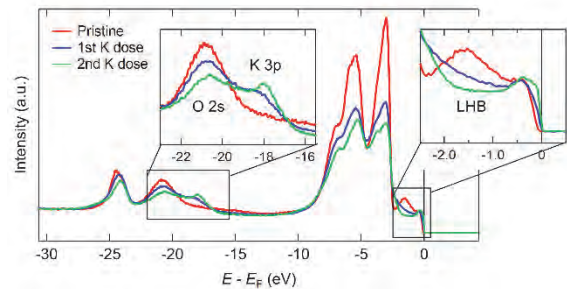


Fig. 1. Energy distribution curves recorded with varying the K deposition level.

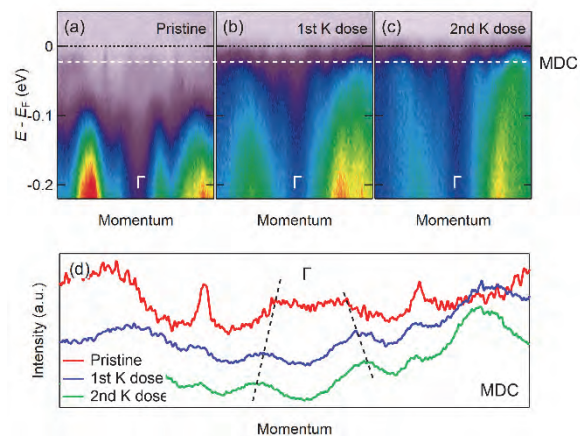


Fig. 2. Electronic structure change in $\text{Ca}_3\text{Ru}_2\text{O}_7$ by K adsorption. (a)-(c) ARPES spectra of pristine and K-dosed $\text{Ca}_3\text{Ru}_2\text{O}_7$. (d) Momentum distribution curves (MDCs) at $E - E_F = -0.02$ eV.

- [1] S. Nakatsuji and Y. Maeno, Phys. Rev. Lett. **84** (2000) 2666.
- [2] H. Fukazawa and Y. Maeno, J. Phys. Soc. Jpn. **70** (2001) 460.
- [3] S. Ricco *et al.*, Nat. Commun. **9** (2018) 4535.
- [4] R. Okazaki *et al.*, J. Phys. Soc. Jpn. **82** (2013) 103702.
- [5] Y. Yoshida *et al.*, Phys. Rev. B **69** (2004) 220411(R).
- [6] Y. Yoshida *et al.*, Phys. Rev. B **72** (2005) 054412.
- [7] H. Xing *et al.*, Phys. Rev. B **97** (2018) 041113(R).
- [8] M. Horio *et al.*, npj Quantum Mater. **6** (2021) 29.
- [9] Y. K. Kim *et al.*, Science **345** (2014) 187.
- [10] C. Hu *et al.*, Nat. Commun. **12** (2021) 1356.

BL5U

Quadrupole Electronic Structure in Mn_{3-x}Ga Studied by Angle-resolved Photoemission Spectroscopy

J. Okabayashi¹, Y. Miura², K. Tanaka³, K. Z. Suzuki⁴ and S. Mizukami⁴

¹Research Center for Spectrochemistry, The University of Tokyo, Tokyo 113-0033, Japan

²National Institute for Materials Science (NIMS), Tsukuba 305-0047, Japan

³UVSOR Synchrotron Facility, Institute for Molecular Science, Okazaki 444-8585

⁴WPI Advanced Institute for Materials Research, Tohoku University, Sendai 980-8579, Japan

Magnetic ordered alloys have attracted significant attention for use as spintronics materials because they are highly likely to exhibit perpendicular magnetic anisotropy (PMA). Tetragonal Mn_{3-x}Ga alloys are widely recognized as hard magnets which exhibit highly anisotropic, ferrimagnetic, and metallic properties [1]. We have investigated the mechanism of PMA and large coercive fields in Mn_{3-x}Ga by x-ray magnetic circular and linear dichroisms (XMCD /XMLD) [2]. The origin of PMA in Mn_{3-x}Ga alloys can be explained by the quadrupole contribution along the z -axis by the charge asphericity. The specific crystalline structures provide the elongated c -axis direction, which induces the anisotropic chemical bonding, resulting in the anisotropy of electron occupancies in $3d$ states and charge distribution. However, orbital magnetic moments in the Mn sites are almost quenched because of half-filled occupation.

Although the site-specific charge distributions can be accessed by x-ray absorption spectroscopies, the origin of quadrupole-induced PMA from the viewpoint of the band structures in Mn_{3-x}Ga alloys is not fully understood. Here, we employ the angle-resolved photoemission spectroscopy (ARPES) to unveil the anisotropic band structures in Mn_{3-x}Ga by the comparison with the density-functional theory (DFT) calculations.

30-nm-thick Mn_{3-x}Ga samples were prepared on MgO (001) substrate using sputtering technique. On the surface of Mn_{3-x}Ga layer, Mg and MgO capping layers were deposited. The MgO layer was removed by Ar-ion sputtering and the Mg layer was removed by annealing just before the ARPES measurements. We construct the method to remove the Mg layer which does not react chemically with Mn atoms at the interface. Clear low-energy electron diffraction (LEED) patterns were also obtained.

ARPES was performed at BL5U, UVSOR, where the photoemission chamber is connected to the sample preparation chamber. The measurement conditions were set at 15 meV energy resolution and 10 K. Linear polarized beams of s - and p -polarization were used to detect the orbital symmetry. We employ the photon energy ranges of 60 – 80 eV to enhance the Fe $3d$ photo-ionization cross section, where the Γ -X(M) line is scanned by the angular mode of $\pm 15^\circ$.

Figure 1 shows the Fermi surface mapping taken at photon energy of 80 eV. Four-fold symmetric lines are detected, which is consistent with the LEED patterns.

High intensity spots appear at both Γ and X points. Nodal lines are also developed from each symmetric point. Energy-momentum (E - k) dispersion curves also exhibit the intensities at Γ and X points with the dispersive bands. These bands are comparable with the DFT calculation. The band from the Γ point has a character of yz orbital, which can be detected by the s -polarized beam in vertical geometry.

We discuss the quadrupole formation. In the DFT calculation, the virtual spin-flip transitions from occupied up-spin yz to down-spin z^2 orbitals correspond to the finite matrix element to the PMA in the perturbation. Therefore, occupied yz orbitals detected by ARPES contribute to spin-flipped yz - z^2 oblate quadrupole charge distribution, resulting in the PMA. Our finding explains the origin of PMA in Mn_{3-x}Ga comes from not orbital moment anisotropy but elongated charge distribution through the spin-flipped transition in specific orbitals, whose results are also supported by XMCD and XMLD.

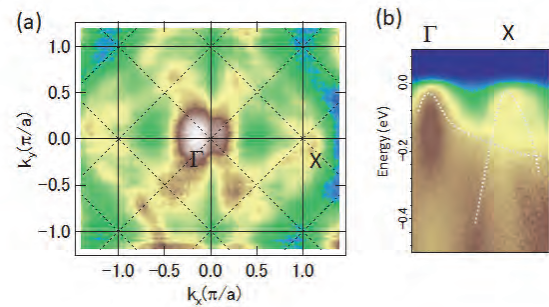


Fig. 1. ARPES images of Mn_3Ga taken at $h\nu=80$ eV using s -polarized beam. (a) The k_x - k_y mapping. (b) Band dispersions along Γ -X direction in primitive Brillouin zone. Dot curves in (b) show the results of DFT calculation.

[1] S. Mizukami *et al.*, *Scr. Mater.* **118** (2016) 70.

[2] J. Okabayashi *et al.*, *Sci. Rep.* **10** (2020) 9744.

BL5U

Change of the Fermi Surface of $\text{Bi}_2\text{Sr}_2\text{CaCu}_2\text{O}_{8+\delta}$ Observed by ARPES

Y. Tsubota¹, S. Kumar², Y. Miyai², K. Tanaka³, S. Ishida⁴, H. Eisaki⁴, S. Nakagawa⁵,
T. Kashiwagi⁵, M. Arita², K. Shimada² and S. Ideta²

¹Department of Physics, School of Science, Hiroshima University, Higashi-Hiroshima 739-0046, Japan

²Hiroshima Synchrotron Radiation Center, Hiroshima University, Higashi-Hiroshima 739-0046, Japan

³UVSOR Synchrotron Facility, Institute for Molecular Science, Okazaki 444-8585, Japan

⁴National Institute of Advanced Industrial Science and Technology, Tsukuba 305-8560, Japan

⁵Division of Material Science, Tsukuba University, Tsukuba 305-8577, Japan

It has been known that the cuprate superconductors show a high superconducting (SC) transition temperature (T_c) and exotic physical properties, on the other hand, the SC mechanism has been unclear yet. In order to understand the mechanism of high- T_c cuprates, $\text{Bi}_2\text{Sr}_2\text{CaCu}_2\text{O}_{8+\delta}$ (Bi2212) is one of the promising candidates to study the electronic structure and reveal the physical properties. Bi2212 has two CuO_2 planes in the unit cell and shows the high T_c around 95 K at the optimally doped sample. Superconductivity occurs upon hole doping into the CuO_2 plane and the amount of hole doping can control T_c , and therefore, carrier doping (hole/electron concentration) plays an important key parameter in cuprates [1,2]. According to the previous report, we consider that differences of the electronic states in Bi2212 depending on the sample with several compositions might exist, even though samples are expected to be the same hole concentration, where the optimally doped sample shows the maximum T_c ($T_{c,\text{max}}$); however, the compositions are different, which shows a different $T_{c,\text{max}}$ [1,2]. Therefore, in the present study, we have performed an angle-resolved photoemission spectroscopy (ARPES) measurements to study the Fermi surface changes of Bi2212 due to differences in sample compositions.

We have demonstrated ARPES measurements to investigate the electric structure on wide momentum space for Bi2212 with two compositions. ARPES experiments were carried out at BL5U and we measured two optimally doped samples: $\text{Bi}_{2.3}\text{Sr}_{1.7}\text{CaCu}_2\text{O}_{8+\delta}$ ($T_c \sim 85$ K) and $\text{Bi}_{2.1-x}\text{Pb}_x\text{Sr}_2\text{CaCu}_2\text{O}_{8+\delta}$ ($x = 0.66$, $T_c \sim 95$ K) in the SC and the normal states. High quality single crystals of Bi2212 were cleaved *in-situ* in the ultrahigh vacuum $\sim 4 \times 10^{-9}$ Pa.

Figures 1(a) and 1(b) show the Fermi surfaces taken at $h\nu = 60$ eV and $T = 30$ K in the SC state for $\text{Bi}_{2.3}\text{Sr}_{1.7}\text{CaCu}_2\text{O}_{8+\delta}$ and $\text{Bi}_{2.1-x}\text{Pb}_x\text{Sr}_2\text{CaCu}_2\text{O}_{8+\delta}$ ($x = 0.66$), respectively. Fermi surfaces are clearly observed in wide momentum space for both samples. In Fig. 1(a), in addition to the main Fermi surfaces as shown by a red arrow at -0.4 \AA^{-1} in momentum space on the horizontal axis, the spectrum at -0.2 \AA^{-1} in momentum space is observed, indicating that the modulation from the BiO layer, so called replicas, is observed as shown by a blue arrow. If replicas are observed in the ARPES results, we cannot understand the electric structure precisely in momentum space because the main and replica bands

are overlapped. Figure 1(b) shows Fermi surfaces of $\text{Bi}_{2.1-x}\text{Pb}_x\text{Sr}_2\text{CaCu}_2\text{O}_{8+\delta}$ ($x = 0.66$). Substitution of the Bi site with Pb suppresses the modulated structure from the BiO layer and as a result, the replica is strongly suppressed. In Fig 1(b), the replicas on Fermi surfaces are well suppressed and the main bands are dominantly observed.

We have analyzed the ARPES spectra around the nodal region for each sample and determined the Fermi momentum (k_F) for each Fermi surface by fitting of momentum-distribution curves (MDCs) with a Lorentzian. The k_F 's are plotted as shown by red dots (Fig. 1). As a result, we have found that two samples with different compositions show that the distance between two nodal points has a different value. This means that the Fermi surface might change due to differences in sample compositions. As a future work, we will demonstrate ARPES experiments in a different composition and doping level.

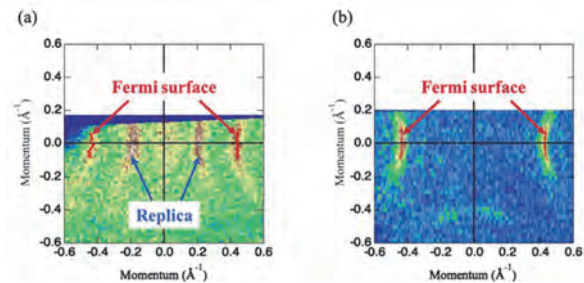


Fig. 1. Electronic structure of Bi2212. (a) Fermi surfaces of $\text{Bi}_{2.3}\text{Sr}_{1.7}\text{CaCu}_2\text{O}_{8+\delta}$ in the superconducting state (30 K). (b) Fermi surfaces of $\text{Bi}_{2.1-x}\text{Pb}_x\text{Sr}_2\text{CaCu}_2\text{O}_{8+\delta}$ ($x = 0.66$) in the superconducting state (30 K). Main Fermi surfaces are shown by a red arrow. Red dots are the Fermi momentum estimated from the MDC peak near the Fermi level.

[1] J. L. Tallon *et al.*, Phys. Rev. B **51** (1995) 12911.

[2] I. M. Vishik *et al*, Proc. Nat. Acad. Sci. **6** (2012) 18332.

BL5U

CDW-induced Electronic Reconstruction in a Kagome Metal KV_3Sb_5

T. Kato¹, K. Nakayama^{1,2}, T. Kawakami¹, A. Moriya¹, Yongkai Li^{3,4}, Z. Wang^{3,4}, S. Ideta^{5,6},
K. Tanaka^{5,6}, T. Takahashi^{1,7,8}, Y. Yao^{3,4} and T. Sato^{1,6,7}

¹Department of Physics, Graduate School of Science, Tohoku University, Sendai 980-8578, Japan

²Precursory Research for Embryonic Science and Technology (PRESTO), Japan Science and Technology Agency (JST), Tokyo 102-0076, Japan

³Centre for Quantum Physics, Key Laboratory of Advanced Optoelectronic Quantum Architecture and Measurement (MOE), School of Physics, Beijing Institute of Technology, Beijing 100081, China

⁴Beijing Key Lab of Nanophotonics and Ultrafine Optoelectronic Systems, Beijing Institute of Technology, Beijing 100081, China

⁵UVSOR Synchrotron Facility, Institute for Molecular Science, Okazaki 444-8585, Japan

⁶School of Physical Sciences, The Graduate University for Advanced Studies (SOKENDAI), Okazaki 444-8585, Japan

⁷Center for Spintronics Research Network, Tohoku University, Sendai 980-8577, Japan

⁸Advanced Institute for Materials Research (WPI-AIMR), Tohoku University, Sendai 980-8577, Japan

Recently, a new kagome-lattice material AV_3Sb_5 ($A = K, Rb, \text{ and } Cs$) has been discovered. AV_3Sb_5 undergoes a charge-density wave (CDW) transition below $T_{CDW} = 78\text{-}103$ K, accompanied by the in-plane unit-cell doubling with the 2×2 periodicity. This CDW state shows an intriguing entanglement with the superconductivity (transition temperature T_c of 0.9-2.5 K) and non-trivial topological surface states. Also, exotic properties, e.g., strong anomalous Hall effect and possible time-reversal symmetry breaking have been reported, highlighting the unconventional nature of CDW.

Despite intensive studies, the origin of CDW in AV_3Sb_5 is highly controversial. In particular, the type of structural distortion responsible for the CDW has yet to be clarified. First-principles calculations proposed two types of distortions sharing the same space group to account for the in-plane 2×2 periodicity. One is the ‘‘Star-of-David’’ (SoD) distortion of V atoms. The other is an inverse type of the SoD distortion, where V atoms show an opposite displacement compared with the SoD case, resulting in a periodic arrangement of triangular and hexagonal patterns, called ‘‘Tri-Hexagonal’’ structure. It is experimentally highly controversial which distortion actually takes place.

To gain insight into the origin of CDW from the electronic structure perspective, we have performed high energy and spatial resolution ARPES of KV_3Sb_5 by using a micro-focused beam at BL5U in UVSOR [1].

Figure 1 shows a side-by-side comparison of the ARPES intensity plots along the M-M cut measured in the normal and CDW states (left and right panels, respectively). In the normal state, one can see a strong intensity near the Fermi level (E_F) at the M point, together with a hole-like dispersion topped at slightly below E_F at the M point. One can recognize an obvious difference in the intensity distribution in the CDW phase. A new shallow holelike bands crossing E_F appear at the middle of the two M points, as also identified from the momentum distribution curve at E_F (white curves shown in the inset; folded bands are

highlight by white triangles). This indicates the CDW-induced band folding. A comparison of the observed electronic reconstruction with the band structure calculations assuming SoD/TrH structural distortion would help to clarify the origin of CDW.

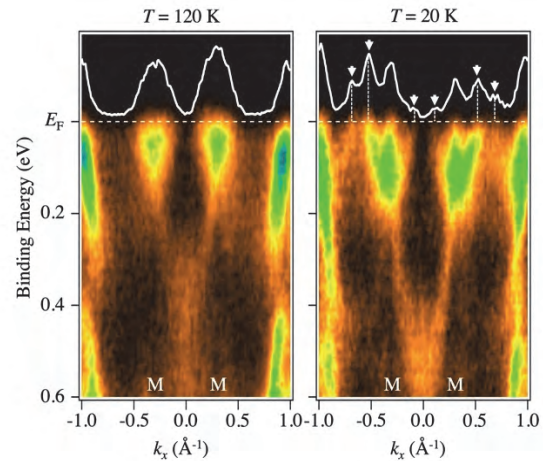


Fig. 1. ARPES intensity measured along the M-M cut at $T = 120$ K (left) and 20 K (right), respectively. White curve in the inset shows the MDC at E_F .

[1] T. Kato *et al.*, submitted.

BL5U

Electronic Structure of VNb_3S_6 : a Transition-metal Intercalated NbS_2

M. Horio¹, T. Wada¹, S. Okazaki², K. Tanaka³, T. Sasagawa² and I. Matsuda¹

¹*Institute for Solid State Physics, The University of Tokyo, Kashiwa 277-8581, Japan*

²*Materials and Structures Laboratory, Tokyo Institute of Technology, Yokohama 226-8503, Japan*

³*UVSOR Synchrotron Facility, Institute for Molecular Science, Okazaki 444-8585, Japan*

Transition-metal dichalcogenides MX_2 host a rich variety of physical phenomena such as superconductivity [1] and charge density wave [2], and thus have attracted intense interest for decades. In 1970-1980's, there have been extensive attempts to modulate its electronic structure by intercalation of 3d transition metals T [3]. Thus made TM_3X_6 takes crystal structure with broken inversion symmetry and shows various types of magnetic order depending on the intercalated 3d transition metal. Out of these, CrNb_3S_6 has been most intensively studied because of the special type of magnetic order called chiral soliton lattice.

In Recent years, due to the breaking of both the inversion and time-reversal symmetry, TM_3X_6 is attracting interest from a topological perspective. Especially, VNb_3S_6 , which shows a ferromagnetic order below $T_C \sim 44$ K, has been theoretically predicted to possess a magnetically induced Weyl point. Indeed, a recent study has demonstrated large anomalous Hall conductivity potentially associated with the proposed Weyl point [4]. While there recently appears increasing number of ARPES reports made for CrNb_3S_6 [5,6], MnNb_3S_6 [7], FeNb_3S_6 [8], CoNb_3S_6 [8-10], and NiNb_3S_6 [7,8], to the best of our knowledge there have been no such studies on VNb_3S_6 . We therefore attempted an ARPES measurement to reveal the low-energy electronic structure of VNb_3S_6 .

Single crystals of VNb_3S_6 were grown by the chemical vapor transport method from polycrystals with iodine as the transport agent. ARPES measurements were performed at BL5U of UVSOR at temperatures ranging from 10 to 200 K.

Figures 1(a) and (b) show the Fermi surface and band dispersions through the Brillouin-zone center of VNb_3S_6 , respectively, recorded at 10 K. From these, three hole-like Fermi surface sheets centered around the zone center can be clearly identified. This result is distinct from the observations for the antiferromagnets FeNb_3S_6 , CoNb_3S_6 , and NiNb_3S_6 [7-10], where there is only single Fermi surface. Instead, the Fermi surface structure resembles what was reported for the ferromagnet CrNb_3S_6 [5,6]. In the case of CrNb_3S_6 , from temperature dependent systematic APRES measurements across T_C [6], the emergence of multiple Fermi surface sheets has been ascribed to the effect of ferromagnetism. In contrast, as for VNb_3S_6 , the band structure is remarkably robust against temperature variations up to 200 K (Fig. 1), far above $T_C \sim 44$ K. Therefore, the peculiar band structure is likely not rooted in magnetism. Comparisons with first-principles band structure calculations both in the magnetic and non-magnetic states would pave the way to understanding the origin of these observations.

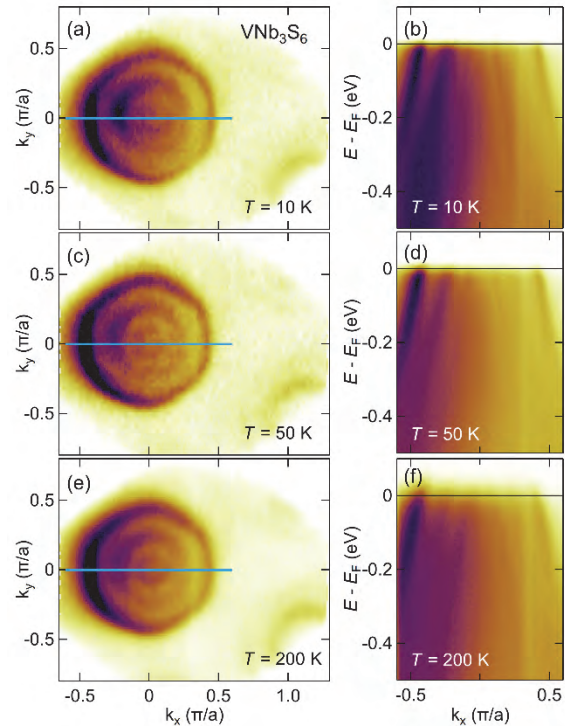


Fig. 1. ARPES results of VNb_3S_6 . (a),(b) Fermi surface and band dispersions, respectively, measured at 10 K. The momentum cut for (b) is indicated in (a). (c),(d) The same plots at 50 K. (e),(f) The same plots at 200 K.

- [1] T. Yokoya *et al.*, *Science* **294** (2001) 2518.
- [2] J. Wilson *et al.*, *Adv. Phys.* **24** (1975) 117.
- [3] S.S.P. Parkin *et al.*, *Philos. Mag. B* **41** (1980) 65.
- [4] S. Okazaki *et al.*, *JPS annual meeting* (2021).
- [5] N. Sirica *et al.*, *Phys. Rev. B* **94** (2016) 075141.
- [6] N. Sirica *et al.*, *Commun. Phys.* **3** (2020) 65.
- [7] C. Battaglia *et al.*, *Eur. Phys. J. B* **57** (2007) 385.
- [8] H. Tanaka *et al.*, *Phys. Rev. B* **105** (2022) L121102.
- [9] X. P. Yang *et al.*, *Phys. Rev. B* **105** (2022) L121107.
- [10] P. Popčević *et al.*, arXiv:2111.12529

BL5U

Angle-resolved Photoemission Study of Zr_3SnC_2

 T. Ito^{1,2}, M. Mita², D. Pinek³, M. Nakatake⁴, K. Tanaka^{5,6} and T. Ouisse³
¹Nagoya University Synchrotron radiation Research center (NUSR), Nagoya University, Nagoya 464-8603, Japan

²Graduate School of Engineering, Nagoya University, Nagoya 464-8603, Japan

³Grenoble Alpes, CNRS, Grenoble INP, LMGP, F-38000 Grenoble, France

⁴Aichi Synchrotron Research Center, Seto 489-0965, Japan

⁵UVSOR Synchrotron Facility, Institute for Molecular Science, Okazaki 444-8585, Japan

⁶The Graduate University for Advanced Studies (SOKENDAI), Okazaki 444-8585, Japan

MAX phase compounds, i.e., $M_{n+1}AX_n$ where M is a transition metal, A belongs to groups 13-16 and X is the C or N element, have recently been attracted much attention due to their possible application for new class of two-dimensional systems called MXenes by removing A atoms [1]. Zr_3SnC_2 is so called 312 MAX phase in which Zr_3C_2 layers separated by Sn layer, then two dimensionality becomes higher than 211 phase. In addition, relatively stronger spin-orbit interaction of Zr and Sn 4d is expected to affect its physical properties. In this study, we have performed angle-resolved photoemission spectroscopy (ARPES) on MAX phase compound Zr_3SnC_2 to directly investigate the electronic structure of this system.

ARPES measurements were performed at the UVSOR-III BL5U. Data were acquired at $T = 30$ K with $h\nu = 82$ eV which enables us to trace around the Γ KM plane with inner potential of $V_0 = 17.7$ eV estimated from the photon energy dependent measurement (not shown).

Figure 1 shows the obtained Fermi surface (FS) image on the Γ KM plane of Zr_3SnC_2 . Along the Γ M and Γ KM high-symmetry lines (orange lines), we have extracted the band structure image as shown in Fig. 2. We have found that the electronic structure near the Fermi level (E_F) consists of two hole-pockets around Γ point and relatively intense dispersive feature just below E_F around M point. While the former seems to be similar with DFT calculation, the latter feature has appeared in the blank of bulk DFT bands around the M(L) point. Therefore, we assigned the dispersive feature around the M(L) point to be surface state. From the band structure near E_F (Fig. 3(a)), the observed surface state was formed by characteristic saddle-like dispersive feature (Fig. 3(b)), in which the saddle-point locates around 150 meV at the M(L) point. From the saddle-like dispersion, it has been expected that the narrow dispersive feature along MK line forms pair of triangular FS around M point, which has been clearly observed in Fig.1. To clarify the essential role of the surface states, further studies with using liner/circular polarization and spin-resolved ARPES are intended.

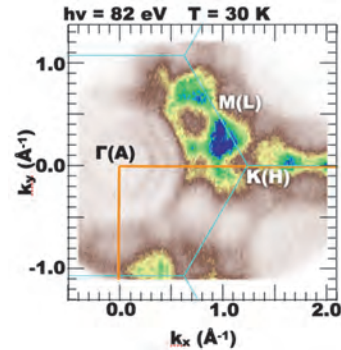


Fig. 1. Fermi surface image of Zr_3SnC_2 . Orange thick lines indicate the high-symmetry lines on which the ARPES image has been extracted in Fig. 2.

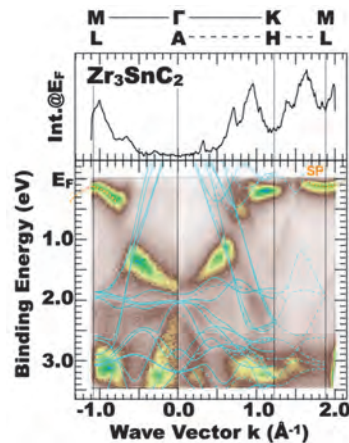


Fig. 2. Band structure (lower panel) and MDC spectra at E_F (upper panel) along Γ M and Γ KM lines of Zr_3SnC_2 . Blue solid and dashed lines are DFT calculation along the MΓK and AHL lines, respectively.

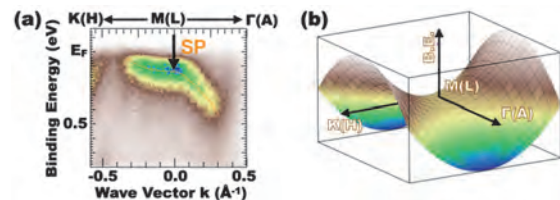


Fig. 3. (a) Band structure near E_F around M point of Zr_3SnC_2 . (b) Example of saddle-like dispersive feature, in which M point corresponds to the saddle point.

[1] M. Basoum, MAX phases (Wiley, Weinheim 2013).

BL5U

Fermi Surface Measurements of TiSe₂ with the CDW Transition

 S. Tanaka¹, K. Ueno² and K. Tanaka³
¹*Sanken, The Institute of Industrial and Scientific Research, Osaka University, Ibaraki 567-0047, Japan.*
²*Graduate School of Science and Engineering Saitama University, Saitama 338-8570, Japan.*
³*UVSOR Synchrotron Facility, Institute for Molecular Science, Okazaki 444-8585, Japan.*

Transition metal dichalcogenides (TMDs) are a class of materials attracting high scientific interest in recent years. They are layered materials where the interlayer distance is considerably larger than the intralayer atomic distance yielding a quasi-two dimensional character. Charge density wave (CDW) transition, which is a transition accompanying a periodical superlattice formation below the transition temperature, is one of the typical phenomena of the low-dimensional system, and has been attracted many researchers. Among TMDCs, (1T-)TiSe₂ exhibits very unique character; its CDW transition provides the $2a \times 2b \times 2c$ superlattice formation where the interlayer periodic distortion occurs. Although several studies, including ARPES studies, have been made for revealing the driving force of the CDW transition in TiSe₂, rather few were made for investigating the interlayer interaction. In this work, we investigate the change in the Fermi surface of TiSe₂ along the interlayer axis due to the CDW transition by measuring the photon-energy dependent ARPES.

The experiments were carried out at BL5U of UVSOR. The temperature of the cleaving/measurements of single-crystalline TiSe₂ were 300K and 10K, which are respectively above and below the CDW transition-temperature (about 200K). The (lateral) CDW formation at 10K was examined by the folding of the valence band from Γ (A) point to M(L) point in the ARPES spectrum. Figure 1 show intensity maps of the photoelectron at the Fermi level, demonstrating the Fermi surface along the Γ -M(A-L) plane. The horizontal axis is along the Γ -M(A-L) line derived from the angular distribution of the photoelectron, and the vertical axis is along the inter-layer axis (k_z) derived from the photon-energy dependent measurements. For deriving value of k_z , the free-electron final state is assumed, and 13.5eV is used as the inner potential after the reference[1].

At 300K [Fig. 1(a)], the Fermi surface of the electron-pocket near the M(L) point shows a tilted elliptical shape. This structure is periodic (except the variation of the intensity) along the k_z axis with a $2\pi/c$ distance which is the periodicity of the inverse lattice. This is consistent with the DFT calculation (not shown here). When the CDW transition occurs at 10K, meanwhile, the periodicity of the Fermi surface along the k_z axis shrieks as half of that at 300K [Fig. 1(b)]. It is due to the superlattice formation whose lattice constant along the inter-layer axis $c^* = 2 \times c$. It is a very clear evidence of the CDW transition of TiSe₂ accompanies the periodic interlayer distortion. Further

studies for investigating the driving force of the interlayer CDW transition in TiSe₂ is under progress with a help of the DFT calculation.

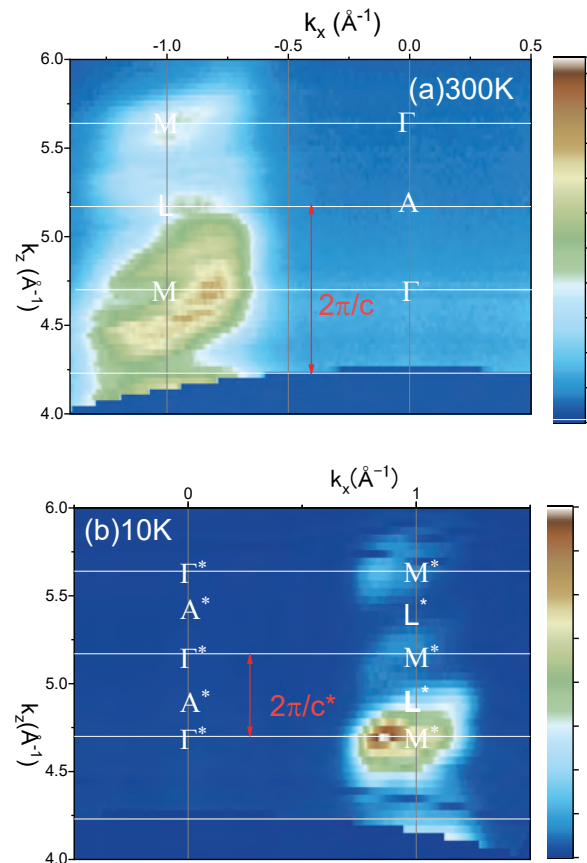


Fig. 1. Intensity maps of the photoelectron at the Fermi level of TiSe₂. The horizontal axis is along the Γ -M(A-L) line derived from the angular distribution of the photoelectron, and the vertical axis is along k_z axis derived from the photon-energy dependent measurements. The sample temperature is 300K (a) and 10K (b).

[1] M. D. Watson *et al.*, Phys. Rev Lett. **122** (2019) 076404.

BL5U

Temperature Dependence of Electronic Structure in Pb-doped La(O,F)BiS₂ Superconductor

 N. Kataoka¹, L. Y. Jun¹, T. Setoguchi¹, S. Demura² and T. Yokoya^{1,3}
¹Graduate School of Natural Science and Technology, Okayama University, Okayama 700-8530, Japan

²Nihon University, Tokyo 102-8275, Japan

³Research Institute for Interdisciplinary Science, Okayama University, Okayama 700-8530, Japan

BiCh₂ compounds are quasi-two-dimensional materials with a layered structure typically represented by the composition of REO_{1-x}F_xBiCh₂ (RE=rare earth; Ch=S, Se). It can be doped electrons by replacing oxygen with fluorine atoms, and electron-doped samples exhibit superconductivity below 2-10 K. Several experimental and theoretical studies have indicated the possibility of unconventional superconducting mechanisms [1]. Since the superconducting transition temperature is sensitive to the pressure applied to the BiCh₂ planes, the effects of many elemental substitutions have been intensively studied [1-2]. Elemental substitution effects are important for understanding the superconducting mechanism, although there are few reports on the electronic structure. Pb-doped La(O,F)BiS₂ shows an anomalous behavior with a sharp decrease in electrical resistance around 100 K, but the origin of this behavior is unknown [2]. In this study, we performed temperature-dependent angle-resolved photoemission spectroscopy (ARPES) measurements of Pb-doped La(O,F)BiS₂ above and below the temperature at which an anomaly in electrical resistance appears in order to investigate the cause of the anomalous electrical resistance.

The measurements were performed using the LaO_{0.5}F_{0.5}Bi_{0.9}Pb_{0.1}S₂ single crystals synthesized by the flux method [2]. The temperature at which the anomaly appears is estimated to be about 100 K from the temperature dependence of the electrical resistance. ARPES measurements were performed at BL5U of UVSOR III. We used the 70 eV photons, and the energy resolution was 35 meV. All samples were cleaved in situ on the (001) plane in an ultrahigh vacuum of less than 5.0×10⁻⁹ Pa. The temperature dependence of the electronic structure was measured in the range of 50-150 K.

Figure 1 shows the Fermi surface mapping from the ARPES intensity between ±25 meV of the Fermi energy (E_F) measured at 70 K and 150 K. Figure 2 shows the angle-integrated energy distribution curves (EDCs) in the X-M and Γ -X directions measured at 70 K and 150 K. The Fermi surface shape was found to be in good agreement with the previously reported La(O,F)BiS₂ (F concentration = 0.5) [3], with no significant difference in the Fermi surface shape at 70 K and 150 K, respectively. On the other hand, the EDC intensity in the X-M and Γ -X directions at 70 K decreased from E_F to around 0.2 eV and increased around 0.3-0.6 eV, compared to those at 150 K. Reproducibility of the results were checked for several

samples. Therefore, this EDC change is considered to be a change in the electronic structure due to an anomaly in the electrical resistance.

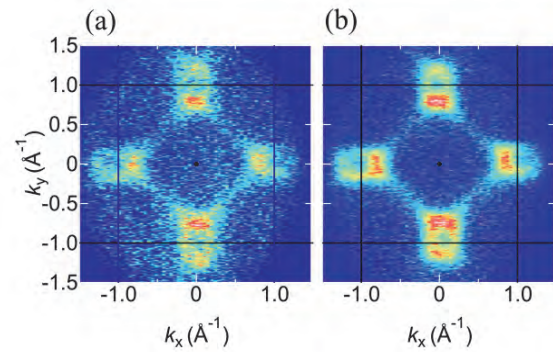


Fig. 1 Temperature dependent Fermi Surfaces map of LaO_{0.5}F_{0.5}Bi_{0.9}Pb_{0.1}S₂ at (a) 70 K and (b) 150K.

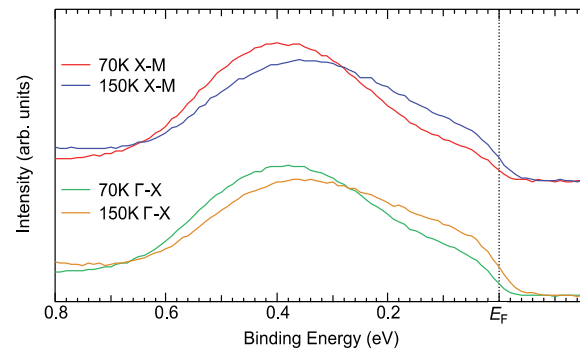


Fig. 2 Angle-integrated EDCs in each direction (top: X-M, bottom: Γ -X). Spectral intensities were normalized by area intensity in the range $E_B = -0.1 \sim 0.8$ eV. The angles are integrated about $\pm 6^\circ$ around the X point.

- [1] Y. Mizuguchi J. Phys. Soc. Jpn. **88** (2019) 041001.
 [2] S. Otsuki *et al.*, Solid State Commun. **270** (2018) 17.
 [3] K. Terashima *et al.*, Phys. Rev. B **90** (2014) 220512(R).

BL5U

Evaluation of Self-Energy in Overdoped Bi2201 by Angle-Resolved Photoemission Spectroscopy

Y. Miyai¹, Shiv Kumar², T. Kurosawa³, M. Oda⁴, S. Ideta² and K. Shimada²

¹Graduate School of Science, Hiroshima University, Higashi-Hiroshima 739-8526, Japan

²Hiroshima Synchrotron Radiation Center, Hiroshima University, Higashi-Hiroshima 739-8526, Japan

³Faculty of Science and Engineering, Muroran Institute of Technology, Muroran 050-8585, Japan

⁴Department of Physics, Hokkaido University, Sapporo 060-0809, Japan

High- T_c cuprate superconductors have attracted much interest since their discovery in 1986 for their high T_c as well as unusual physical properties such as bad metal states and formation of density waves [1, 2]. However, the high- T_c mechanism has not been fully understood yet, and therefore, it is necessary to study the physical properties from the microscopic point of view. Angle-resolved photoemission spectroscopy (ARPES) is one of the most effective and direct experimental methods to investigate the electronic structure in solids. ARPES spectra are related to the imaginary part of the one-particle Green's function and give the quasiparticle excitation spectrum. The one-particle Green's function includes the self-energy derived from the many-body interactions such as the electron-phonon, electron-electron, and electron-impurity interactions. By analyzing the ARPES spectral lineshape quantitatively, one can directly evaluate the magnitudes of each many-body interaction. The previous ARPES studies of cuprates have focused on the investigation of the electron-boson interaction at the vicinity of the Fermi level [3]. In the previous studies, the real part of the self-energy due to the electron-electron interaction was usually estimated by a line [4]. However, the energy dependence of the self-energy due to the electron-electron interaction is not trivial in the wide energy range. It is assumed to induce a so-called “waterfall” structure or a sudden spectral intensity suppression in the ARPES spectra [5]. To understand the mechanism of the high- T_c cuprate superconductivity, it is also important to quantify the magnitudes of the electron-electron interaction as well as electron-phonon(boson) interaction [3].

In this study, to quantitatively evaluate the electron-boson interaction and the electron-electron interaction simultaneously, we have performed a high-resolution ARPES study using synchrotron radiation on the Bi-based high- T_c cuprate $(\text{Bi,Pb})_2\text{Sr}_2\text{CuO}_{6+\delta}$ (Pb-Bi2201) in the wide momentum and energy ranges. We have selected overdoped Pb-Bi2201 with $T_c = 6\text{K}$ because it has a relatively simple electronic structure which allows us to precisely evaluate the self-energy in the normal state (*i.e.*, normal self-energy). While it has been expected that heavily hole-doped cuprates would behave as the 2D Fermi Liquid, ferromagnetic fluctuation has been found recently [6].

Figures 1(a) and 1(b) show ARPES intensity plots

taken at $h\nu = 60$ and 75 eV, respectively. Based on the lineshape analyses using the tight-binding model (here we only considered the x^2-y^2 band), we have evaluated the self-energy in the wide energy range. Figure 1(c) shows the simulation of the ARPES intensity plot using the evaluated self-energy. We clarified that the real part of the self-energy crosses the zero line at the energy of $E - E_F \sim -0.5$ eV and the imaginary part of self-energy has the maximum at that energy (Dashed line in Fig. 1). Because the imaginary part of the self-energy gives the spectral linewidth, the waterfall structure is caused by the suppression of the spectral intensity due to the significant broadening of the linewidth at $E - E_F \sim -0.5$ eV due to the electron-electron interaction. In order to further reproduce the spectral intensity, the matrix element and contribution from other bands at the bottom of the x^2-y^2 band is required.

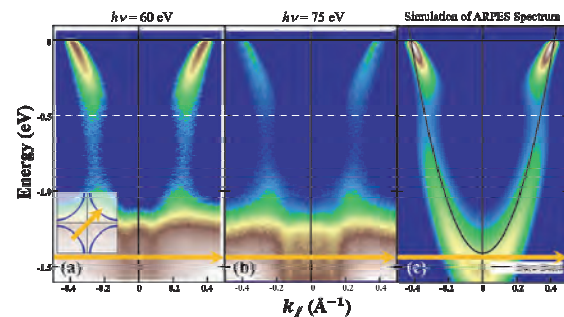


Fig. 1. Electronic structure of Pb-Bi2201. (a), (b) ARPES intensity plots taken at $h\nu = 60$ and 75 eV, respectively. (c) Simulated ARPES intensity plots using the evaluated self-energy. A solid black curve is the x^2-y^2 band in the tight binding model.

- [1] P. Choubey *et al.*, Proceedings of National Academy of Sciences. **117** (2020) 14805.
- [2] Y. Y. Peng *et al.*, Nature Materials. **17** (2018) 697.
- [3] I. M. Vishik *et al.*, Phys. Rev. Lett. **104** (2010) 207002.
- [4] H. Anzai *et al.*, Scientific Reports. **7** (2017) 4830.
- [5] D. S. Inosov *et al.*, Phys. Rev. Lett. **99** (2007) 237002.
- [6] K. Kurashima *et al.*, Phys. Rev. Lett. **121** (2018) 057002.

BL6U

Multi-atom Resonance Photoemission from the Valence Band of TiSe₂

S. Tanaka¹, K. Ueno², K. Fukutani³ and F. Matsui³¹Sanken, Osaka University, Ibaraki 567-0047, Japan²Graduate School of Science and Engineering Saitama University, Saitama 338-8570, Japan³UVSOR Synchrotron Facility, Institute for Molecular Science, Okazaki 444-8585, Japan

“Multi-atom resonant photoemission” (MARPE), which is an interatomic resonant photoelectron emission from neighboring atoms of the core-excited atoms, was reported first for the O1s photoelectron emission at the Mn-2p excitation edge in MnO [1], and attracted significant attention. In this report, we report the MARPE effect on, for the first time, the valence band in TiSe₂ analyzed with the momentum-resolved constant initial state (MR-CIS) spectroscopy using the “Momentum Microscope” apparatus recently installed at BL6U in UVSOR-III, IMS [2].

Figure 1(a) shows a CIS spectrum of TiSe₂ at the Ti-L₃ edge for the whole valence band (0-5.5 eV). The spectrum is well represented by two symmetric Lorentzian peaks. Meanwhile, in Fig. 1(b), the MR-CIS spectrum for a specific state [M-point at the binding energy of 2.0 eV; shown in Fig. 1(c)] is well reproduced by the sum of two Fano-shaped strongly asymmetric curves. According to our photon-energy dependent ARPES studies and DFT calculations (not shown here), this state is mainly provided by Se-4p, while most of the valence band is provided by Ti-3d. The symmetric shape in Fig. 1(a) indicates that the interference between the direct photoexcitation from Ti-3d and the intra-atomic Auger process does not occur since the former probability is so small at this photon energy range [3]. On the contrary, it is suggested that the probability of the photoemission from Se-4p is comparable to that of the inter-atomic Auger decay of Ti-2p core hole, and the interference yields the Fano-type asymmetric shape. It should be noted that the Fano parameter q is negative in the present case, contrary to the conventional resonant photoelectron emission. More work will be needed to reveal the physical origin of negative q .

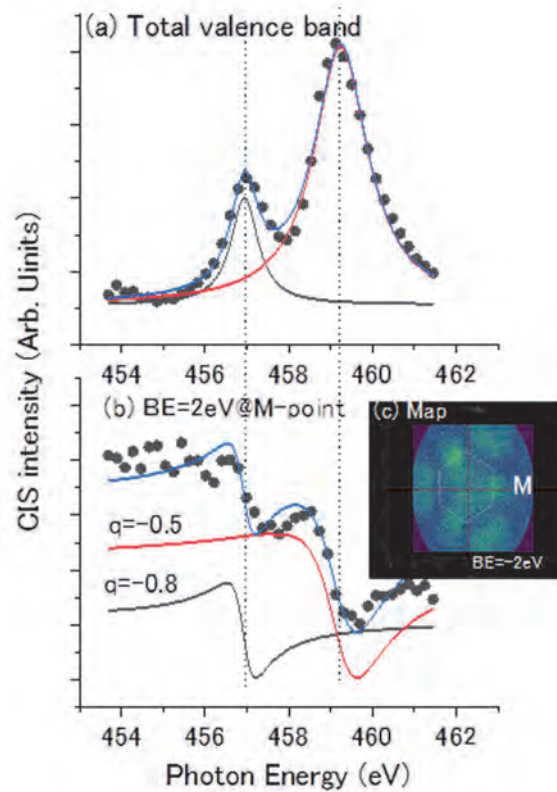


Fig. 1. (a) CIS spectrum for the whole valence band at the Ti-L₃ edge, (b) The MR-CIS spectrum at the specific states (M-points at the binding energy of 2.0 eV), which are shown as bright spots in the photoelectron intensity map (c), where the hexagon is the Brillouin zone of TiSe₂.

[1] A. Kay *et al.*, Science 281 (1998) 679; J. Electr. Spectrosc. Rel. Phenom. **114-116** (2001) 1179.

[2] F. Matsui *et al.* J. Phys. Soc. Jpn. **90** (2021) 124710.

[3] J. J. Yeh and I. Lindau, Atom. Data and Nucl. Dat

BL6U

Temperature-dependent Electronic Structure of η -Mo₄O₁₁ Revealed by Photoelectron Momentum Microscopy

 T. Kobayashi¹, E. Iwamoto², K. Sakamoto², F. Matsui³ and S. Suga⁴
¹Department of Material and Life Science, Osaka University, Suita 565-0871, Japan

²Department of Applied Physics, Osaka University, Suita 565-0871, Japan

³UVSOR Synchrotron Facility, Institute for Molecular Science, Okazaki 444-8585, Japan

⁴SANKEN, Osaka University, Ibaraki 567-0047, Japan

η -Mo₄O₁₁ is a pseudo two-dimensional material that consists of alternating layers of octahedral structure, which contributes to electrical conduction, and tetrahedral structure, which do not contribute to electrical conduction. Owing to the connection of octahedral structure in a form of one-dimensional chain, η -Mo₄O₁₁ can be classed as a material with hidden one-dimensionality. A two-step anisotropic charge density wave (CDW) transition at 109 K (T_{C1}) and 30 K (T_{C2}) has been reported for this material by temperature-dependent conduction measurement [1], and this transition was supported by the observation of change in lattice periodicity [2]. However, though a gap opening and band folding is predicted in case of CDW transition, such phenomena were not observed in the band structure [3]. Therefore we have performed photoemission measurements of η -Mo₄O₁₁ at different temperatures in order to observe traces of CDW in the band structure.

Figures 1 and 2 show the Fermi surface and the band dispersion at $k_y=0 \text{ \AA}^{-1}$ measured at $T=20 \text{ K}$. The thin solid black lines in Figs. 1 and 2 represent the Brillouin zone boundaries. The Fermi surface in Fig. 1 looks different from that reported previously in Ref. [3], probably due to the difference in the energy of the excitation light. The energy used in the present study would make the band visible only in the first Brillouin zone, but not in the second one. In other words, we can explain the results in Ref. [3] by considering the bands in the second Brillouin zone.

Figure 3 shows the photoelectron intensity distribution near the Fermi level. As can be seen in this figure, no band gap opening or band folding can be observed even when the temperature is varied across the transition temperatures, and metallic electronic states are always observed. This result suggests that the charge density wave transition in η -Mo₄O₁₁ may be a metal-metal transition. The nesting vector determined in previous studies is $\mathbf{q}_{c1}=0.23\mathbf{b}^*$ and $\mathbf{q}_{c2}=0.55\mathbf{a}^*+0.47\mathbf{b}^*+0.28\mathbf{c}^*$, suggesting that the charge density wave phase has a fairly long period structure. As a result of the minute modulation of each atom, we consider that the band structure of the metallic phase may not be much affected. This idea is consistent with the slow increase of resistivity below T_{C1} , and the decrease in resistivity indicating the metallic character of this material below T_{C2} .

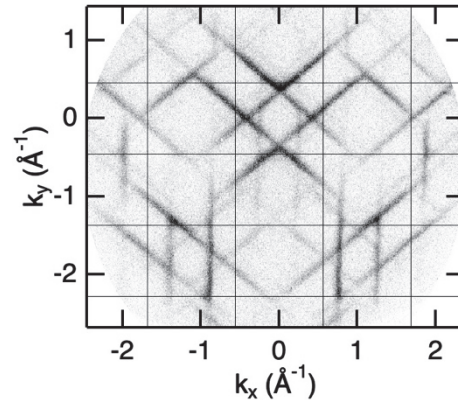
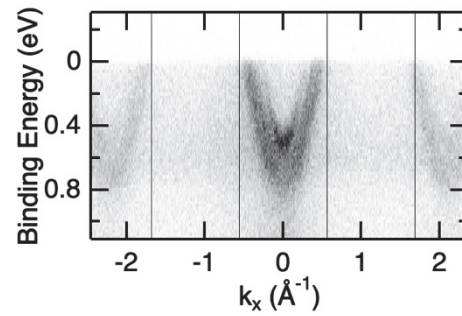
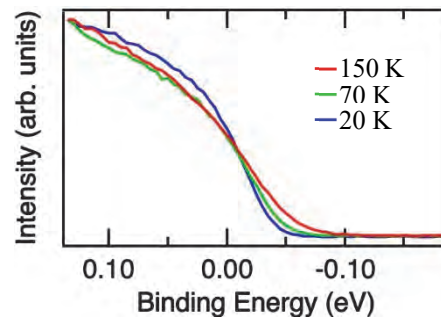

 Fig. 1. Fermi surface of Mo₄O₁₁ measured at $T = 20 \text{ K}$.

 Fig. 2. Band dispersion at $k_y=0 \text{ \AA}^{-1}$.


Fig. 3. Temperature-dependent photoelectron intensity distribution near the Fermi level.

 [1] H. Guyot *et al.*, J. Phys. C **16** (1983) L1227.

 [2] H. Guyot *et al.*, J. Phys. C **18** (1985) 4437.

 [3] G.-H. Gweon *et al.*, Phys. Rev. B **72** (2005) 035126.

BL6U

Characterization of CVD Graphene on Ir(111)/ α -Al₂O₃(0001) by Photoelectron Momentum Microscope

 E. Hashimoto¹, K. Tamura¹, H. Yamaguchi¹, F. Matsui² and S. Koh¹
¹Department of Electrical Engineering and Electronics, College of Science and Engineering, Aoyama Gakuin University, Sagami-hara 252–5258, Japan

²UVSOR Synchrotron Facility, Institute for Molecular Science, Okazaki 444-8585, Japan

Chemical vapor deposition (CVD) is a promising method to synthesize high-quality transferrable graphene sheets for device applications. We have previously reported growth of high-quality graphene on Ir(111)/ α -Al₂O₃(0001) by a low-pressure CVD method and demonstrated the reusability of the substrates [1-2]. In this study, we characterized the crystallinity of graphene/Ir(111)/ α -Al₂O₃(0001) and the electronic interaction between graphene and Ir(111) using photoelectron momentum microscope (PMM) [3].

We carried out CVD growth of graphene on the Ir(111)/ α -Al₂O₃(0001) substrates, using CH₄ and H₂ as precursors at 1000 °C. The gas flow rate of hydrogen and methane were 100 : 10 (#1), and 200 : 10 (#2), respectively. For both #1 and #2, the 2D and G peaks for graphene were observed in the Raman spectra. We characterized the samples (#1 and #2) by valence-band photoelectron spectroscopy (VB-PES) using PMM at the linearly polarized soft X-ray beamline BL6U of the UVSOR-III synchrotron.

Figures 1(a) and (b) show the Iso-energy cross sections of the 2D band dispersion at Fermi energy for sample #1 and #2, respectively. The distinct patterns with 6-fold symmetry were observed, which suggests that the sharp pattern with a low background corresponds to high single crystallinity of graphene. By comparing the patterns for #1 and #2, we found that #1 had the higher single crystallinity for several hundred μm^2 and #2 included the 30° rotated domains (*R*30). The growth of *R*30 domains was promoted by the fast growth rate, which was attributed to the higher hydrogen gas flow rate in the CVD growth condition for #2.

Figures 2(a)-(d) show the momentum-resolved VBP spectra of graphene on Ir(111). No Dirac points were observed in the VBP spectra along the *KTK* direction because the Fermi level located below the Dirac points, which suggests that the charge transfer from graphene to Ir(111) occurred. The binding energy of the *M* saddle point, which was evaluated from the VBP spectra along *M Γ M* direction, reflected the amount of charge transfer. The binding energy of the *M* saddle point for #1 and #2 were 2.30 eV and 2.25 eV, respectively. The lower binding energy for #2, *i.e.*, the higher amount of charge transfer, can possibly be attributed to the presence of the rotated domains (*R*30) in #2. The binding energy for *R*30 was reported to be 0.06 eV lower than that for the perfectly aligned domains [4].

Through this study, we found that the relationship of crystal orientations and the degree of electronic

interaction between graphene and the Ir(111) depended on the CVD growth conditions of graphene, for which PMM is a powerful complementary characterization tool to conventional methods (*e.g.*, Raman spectroscopy and AFM) for comprehensive characterization of graphene/Ir(111).

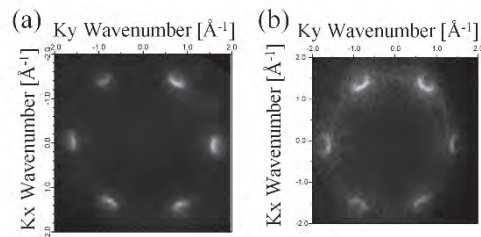


Fig. 1. Iso energy cross sections of 2D band dispersion at Fermi energy for (a) #1, (b) #2.

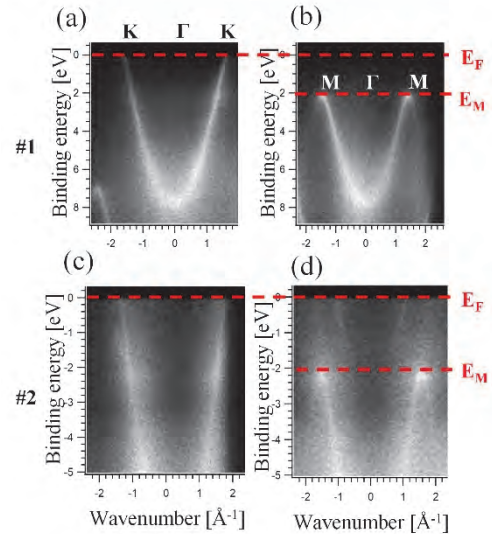


Fig. 2. Momentum-resolved VBP spectra of graphene for (a) #1 along *KTK* direction, (b) #1 along *M Γ M* direction, (c) #2 along *KTK* direction, and (d) #2 along *M Γ M* direction.

[1] S. Koh, Y. Saito, H. Kodama, and A. Sawabe, *Appl. Phys. Lett.* **109** (2016) 023105.

[2] A. Sakurai *et al.*, *Jpn. J. Appl. Phys.* **59** (2020) SIID01.

[3] E. Hashimoto *et al.*, *Jpn. J. Appl. Phys.* (2022) in press.

[4] E. Starodub *et al.*, *Phys. Rev. B* **83** (2011) 125428.

BL6B

Vibrational Spectroscopy of Pentacene Single Crystals in the Mid to Far Infrared Region and its Temperature Dependence

J. Miyamoto, A. Sugiyama, K. Yamauchi and Y. Nakayama

Department of Pure and Applied Chemistry, Tokyo University of Science, Noda 278-8510, Japan

Charge transport in organic semiconductor molecules has become an important issue in the pursuit of organic semiconductor devices with excellent efficiency. However, the decrease in carrier mobility due to molecular vibration is a particular problem for organic semiconductors, and the elucidation of the vibrational interactions that limit the charge carrier transport efficiency is one of the most important subjects in the field of organic semiconductors. In this study, we carried out mid-to-far infrared absorption spectroscopy on the single crystal pentacene ($C_{22}H_{14}$), a typical p-type organic semiconductor material, and attempted to track its temperature dependence.

First, single crystals of pentacene were prepared using the physical vapor transport (PVT) method and fixed to chemical-vapor-deposited (CVD) diamond substrates ($5\text{ mm} \times 5\text{ mm} \times 0.4\text{ mm}$). Infrared (IR) absorption measurements were performed in a transmission configuration at room temperature (RT) or low temperatures (100 K, 40 K). A blank CVD diamond substrate as a reference sample was also measured in identical conditions.

The measurement results are expressed in the top panel of Fig. 1 in terms of the IR absorbance which was derived from the relative transmittance of the pentacene/diamond sample with respect to the blank diamond sample. Quantum-chemical calculation results (Gaussian09, b3lyp, 6-31g*) for intramolecular vibration modes and calculated intermolecular A_g and A_u phonon modes of the pentacene single crystals taken from a literature [1] are shown in the lower panels of Fig. 1. To track how the absorption intensity and peak positions change when the effect of thermal vibration is reduced by cooling, the measurements were performed at three different temperatures (RT, 100 K, and 40 K). Figure 1 shows two peaks around $460\text{--}500\text{ cm}^{-1}$ for the spectra at RT and 100 K. Whereas, the calculation results predict three modes around $480\text{--}500\text{ cm}^{-1}$, the former two modes were presumed to be merged in the experimental spectra. Although, the two peaks appeared in a low wavenumber region compared to the calculated positions. On the other hand, the spectrum at 40 K exhibited a single peak, instead of two, at approximately the same wavenumber as the calculation results. The reason for this is unclear at this stage, but may be attributed to changes in intermolecular interactions as previously reported as shifts in Raman bands for amorphous thin-films of N,N' -di-naphthaleyl- N,N' -diphenyl-1,10-biphenyl-4,4'-diamine and copper-phthalocyanine [2].

For the spectral features below 200 cm^{-1} observed in Fig. 1 are not able to be assigned to which vibrations at this stage mainly due to a poor signal-to-noise ratio. More accurate and reliable measurements in this wavenumber region are future subjects to identify plausible phonon/vibration modes that inhibit the electrical conduction at RT.

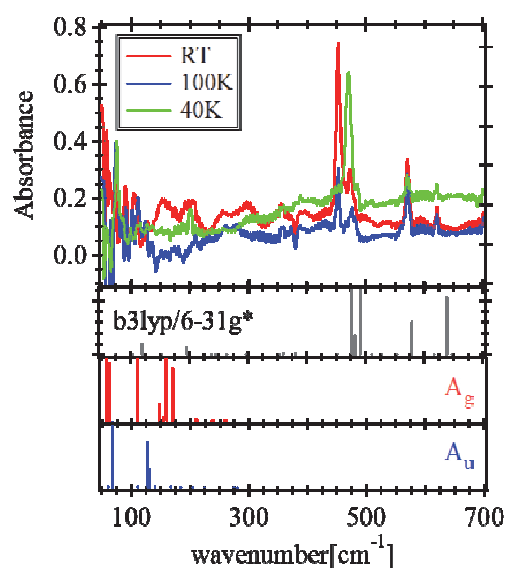


Fig. 1 Far-infrared spectra of a pentacene single crystal sample measured in a transmission configuration at various temperatures (RT, 100 K, 40 K). Calculated intramolecular vibrational modes using the ab-initio density functional theory and lattice phonons of pentacene single crystals taken from Ref. [1] are also presented.

[1] A. Girlando *et al.*, *J. Chem. Phys.* **135** (2011) 084701.

[2] T. Sugiyama and Y. Furukawa, *Jpn. J. Appl. Phys.* **45** (2007) 3537.

BL6B

Spectral Evidence of Current-Induced Local-to-Nonlocal Transition of SmS

H. Watanabe^{1,2}, S. Tatsukawa², K. Imura³, H. S. Suzuki⁴, N. K. Sato⁵ and S. Kimura^{1,2,6}

¹Graduate School of Frontier Biosciences, Osaka University, Suita 565-0871, Japan

²Department of Physics, Graduate School of Science, Osaka University, Toyonaka 560-0043, Japan

³Department of Physics, Graduate School of Science, Nagoya University, Nagoya 464-8602, Japan

⁴Institute for Solid State Physics, The University of Tokyo, Kashiwa 277-8581, Japan

⁵Aichi Institute of Technology, Toyota, 470-0392 Japan

⁶Institute for Molecular Science, Okazaki 444-8585, Japan

Samarium monosulfide SmS shows a pressure-induced insulator-to-metal transition from a black-colored semiconductor to a golden-colored metal (BGT) [1,2]. Even though BGT was discovered more than 50 years ago, its origin remains unclear. One possible origin has been proposed as a transition between the Bose-Einstein condensation (BEC) and the BCS state of excitons [3], but no definitive evidence has been obtained.

Recently, Ando *et al.* reported that the nonlinear relationship between voltage (V) and electric current (I) occurs with increasing I at temperatures lower than 100 K, which suggests the electronic state changes by applying current [4]. However, whether the current-induced electronic state change is related to the BGT is now under debate. To clarify the origin of the nonlinear V/I curve and the link to the BGT, we investigate the current and temperature dependence of the reflectivity spectrum, which reflects electronic structure, in the nonlinear V/I region. We have already reported the rapid increase of the effective carrier density at the nonlinear V/I region by observing the THz reflectivity spectrum [5], which suggests the appearance of the current-induced local-to-nonlocal transition of the electronic structure. To clarify the whole picture of the current-induced electronic structure change, we measured the current dependence of the mid- and near-infrared reflectivity spectrum using THz and IR microscopes at BL6B.

The single crystalline SmS with a typical sample size of $1 \times 1 \times 1 \text{ mm}^3$ was sandwiched by the electrodes connected to the current source and mounted in a liquid-helium-cooled cryostat.

Figure 1 shows the I -dependent reflectivity spectra at temperatures of 50 and 100 K. With increasing I , the reflectivity intensity below 0.1 eV increases, suggesting the carrier density increase. The peak at 0.6 eV corresponds to the exciton peak of the direct bandgap at the X point in the Brillouin zone [6,7]. The peak was broadened and slightly shifted to the higher energy side with increasing I . The spectra at 50 K (a) and 100 K (b) qualitatively showed the same behavior. In the case of a normal insulator-to-metal transition, the bandgap size decreases toward the metallic phase. However, this change in Fig. 1 is the opposite of that expected. The spectral shift is consistent with that with increasing temperature [2]. Our THz reflectivity spectrum results suggest that the current-induced increase of the carrier

density could not be explained by the increase of lattice temperature [5].

From these results, the current flow induces the delocalization of electrons without increasing lattice temperature. However, the golden-colored metallic phase does not appear by the current. This result suggests that the BGT needs other factors, such as lattice deformation.

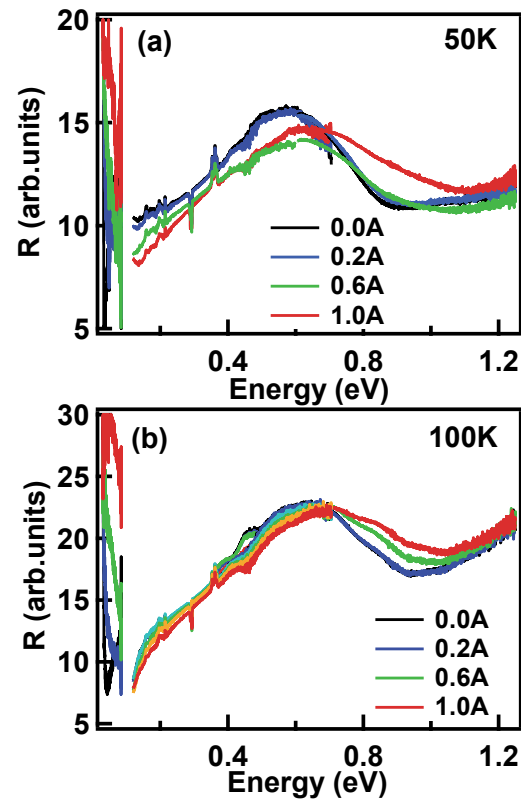


Fig. 1. Current dependence of mid- to near-infrared reflectivity spectra of SmS at 50 K (a) and 100 K (b).

- [1] A. Jayaraman *et al.*, Phys. Rev. Lett. **25** (1970) 1430.
- [2] T. Mizuno *et al.*, J. Phys. Soc. Jpn. **77** (2008) 113704.
- [3] B. I. Halperin and T. M. Rice, Rev. Mod. Phys. **40** (1968) 755.
- [4] H. Ando *et al.*, JPS Conf. Proc. **30** (2020) 011132.
- [5] H. Watanabe *et al.*, UVSOR Activity Report 2020 **48** (2021) 81.
- [6] S. Kimura *et al.*, Physica B **403** (2008) 805.
- [7] V. N. Antonov *et al.*, Phys. Rev. B **66** (2002) 165208.

BL6B

Structural Analysis of Fiber Biomaterials by Synchrotron-Radiation Infrared Microspectroscopy

T. Kawasaki¹, F. Teshima² and K. Tanaka²

¹Accelerator Laboratory, High Energy Accelerator Research Organization, Tsukuba 305-0801, Japan

²UVSOR Synchrotron Facility, Institute for Molecular Science, Okazaki 444-8585, Japan

Recently, fiber biomaterials such as cellulose fiber and peptide fiber have been getting attention in medical and materials fields. The common feature in their structures is a rigid sheet-like conformation, and it is usually difficult to regulate the stacking format without uses of extreme heating and organic solvents. As an alternate approach, physical technique such as high-power radiation can be proposed to control the fiber structure. Here, two-kinds of terahertz waves were applied to regulate the cellulose fiber: one is terahertz free electron laser (THz-FEL) and the other is submillimeter wave from gyrotron [1]. The THz-FEL has a double pulse structure that is composed of micropulse and macropulse where the duration of the former is 10-20 ps and that of the latter is about 4 μ s. The oscillation wavelength covers from 30 to 300 μ m, and the irradiation power is given as avg. 5 mJ per macropulse. The submillimeter wave from the gyrotron is a single pulse (1-2 ms half width) having 10 W power. After the cellulose fiber was irradiated by the THz-FEL that was tuned to 80 μ m and the submillimeter wave that was tuned to 720 μ m under atmospheric conditions at room temperature, those samples were added on metal-coating plate and analyzed by using BL6B synchrotron-radiation infrared microspectroscopy. The measurement was performed by reflection mode with 64 scans.

In the FT-IR spectrum of cellulose (Fig. 1), strong band at 1050 cm^{-1} and middle peak at about 1300 cm^{-1} were observed (Black). The former band corresponds to stretching vibrational mode of glycoside bond (ν C-O), and the latter peak can be assigned to bending vibrational mode of H-C-O, respectively [2]. After THz-FEL irradiation (blue), the former peak was decreased and the latter peak was increased. On the other hand, the former peak was largely increased accompanied by slight increase of the latter peak after the submillimeter wave from gyrotron (red). These spectral changes indicate that submillimeter wave gave the irradiation effect on cellulose fiber opposite to THz-FEL. Interestingly, when the cellulose fiber was irradiated by submillimeter wave following THz-FEL (green), the whole spectral pattern was almost the same as that of the non-irradiation sample (black). One interpretation on this phenomenon is that the cellulose fiber was dissociated to the monomeric chain by the THz-FEL irradiation, and the cellulose monomers were re-associated by the submillimeter wave radiation to produce the original cellulose fiber.

We have ever found that amyloid fibrils that form fiber structure like cellulose can be dissociated by the

THz-FEL and be promoted to form the aggregate by the gyrotron. [3,4]. Therefore, it can be enough considered that cellulose fiber can be dissociated and re-associated by those terahertz waves similarly with amyloid fibrils. The high-power terahertz waves can be expected as a physical tool for regulation of the fiber biomaterials in future.

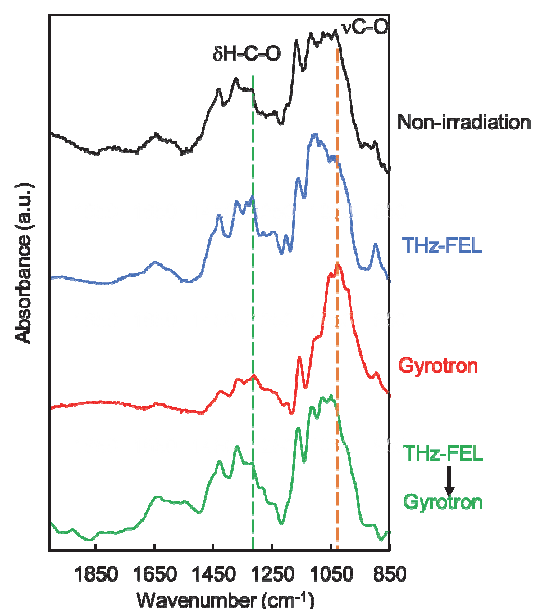


Fig. 1. Infrared spectra of cellulose fiber after irradiation by terahertz waves. Black: non-irradiation; blue: cellulose irradiated by THz-FEL; red: cellulose irradiated by submillimeter wave from gyrotron; green: cellulose irradiated by submillimeter wave behind THz-FEL.

[1] T. Kawasaki *et al.*, *J. Jpn. Soc. Infrared Science & Technology* **31** (2022) 52.

[2] N. C. Carpita *et al.*, *Plant Physiol.* **127** (2001) 551.

[3] T. Kawasaki, K. Tsukiyama and A. Irizawa, *Sci. Rep.* **9** (2019) 10636.

[4] T. Kawasaki *et al.*, *Biomed. Opt. Express* **11** (2020) 5341.

BL7U

Low-energy ARPES Study of Iron-chalcogenide High-temperature Superconductors

K. Nakayama^{1,2}, T. Kato¹, A. Moriya¹, F. Nabeshima³, N. Shikama³, T. Ishikawa³, Y. Sakishita³, S. Ideta^{4,5}, K. Tanaka^{4,5}, T. Takahashi^{1,6,7}, A. Maeda³ and T. Sato^{1,6,7}

¹Department of Physics, Graduate School of Science, Tohoku University, Sendai 980-8578, Japan

²Precursory Research for Embryonic Science and Technology (PRESTO), Japan Science and Technology Agency (JST), Tokyo 102-0076, Japan

³Department of Basic Science, University of Tokyo, Tokyo 153-8902, Japan

⁴UVSOR Synchrotron Facility, Institute for Molecular Science, Okazaki 444-8585, Japan

⁵School of Physical Sciences, The Graduate University for Advanced Studies (SOKENDAI), Okazaki 444-8585, Japan

⁶Center for Spintronics Research Network, Tohoku University, Sendai 980-8577, Japan

⁷Advanced Institute for Materials Research (WPI-AIMR), Tohoku University, Sendai 980-8577, Japan

Since the discovery of high-temperature superconductivity in LaFeAs(O,F), iron-based compounds are attracting great attention. Among known iron-based superconductors, iron selenide FeSe is the structurally simplest material. It exhibits various exotic properties such as anisotropic superconductivity and electronic nematicity without long-range magnetic order. These properties are sensitive to chemical substitution, high-pressure application, and/or carrier doping. Therefore, FeSe provides an opportunity to investigate the interplay between nematicity and superconductivity while controlling some physical parameters. In particular, isovalent-substituted FeSe_{1-x}Te_x and FeSe_{1-x}S_x films offer an excellent platform. Nematicity is realized in FeSe ($x = 0$) as in bulk FeSe, and the highest T_c of 23 K among non-carrier-doped FeSe-based compounds has been reported at the critical Te concentration x_c of ~ 0.2 at ambient pressure [1]. On the other hand, for the S-substituted counterpart, large T_c enhancement is absent and possible emergence of magnetism has been reported [2]. Comparative studies on these contrasting behaviors would provide a key to understand the origin of exotic properties.

In this study, we performed low-energy angle-resolved photoemission spectroscopy (ARPES) study of FeSe_{1-x}Te_x and FeSe_{1-x}S_x films. High-quality thin films were grown by the pulsed laser deposition method. ARPES measurements were performed using a MBS-A1 spectrometer at BL7U in UVSOR with energy-tunable photons of 12-25 eV.

Figures 1(a) and 1(b) show a comparison of the ARPES intensity around the Brillouin-zone center measured in pristine FeSe and FeSe_{1-x}S_x films, respectively. In pristine FeSe, highly dispersive hole band with the dominant Fe 3d_{xz/yz} orbital character (blue) crosses the Fermi level (E_F) and a relatively flat band with the Fe 3d_{xy} orbital (red) is located well below E_F . On the other hand, Se/Te substitution leads to an upward energy shift of the d_{xy} band, resulting in the appearance of the dxy-orbital character at E_F . The large electron mass of the d_{xy} band enhances the density of states at E_F , which is likely responsible for the T_c enhancement. We also determined the evolution of the electronic structure

upon Se/S substitution, and compared the results with those on FeSe_{1-x}Te_x films to elucidate the mechanisms of nematicity and superconductivity as well as the origin of contrasting phase diagram between FeSe_{1-x}S_x and FeSe_{1-x}Te_x.

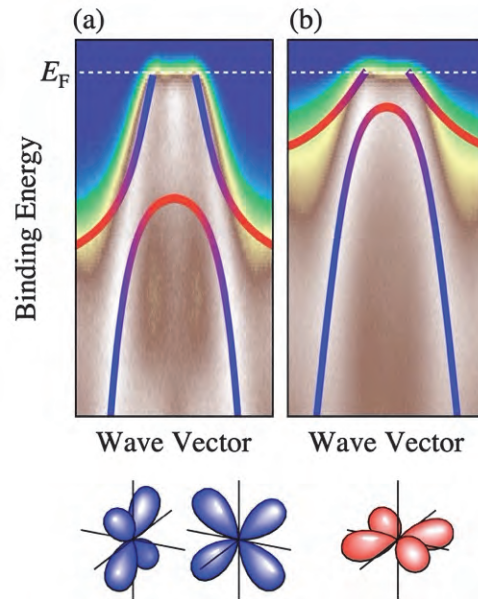


Fig. 1. (a) and (b) ARPES intensity plotted as a function of binding energy and wave vector measured in FeSe and FeSe_{1-x}Te_x films, respectively. Blue and red curves are a guide for the eyes to trace the $d_{xz/yz}$ and d_{xy} band dispersions, respectively.

[1] Y. Imai *et al.*, Sci. Rep. **7** (2017) 46653.

[2] F. Nabeshima *et al.*, J. Phys. Soc. Jpn. **87** (2018) 073704.

BL7U

Elucidations of Electronic Structure and the Many-body Interactions of Organic Molecular Materials

K. Fukutani^{1,2}, Y. Hasegawa³, M. Murakami⁴, D. Okaue⁵, K. Fukui^{1,5}, H. Ishii⁶,
K. Tanaka^{1,2} and S. Kera^{1,2,4}

¹Institute for Molecular Science, Okazaki 444-8585, Japan

²The Graduate University for Advanced Studies (SOKENDAI), Okazaki 444-8585, Japan

³Department of Physical Sciences, Ritsumeikan University, Kusatsu 525-8577, Japan

⁴Graduate School of Science and Engineering, Chiba University, Chiba 263-8522, Japan

⁵Graduate School of Engineering Science, Osaka University, Toyonaka 560-8531, Japan

⁶Department of Applied Physics, University of Tsukuba, Tsukuba 305-8573, Japan

As the sustainability of our global resources and energy-harvesting rapidly becomes a central issue in navigating our technological advancements, the development of quantum devices made of organic molecular materials, characterized by their low fabrication cost using abundant elements and high biodegradability, is of paramount importance.

Among such organic molecular materials, single crystalline rubrene ($C_{42}H_{28}$) is known to exhibit exceptionally high carrier mobility ($40 \text{ cm}^2/\text{Vs}$ [1]) and is considered as a promising semiconductor material for the next-generation electronics.

However, despite the numerous superiorities mentioned above, what should be the most fundamental building blocks for the future development are still incomplete; that is, the understanding of the electronic structure and their interactions with phonons and molecular vibrations.

For the purpose of elucidating these aspects of organic materials, angle-resolved photoemission spectroscopy (ARPES) is a premier experimental technique, which can simultaneously reveal the energies and momenta of the transport carriers (i.e., electrons and holes). Indeed, ARPES has been extensively utilized for rubrene and unveiled, for instance, the existence of discernable band dispersions for HOMO-derived bands [2], and the band gap induced by the interactions of electrons with molecular vibrations, revealed in our recent work [3]. On the other hand, there remain numerous critical questions about this material that are yet to be answered, including whether or not there are two HOMO-derived bands (as theoretically predicted), and whether there exists an interplay between the modes of molecular vibrations and the directions of electron propagation.

In our attempt to give the answers to these questions, we have utilized the BL7U at UVSOR to perform the high-resolution ARPES experiments.

For elucidating the many-body interactions, we have utilized the low photon energy of $h\nu = 8.0 \text{ eV}$ to maximize the momentum resolution. From the data we have obtained (see Fig. 1), we observe a discernable difference in the magnitude of the band gap formed by the electronic interaction with the intramolecular vibrations at different locations of the Brillouin zone. This is likely a signature of anisotropy in the electron-molecular-vibration interactions in the rubrene crystal.

Further quantitative analyses are expected to give us the first opportunity to understand the interplay between the molecular vibrational modes and the direction of electron propagations in molecular crystals

Furthermore, the ARPES data obtained at higher photon energy (see Fig. 2) show two different HOMO-derived bands which are degenerate at their maximum binding energy. These are in agreement with the calculated band structure and are expected to serve as a key for resolving the long-standing discrepancy between the theoretical predictions and experimental observations in rubrene band structure.

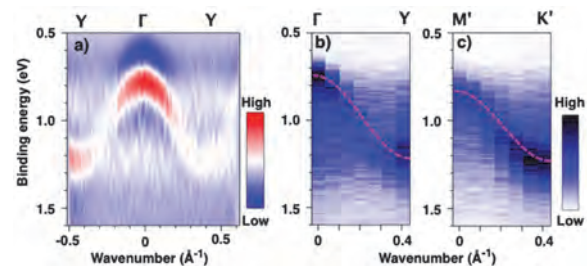


Fig. 1. ARPES second derivative plots obtained for (a) $k_x = 0 \text{ \AA}^{-1}$ (Γ -Y line) and (b) $k_x = 0.14 \text{ \AA}^{-1}$.

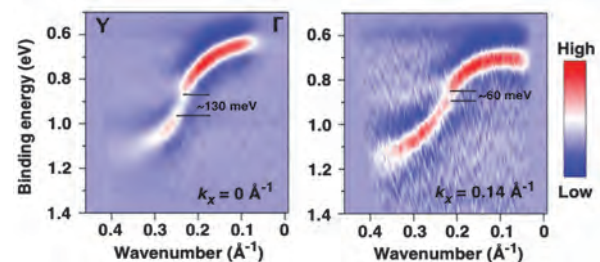


Fig. 2. ARPES plots for two HOMO-derived bands with (a, b) wider and (c) narrower dispersions. The dashed curves in (b), (c) are visual guides.

[1] J. Takeya *et al.*, Appl. Phys. Lett. **90** (2007) 102120.

[2] S. Machida *et al.*, Phys. Rev. Lett. **104** (2010) 156401; H. Ding *et al.*, Appl. Phys. Lett. **96** (2010) 222106; Y. Nakayama *et al.*, Appl. Phys. Express **5** (2012) 111601.

[3] F. Bussolotti *et al.*, Nat. Commun. **8** (2017) 173.

BL7U

Dirac-cone and Saddle-point Energy Bands in a Kagome Superconductor AV_3Sb_5

K. Nakayama^{1,2}, T. Kato¹, Y. Li^{3,4}, Z. Wang^{3,4}, K. Tanaka^{5,6}, T. Takahashi^{1,7,8}, Y. Yao^{3,4}
and T. Sato^{1,6,7}

¹Department of Physics, Graduate School of Science, Tohoku University, Sendai 980-8578, Japan

²Precursory Research for Embryonic Science and Technology (PRESTO), Japan Science and Technology Agency (JST), Tokyo 102-0076, Japan

³Centre for Quantum Physics, Key Laboratory of Advanced Optoelectronic Quantum Architecture and Measurement (MOE), School of Physics, Beijing Institute of Technology, Beijing 100081, China

⁴Beijing Key Lab of Nanophotonics and Ultrafine Optoelectronic Systems, Beijing Institute of Technology, Beijing 100081, China

⁵UVSOR Synchrotron Facility, Institute for Molecular Science, Okazaki 444-8585, Japan

⁶School of Physical Sciences, The Graduate University for Advanced Studies (SOKENDAI), Okazaki 444-8585, Japan

⁷Center for Spintronics Research Network, Tohoku University, Sendai 980-8577, Japan

⁸Advanced Institute for Materials Research (WPI-AIMR), Tohoku University, Sendai 980-8577, Japan

Kagome lattice is an excellent playground to study the physics intertwining electron correlation and non-trivial topology, owing to its peculiar band structure. Theoretical studies on the kagome lattice predict the formation of nearly flat band, Dirac-cone band, and saddle point van Hove singularity. When either of these bands is placed near the Fermi level (E_F), various unusual properties would be realized, e.g., Weyl magnet, density wave orders, charge fractionalization, and superconductivity.

Recently, a new family of kagome-lattice materials AV_3Sb_5 ($A = K, Rb, \text{ and } Cs$) has been discovered. AV_3Sb_5 shows superconductivity with the superconducting transition temperature T_c of 0.93–2.5 K, providing a rare opportunity to study superconducting properties in the kagome lattice. AV_3Sb_5 also exhibits a charge-density wave (CDW) transition at $T_{CDW} = 78\text{--}103$ K, possibly accompanied with time-reversal symmetry breaking. To understand the origin of these exotic properties, experimental investigations of electronic states are of crucial importance [1].

In this study, we performed low-energy angle-resolved photoemission spectroscopy (ARPES) study of KV_3Sb_5 and studied the electronic states with a high momentum resolution, which enables us to determine momentum dependence of the CDW gap.

High-quality single crystals of KV_3Sb_5 were grown by the self-flux method. ARPES measurements were performed by using a MBS-A1 spectrometer at BL7U in UVSOR. Clean surfaces of the samples were obtained by cleavage in an ultrahigh vacuum.

Figure 1 shows the ARPES intensity measured along the Γ KM high-symmetry line of bulk hexagonal Brillouin zone. One can identify an electron pocket centered at the Γ point. This band is attributed to the $5p$ band of Sb atoms. One can also recognize linear dispersions that produce multiple Dirac points near the K point. These bands are attributed to the kagome-lattice band with mainly $V-3d_{xy}$ character. One of the Dirac-cone band (indicated by red arrow) shows a

flattening with approaching the M point and forms a saddle-point dispersion. Upon decreasing the temperature below T_{CDW} , we found an opening of the CDW gap on V-derived bands. Our detailed momentum-dependent study demonstrates the largest gap opening on the saddle-point band at the M point as well as the absence of clear gap opening on the Sb-derived band. Our observations suggest that the scattering between the saddle-point bands and resultant large gap opening stabilizes CDW, and Sb-derived parabolic band at the Γ point is likely responsible for the superconductivity that coexists with CDW.

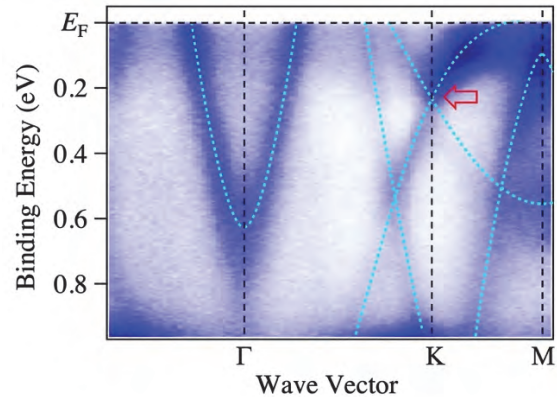


Fig. 1. ARPES intensity plotted as a function of binding energy and wave vector measured in KV_3Sb_5 .

[1] K. Nakayama *et al.*, Phys. Rev. B **104** (2021) L161112.

BL7U

Angle-resolved Photoemission Study of TPP[FePc(CN)₂]₂

T. Ito^{1,2}, T. Hoshina², K. Tanaka^{3,4}, M. Matsuda⁵ and N. Hanasaki⁶

¹Nagoya University Synchrotron radiation Research center (NUSR), Nagoya University, Nagoya 464-8603, Japan

²Graduate School of Engineering, Nagoya University, Nagoya 464-8603, Japan

³UVSOR Synchrotron Facility, Institute for Molecular Science, Okazaki 444-8585, Japan

⁴The Graduate University for Advanced Studies (SOKENDAI), Okazaki 444-8585, Japan

⁵Graduate School of Science and Technology, Kumamoto University, Kumamoto 860-8555, Japan

⁶Department of Physics, Osaka University, Toyonaka 560-0043, Japan

Molecular conductors are known to exhibit a variety of properties ranging from magnetism to superconductivity, depending on the addition of inorganic elements or the combination of cationic and anionic molecules. In particular, axially substituted metal phthalocyanine (MPc, M = metal) molecules have attracted attentions because of their unique physical properties such as a giant negative magnetoresistance effect [1]. Though their anomalous properties have been expected to originate from strong π -d interactions, being similar with those in strongly correlated transition metal, the electronic structure of this system has never been reported yet. In this study, we have investigated the electronic structure of axially-substituted quasi-one-dimensional (Q1D) molecular conductor TPP[FePc(CN)₂]₂ single crystal by using angle-resolved photoemission spectroscopy (ARPES).

ARPES measurements were performed at the UVSOR-III BL7U. Data were acquired with $h\nu = 40$ eV at $T = 10$ K. Measurement axis was set along 1D conducting axis ($//c$). Needle-shaped single-crystals (typical size $< 1 \times 0.1 \times 0.1$ mm³) were cleaved *in situ* along (110) plane. The relation between the cleavage plane and conducting axis is shown in Fig. 1. To minimize photoirradiation damage photon flux was sufficiently reduced during all measurements.

Figure 2 shows valence band ARPES spectra of TPP[FePc(CN)₂]₂ along the conducting axis. We have successfully observed several peak structures (A-G) from E_F to 15 eV. Small background relative to peaks suggests the cleanliness of the cleaved surface. From the comparison of the ARPES spectra (Fig. 2) with the valence band structure image (Fig. 3), peak B around 4 eV seems to show symmetric intensity reduction together with sizable energy shift from Γ to Z point. In addition, systematic energy shift has also been recognized around 5-7 eV (blue dashed lines). On the other hand, the energy shift of the peaks cannot be observed at high-binding energy side (peaks E-G). We expect that the observed change of ARPES spectra originates from the energy dispersive feature on TPP[FePc(CN)₂]₂.

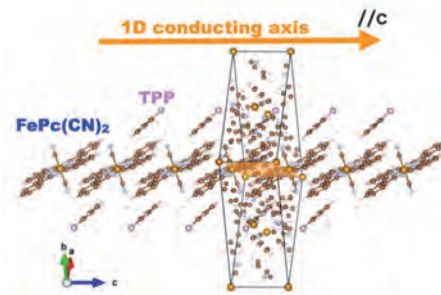


Fig. 1. Crystal structure of TPP[FePc(CN)₂]₂. Due to the existence of the axial CN ligands, Pc units form a one-dimensional chain along c axis, which corresponds to π conducting axis.

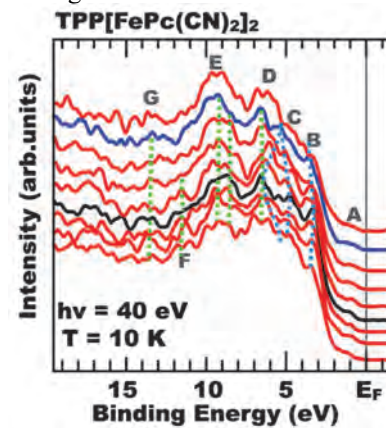


Fig. 2. Valence band ARPES spectra along the Γ Z line of TPP[FePc(CN)₂]₂. Blue and green dashed lines are guide for dispersive and non-dispersive features.

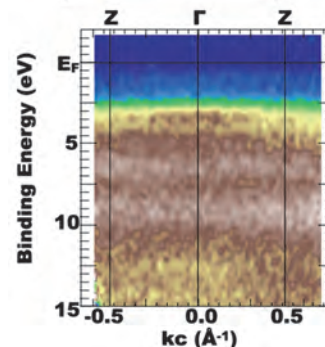


Fig. 3. Valence band structure along the Γ Z line of TPP[FePc(CN)₂]₂.

[1] N. Hanasaki, *et al.*, J. Phys. Soc. Jpn. **75** (2006) 033703.

BL7U

Relationship between Chemical Pressure Effect and Electronic Structure in $R_{1-x}Ce_xOBiS_2$ ($R=Nd, La$)

N. Kataoka¹, T. Wakita^{1,3}, Y. Hanada², M. Nagao² and T. Yokoya^{1,3}¹Graduate School of Natural Science and Technology, Okayama University, Okayama 700-8530, Japan²University of Yamanashi, Kofu 400-8511, Japan³Research Institute for Interdisciplinary Science, Okayama University, Okayama 700-8530, Japan

BiCh₂ compounds are quasi-two-dimensional materials with a layered structure typically represented by the composition of $RO_{1-x}F_xBiCh_2$ (R =rare earth; Ch= S, Se). It can be doped electrons by replacing oxygen with fluorine atoms or by introducing mixed valence R atoms such as Ce and Eu into R sites. Electron-doped samples show superconductivity below 2-10 K. Several experimental and theoretical studies have indicated the possibility of unconventional superconducting mechanisms [1]. Since the superconducting transition temperature (T_c) is sensitive to the pressure applied to the BiCh₂ planes, the chemical pressure effects of many elemental substitutions have been intensively studied [1-3]. The chemical pressure effects are important for understanding the superconducting mechanism, although there are few systematic reports on the electronic structure. In $R_{1-x}Ce_xOBiS_2$, the ratio of Ce^{4+} at the R site is about 0.1~0.15 despite the composition, so the average ionic radius of the R site can be controlled while keeping the electron doping level fixed [2,3]. Therefore, it is the best material for investigating the relationship between pressure and electronic structure in the BiCh₂ systems. In this study, angle-resolved photoemission spectroscopy (ARPES) measurements of $R_{1-x}Ce_xOBiS_2$ were performed to investigate the relationship between pressure and the electronic structure.

The measurements were performed using $R_{1-x}Ce_xOBiS_2$ ($R=La, Nd; x=0.2\sim 0.75$) single crystals synthesized by the flux method [2,3]. ARPES measurements were performed at BL7U of UVSOR III, using 20 eV photons with an energy resolution of 15~20 meV. All samples were cleaved in situ on the (001) plane in an ultrahigh vacuum of less than 5×10^{-9} Pa.

Figures 1 (a) and (b) show the Fermi surfaces of $Nd_{0.7}Ce_{0.3}OBiS_2$ and $La_{0.75}Ce_{0.25}OBiS_2$, respectively, and (c) and (d) show the respective band dispersions. $Nd_{0.7}Ce_{0.3}OBiS_2$ is a superconductor with T_c of ~5K, while $La_{0.75}Ce_{0.25}OBiS_2$ is non-superconductive at least above 1.5K. $Nd_{0.7}Ce_{0.3}OBiS_2$ and $La_{0.75}Ce_{0.25}OBiS_2$ have inner and outer electron pockets, respectively, centered at the X point. $Nd_{0.7}Ce_{0.3}OBiS_2$ is a relatively low-dimensional Fermi surface, with nested quadrilateral Fermi surfaces on both the inner and outer sides. On the other hand, $La_{0.75}Ce_{0.25}OBiS_2$ has an inner Fermi surface distorted into an elliptical shape extending in the Γ -X direction (perpendicular to X-M-X direction). The outer Fermi surface also seems to be distorted. The difference in the shape of the Fermi surface may be, to a first approximation, due to differences in electron

doping levels rather than chemical pressure. In fact, the sizes of the Fermi surfaces are different and there is a difference of about 0.1 eV in the energy at the bottom of the band. Furthermore, their Fermi surface shapes are similar for $n = 0.125$ and $n = 0.25$ electron doping levels [4]. In this regard, it may be possible here that the nested Fermi surfaces are more favorable for achieving higher superconducting transition temperatures, given that $Nd_{0.7}Ce_{0.3}OBiS_2$ has a higher superconducting transition temperature. For a more comprehensive understanding, comparisons with other compositions of the material should be made.

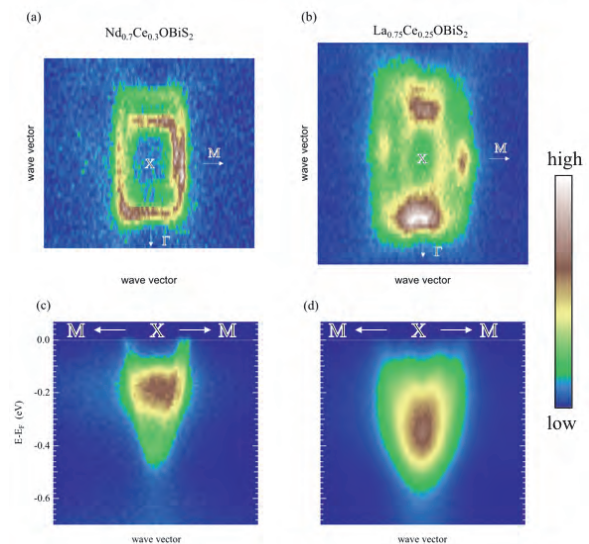


Fig. 1 (a) and (b) Fermi surfaces, as well as (c) and (d) band dispersions along X-M lines, for $Nd_{0.7}Ce_{0.3}OBiS_2$ and $La_{0.75}Ce_{0.25}OBiS_2$, respectively.

- [1] Y. Mizuguchi *J. Phys. Soc. Jpn.* **88** (2019) 041001.
 [2] Y. Hanada *et al.*, *Jpn. J. Appl. Phys.* **58** (2019) 063001.
 [3] Y. Fujita *et al.*, *ACS Omega* **5** (2020) 16819.
 [4] M. Ochi *et al.*, *J. Phys. Soc. Jpn.* **85** (2016) 094705.

BL7B

Photoluminescence Properties of Cs_2ZnCl_4 and Cs_3ZnCl_5 with Vacuum Ultraviolet Excitation

K. Takahashi, M. Koshimizu, Y. Fujimoto and K. Asai
Graduate School of Engineering, Tohoku University, Sendai 980-8579, Japan

Auger-free luminescence (AFL) is owing to the radiative transition between the valence band and the outermost core level. Generally, AFL is not efficient because the transition is competitive with the Auger process, which is generally a much faster process than that of AFL. In other words, efficient AFL has been observed in limited compounds such as alkaline- or alkaline-earth fluorides or CsCl-based compounds.

In recent years, we have developed fast scintillators exhibiting AFL on the basis of ternary CsCl-based compounds, such as Cs_2ZnCl_4 [1], CsCaCl_3 [2], and Cs_2BaCl_4 [3]. Fast scintillation decay within 2 ns has been achieved. The scintillation light yields of these compounds were less than 1,500 photons/MeV, which is significantly smaller than those of Ce-doped inorganic scintillators. Hence, we further investigated novel compounds based on CsCl. As an example of the further investigation, we have recently reported the photoluminescence and scintillation properties of Cs_3ZnCl_5 in comparison to those of Cs_2ZnCl_4 [4]. In the present report, we present the excitation spectra of Cs_2ZnCl_4 and Cs_3ZnCl_5 , which clearly indicates that the emission was attributed to AFL.

Crystalline samples of Cs_2ZnCl_4 and Cs_3ZnCl_5 were used for the measurements. The measurements of the photoluminescence under irradiation with vacuum ultraviolet light were performed at BL7B of UVSOR at room temperature. The excitation wavelength between 50 to 200 nm was used for the measurements. The photoluminescence from the samples were observed with a CCD-based spectrometer via an optical fiber. The photoluminescence spectra with different excitation wavelengths were recorded. On the basis of the photoluminescence spectra, the excitation spectra were obtained.

To verify the origins of the emission bands at 260 and 310 nm of Cs_2ZnCl_4 and 240 and 290 nm of Cs_3ZnCl_5 crystals, we obtained the excitation spectra monitoring the wavelengths. Figures 1 and 2 present the excitation spectra. The excitation spectra of Cs_2ZnCl_4 are well consistent with those in a previous report [1]. A steep rise was observed in both excitation spectra at around 90 nm, which corresponds to the excitation of electrons at the outermost core level to the conduction band. Hence, based on the excitation spectra, the emission bands are attributed to AFL.

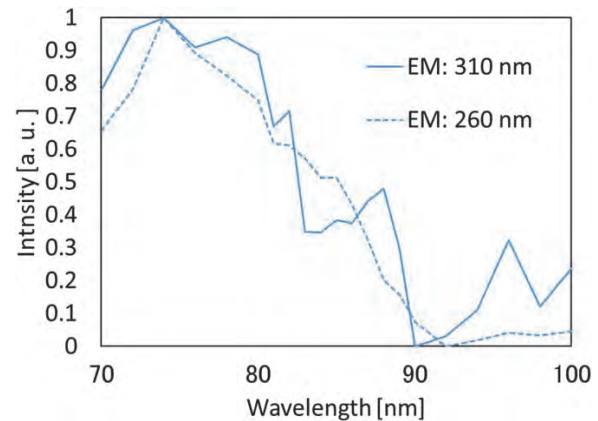


Fig. 1. Excitation spectra of Cs_2ZnCl_4 for monitored wavelengths of 260 and 310 nm [4]. Copyright (2020) The Japan Society of Applied Physics.

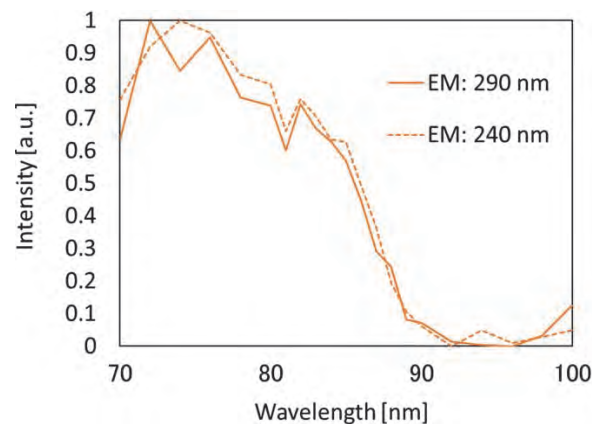


Fig. 2. Excitation spectra of Cs_3ZnCl_5 for monitored wavelengths of 240 and 290 nm [4]. Copyright (2020) The Japan Society of Applied Physics.

[1] N. Yahaba, M. Koshimizu, Y. Sun, T. Yanagida, Y. Fujimoto, R. Haruki, F. Nishikido, S. Kishimoto, and K. Asai, *Appl. Phys. Express* **7** (2014) 062602.

[2] M. Koshimizu, N. Yahaba, R. Haruki, F. Nishikido, S. Kishimoto, and K. Asai, *Opt. Mater.* **36** (2014) 1930.

[3] K. Takahashi, M. Arai, M. Koshimizu, Y. Fujimoto, T. Yanagida, and K. Asai, *Jpn. J. Appl. Phys.* **59** (2020) 032003.

[4] K. Takahashi, M. Arai, M. Koshimizu, Y. Fujimoto, T. Yanagida, and K. Asai, *Jpn. J. Appl. Phys.* **59** (2020) 072002.

BL7B

Investigation of Gamma-ray-irradiated Oxide Glasses for Deep Ultraviolet Detector with High Efficiency

T. Shimizu, K. Shinohara, D. Umeno, K. Yamanoi and N. Sarukura
Institute of Laser Engineering, Osaka University, Suita 565-0875 Japan

Vacuum ultraviolet (VUV) light is used in important technological applications such as photochemical processing, surface treatment, optical cleaning of semiconductor substrates, and sterilization. In particular, it has been suggested that non-contact sterilization, treatment, and processing could be advanced by using VUV in the current corona disaster. For such recent progress in VUV research and applications, it is necessary to develop detectors in the short wavelength range. In the development of VUV detectors, it is important to evaluate spectral characteristics in VUV region.

Previously, we have studied fluoride crystals, such as MgF_2 and CaF_2 , for VUV optical devices [1,2]. Fluoride crystals are widely used in ultraviolet (UV) optics because of their wide band gaps. And also we have investigated fluoride glasses for VUV optical devices [3].

In addition, there are high expectations for material modification by gamma-ray irradiation. We have investigated the improvement of time resolution of scintillators such as ZnO by gamma-ray irradiation. Gamma-ray irradiation can be used as a post-processing step and is expected to improve the performance of various devices.

In our recent study, gamma-ray induced optical property changes in non-doped and Ce-doped lithium-rich oxide glasses are investigated [4]. However, optical properties of these material in VUV region has not been fully researched. Neutron measurements are important in fusion experiments, and lithium-rich oxide glasses are used as scintillator to detect neutrons. Evaluation of VUV characteristics of scintillator material is important to improve the performance of neutron detection. In high dose rate environment such as nuclear fusion experiment, optical materials are easily damaged. It is reported that Ce doping in the base material prevents degradation of optical materials.

In this study, we measured transmittance of gamma-ray-irradiated oxide glasses from VUV to visible region. We used a lithium borosilicate glass (LBS) and CeF_3 -doped LBS. All glass samples were fabricated by the melt-quenching method [4]. To fabricate LBS, a mixture of high purity 99.99% boric acid (H_3BO_3), high purity silica (SiO_2) and lithium carbonate (Li_2CO_3) was melted at 1100°C for 2 h under air atmosphere. Natural Li was used for all sample fabrication. The melted glass was quenched in air in a graphite mold and then annealed at 500°C for 3 h. The CeF_3 -LBS glasses were fabricated using similar precursors with the addition of CeF_3 powder. Precursors for Ce-doped samples were

melted in an aluminum crucible for 3 h at 1200°C and were quenched in air in a graphite mold, then subsequently annealed at 350°C for 3 h. After fabrication, the non-doped glass samples were cut and polished into $10\text{ mm} \times 10\text{ mm}$ flat plates with thicknesses ranging from 3.8 mm to 4.2 mm. The Ce-doped samples were cut and polished into $15\text{ mm} \times 10\text{ mm}$, with thickness ranging from 3.1 mm to 3.8 mm. The glass samples were irradiated with gamma rays carrying 1.17 and 1.33 MeV energies from a cobalt-60 (^{60}Co) source. The ^{60}Co source was calibrated with water and had a dose rate of 36.82 Gy/h at a distance of 1.0 m. The samples were set approximately 10 cm away from the radiation source. The irradiation was performed at room temperature and in ambient atmosphere.

Figure 1 shows measured transmittance of gamma-ray-irradiated LBS and CeF_3 -LBS. In both samples, high transmittance was measured even with VUV. Although Ce was not seen to have much of an effect in this measurement, it is expected to reduce the effect of gamma irradiation.

In the future, we will compare more detailed conditions and develop materials for high-efficiency deep-ultraviolet photodetectors.

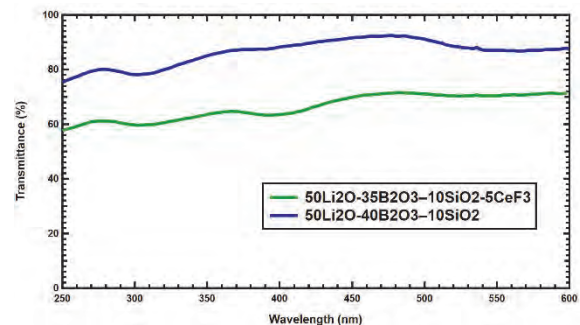


Fig. 1. Transmittance of gamma-ray-irradiated oxide glasses.

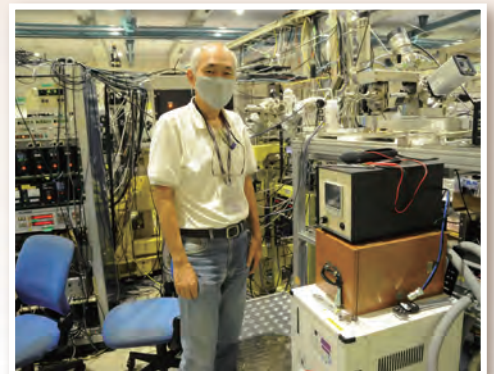
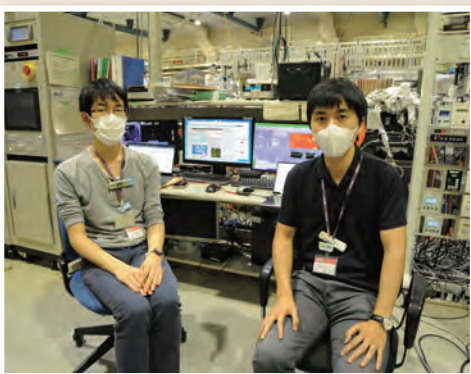
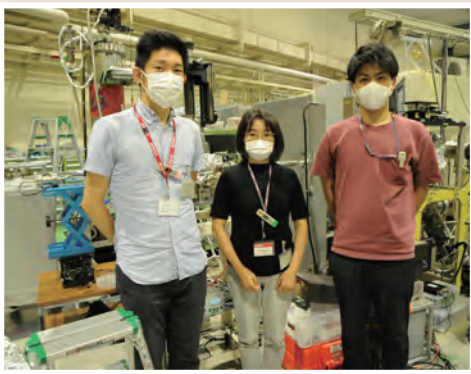
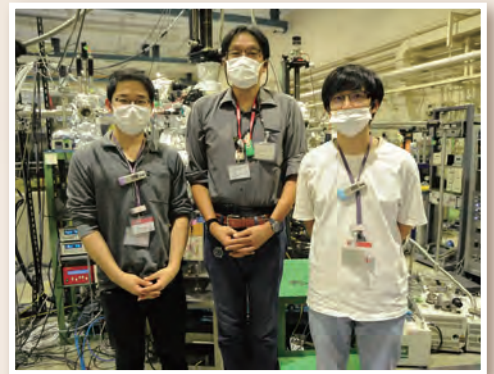
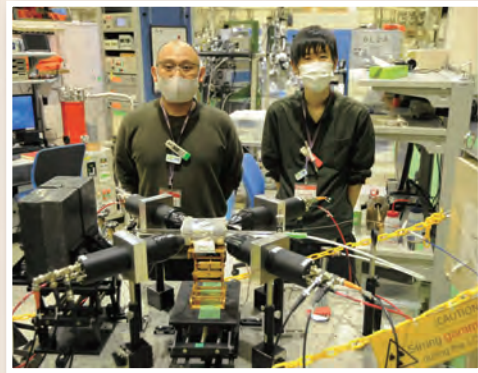
[1] T. Shimizu *et al.*, UVSOR Activity Report 47 (2019) 107.

[2] K. Yamanoi *et al.*, Opt. Mater. 36 (2014)769.

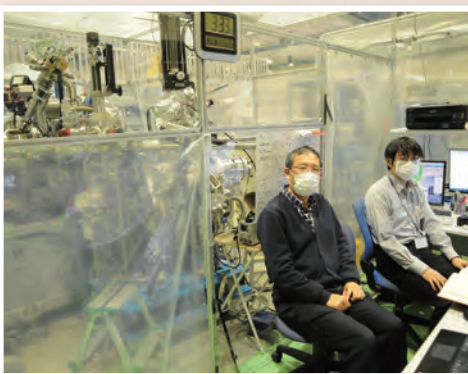
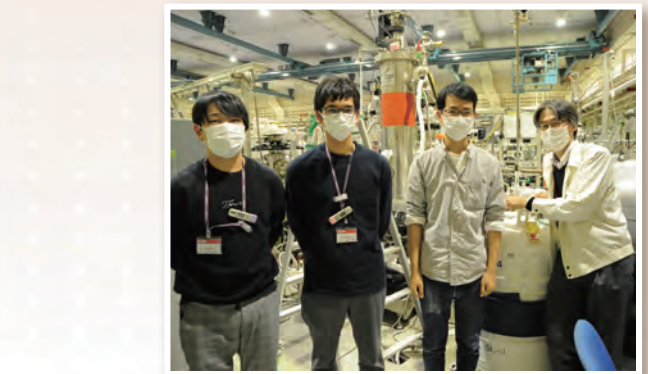
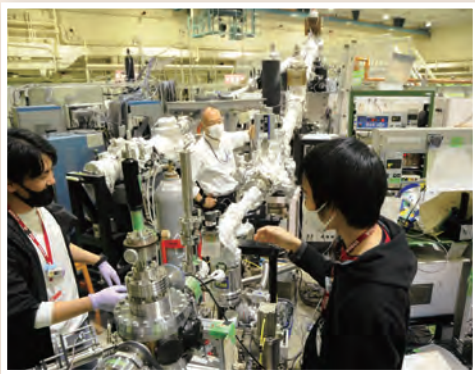
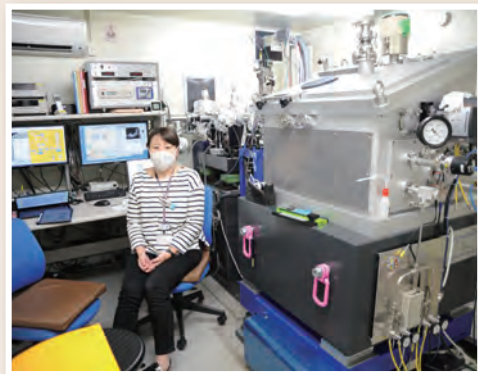
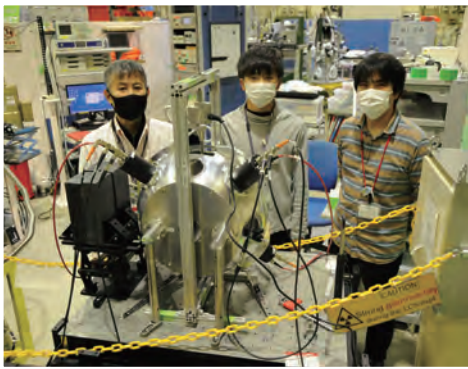
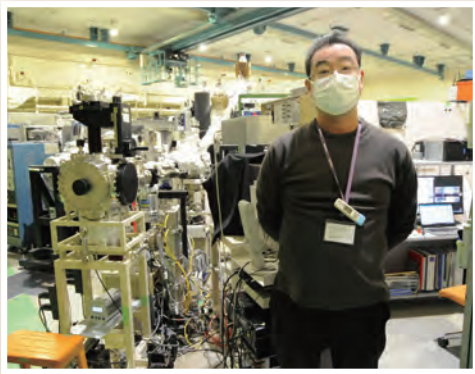
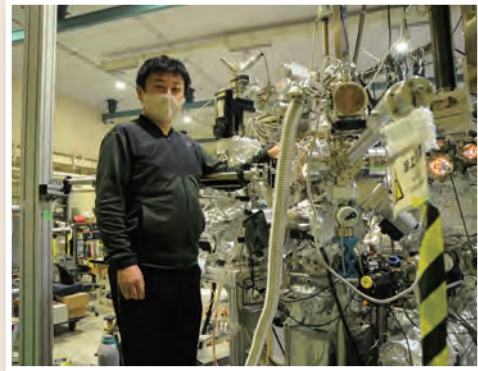
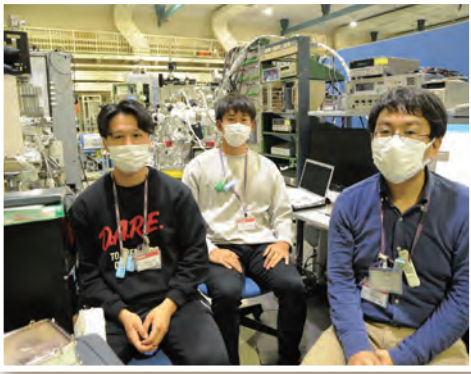
[3] T. Shimizu *et al.*, UVSOR Activity Report 2020 48 (2021) 88.

[4] Y. Lai *et al.*, Radiat. Phys. Chem. 179 (2021) 109272.

UVSOR User 4



UVSOR User 5



III-3

Chemistry

BL3U

Solvent-Induced Transition of Polymorphological Chiral Supermolecular Architectures in Bent-Core Liquid Crystal Dimer/Nematic Binary Mixtures as Studied by Resonant Soft X-ray Scattering (RSoXS) at UVSOR

F. Araoka¹, Y. Takanishi², K. V. Le³ and H. Iwayama^{4,5}¹RIKEN Center for Emergent Matter Science (CEMS), Wako 351-0198, Japan²Faculty of Science, Kyoto University, Kyoto 606-8502, Japan³Faculty of Science, Tokyo University of Science, Tokyo 162-8601, Japan⁴UVSOR Synchrotron Facility, Institute for Molecular Science, Okazaki 444-8585, Japan⁵School of Physical Sciences, The Graduate University for Advanced Studies (SOKENDAI), Okazaki 444-8585, Japan

Nano-scaled chiral superstructures, such as tilted lamellar (smectic) structures or helical nanofilaments (HNFs), are often observed in polar (or apolar) soft-mesophases of achiral bent-core molecules, although their chemical structure has no chiral carbon. The so-called B4 phase is one of such soft-mesophases, in which chirality is macroscopically recognizable as millimeter-sized domains optically segregated under a polarizing microscope. There are two types of B4 domains resembling each other, originated from two different nanoscopic structures; One is filled with bundles of polar HNFs with a pitch of several tens to hundreds nm, and the other is the so-called dark conglomerate (DC) in which concentric polar lamellar structures are interconnected to form bicontinuous pores like a sponge. However, in both cases, the polar tilted lamellar structure is essential and thus almost identical diffraction patterns are obtained by conventional small angle X-ray scattering (SAXS).

Recently, we discovered that these two structures are interchangeable by adding a nematic solvent (ZLI-2293, Merck) to the host bent-core molecule (12OAz5AzO12). Besides, further addition of the nematic solvent induced an unprecedented nano-tubular structure like a “macaroni” as a novel chiral state. This nanoscopic morphological change was first confirmed with scanning electron microscopy (SEM, Fig. 1) – the result suggests that phase separation reduces interfacial free energy and creates spaces to allow the lamellar to be more twisted, leading to the structural transition from DC to macaroni via HNF. However, the SEM technique requires vacuum for electrons to fly, and thus the samples were fractured to expose the internal structure and washed with Hexane to completely remove the solvent nematic molecule. This leaves uncertainty if the bulk structures are surely preserved during the fracturing/washing process or not. Meanwhile, HNF/DC are just morphologically characterized, and hence electron density is basically not spatially modulated by these structures. This means that usual X-ray diffraction/scattering is not very useful to investigate the present system. For these reasons, we performed resonant soft X-ray scattering (RSoXS) measurements using X-ray whose energy is close to the carbon K-edge absorption, which allows us to analyze the nanoscopic structural change in such a morphologically transformable system.

Our RSoXS setup was prepared in BL3U of UVSOR at IMS – A homemade vacuum chamber equipped with a cooled CCD camera (Newton, Andor) was newly designed for small angle detection ($2\theta \sim 1\text{--}15^\circ$). In the present study, the X-ray photon energy was chosen as 284.5 eV, corresponding to the carbon K-edge absorption of the present sample mixtures.

RSoXS patterns for HNF, DC and Macaroni are compared in Fig. 2, which clearly shows transitions due to the morphological change among these states. HNFs, appearing in the middle doping range, show relatively sharp scattering patterns at the scattering angle corresponding to the half-pitch periodicity of the twisting filaments. On the other hand, DCs show broad peaks at the slightly smaller scattering angle region than HNFs, which would be corresponding to the average distances between the lamellar inter-connections. Interestingly, the macaroni state shows just scarce signals in this region, meaning almost no nanoscopic structural periodicity. Needless to say, these confirm that the present RSoXS setup works well for structural investigation for such soft-mesophases.

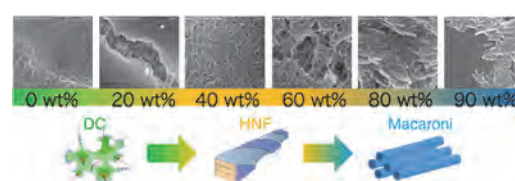


Fig. 1. Nanoscopic morphological transformation among DC, HNF, and macaroni as observed by SEM.

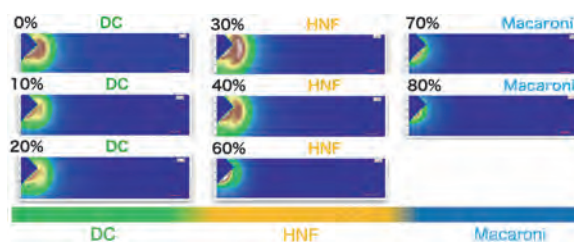


Fig. 2. RSoXS pattern alteration corresponding to the nanoscopic morphological transformation.

BLIU

Energy-Dependence of Photoelectron Circular Dichroism of Chiral Molecules

H. Kohguchi¹, Y. Hikosaka², T Kaneyasu³, S. Wada¹, H. Ohta⁴, M. Fujimoto⁴, M. Katoh⁴
and Y-I. Suzuki⁵

¹Graduate School of Advanced Science and Engineering, Hiroshima University,
Higashi-Hiroshima 739-8526, Japan

²Institute of Liberal Arts and Sciences, University of Toyama, Toyama 930-0194, Japan

³SAGA Light Source, Tosu 841-0005, Japan

⁴UVSOR Synchrotron Facility, Institute for Molecular Science, Okazaki 444-8585, Japan

⁵School of Medical Technology, Health Sciences University of Hokkaido, Tobetsu 061-0293, Japan

A simple explanation of the manifestation of photoelectron circular dichroism (PECD), which is measured as forward-backward asymmetry of the photoelectron angular distribution with circularly polarized light, can be that the outgoing photoelectron is affected by a chiral potential originated from the chiral core ion. The intuitive model indicates that the slower photoelectron can exhibit the larger PECD. Actually, most of the PECD measurements so far carried out for various chiral molecules demonstrated decreasing PECD parameters (b_1) as the higher photon energies. However, the b_1 parameters of the individual electronic states varied in an independent manner, showing the state-specificity. The energy-dependence and state-dependence of PECD are not simply understood with a simple model but should be examined based on the precise measurements and accurate theoretical calculations, both of which can provide novel pictures for the PECD mechanism.

We have conducted the PECD measurements for S-methyl oxirane and other chiral molecules with employment of circular polarized light at BLIU at varied photon energies [1]. Methyl oxirane (propylene oxide) is a typical chiral molecule, whose PECD has been intensively studied. Our results are shown in Fig. 1, where the photon energy-dependence is shown in a series of the image data for (a) 10.3 eV, (b) 11.0 eV, (c) 12.0 eV, (d) 12.7 eV, (e) 13.3 eV, and (f) photoelectron kinetic energy (PKE) scale. Distinct ring structures corresponding to individual electronic states appeared at the higher photon energy than (a) 10.3 eV (close to the ionization threshold) with particular PECD, whose positive and negative b_1 values are represented by red and blue colors. The b_1 value of each ring decreases as the elevated photon energy, but the decreasing behaviors were not monotonic but rather dependent on the states. The strongest PECD observed in the 2 eV PKE region at (c) $h\nu = 12.0$ eV rapidly disappeared at an only slightly larger photon energy of (d) $h\nu = 12.7$ eV, while other bands kept the contrast of the blue/red color (b_1 PECD parameter) for the wider photon energy variations.

The present results are qualitatively similar to the previous study of methyl oxirane [2]: the sign of the b_1 parameters of the three electronic states were well reproduced. We extended our measurements for the finer intervals of the photon energy to examine the

energy-dependence of PECD. A faint feature of the sign change of PECD with the varied photon energy was found in the second band, which is more visible in the polar representation of the observed results (Fig. 1. lower). These results will be verified in comparison with theoretical calculations.

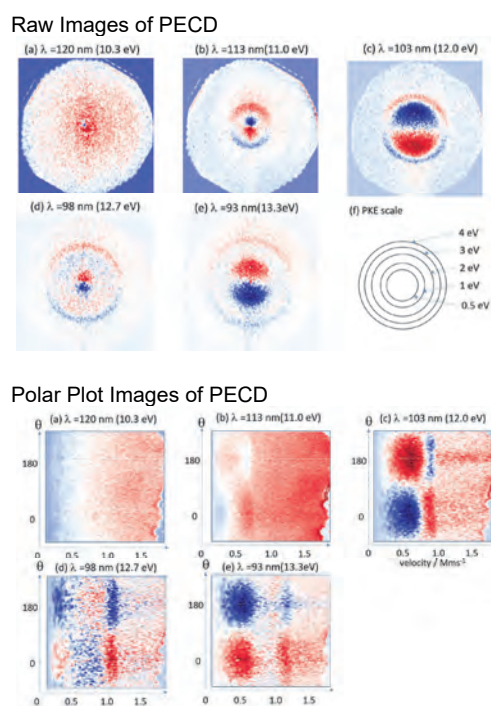


Fig. 1. (Upper) Difference images of photoelectron scattering with left-hand and right-hand circularly polarizations and (Lower) the polar plot presentations of PECD of S-methyl oxirane at varied photon energies.

[1] H. Kohguchi, Y. Hikosaka, T Kaneyasu, S. Wada and Y-I. Suzuki, UVSOR Activity Report 2019 **47** (2020) 107.

[2] G. A. Garcia, H. Dossmann, L. Nahon, S. Daly and I. Powis, Phys. Chem. Chem. Phys. **16** (2014) 16214.

BL1U

Photoionization of Atoms by Double-pulsed Radiation from a Tandem-Undulator

T. Kaneyasu¹, Y. Hikosaka², S. Wada³, M. Fujimoto^{4,5}, H. Ota⁴, H. Iwayama^{4,5}
and M. Katoh^{6,4}

¹SAGA Light Source, Tosu 841-0005, Japan

²Institute of Liberal Arts and Sciences, University of Toyama, Toyama 930-0194, Japan

³ Graduate School of Advanced Science and Engineering, Hiroshima University,
Higashi-Hiroshima 739-8526, Japan

⁴Institute for Molecular Science, Okazaki 444-8585, Japan

⁵The Graduate University for Advanced Studies (SOKENDAI), Okazaki 444-8585, Japan

⁶Hiroshima Synchrotron Radiation Center, Hiroshima University, Higashi-Hiroshima 739-0046, Japan

Recently, we have shown a new ability of a tandem-undulator in a synchrotron to perform wave packet interferometry using double-pulsed light wave packets. This has enabled the quantum manipulation of the atomic system, so-called coherent control, by synchrotron radiation. The potential of this method has been demonstrated in the proof-of-principle experiments on gas-phase atoms [1-3]. In these experiments, we used a double-pulsed light wave packet to produce a pair of electron wave packets (superposition of eigenstates) that interfere in the single atom. The quantum phase difference between the interfering electron wave packets determines the behavior of the quantum state to be controlled or probed, and is precisely controlled by varying the time delay between the double-pulsed components of light wave packet in the attosecond level.

Here, we extend this approach to the electron wave packets produced in an ionization continuum. The experiment was carried out at the undulator beamline BL1U. The double-pulsed light wave packet was generated by a tandem-undulator in the synchrotron ring. The waveform of the light wave packet was characterized by time-separated 10-cycle oscillations. The fundamental radiation wavelength was set to ~40 nm. The double-pulsed light wave packet interacted with a helium atom, leading to the production of a pair of photoelectron wave packets that interfere in free space. To verify the interference between the photoelectron wave packets, we measured a photoelectron spectrum using a hemispherical electron analyzer fixed at an angle of 55° with respect to the polarization axis.

Figure 1 compares the photoelectron spectra measured for the radiation from a single undulator (a and b) and tandem-undulator (c and d) configuration. The photoelectron spectra in a and b show single peaked distributions centered at around 5 eV. This spectral shape simply reflects the spectral distribution of the radiation from the single undulator which is characterized by a Gaussian-like distribution with 10 % width of the central photon energy. In contrast, the photoelectron spectra show clear interference patterns when the tandem undulator is used to ionize the helium atoms. Moreover, the spacing between interfering fringes

depends on the time separation between the double-pulsed components of the light wave packet. To interpret the experimentally measured data, we have calculated the photoelectron spectrum (not shown here), and a good agreement between the experimental and calculation results is obtained. Therefore, it is reasonable to conclude that we observed the interference between the photoelectron wave packets in the present study.

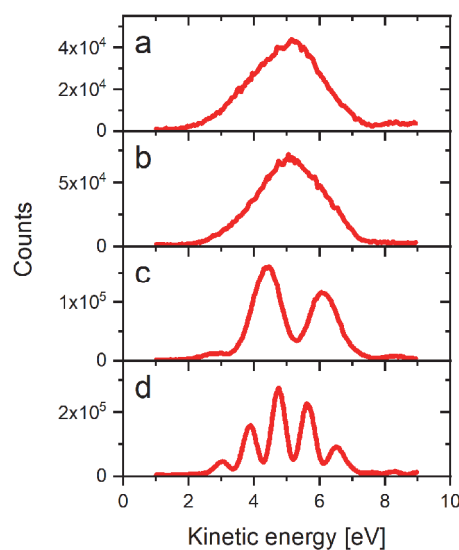


Fig. 1. Photoelectron spectra of helium atoms measured by using radiation from (a) upstream undulator, (b) downstream undulator, (c) and (d) tandem undulator. The time delays between the double-pulsed components of light wave packet are (c) 2 fs and (d) 4.5 fs.

[1] Y. Hikosaka *et al.*, Nat. Commun. **10** (2019) 4988; *ibid.* **12** (2021) 3782.

[2] T. Kaneyasu *et al.*, Phys. Rev. Lett. **123** (2019) 233401.

[3] T. Kaneyasu *et al.*, Phys. Rev. Lett. **126** (2021) 113202.

BL2B

Electronic State Changes of Cu Nanoparticles on Rutile TiO₂(110) by CO Exposure

K. Mitsuhashi¹, K. Ide², H. Takatani², Y. Hasegawa² and M. Takizawa²

¹Ritsumeikan Global Innovation Research Organization, Ritsumeikan University, Kusatsu 525-8577, Japan

²Department of Physical Science, Faculty of Science and Engineering, Ritsumeikan University, Kusatsu 525-8577, Japan

For Cu based catalysts, it exhibits strong catalytic activities for the carbon monoxide oxidation, water-gas shift reaction, methanol oxidation and others [1]. However, their performance is not fully understood. In previous study, we have found the growth mode of Cu nanoparticles deposited on the rutile TiO₂(110) surfaces by medium energy ion scattering (MEIS) [2]. As a result, the two-dimensional (2D) islands grow initially up to Cu coverage of ~0.5 ML and then the three-dimensional (3D) island-growth becomes dominant. The electronic state of supported metal particles is also known to play a critical role in determining catalytic activity. Understanding the adsorbate-induced changes in the surface electronic state is therefore important. In this study, we manifest the reaction of Cu nanoparticles supported rutile TiO₂(110) with carbon monoxide by photoelectron and photon-induced secondary electrons emission spectroscopy.

The experiment was performed at beamline BL2B of the UVSOR synchrotron factory at the Institute for Molecular Science. We prepared the oxygen-rich rutile TiO₂(110) surfaces (O-TiO₂) by exposure of O₂ (5 N) onto the reduced surfaces (R-TiO₂), which were formed by sputtering with 0.75 keV Ar⁺ followed by annealing at 870 K for 10 min in UHV. Cu was deposited on the clean surfaces at RT with a Knudsen cell at a rate of 0.08 ML/min under UHV condition. Here, 1 ML means 1.77×10^{15} atoms/cm², corresponding to the areal density of Cu(111).

Figure 1 (a) shows secondary electron spectra taken for Cu(0.2 ML)/O-TiO₂(110) and oxidized Cu(0.2 ML)/O-TiO₂(110) before and after CO exposure, respectively. After O₂ exposure of 500 L, the work function increases. This electronic state changes indicate an upward band bending. The mechanism of this upward band bending may be considered as follows: Cu nanoparticles are oxidized to Cu₂O by oxygen exposure and then the upward band bending is caused by a p-n junction between Cu₂O and TiO₂ substrate. After CO exposure of 15,000 L, the work function slightly decreased, while the valence band spectra and Ti 3p and O 2s lines did not change nor shift significantly (not shown). The change in work function showed the same tendency even for Cu coverage of 1.0 ML [see Fig.1 (b)]. The work function of TiO₂(110) surfaces scatter largely owing to strong dependence upon bulk and surface defect densities. Note that work function consists of bulk and surface dipole terms and the surface term originates from a surface dipole consisting of positive

cores and valence electrons near a surface. Therefore, this result is ascribed to elimination of the electronegative adsorbate oxygen on top of the surface resulting in weakening the surface dipole with a negative polarity on the vacuum side. These results may suggest that presence of Cu nanoparticles on O-TiO₂(110) strongly enhances the reaction between O and CO.

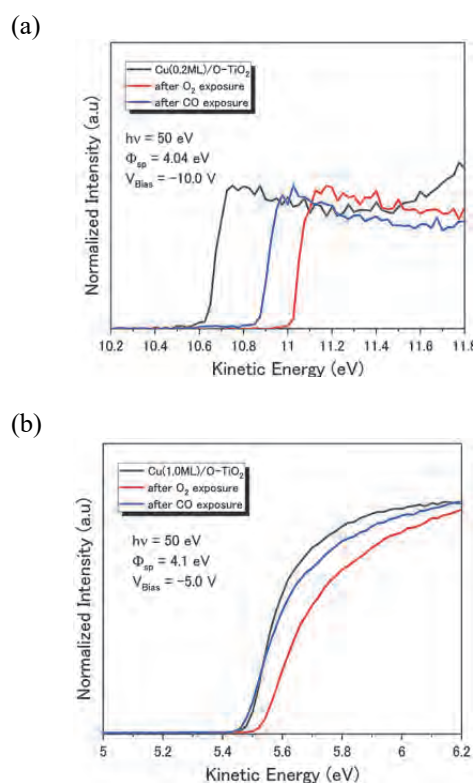


Fig. 1 Secondary electron spectra taken for (a) Cu(0.2 ML)/O-TiO₂(110) and (b) Cu(1.0 ML)/O-TiO₂(110) before and after CO exposure

[1] J. M. Thomas *et al.*, Principles and Practice of Heterogeneous Catalysis, VCH, New York, 1997.

[2] T. Aoki *et al.*, *e-J. Surf. Sci. Nanotechnol.* **16** (2018) 225.

BL3U

X-ray Absorption Spectra of Aqueous Cellobiose

T. Sasaki and D. Akazawa

Department of Complexity Science and Engineering, Graduate School of Frontier Sciences, The University of Tokyo, Kashiwa 277-8561, Japan

Biomass conversion using water or an ionic liquid as a solvent without using an organic solvent is an important research topic. There have been many studies on biomass-related compounds in solution, but there are few reports on their molecular theory. We have studied the conversion process by dehydration reaction of polyalcohol as models of sugar molecules and found that the solvation structure with water molecules and the interaction with protons are important for the reaction process [1,2].

The purpose of this study is to explore the solvation structure of sugar molecules in aqueous solution, which is important in the conversion process from cellobiose to glucose, that is typical of biomass-derived sugar alcohol conversion using water or ionic liquids. Cellobiose, a disaccharide, is taken up as a model substance for cellulose, which is one of the starting materials in biomass conversion.

XAS measurements for liquid samples were conducted at UVSOR BL3U using facilities developed by Nagasaka et al. [3]. The liquid sample cell with Si_3N_4 membranes was adopted, where the thickness of the liquid layer was controlled by the He gas pressure around the cell.

Figure 1 shows C-K edge XAS spectra for cellobiose aqueous solutions with concentrations specified in the figure. Fig. 2 shows O-K edge XAS spectra for cellobiose aqueous solutions as well as the spectrum for water (0 M). Molecular dynamics calculations for the solutions and the XAS simulations were conducted using CP2K program to interpret the XAS spectra.

In Fig. 1 three peaks were observed at 289.3, 290.7 and 293.6 eV, named as “A”, “B”, and “C”, respectively. A peak at 290.0 eV was defined as “A’”, which does not appear for the aqueous solution but is expected to appear in the gaseous isolated cellobiose molecule as found by MD and XAS simulation. With the XAS simulation it was concluded that A, B and C correspond to the absorption by carbon atoms of the alcohol group, the hemiacetal group and the both of these groups, respectively. Temperature and concentration dependences of XAS spectra for cellobiose aqueous solutions were measured and relative intensity change of three peaks were observed, which can be explained by the change in the number of hydrogen bond between cellobiose and water. These results were published recently [4]. The analysis of O-K XAS spectra for cellobiose aqueous solutions is under way.

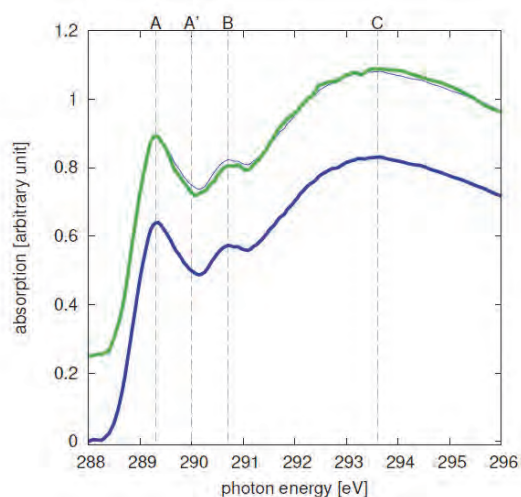


Fig. 1. C-K XAS spectra for cellobiose aqueous solutions at 25 °C. Blue : 0.20 M, Green : 0.15 M.

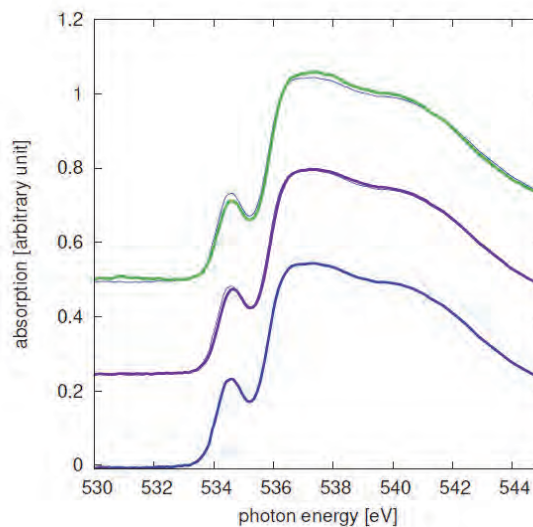


Fig. 2. O-K XAS spectra for cellobiose aqueous solutions at 25 °C. Blue : 0 M, Purple : 0.20 M, Green : 0.05 M.

- [1] Y.L. Chang *et al.*, *J. Phys. Chem. B.* **123** (2019) 1662.
- [2] T. Kondo *et al.*, *J. Computational Chem.* **42** (2021) 156.
- [3] M. Nagasaka *et al.*, *J. Electrosc. Relat. Phenom.* **200** (2015) 293.
- [4] D. Akazawa *et al.*, *J. Chem. Phys.* **156** (2022) 044202.

BL3U

X-ray Absorption Spectroscopy Study of 4-MBA on Gold Surfaces

I. Sakaida¹, S. Ohno¹, M. Nagasaka²¹Graduate School of Engineering Science, Yokohama National University, Yokohama 240-8501, Japan²Institute for Molecular Science, Okazaki 444-8585, Japan

It is important to understand the behavior of biomolecules on solid surfaces for the application to medical device, biosensor and biocompatible material. It is essential to study the adsorption and desorption behavior of molecules and their response to the applied fields. It is of particular importance to analyze the dynamic behavior of biomolecules on surface in electrolyte solutions close to the realistic condition in the body of living creatures [1,2]. However, the number of studies appears to be still quite limited, especially for the investigation of the dependence of the molecular orientation and ionization on the electrolyte solutions.

In this study, potential-dependent adsorption/desorption behavior of 4-mercaptobenzoic acid (4-MBA) on Au(111) and Au membrane surfaces have been investigated using soft X-ray absorption spectroscopy (XAS) in the fluorescence yield mode for the former case, and in the transmission mode in the latter case. The experiments were performed on the soft X-ray undulator beam line at UVSOR-III, BL3U. We used NaClO₄ as the electrolyte solution. For the adsorption of 4-MBA molecules, the samples were immersed in 1mM 4-MBA/ethanol solution for more than 30 min.

In our previous study, we have studied the adsorption/desorption behavior of 4-MBA on Au films using surface differential reflectance spectroscopy (SDRS) combined with cyclic voltammetry (CV) [3]. The key issue was the interaction between functional group (-COOH) and Au films through Coulomb interaction depending on the applied biases and pH conditions. Redox processes involving charge transfer were clearly observed CV and the relation between the change in the reflectance spectra were investigated in detail. Interestingly, we found some precursor phenomena to cause significant changes in the reflectance spectra with no corresponding signal in the cyclic voltammogram. This indicates that the such changes in the reflectance spectra are not related to the charge-transfer-type reactions but rather to the subtle change in the orientation/conformation of 4-MBA molecules.

To our knowledge, there has been no serious effort to study the 4-MBA/Au system using XAS. We, therefore, tried to investigate the possible precursor phenomena addressed above. Firstly, we have tried to observe the effects on Au(111). However, we could not obtain the clear data showing the adsorption/desorption behavior of 4-MBA. This could be understood because of the relatively low signal-to-noise ratio in the fluorescence yield mode, and the amount of the adsorbed 4-MBA might be less than the detection limit. In order to improve the surface sensitivity, we next tried to observe

the effects on membrane Au surface.

Our preliminary results showed clear spectral features in the O K-edge region, as shown in Fig. 1. One is due to the π^* component assigned to the C=O double bond, and the other is possibly due to the formation of the hydrogen bond. The investigation of the C K-edge region is underway.

The next step should be the observation of the slight effects due to the change in the orientation/conformation depending on the applied bias to the electrode (Au membrane). Obviously, we have to conduct the surface-sensitive measurements further to elucidate such subtle effects.

It should be noted that more distinct change in the XAS spectra can be envisioned in the case of cysteine molecules, for which two of them can attach to form a cystine molecule [3]. At this point, we have established the measurement set up for the transmission mode. Therefore, we now also plan to re-investigate the reactions of biomolecules, in terms of the ionization of the functional groups (-COOH, -NH₃).

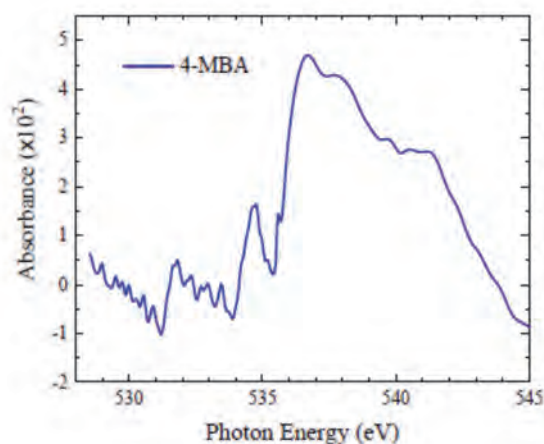


Fig. 1. O K-edge XAS spectrum for 4-MB.

- [1] R. LeParc *et al.*, *Langmuir* **22** (2006) 3413.
- [2] C. I. Smith *et al.*, *J. Electrochem. Soc.* **150** (2003) 1.
- [3] N. Ikeda *et al.*, *ALC'19, AP-52* (2019) 22.

BL3U

Resonant Soft X-ray Scattering Equipment Evaluated by Chicken Leg's Collagens and 100-nm Silica Nanoparticles

H. Iwayama^{1,2}, F. Araoka³ and Y. Takanishi⁴

¹UVSOR Synchrotron Facility, Institute for Molecular Science, Okazaki 444-8585, Japan

²School of Physical Sciences, The Graduate University for Advanced Studies (SOKENDAI), Okazaki 444-8585, Japan

³RIKEN Center for Emergent Matter Science, Wako 351-0198, Japan

⁴Faculty of Science, Kyoto University, Kyoto 606-8502, Japan

Resonant Soft X-ray Scattering (RSoXS) is similar to Small Angle X-ray Scattering (SAXS) and can provide information on the mesoscopic structure (1 ~ 100 nm) of samples. Due to the resonance process, RSoXS have selectivities of elements, functional groups and molecular orientations. In particular, since soft x-ray region include K-edge energies of light element such as carbon, nitrogen and oxygen, RSoXS will be a powerful tool to investigate soft matter, which mainly consists on light element atoms. In 2020, we started to develop RSoXS equipments and succeeded in characterizing liquid-crystal materials. To improve an accuracy of our RSoXS equipments, we measured chicken collagen and silica nanoparticles as standard substances.

Our RSoXS measurements were performed at UVSOR BL3U. Figure 1 shows a schematic draw of an experimental setup. Samples of chicken leg's collagen and 100nm-silica nanoparticle were fixed on Si₃N₄ membranes. The photon energy is 284 eV. Scattering light were detected by soft x-ray camera (Andor BN940P). This RSoXS equipment covers scattering angles, 2θ , ranging from 0 to 15°.

Figure 2(a) shows a scattering image of the chicken leg's collagens. We find three weak ring structures. From the image, we obtained a scattering intensity as a function of scattering vector, q , which are shown in Fig. 2(b). Three peaks at $q = 0.105, 0.212, 0.320 \text{ nm}^{-1}$ indicates that the sample of the chicken collagen have periodic structure of 59.3 nm, which is slightly different from the reference value of 63.8 nm.

Figure 3(a) shows a scattering image of 100-nm (diameter) silica nanoparticles. We find striped ring structures. From the image, we also obtained a scattering intensity as a function of scattering vector, q . As shown in Fig. 3(b), we find oscillation structures. By using theoretical equation of a scattering intensity for spherical sample, we fitted experimental curves with those of the 110-nm nanoparticle.

Thus experimental results are slightly different from actual values, suggesting that we need the standard sample for calibrations of our RSoXS equipment.

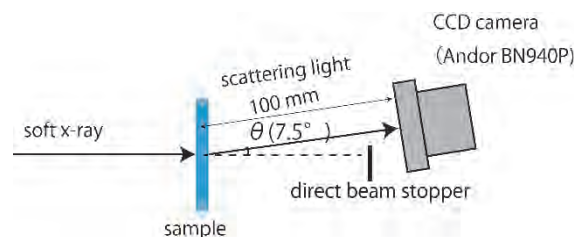


Fig. 1. Schematic view of our RSoXS equipment.

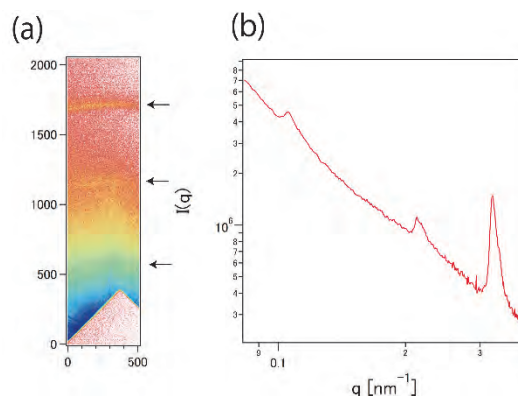


Fig. 2 (a) Scattering image of chicken leg's collagens. The color scale is a log scale. (b) Scattering intensity as a function of scattering vector, q .

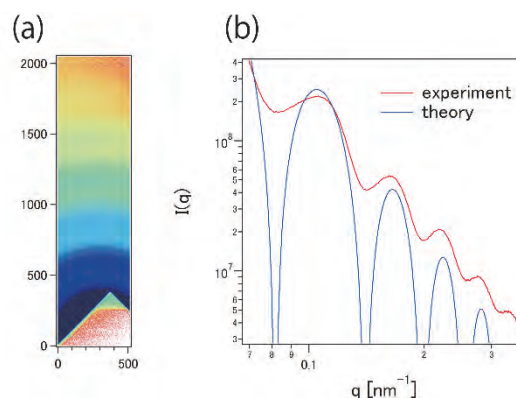


Fig. 3 (a) Scattering image of 100-nm silica nanoparticles. The color scale is a log scale. (b) Scattering intensity as a function of scattering vector, q . Red and blue lines are experimental and theoretical one, respectively.

BL3U

Oxygen K-edge X-ray Absorption Spectroscopy of Aqueous Dimethyl Sulfoxide Solutions at Different Concentrations

M. Nagasaka^{1,2}¹Institute for Molecular Science, Okazaki 444-8585, Japan²The Graduate University for Advanced Studies (SOKENDAI), Okazaki 444-8585, Japan

Dimethyl sulfoxide (DMSO) is a widely used cosolvent, and aqueous DMSO solutions show numerous physical properties that show maxima or minima in the middle concentration region [1]. Several studies determined microscopic structures of aqueous DMSO solutions, where hydrogen bond (HB) structures of S=O groups in DMSO with water are formed and are changed at different molar fractions [2]. However, the mechanism of the HB formation of DMSO with water have not fully understood. In this study, we have studied the concentration dependence of the HB structures of DMSO with water in aqueous solutions by using O K-edge X-ray absorption spectroscopy (XAS).

The experiments were performed at soft X-ray beamline BL3U. O K-edge XAS of aqueous DMSO solutions were measured by using a transmission-type liquid flow cell [3]. Liquid samples are exchanged by a tubing pump without changing the beam positions.

Figure 1 shows O K-edge XAS spectra of aqueous DMSO solutions $(\text{DMSO})_x(\text{H}_2\text{O})_{1-x}$ at different concentrations at 25 °C. In O K-edge XAS of neat water ($x = 0.0$), the pre-edge peak at 535 eV is assigned as the transition of O 1s electron to the $4a_1$ unoccupied orbital in water and reflects HB structures among water molecules, as observed in O K-edge XAS of liquid water at different temperatures [4]. On the other hand, the peak at 532 eV corresponds to the transition of O 1s electron to the S=O π^* orbital in DMSO [5]. From the fitting procedures, we have determined the energy shifts of the pre-edge peaks in water and the first peaks of S=O π^* orbitals in DMSO at the different molar fractions of DMSO.

Figure 2 shows the energy shifts of the first peaks of DMSO S=O π^* orbitals from that of neat DMSO ($x = 1.0$). By increasing the molar fraction of water ($1 - x$), the S=O π^* peaks show the higher energy shifts, which shows two concentration regions with the border of $x = 0.4$. In the DMSO-rich region ($0.4 < x < 1.0$), the slope of the energy shift is $164 \text{ meV} / (1 - x)$. In the water-rich region ($0.05 < x < 0.4$), on the other hand, the higher energy shift of the S=O π^* peak is accelerated ($271 \text{ meV} / (1 - x)$). The pre-edge peaks in water also show characteristic concentration dependence, which shows three concentration regions with the borders of $x = 0.2$ and $x = 0.6$. For revealing the concentration dependence of the energy shifts in O K-edge XAS, we will perform molecular dynamics simulations and inner-shell quantum chemical calculations of aqueous DMSO solutions.

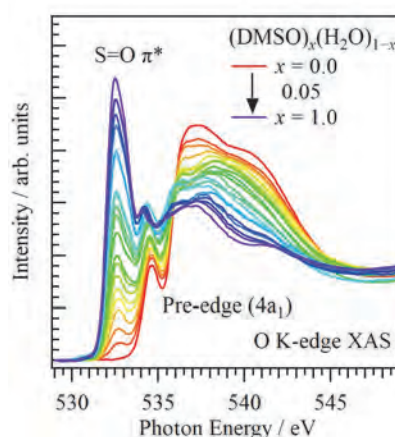


Fig. 1. O K-edge XAS spectra of aqueous DMSO solutions at different concentrations.

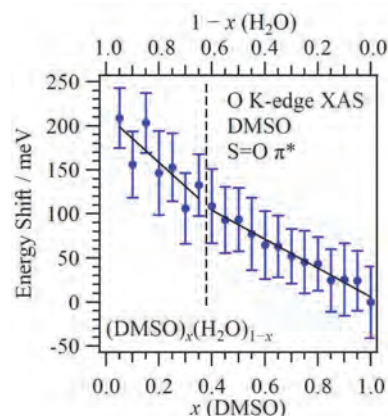


Fig. 2. Energy shifts of the first peaks of DMSO S=O π^* orbitals from that of neat DMSO ($x = 1.0$) as a function of molar fraction of DMSO.

- [1] S. Roy and B. Bagchi, *J. Chem. Phys.* **139** (2013) 034308.
- [2] K.-I. Oh *et al.*, *Angew. Chem. Int. Ed.* **56** (2017) 11375.
- [3] M. Nagasaka and N. Kosugi, *Chem. Lett.* **50** (2021) 956.
- [4] M. Nagasaka *et al.*, *J. Phys. Chem. B* **121** (2017) 10957.
- [5] L. I. Vogt *et al.*, *RSC Adv.* **10** (2020) 26229.

BL3U

Carbon K-edge X-ray Absorption Spectroscopy of Aqueous Ethanol Solutions at Different Concentrations

M. Nagasaka^{1,2}, M. Bouvier¹, H. Yuzawa¹ and N. Kosugi^{1,2}¹Institute for Molecular Science, Okazaki 444-8585, Japan²The Graduate University for Advanced Studies (SOKENDAI), Okazaki 444-8585, Japan

Aqueous ethanol (EtOH) solutions show anomalies of thermodynamic and transport properties [1]. These anomalies would be occurred by the intermolecular interactions between EtOH and water (H₂O). In the previous studies, it is suggested that the EtOH-H₂O mixed clusters are formed in the middle concentration region [2] and the hydrophobic hydration of EtOH is formed in the low concentration region [3]. In this study, we have investigated the local structures around the ethyl group in EtOH by using carbon K-edge X-ray absorption spectroscopy (XAS) of aqueous EtOH solutions at different concentrations.

The experiments were performed at soft X-ray beamline BL3U. C K-edge XAS of aqueous EtOH solutions were measured by using a transmission-type liquid flow cell [4]. Liquid samples are exchanged by a tubing pump without changing the beam positions.

Figure 1(a) shows C K-edge XAS spectra of aqueous EtOH solutions at different concentrations at 25 °C. Each spectrum is fitted by four peaks, where peak A is the lowest peak around 287.3 eV. Figure 1(b) shows the energy shifts of peak A relative to that of liquid EtOH ($x = 1.0$) as a function of the molar fraction of EtOH (x). We have found that the energy shift of peak A shows four concentration regions (I, II, III, and IV). In the region I ($1.0 > x > 0.8$), peak A shows the lower energy shift by increasing the molar fraction of H₂O. In the region II ($0.8 > x > 0.25$), peak A shows the slightly higher energy shift by increasing the molar fraction of H₂O. The lower energy shift of peak A is observed in the region III ($0.25 > x > 0.15$) and is accelerated by increasing the molar fraction of H₂O in the region IV ($0.15 > x > 0.05$).

From the inner-shell quantum calculations, we have investigated the molecular interaction between EtOH and H₂O at the four concentration regions. In the region I, the hydrogen bond (HB) structure of EtOH – EtOH is simply substituted to that of EtOH – H₂O. In the region II, the EtOH clusters are formed by the hydrophobic interactions of the ethyl group in EtOH, resulting in the enhancement of the HB structure of H₂O – H₂O as observed by O K-edge XAS [5]. Whereas a phase-transition like behavior is observed in aqueous methanol solutions [6], there is no phase-transition like behavior in aqueous EtOH solutions due to the strong hydrophobic interactions in EtOH. In the regions III and IV, the size of EtOH clusters becomes smaller, resulting in the increase of the hydrophobic hydration of EtOH in the HB network of H₂O.

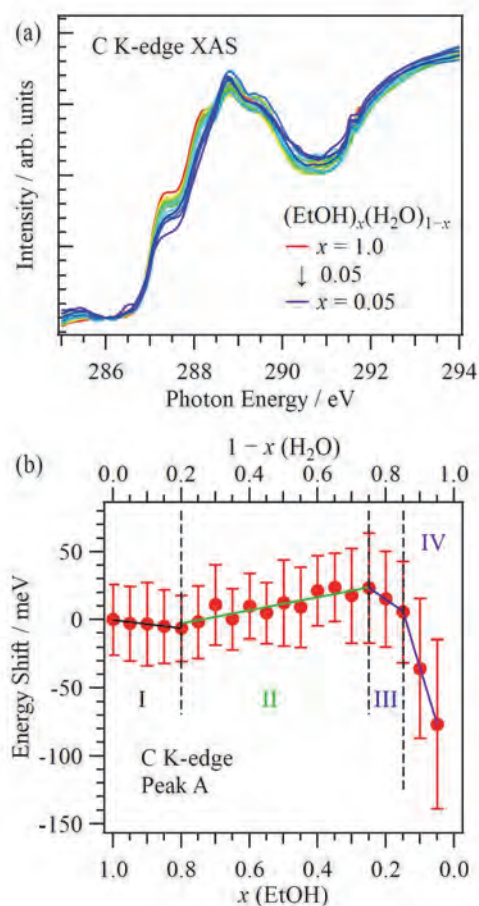


Fig. 1. (a) C K-edge XAS spectra of aqueous EtOH solutions at different concentrations. (b) Energy shifts of peak A relative to that of liquid EtOH ($x = 1.0$) as a function of molar fraction of EtOH (x).

[1] F. Franks and D. J. G. Ives, *Q. Rev. Chem. Soc.* **20** (1966) 1.

[2] K. Nishikawa *et al.*, *J. Phys. Chem.* **97** (1993) 10824.

[3] H. S. Frank and M. W. Evans, *J. Chem. Phys.* **13** (1945) 507.

[4] M. Nagasaka and N. Kosugi, *Chem. Lett.* **50** (2021) 956.

[5] M. Nagasaka *et al.*, *UVSOR Activity Report* 2019 **47** (2020) 114.

[6] M. Nagasaka *et al.*, *J. Phys. Chem. B* **118** (2014) 4388.

BL3U

The C–Si Bond Length of Organosilicon Compounds in Organic Solvent Probed by Carbon K-edge X-ray Absorption Spectroscopy

S. Okumura^{1,2}, M. Nagasaka^{1,2}, H. Takaya^{1,3}, and Y. Uozumi^{1,2}¹Institute for Molecular Science, Okazaki 444-8585, Japan²The Graduate University for Advanced Studies (SOKENDAI), Okazaki 444-8585, Japan³Institute for Chemical Research, Kyoto University, Uji 611-0011, Japan

Although the reactivity of organic compounds is closely related to the bond length at the reactive site, it is difficult to know the bond length in organic solvents experimentally. Soft X-ray absorption spectroscopy (XAS) has a potential to determine the chemical bond since soft X-ray XAS observes electronic structures of light elements such as C, N, O, *etc.* Recently, we have developed liquid flow cells for XAS in transmission mode [1]. Hydration of cyanopyrazine on titanium oxide catalysts has been studied by C K-edge XAS, but this study only observed the reaction kinetics [2]. It is still difficult to reveal the relation of the bond length at the reactive site with the reactivity by soft X-ray XAS. In this study, we have investigated the C–Si bond lengths of the organosilicon compounds in organic solvents, which are key compounds for the Hiyama cross-coupling reaction [3], by using C K-edge XAS.

The experiments were performed at soft X-ray beamline BL3U. C K-edge XAS of the organosilicon compounds in organic solvents were measured by using a transmission-type liquid flow cell [1]. The liquid samples were prepared in argon filled glovebox and were flown to the liquid cell by using a syringe pump. Liquid temperature was set to 25 °C.

Figure 1 shows the C K-edge XAS spectra of 100 mM trimethoxy(phenyl)silane (**1**) in tetrahydrofuran (THF), ethylene glycol-derived pentacoordinate spiro-silicate (**2**) in ethylene glycol, and fluorotrimethoxy(phenyl)silicate (**3**) in THF solution. The peak around 285 eV in silane **1** is assigned as the transition from the C 1s orbital to the C=C π^* unoccupied orbital in the phenyl group. This peak is fitted by three peaks: Peak A is the transition from the C atom bonded with Si, peak B is that from the ortho sites, and peak C is that from the meta sites in the phenyl group. It means that peak A reflects the C–Si bond lengths of the organosilicon compounds. The energy position of peak A in silane **1** is 284.56 eV. The peak A in silicates **2** and **3** show lower energy shifts by -0.02 eV and -0.06 eV from that in silane **1**, respectively. We have performed the structural optimization of these organosilicon compounds by the quantum chemical calculations and found that the C–Si bond length becomes longer with the order of compounds **1**, **2**, and **3**. C K-edge inner-shell calculations revealed that the peak A shows lower energy shifts by increasing the C–Si bond lengths. These results are consistent with the experiments. Therefore, it is revealed that due to the longer C–Si bond of silicate **2**, it showed the higher reactivity in the Hiyama cross-coupling reaction than

that of silane **1**. On the other hand, the reactivity of silicate **3** was lower than that of silane **1** despite the longest C–Si bond length [4]. The inertness of silicate **3** would be caused by other factors such as a steric barrier, which is now investigating by the quantum calculation of the transition state in the reaction.

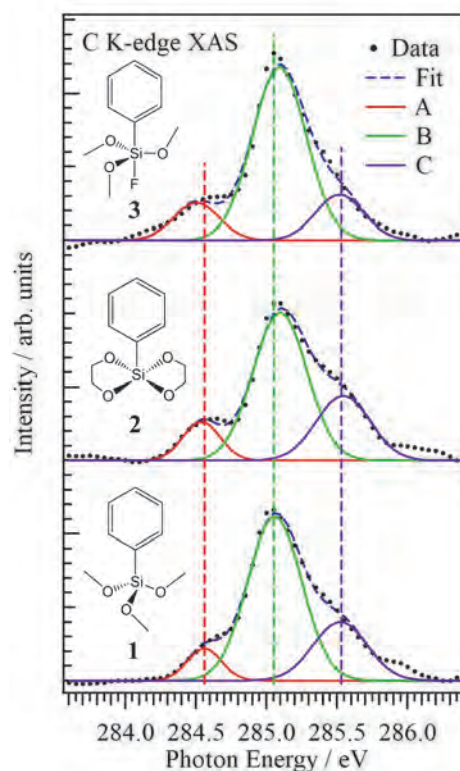


Fig. 1. C K-edge XAS spectra of compounds **1**, **2**, and **3** in THF or ethylene glycol. Dashed lines show the peak positions of silane **1** obtained by curve fitting procedures.

[1] M. Nagasaka and N. Kosugi, *Chem. Lett.* **50** (2021) 956.

[2] H. Yuzawa, M. Nagasaka and N. Kosugi, *J. Phys. Chem. C* **119** (2015) 7738.

[3] S. Ichii, G. Hamasaka and Y. Uozumi, *Chem. Asian J.* **14** (2019) 3850.

[4] C. Amatore *et al.*, *Angew. Chem. Int. Ed.* **53** (2014) 6982.

BL3U

Direct Observation of a High Valent Oxo Species of a μ -Nitrido-Bridged Iron Phthalocyanine Dimer Deposited on a Graphite Surface in Aqueous Solution by Soft X-ray Absorption Spectroscopy

Y. Yamada^{1,2} and M. Nagasaka³¹Department of Chemistry, Graduate School of Science, Nagoya University, Nagoya 464-8602, Japan²Research Center for Materials Science, Nagoya University, Nagoya 464-8602, Japan³Institute for Molecular Science, Okazaki 444-8585, Japan

Methane is abundant in nature as natural gas or methane hydrate. Therefore, efficient conversion of methane into valuable raw chemicals such as methanol is highly desired in order to use methane as a next-generation carbon resource. However, since high chemical stability of methane prevent its efficient C-H bond activation, development of novel catalysts that allow facile C-H bond dissociation of methane under mild reaction condition is indispensable. We recently found that a μ -nitrido-bridged iron phthalocyanine dimer adsorbed on a graphite surface **1** (Fig. 1) efficiently convert methane into methanol, formaldehyde, and formic acid in an acidic aqueous solution containing H_2O_2 at a temperature below than 100 °C. It was demonstrated that **1** showed one of the most potent methane oxidation activity among a variety of molecule-based catalysts and its activity was almost comparable as that of natural particulate methane monooxygenase (pMMO)[1]. Although its reactive intermediate was confirmed to be a high valent iron-oxo species **1_{oxo}** generated by the reaction with H_2O_2 , the electronic structure of **1_{oxo}** has never been investigated. In our previous report, we confirmed that it is possible to observe **1_{oxo}** directly by XAS under vacuum by using a highly oriented pyrolytic graphite (HOPG) substrate modified with the μ -nitrido-bridged iron phthalocyanine dimer. In this study, we attempted to observe the conversion of **1** into **1_{oxo}** in an aqueous solution by using XAS.

We first prepared a SiN membrane tip modified by **1** (Fig. 2a). A SiN membrane tip coated by 20 nm thickness of carbon membrane was dipped in a pyridine solution of the μ -nitrido-bridged iron phthalocyanine dimer. It was confirmed that the μ -nitrido-bridged iron phthalocyanine dimer was successfully deposited on the carbon surface of the SiN membrane tip by detecting the Fe L-edge XAS signals.

The SiN substrate modified with **1** was used for the XAS measurement in an aqueous solution by using a beamline equipped with a transmission-type liquid flow cell in BL3U of UVSOR [2]. The O K-edge XAS spectra of **1_{oxo}** formed by the reaction with H_2O_2 were obtained by using the Lambert-Beer law, $\ln(I_0/I)$, where I_0 and I are the transmission signals of **1** in pure water and **1** in a 0.5 % H_2O_2 aqueous solution, respectively.

It was found that the peak at around 532.5 eV was significantly increased after treatment with H_2O_2 (Fig. 2b). DFT calculation suggested that the peak assignable

to the excitation of $\text{O}1s - \pi^*$ of $\text{Fe}=\text{O}$ for **1_{oxo}** should be observed at around 529 eV (Fig. 2c), whereas the peaks for **1** having a coordinating H_2O should be observed at higher energy than 534 eV as shown in Fig. 2d (Fig. 2d). Therefore, it is considered that the peak appeared at around 532.5 eV is assignable to the excitation of $\text{O}1s - \pi^*$ of $\text{Fe}=\text{O}$ for **1_{oxo}**. Next, we are going to observe the electrochemically generated **1_{oxo}** in H_2O .

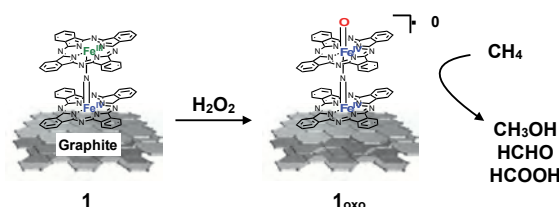


Fig. 1. Potent methane oxidation catalyst **1** and its reactive species **1_{oxo}**.

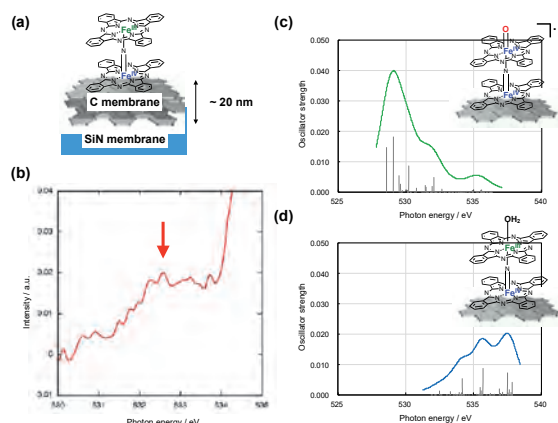


Fig. 2. (a) Structure of a SiN tip coated with **1**, (b) Comparison of O K-edge XAS spectra of **1** before and after treatment with H_2O_2 . DFT-calculated O K-edge XAS spectra for **1_{oxo}** (c) and **1(OH₂)** (d).

[1] Y. Yamada, M. Nagasaka *et al.*, Chem Rxiv. DOI : <https://doi.org/10.26434/chemrxiv.14728860.v1>.
[2] M. Nagasaka and N. Kosugi, Chem. Lett. **50** (2021) 956.

BL3U

Soft X-ray Absorption of Photocatalysts for Artificial Photosynthesis: A Feasibility Study under Ultraviolet Light Irradiation

H. Onishi^{1,2}, T. Hirai¹, N. Ichikuni³ and T. Yoshida⁴

¹School of Science, Kobe University, Kobe 657-8501, Japan

²Division of Advanced Molecular Science, Institute for Molecular Science, Okazaki 444-8585, Japan

³Graduate School of Engineering, Chiba University, Chiba 263-8522, Japan

⁴Reserch Center for Artificial Photosynthesis, Osaka City University, Osaka 558-8585, Japan

Sodium tantalate (NaTaO_3) is a semiconductor photocatalysts which produces hydrogen–oxygen mixed bubbles in the overall water splitting reaction, when properly doped with metal cations [1]. We are conducting a series of studies to answer the question of why doping with metal cations raised the quantum yield of the reaction. Here, soft X-ray absorption is applied for characterizing the electronic structure of the photocatalysts in the presence and absence of ultraviolet (UV) light for bandgap excitation.

NaTaO_3 particles doped with and without Sr cations were prepared thorough a solid-state reaction. Oxygen K-edge absorption of the particles was observed in vacuum at room temperature with total electron yield. Figure 1 shows the spectra of the pristine, undoped particles.

The spectrum in the absence of UV light was well fitted with three Gaussian functions peaked at 531.8, 532.8, and 537.2 eV (upper panel). The first and second peaks were assigned to electron transition from oxygen 1s to 2p states which were covalently hybridized with t_{2g} states of Ta 5d orbitals. The third peak present at a larger photon energy was assigned to the transition to oxygen 2p states hybridized with e_g states of the Ta orbitals. NaTaO_3 is a perovskite-structured compound involves TaO_6 octahedra, which provide the 5d orbitals split into t_{2g} and e_g states.

When the photocatalyst particles were irradiated with steady UV light produced by a 200-W Hg–Xe lamp, absorption related to the t_{2g} final states, the first peak at 531.8 eV in particular, weakened relative to the third peak, as presented in the lower panel of Fig. 1. A possible reason of the weakened absorption is the conduction band partially filled with bandgap-excited electrons. The density of vacant states, the final states of the K-edge absorption, should have decreased by the electrons excited from the valence band. Covalent hybridization of the oxygen 2p and Ta 5d orbitals would also be limited to weaken 5d-states character of the final states [2], since the oxidation state of Ta cations decreased from +5 to 4+ by the bandgap excitation.

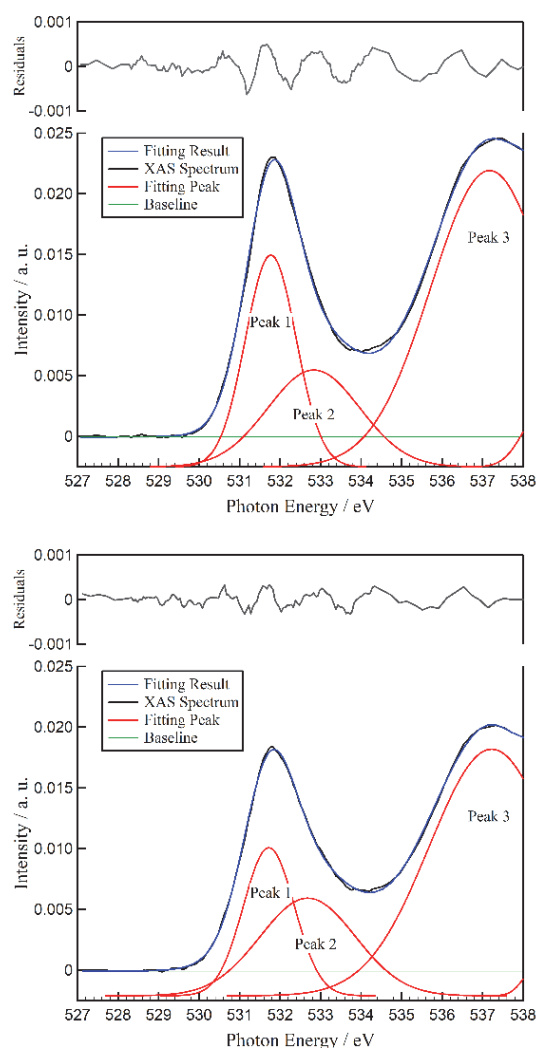


Fig. 1. Oxygen K-edge absorption spectra of pristine NaTaO_3 photocatalyst particles observed in the absence (upper panel) and presence (lower panel) of UV light for bandgap excitation. The observed spectra (black curves) were fitted with Gaussian functions (red curves). The spectra reconstructed with the functions (blue curves) are shown with residuals (thin black curves at the top).

[1] H. Onishi, *ChemSusChem* **12** (2019) 1825.

[2] F. Frati, M. O. J. Y. Hunault, F. M. F. de Groot, *Chem. Rev.* **120** (2020) 4056.

BL3U

Variation of the Resonance Band of Water in Soft X-Ray Absorption Spectra of Aqueous Acetone Solutions

K. Okada^{1,2}, C. Sugahara², H. Iwayama^{3,4} and M. Nagasaka^{3,4}

¹Graduate School of Advanced Science and Engineering, Hiroshima University, Higashi-Hiroshima 739-8526, Japan

²School of Science, Hiroshima University, Higashi-Hiroshima 739-8526, Japan

³Institute for Molecular Science, Okazaki 444-8585, Japan

⁴School of Physical Sciences, The Graduate University for Advanced Studies (SOKENDAI), Okazaki 444-8585, Japan

Acetone is miscible with water in any ratio. The binary mixture is a typical aprotic–protic solvent system [1]. A role of the acetone molecule acting as a hydrogen-bond acceptor adds characteristic properties of water. For instance, the partial molar volume of water in this mixture is 14.25 cm³/mol at 25 °C [2], which is much less than the molar volume of water. Such specific water molecules have a different electronic structure from that of bulk water. The study of the electronic structure of hydrated water is of essential importance because it provides fundamental information on the structure of aqueous solutions in general (e.g., [3]). In this report the O K-edge absorption spectra with various fractions of acetone are recorded for extracting the hydrated water components through an excess function: We expect that there exists some correlation between the hydration and a deviation from Beer's law at some photon energy.

Photoabsorption spectra of the solutions were measured in the oxygen K-edge region on the soft X-ray beamline, BL3U. A pair of windows made of thin silicon nitride membrane was used for the sample cell. The incident photon energy was calibrated to the peak at 530.88 eV of a polymer film [4]. The absorption coefficient was evaluated so as to match the value at 547.85 eV to that tabulated in the database [5]. The sample solutions were prepared by mixing acetone with purified water to give 0–0.50 molar fractions of acetone.

Distinct features are found in the absorption spectra. Figure 1 displays some of the measured absorption spectra of water and aqueous acetone solutions. The π^* resonance peak of acetone located at 531.13 eV for pure liquid is now observed at 531.33 eV for the solution with the molar fraction of acetone of 0.10. The shift depends non-linearly on the molar fraction: The change is larger for a dilute region. The 4a₁ resonance band of water has a peak at 534.56 eV for pure water and at 534.46 eV for the 1:1 molar mixture (not shown in Fig. 1). The change around the molar fraction of 0.25 is noticeable, indicating a greater change in the electronic structure of water around this concentration. Apparent bathochromic shift (or red shift) of the latter resonance peak is reasonable on the basis of chemical shift because the water molecule gets electron-rich if it receives electrons from the carbonyl oxygen of the acetone molecule. One can safely conclude that the absorption component of the hydrated water is embedded in the lower energy side of the band and is

assigned to the resonance transition of water acting as a hydrogen-bond donor.

Further discussion requires a quantitative analysis of the spectra. Additivity of Beer's absorption law is valid for non-interacting mixtures. Conversely, a deviation from the absorption law indicates an extent of interaction between the components. The deviation is expressed as the excess absorbance. The results of the analysis will be published elsewhere.

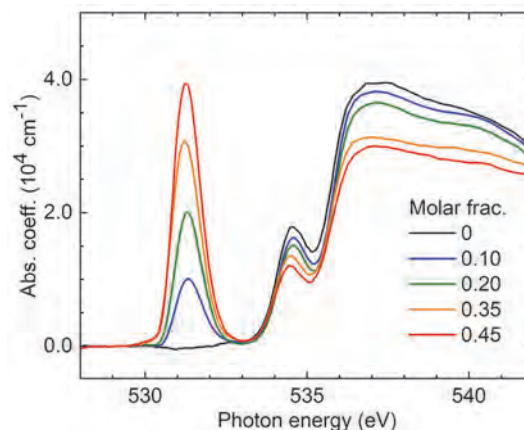


Fig. 1. The O K-edge absorption spectra of liquid water and aqueous acetone solutions measured for a series of molar fractions of acetone.

[1] A. J. Parker, *Quart. Rev. Chem. Soc. (London)* **16** (1962) 163.

[2] E. V. Ivanov, V. K. Abrosimov and E. Y. Lebedeva, *J. Sol. Chem.* **37** (2008) 1261.

[3] S. Ohsawa, T. Tokushima and K. Okada, *J. Phys. Chem. B* **125** (2021) 1881.

[4] M. Nagasaka, H. Yuzawa, T. Horigome and N. Kosugi, *J. Elec. Spectrosc. Relat. Phenom.* **224** (2018) 93.

[5] C. T. Chantler *et al.*, NIST Standard Reference Database 66 (1995; last update in 2005), available at <https://www.nist.gov/pml/x-ray-form-factor-attenuation-and-scattering-tables>.

BL3U

Oxygen K-edge X-ray Absorption Spectroscopy of Molecular Oxygen Adsorbed on Lipid Bilayers

F. Kumaki^{1,2}, M. Nagasaka^{3,4}, Y. Kinjo⁵, R. Tero⁵, Y. Okano³, M. Fujimoto^{3,4} and J. Adachi^{1,2}

¹*Institute of Materials Structure Science, High Energy Accelerator Research Organization, Tsukuba 305-0801, Japan*

²*School of High Energy Accelerator Science, The Graduate University for Advanced Studies (SOKENDAI), Tsukuba 305-0801, Japan*

³*Institute for Molecular Science, Okazaki 444-8585, Japan*

⁴*School of Physical Sciences, The Graduate University for Advanced Studies (SOKENDAI), Okazaki 444-8585, Japan*

⁵*Toyohashi University of Technology, Toyohashi 441-8580, Japan*

Some porphyrin complexes, such as the photosynthetic pigment chlorophyll, are known to produce singlet oxygen ($^1\text{O}_2$) by transferring energy to oxygen molecules that is triplet oxygen ($^3\text{O}_2$) in the surrounding environment at the photo-excitation and relaxation processes due to light absorption. Singlet oxygen is high-reactive. It can cause damage to biological cells or the sample itself in spectroscopic experiments. In generally, the sample solution is bubbled with argon gas to displace the dissolved oxygen to avoid the generation of singlet oxygen at the measurement of a spectrum in visible right region. On the other hand, the process of singlet oxygen generation accompanying with photoexcitation and relaxation processes of photosensitizers such as porphyrin complexes is applied in cancer treatment as photodynamic therapy [1]. Elucidating the dynamics of singlet oxygen production in such a wet environment is expected to contribute to further research of chemistry and medicine.

We designed the way to measure directly the electric states of singlet oxygen occurred in solution by O K-edge x-ray absorption spectroscopy (XAS). Time-resolved XAS measurement system with synchronized soft X-rays pulse (530 eV, 128 ps) and visible laser pulses (400 nm, 130 fs) have been developed and will be applied. The lifetime of singlet oxygen in liquid is 3 μs [2], which can be measured with the 128 ps time resolution of synchrotron radiation. In this measurement, a method to measure a dissolved oxygen spectrum was established as a preliminary step for XAS measurements of singlet oxygen.

The XAS spectrum was measured by using the solution XAS measurement system at UVSOR BL3U [3]. The liquid cell consists of a solution layer sandwiched between two Si_3N_4 membranes. Lipid bilayers were formed on Si_3N_4 membranes by pumping the lipids vesicle aqueous solution to flow into the liquid cell. Then, dissolved oxygen was kept on the lipid bilayers by continuously pumping the buffer solution (NaCl 100 mM, HEPES 25 mM) bubbled with oxygen gas at a flow rate of 100 $\mu\text{l/hr}$. By increasing the helium pressure in the sample chamber and making the solution layer as thin as possible, the spectrum that has the emphasized peak of dissolved oxygen on the lipid bilayer was measured. In the measurement of singlet oxygen, chlorophyll *a*, added as a photosensitizer to the

lipid bilayer, is photoexcited by visible laser with 400 nm which is SH (second order harmonic) of Ti:sapphire laser. We are planning to measure an O K-edge XAS spectrum of the singlet oxygen produced by the energy transfer at the relaxation process of the photo-excited triplet state of chlorophyll *a*.

Figure 1 shows the O K-edge XAS spectrum of liquid bilayer measured in this experiment. The peak at around 531 eV corresponds to dissolved oxygen adsorbed on lipid bilayer which is in the ground state. Since the O K-edge XAS spectrum of water is in higher energy region than 533 eV, the spectrum of dissolved oxygen can be clearly distinguished.

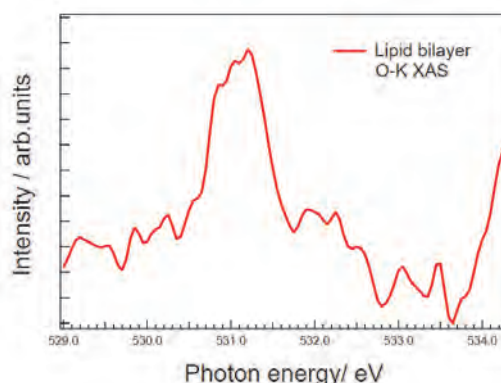


Fig. 1. The O K-edge XAS spectrum of the lipid bilayer. The peak around 531 eV corresponds to a peak of dissolved oxygen adsorbed on the lipid bilayer.

[1] M. Ethirajan *et al.*, Chem. Soc. Rev. **40** (2011) 340.

[2] C. A. Long and D. R. Kearns, J. Am. Chem. Soc. **97** (1975) 2018.

[3] M. Nagasaka *et al.*, J. Electron Spectrosc. Relat. Phenom. **224** (2018) 93.

BL4U

Position-Sensitive Soft X-ray Absorption Spectroscopy of Carbon-based Catalysts for Redox Flow Battery

E. Hosono^{1,2,3}, D. Asakura^{1,2,3}, H. Yuzawa⁴, T. Ohigashi^{4,5} and A. Ohira^{1,2,3}¹Global Zero Emission Research Center, National Institute of Advanced Industrial Science (AIST), Tsukuba 305-8569, Japan²Research Institute for Energy Conservation, AIST, Tsukuba 305-8565, Japan³AIST-UTokyo Advanced Operando Measurement Technology Open Innovation Laboratory (Operando-OIL), Kashiwa 277-8565, Japan⁴UVSOR Synchrotron Facility, Institute for Molecular Science, Okazaki 444-8585, Japan⁵School of Physical Sciences, The Graduate University for Advanced Studies (SOKENDAI), Okazaki 444-8585, Japan

Utilization of renewable energy such as solar cell and wind power is indispensable for reduction of CO₂ emission and realizing zero emission society. To stably use the renewable energy in practical use, development of large-scale energy storage devices is needed. Redox flow battery (RFB) is one of the candidates [1] as well as Li-ion battery (LIB).

The electrolyte solutions of RFB play a role on the redox reaction as both positive and negative electrodes (i.e., catholyte and anolyte) (Fig. 1), which is different from LIB where the solid-state electrodes (cathode and anode) exhibit the redox reaction. The carbon-based electrodes are soaked in electrolyte solutions and H⁺ in the solutions can move through an ion-exchange membrane between the two electrodes by charge/discharge (Fig. 1). To raise the efficiency of the redox and H⁺ conduction, the performance of carbon-based catalysts combined with the electrodes should be investigated. Electronic-structure analysis using soft X-ray absorption spectroscopy (XAS) is suitable for studying the performance. Then, scanning transmission X-ray microscopy (STXM) provides not only the information of electronic structure, but also its distribution with a high spatial resolution (<100 nm). Thus, we adopted STXM at the C K-edge to carbon-based catalysts for RFB. The STXM measurements were conducted at BL4U, UVSOR.

Figure 2 shows a pinpoint C K-edge absorption spectrum (in transmission mode) of a selected area for a graphene sample. The peaks at 285.4 and 291.8 eV in Fig. 2 correspond to π^* and σ^* peaks, respectively [2,3,4]. The weak π^* peak compared to the σ^* peak is similar to the spectrum for graphite with normal incidence [2,3], which suggests that the graphene layers stack along the X-rays. Almost all the area of the graphene particle in the STXM image showed similar XAS line shape. This is important information because the catalytic performance would be dependent on the orientation of stacking. Furthermore, the spectrum shows no peak between the π^* and σ^* peaks, indicating almost no contamination.

In future, we will try *in situ/operando* STXM by constructing a special cell for RFB.

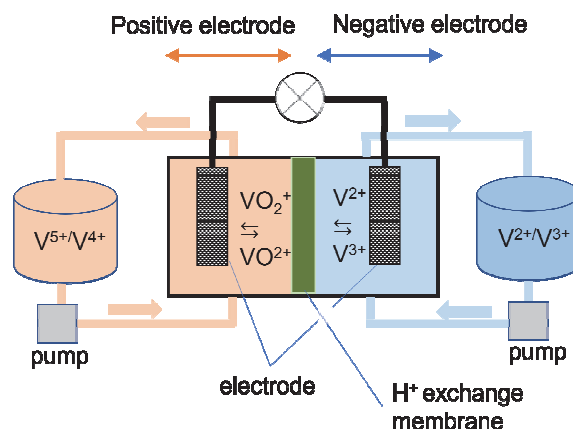


Fig. 1. A schematic picture of RFB using vanadium.

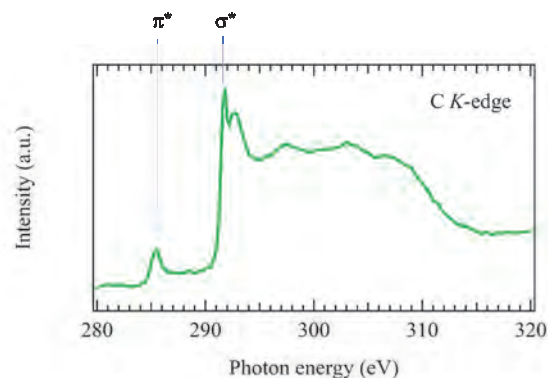


Fig. 2. A pinpoint C K-edge XAS spectrum of a specific area (~ 350 nm \times ~ 180 nm) of the graphene sample.

[1] For example, A. Z. Weber *et al.*, *J. Appl. Electrochem.* **41** (2011) 1137.

[2] M. T. Chowdhury *et al.*, *Phys. Rev. B* **85** (2012) 115410.

[3] M. Abbas *et al.*, *Appl. Phys. Lett.* **87** (2005) 051923.

[4] A. Li *et al.*, *Electrochim. Acta* **276** (2018) 153.

BL4U

Investigating Electrochemical Reactivity on Ni(OH)₂ Electrocatalyst in Alkaline Electrolytes

J. Kim¹ T. Ohigashi^{2,3} and J. Lim¹¹Department of Chemistry, Seoul National University; 1 Gwanak-ro, Gwanak-gu, Seoul 08826, Republic of Korea²Editorial Board, UVSOR Synchrotron Facility, Institute for Molecular Science, Okazaki 444-8585, Japan³School of Physical Sciences, The Graduate University for Advanced Studies (SOKENDAI), Okazaki 444-8585, Japan

During the electrochemical reaction, the phase transformation of energy storage/conversion materials accompanies intrinsic variation on physico-chemical properties. In particular, the energy conversion materials (catalysts) in aqueous system suffer severe chemical and/or morphological changes during reaction. [1] These changes are governed by the thermodynamics that the material exists as a possible stable phase according to pH or potential. In dynamic condition, the locally generated chemical equilibrium induces the evolution of electrochemical active phase in nanoscale, which are responsible for electro- catalytic activity and stability.

Among various energy conversion materials, Ni(OH)₂, which exhibits superior oxygen evolution reaction (OER) activity, experience multiple phase transformation via dehydrogenation process during OER. [2] Specifically, as hydrogen atom is extracted from the lattice, β-Ni(OH)₂ (Ni²⁺) can convert to more oxidized phase such as β-NiOOH (Ni³⁺) and γ-NiOOH (Ni^{3.6+}), and the OER activity is highly dependent on these high valence state of Ni phases. Additionally, lattice oxygen atoms also play an important role in the OER due to bond formation /breaking process with active metal site. An understanding of the active phase evolution and the coordination of oxygen atom with active metal site is a fundamental prerequisite for designing improved OER catalysts, but it remains a crucial challenge to identify the generation and evolution of nanoscale active phase spatially due to a lack of characterization technique. To investigate the evolution of OER active phase (β-NiOOH or γ-NiOOH), we implemented operando scanning transmission X-ray microscopy (STXM) to track the change in Ni oxidation state that indicates the phase transformation of Ni(OH)₂ during OER at the Pohang Light Source STXM beamline 10A1.

Distinctive feature in the phase transformation of β-Ni(OH)₂ is that Ni^{3.6+} phases, γ-NiOOH at 1.70 V versus reversible hydrogen electrode (RHE), are reduced at 1.8 V and 1.9 V versus RHE, where OER is highly occurred. (Fig. 1) From this observation, we speculate that there are two possibilities. First, potassium ion (K⁺) in electrolyte could intercalate into the slab, leading to reduction of the Ni oxidation state owing to the charge neutrality. [2] Second, during OER, oxygen vacancies are generated in the catalyst. [3] To confirm the generation of oxygen vacancies in high anodic potential region, we conducted ex situ STXM measurement of β-

Ni(OH)₂ at UVSOR BL4U for investigating the change in O K-edge absorption spectra.

Figure 2a shows particle-averaged O K-edge spectra of β-Ni(OH)₂ at different potentials, revealing that the pre-peak A (532 eV), assigned to the hybridization of Ni 3d and O 2p orbitals states with e_g orbital symmetry and the d₇ (Ni³⁺) electron configuration, is varied at different potentials. [3] In particular, the intensity of peak A suddenly decreases at 1.65 V, suggesting the return of electrons to Ni site. It can be attributed to the formation of oxygen vacancies and the decreased oxidation state of Ni site. From our results, we conclude that generation of the oxygen vacancy during OER could induce reduction of the active phase (γ-NiOOH), consistent with our operando STXM results.

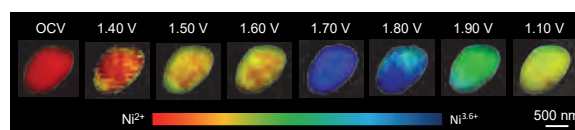


Fig. 1. Operando chemical composition mapping images of β-Ni(OH)₂ electrocatalyst during OER. (Unpublished)

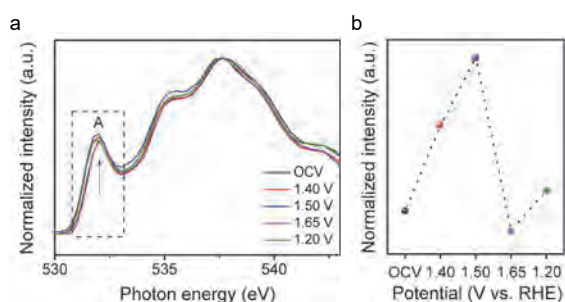


Fig. 1. a. Voltage-dependent particle-averaged O K-edge STXM-XAS spectra. b. Intensity of peak A at different potentials.

[1] Chung, D.Y., Lopes, P.P., Farinazzo Bergamo Dias Martins, P. *et al.*, *Nat Energy* **5** (2020) 222.

[2] Mario González-Perea *et al.*, *ECS Trans.* **36** (2011) 299.

[3] Kang, J., Qiu, X., Hu, Q. *et al.*, *Nat Catal.* **4** (2021) 1050.

BL4B

Quadruple Auger Decay of the Xe $3d_{5/2}$ Core-Hole State Investigated by Multielectron–Ion Coincidence Spectroscopy

Y. Hikosaka

Institute of Liberal Arts and Sciences, University of Toyama, Toyama 930-0194, Japan

Magnetic bottle electron spectrometer is a very efficient electron spectroscopic method, utilizing an inhomogeneous magnetic field to capture all the electrons formed by photoionization. Its use enables us to perform multielectron coincidence spectroscopy very effectively. While the electrons captured over 4π -steradian solid angle are guided to an MCP detector ending a long flight path, ions formed together with electrons can be also detected with the same detector, by applying a pulsed electric field to the photoionization region [1]. To improve the efficiency in multielectron coincidence measurements, an MCP detector with a large open area ratio (nominally 90 %) was recently introduced in our magnetic bottle electron spectrometer [2].

The usefulness of this improved coincidence efficiency is demonstrated by a six-fold coincidence about the quadruple Auger decay of the Xe $3d_{5/2}$ core-hole state. Figure 1 shows energy correlations between the two Auger electrons emitted from $\text{Xe}^{3+} 4d^{-2}5p^{-1}$, which was derived from six-fold coincidences including the $3d_{5/2}$ photoelectron, first-step Auger electron forming $4p^{-1}4d^{-1}$, second-step Auger electron forming $4d^{-2}5p^{-1}$, and Xe^{5+} . The additional coincidence with the product Xe^{5+} ions effectively isolates the events associated with the quadruple Auger decay. On the two-dimensional map in Fig. 1, remarkable island structures are observed in the area indicated by a square. The faster and slower electrons forming the island structures are assignable to the third-step Auger decay of $\text{Xe}^{3+} 4d^{-2}5p^{-1} \rightarrow \text{Xe}^{4+} 4d^{-1}5p^{-3}$ and the fourth-step Auger decay of $\text{Xe}^{4+} 4d^{-1}5p^{-3} \rightarrow \text{Xe}^{5+} 5p^{-5}$, respectively. Essentially the same coincidence structure was observed in a previous multi-electron coincidence measurement [3]. Note that the previous observation was occurred in correlations between two electrons observed in coincidence with the 3d photoelectron and first-step Auger electron, and thus as four-electron coincidences.

One may see that the island structures lie on several diagonal lines defined by $x + y = \text{constant}$. This is because the sums of the two Auger electrons correspond to the energy differences between $\text{Xe}^{3+} 4d^{-2}5p^{-1}$ and $\text{Xe}^{5+} 5p^{-5}$ levels. Here, the appearance of multiple diagonal lines is due to the contributions from different levels of initial $4d^{-2}5p^{-1}$ and final $5p^{-5}$. The right panel of this figure shows the projection of the island structures toward the y axis of the two-dimensional map. The projection curve exhibits sharp peaks due to the fourth-step Auger decay of $\text{Xe}^{4+} 4d^{-1}5p^{-3} \rightarrow \text{Xe}^{5+} 5p^{-5}$. The kinetic energies of the sharp peaks correspond to

the state energies of the $\text{Xe}^{4+} 4d^{-1}5p^{-3}$ levels measured from $^2P_{1/2}$ or $^2P_{3/2}$ of $5p^{-5}$, and thus many different $\text{Xe}^{4+} 4d^{-1}5p^{-3}$ levels are formed through the third-step Auger decay of $\text{Xe}^{3+} 4d^{-2}5p^{-1} \rightarrow \text{Xe}^{4+} 4d^{-1}5p^{-3}$.

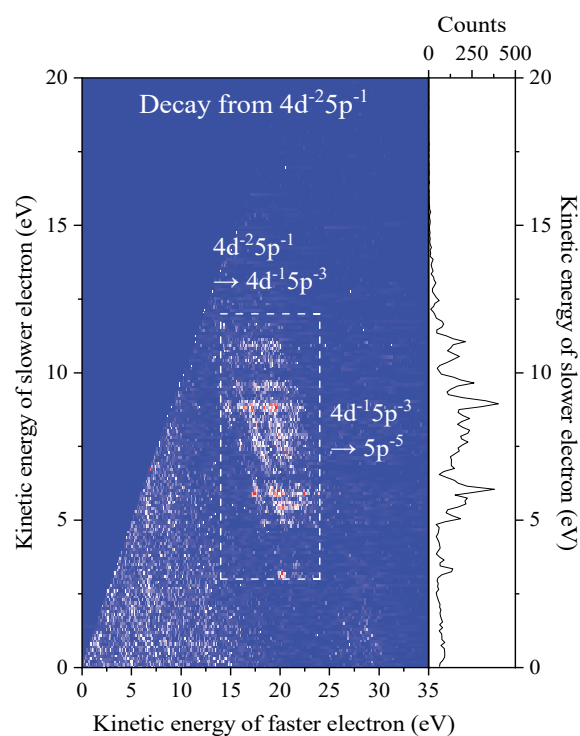


Fig. 1. Energy correlation map between two Auger electrons ejected in the quadruple Auger decay of the Xe $3d_{5/2}$ core-hole state, derived from six-fold coincidences including the $3d_{5/2}$ photoelectron, first-step Auger electron forming $4p^{-1}4d^{-1}$, second-step Auger electron forming $4d^{-2}5p^{-1}$, and Xe^{5+} ion, and thus it displays the energy correlation between the two Auger electrons emitted in the decay of $\text{Xe}^{3+} 4d^{-2}5p^{-1}$. The right panel plots the projection of the coincidence counts in the region $x = 14\text{--}24$ eV toward the y axis, which exhibits the structures resulting from the fourth-step Auger decay of $\text{Xe}^{4+} 4d^{-1}5p^{-3} \rightarrow \text{Xe}^{5+} 5p^{-5}$.

[1] Y. Hikosaka and E. Shigemasa, *Int. J. Mass Spectrom.* **439** (2019) 13.

[2] Y. Hikosaka, *J. Electron Spectrosc. Rel. Phenom.* **255** (2022) 147158.

[3] I. H. Suzuki *et al.*, *J. Phys. B: At. Mol. Opt. Phys.* **44** (2011) 075003.

BL4B

Ion Branching Ratio for the Xe 4p Auger Decay Studied by Photoelectron–Ion Coincidence Spectroscopy

Y. Hikosaka

Institute of Liberal Arts and Sciences, University of Toyama, Toyama 930-0194, Japan

Photoelectron spectroscopy has revealed an anomalous photoelectron structure of the 4p core-hole state in Xe [1]. In a photoelectron spectrum, the expected $4p_{1/2}$ photoelectron line is dissolved and no longer visible, whereas the $4p_{3/2}$ structure consists of several fine components. These observations imply the breakdown of the independent particle model, resulting from the strong interaction between the $4p^{-1}$ and $4d^{-2}nf/4d^{-2}\epsilon f$ configurations [2]. In this work, the ion branching ratio associated with the Auger decay of the 4p core-hole state is inspected. A magnetic bottle electron spectrometer with ion detection capability [3,4] was employed in this study, to conduct an efficient photoelectron-ion coincidence measurement. The measurement was implemented at a photon energy of 391.7 eV (bandwidth of ~ 0.2 eV), *i.e.* ~ 240 eV above the 4p threshold.

Figure 1 presents a photoelectron spectrum of Xe and those filtered by coincidences with different Xe^{Z+} ions ($Z = 1-6$). Photoelectron structures associated with ejections of electrons from the N and O shells are exhibited in these spectra. The ion detection efficiencies were compensated for the spectral intensities of the coincidence spectra; thus, the relative intensities of individual photoelectron structures in these spectra reflect the ion branching ratios associated with the decays of these core-hole states. The ion branching ratios of the individual core-holes states were already studied by Eland *et al.* with the same coincidence method [5].

The photoelectron spectrum (Fig. 1 top) shows the 4p photoelectron structure consisting of a peak around a kinetic energy of 245 eV and a remarkable shoulder in the lower kinetic energy side. As already pointed out by Eland *et al.* [5], the determination of the ion branching ratio of the 4p decay is not straightforward, because the determined ratio varies greatly with the photoelectron range considered. When only the peak range around a kinetic energy of 245 eV is considered, the formation of Xe^{3+} is dominant and a sizable Xe^{4+} formation is probably identified. This is consistent with a multi-electron coincidence study which reports a dominant Xe^{3+} formation for the main 4p photoelectron peak [6] and also with a recent calculation [7]. On the other hand, the shoulder part of the 4p photoelectron structure mainly produces Xe^{4+} ion. The shoulder part can be ascribed to double photoionization into the $4d^{-2}$ states, which is enhanced by the virtual super Coster-Kronig transition [2] of $4p^{-1} \rightarrow 4d^{-2}\epsilon f$ over several tens of electron volts [8]. The formed $4d^{-2}$ states dominantly proceed to sequential fillings of the double 4d core-holes [8], resulting in the dominant formation of Xe^{4+} ion.

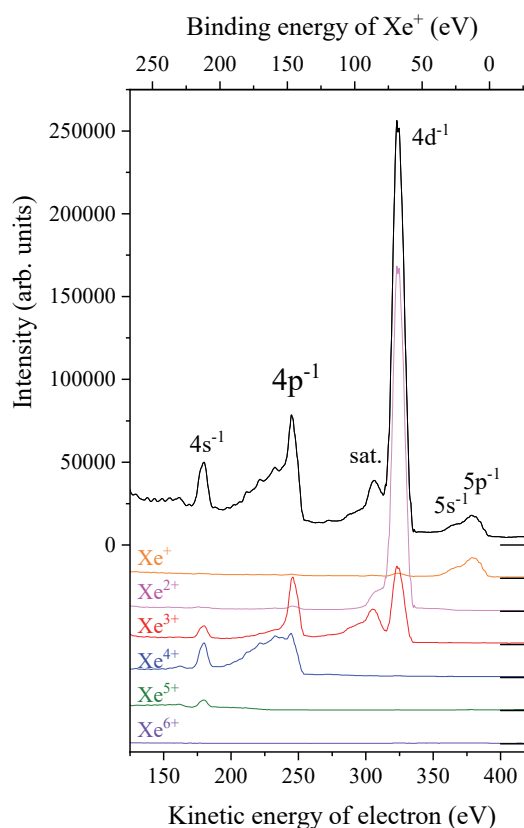


Fig. 1. Photoelectron spectrum of Xe measured at a photon energy of 391.7 eV, and coincidence spectra obtained by filter with different Xe^{Z+} ions ($Z = 1-6$). The intensities of the coincidence spectra were corrected by the ion detection efficiencies.

- [1] S. Svensson *et al.*, Phys. Scr. **14** (1976) 141.
- [2] G. Wendin and M. Ohno, Phys. Scr. **14** (1976) 148.
- [3] Y. Hikosaka and E. Shigemasa, Int. J. Mass Spectrom. **439** (2019) 13.
- [4] Y. Hikosaka, J. Electron Spectrosc. Rel. Phenom. **255** (2022) 147158.
- [5] J. H. D. Eland *et al.*, J. Phys. B **48** (2015) 205001.
- [6] Y. Hikosaka *et al.*, Phys. Rev. A **76** (2007) 032708.
- [7] Z. Liu *et al.*, Chin. Phys. Lett. **38** (2021) 023201.
- [8] Y. Hikosaka *et al.*, Phys. Rev. Lett. **98** (2007) 183002.

BL4B

Electronic Structure Analysis of Ni Complex Bearing *N*-Heterocyclic Carbene Ligand Using Ni L_{2,3}-edge X-ray Absorption Spectroscopy

Y. Uetake^{1,2}, Y. Yamauchi¹ and Y. Hoshimoto¹¹Division of Applied Chemistry, Graduate School of Engineering, Osaka University, Suita 565-0871, Japan²Innovative Catalysis Science Division, Institute for Open and Transdisciplinary Research Initiatives (ICS-OTRI), Osaka University, Suita 565-0871, Japan

Recently, we have synthesized a Ni(0) complex bearing tris(pentafluorophenyl)borane (BCF) as an electron accepting Z-type ligand and *N*-heterocyclic carbene as an ancillary ligand (**1**). Single crystal X-ray diffraction (SC-XRD) analysis of **1** revealed that it exhibits a square-planar structure typical of Ni(II) complexes, unlike the tetrahedral geometry that is common for Ni(0) complexes probably due to the sterically demanding BCF ligand. Interested in the electronic structure of **1** which contradicts the ligand field theory, we have performed Ni K-edge X-ray absorption spectroscopy (XAS) of this complex at SPring-8 BL14B2 beamline and found that this complex possessed low-valent Ni(0)-like electronic structure. However, since Ni K-edge XAS basically corresponds to the electron transitions from 1s to a vacant 4p orbital because of the Fermi's golden rule [1], it is difficult to clarify the details of the electronic structure of 3d orbitals which determines the characteristics of metal complexes. In this study, Ni L_{2,3}-edge XAS experiments of the Ni-BCF complex were investigated.

Ni L_{2,3}-edge XAS experiments were performed at the BL4B beamline using partial fluorescent yields (PFYs) method with silicon drift detector (SDD). A stainless-steel sample holder with double-sided conductive carbon tapes was attached to a transfer vessel, which was connected to a glovebox. The inside of the glovebox was evacuated using a rotary pump for at least 30 min, and then, filled with argon gas. The powder sample was applied on a carbon tape, and rubbed with the back of a spatula. After storing the sample holder in the vessel, the gate valve was closed. The vessel was detached from the glovebox, and then, attached to the main chamber. The air in the main chamber was evacuated by a rotary pump, and the gate valve was slowly opened after the pressure level reached in the order of 10⁻³ Pa. A turbo-molecular pump was then activated to create a high vacuum environment. XAS measurements were performed under the pressure less than 5 × 10⁻⁵ Pa.

Ni L_{2,3}-edge XAS data of **1**, **2** and **3** are shown in Fig. 1. Although the peak intensity of **1** was different from Ni(II) complex **3**, the peak position of **1** was similar to that of **3** which has octahedral ligand field rather than tetrahedral Ni(0) complex **2**, indicating the intrinsic geometrical similarity between the square-planar and the octahedral. Meanwhile, slightly intense first peak of **1** observed at 852.5 eV was assigned as the electron transition from 2p_{3/2} to 3d_{x₂-y₂} orbital. This result

indicated the low d-electron occupancy in 3d_{x₂-y₂} level due to the σ-backdonation from Ni 3d_{x₂-y₂} orbital to vacant p orbital of BCF. In addition, the peak area of **1** (15.5) was closer to **2** (11.5) rather than **3** (25.3) (Table 1). Considering that the peak area reflects the transition probabilities of the electrons [2,3], the d-electron occupancy of **1** would be closer to the Ni(0) state rather than to the Ni(II) state, which is consistent with the Ni K-edge XAS experiment. In addition, the slight increase of the L_{2,3}-edge intensity of **1** would reflect the polarized Ni^{δ+}-B^{δ-} bonding state.

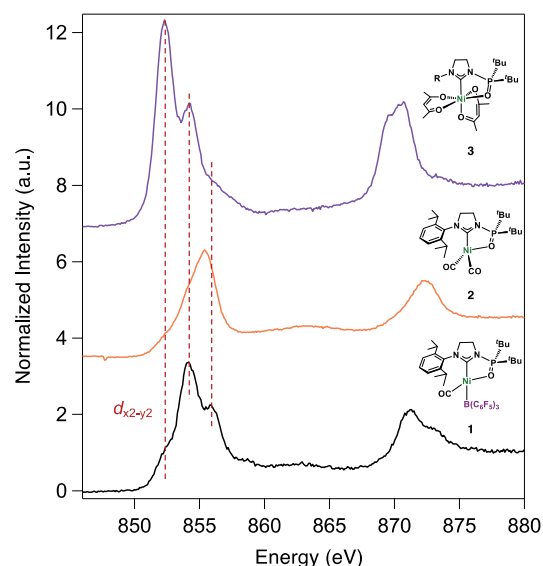


Fig. 1. Ni L_{2,3}-edge XAS data of **1**, **2** and **3**.

Table 1. Peak area of Ni L_{2,3}-edge XAS data after normalization.

	Peak area		
	L ₃	L ₂	L ₃ + L ₂
1	10.5	5.1	15.5
2	7.8	3.7	11.5
3	17.3	8.0	25.3

- [1] P. M. A. Dirac, Proc. Roy. Soc. A **114** (1927) 243.
 [2] E. I. Solomon, S. P. Cramer *et al.*, J. Am. Chem. Soc. **115** (1993) 2968.
 [3] K. M. Lancaster *et al.*, J. Am. Chem. Soc. **141** (2019) 18508.

BL5B

Evaluation of Absorption Stability of a Hydrogen Absorption Cell

M. Taguchi¹, M. Kuwabara¹, T. Katsumata¹, M. Tateyama¹, K. Yoshioka^{2,3}, Y. Suzuki³,
K. Goda⁴, K. Inoue⁴, A. Tomioka⁴ and A. Yamazaki⁴

¹Department of Physics, College of Science, Rikkyo University, Tokyo 171-8501, Japan

²Department of Complexity Science and Engineering, Graduate School of Frontier Sciences, The University of Tokyo, Chiba 277-8561, Japan

³Department of Earth and Planetary Science, Graduate School of Science, The University of Tokyo, Tokyo 113-0033, Japan

⁴Department of Earth and Planetary Physics, Faculty of Science, The University of Tokyo, Tokyo 113-0033, Japan

A hydrogen absorption cell (HAC) is a unique optical filter which enables us to estimate density and temperature distributions and an isotope ratio of hydrogen atoms escaping from a planetary atmosphere by detecting a hydrogen Lyman α emission of a planetary corona. The HAC is especially suitable for a payload of a planetary mission because of its small size and light weight. However, no measurement of a planetary corona by a HAC has been successful so far. Development of a newly designed HAC has been proceeded by the proposers, and it has been decided that the HAC is on board Comet Interceptor which is an ESA mission to investigate an atmosphere of a comet.

Absorption efficiency of the HAC has been improved, but its lifetime has not yet been confirmed. Absorption performance should be highly stable during the mission lifetime of several years. Here we present a result of an experiment in which absorption stability of a proto-model HAC was evaluated using the spectrometer at BL5B of UVSOR.

The HAC and a Kr cell were installed in the beamline. The Kr cell, which contains Kr gas with a pressure of 500 Pa, was used for wavelength calibration of the spectrometer. The grating and mirror combination of "G3M5" was selected. The slit width and the pinhole diameter were 0.01 mm and 1 mm, respectively.

Dimension of the HAC is ϕ 35 mm and L40 mm. Pure hydrogen gas filtered by a palladium filter with a pressure of 200 Pa was filled in the HAC. One of the filaments on the HAC was used for this stability test. Filament voltage was fixed at 5.73 V, which heats up the filament at a temperature of approximately 1800 K. A set of data consists of four spectra obtained with combinations of the filament on and off and the beam on and off from 121.1 nm to 122.0 nm with a scan step of 0.01 nm. It took approximately 70 min to acquire a set of data.

Figure 1 shows 8 absorption spectra of hydrogen Lyman α consecutively obtained by the HAC during a beamtime of 12 h. The depth of absorption almost unchanged, though the filament current slightly decreased from 0.170 A at the beginning to 0.167 A at the end. Accordingly, the filament temperature estimated from the voltage and current slightly increased. During the beamtime of four weeks this filament was activated for longer than 30 h, but no significant degradation was observed.

All the absorption spectra show an increasing trend from the shorter wavelength to the longer wavelength. The reason for this trend is unclear, but it might be related to any variation in the environment.

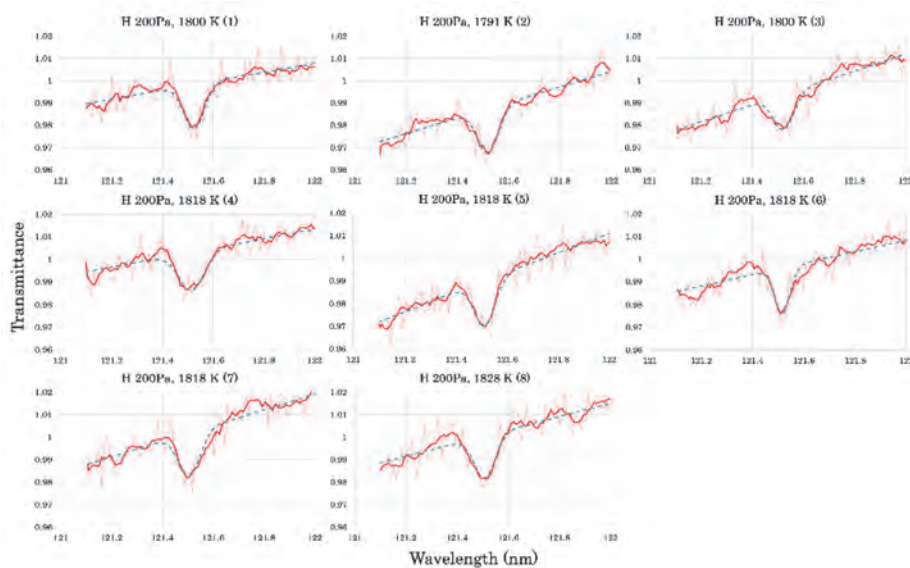


Fig. 1. Absorption spectra of hydrogen Lyman α consecutively obtained by a HAC under the same condition of gas pressure and filament voltage with the same filament.

The background is a solid purple color with several abstract geometric elements. A large, semi-transparent circular graphic is centered on the right side, featuring concentric rings and a dotted pattern. Diagonal lines and a grid of small dots are also visible, creating a sense of depth and movement.

III-4

Surface,
Interface and
Thin Films

BL5U

Polarization-dependent Photoelectron Intensity in Ca-doped Graphene

S. Ichinokura¹, K. Tokuda¹, K. Tanaka² and T. Hirahara¹¹Department of Physics, Tokyo Institute of Technology, Tokyo 152-8551, Japan²UVSOR Facility, Institute for Molecular Science, Okazaki 444-8585, Japan

Orbital symmetry strongly influences the interaction between light and electrons. When polarized light is irradiated on a material, the electronic excitation obeys the dipole selection rule; electrons in orbitals with odd- and even-parity are excited by *s*- and *p*-polarized light (described as *s*- and *p*-pol. hereafter), respectively. Therefore, in angle-resolved photoemission spectroscopy (ARPES), complementary intensity maps will be obtained when the *s*- and *p*-linear polarized lights are used.

The remarkable high-carrier mobility in graphene originates from its characteristic π -orbital band called Dirac cone. The light-matter interaction of graphene through the π -electron has attracted considerable attention. For example, the photoelectron intensity of the Dirac electronic state varies cyclically on the k_x - k_y plane for the polarized light [1]. Here, chirality plays an essential role in polarization dependence. In Li-intercalated bilayer graphene (C_6LiC_6), two Dirac cones with different chirality overlap around the Γ point of the Brillouin zone (BZ). The chiral symmetry is broken due to the lattice distortion by Li, leading to the gap opening at the Dirac point. These properties were clarified by laser-ARPES measurements [2].

Ca-intercalated graphite and graphene become superconducting at relatively high temperatures in layered and two-dimensional materials [3-5]. In addition to the Dirac cones, a free-electron-like state called interlayer band (ILB) exists as an occupied state in those systems. Since ILB has different symmetry from π -band, dipole selection rule and chirality effects are expected to coexist in C_6CaC_6 .

To resolve the coexistence of the two effects, we performed high-resolution polarization-dependent ARPES measurements on Ca-intercalated bilayer graphene, C_6CaC_6 at BL5U and BL7U. As shown in Figure 1(a), C_6CaC_6 was prepared on a Ca-terminated SiC substrate. Figure 1(b) shows the ARPES spectrum obtained by *s*-pol. A double Dirac cone was seen. The Dirac cones are folded into Γ point from K point of the graphene's BZ due to the $\sqrt{3}\times\sqrt{3}$ periodicity of Ca. The doubling is caused by the interlayer interaction between two graphene layers.

On the other hand, a parabolic band (stressed by dashed line) was much more prominently observed than the double Dirac cones when *p*-pol. is used, as shown in Figure 1(c). The free-electron-like character is consistent with the ILB. Since the spectrum by *p*-pol. and *s*-pol. are complementary, dipole selection rule mainly determines the intensity distribution; odd- and even-parity components are excited by *s*- and *p*-polarization, respectively.

Figures 1(d) and 1(e) show the photoelectron intensity maps on the Fermi energy obtained for *s*- and *p*-polarized light. In Fig. 1(d), the photoelectron intensity has an anisotropy; intensity map along Γ -K and Γ -K' direction (shown by dashed lines) is not identical. On the other hand, in Fig. 1(e), the intensity distribution is almost isotropic. Since the Dirac state is mainly excited by *s*-pol., the anisotropy is estimated to be caused by chirality effect.

In conclusion, it was revealed that the dipole selection rule has a stronger effect on the intensity distribution of photoelectron in C_6CaC_6 than the chirality effect. Reflecting the different symmetry of π -bands and ILB, complementary distribution was observed in the Fermi contour for the *s*- and *p*-polarized light. The chirality effect appears as the anisotropy in the Fermi contour of the Dirac cone component.

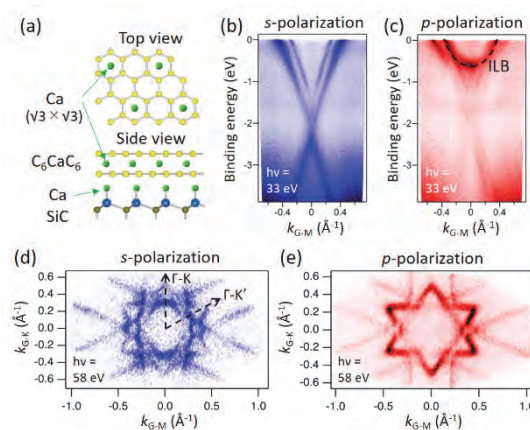


Fig. 1. (a) Schematic atomic model of Ca-intercalated bilayer graphene (C_6CaC_6) on Ca-terminated SiC substrate. (b)-(c) Band structure of C_6CaC_6 around Γ point, obtained by (b) *s*- and (c) *p*-polarized light. Parabolic band is stressed by the dashed guideline. (d), (e) Intensity mapping at Fermi level using (d) *s*- and (e) *p*-polarized light. Γ -K and Γ -K' direction are shown by dashed lines in (d). ARPES measurements were performed with $h\nu = 33$ or 58 eV under $T = 6 - 13$ K.

- [1] Y. Liu *et al.*, Phys. Rev. Lett. **107** (2011) 166803.
- [2] C. Bao *et al.*, Phys. Rev. Lett. **126** (2021) 206804.
- [3] T. E. Weller *et al.*, Nat. Phys. **1** (2005) 39.
- [4] S. Ichinokura *et al.*, ACS Nano **10** (2016) 2761.
- [5] H. Toyama *et al.*, ACS Nano **16** (2022) 3582.

BL3U

Elucidation of the Function of Adsorbed Anions on the Surface of Cobalt Catalysts by Operando Observation

K. Harada¹, S. Tsunekawa¹, A. Sakai¹, M. Nagasaka² and M. Yoshida^{1,3}

¹Yamaguchi University, Ube 755-8611, Japan

²Institute for Molecular Science, Okazaki 444-8585, Japan

³Blue Energy Center for SGE Technology (BEST), Ube 755-8611, Japan

Recently, hydrogen production by electrolysis of water has been attracting attention. In this system, cobalt catalysts are known to be one of the efficient oxygen production catalysts [1]. Thus, various spectroscopic analyses have applied to the catalysts in order to investigate the physical properties and functions. However, the role of anions in the electrolyte solution is still not fully understood. From this background, in this study, the role of adsorbed anions on cobalt catalysts was investigated by attenuated total reflection infrared spectroscopy (ATR-IR) and X-ray absorption fine structure (XAFS) measurements under operando conditions.

The electrochemical cell was used with a Pt counter and an Ag/AgCl reference electrode. The cobalt catalyst was prepared by electrodeposition on Au thin film in a solution containing Co^{2+} and carbonate anion (Co-C_i catalyst). Under electrochemical control, the operando Co K-edge XAFS were measured by fluorescence mode in the PF BL-9A, and the operando O K-edge and C K-edge XAFS were measured by transmission mode at BL3U in the UVSOR synchrotron.

First, we checked the OER activity and found that Co-C_i functioned as highly efficient water splitting catalyst. Next, SEM, EDX, and XPS measurements were also performed to confirm that the catalyst was electrodeposited on the substrate surface. Furthermore, the electrolyte solution was exchanged from potassium carbonate solution (K-C_i) to potassium sulfate solution (K-S_i) during monitoring the OER activity, indicating that the water splitting activity of the Co-C_i catalyst was improved in the K-C_i electrolyte solution.

To investigate the electronic state and local structure, the operando Co K-edge XAFS measurements were performed with the cobalt carbonate catalyst. EXAFS analysis showed that the peaks of Co-O and Co-Co bonds were observed at similar positions compared to the CoOOH reference sample, suggesting that the local structure of Co in the catalyst was consistent with that of CoOOH.

Then, operando O K-edge XAFS was measured, and the peak of Co(IV) as an active species [2-4] was observed at the electrode potential of water splitting reaction. This indicates the occurrence of high oxidation number Co in the Co-C_i catalyst at the catalytic active potential.

Finally, the operando C K-edge XAFS measurements under the catalytic reaction (Fig. 1) showed that carbonate ions were adsorbed on the catalyst surface.

The adsorbed peak was remained even after exchanging the electrolyte solution from K-C_i to K-S_i. In addition, the same result was obtained in the operando ATR-IR measurement. Therefore, these results suggest that the carbonate ions are strongly adsorbed on the Co-C_i catalyst to maintain the high oxidation number Co as active site.

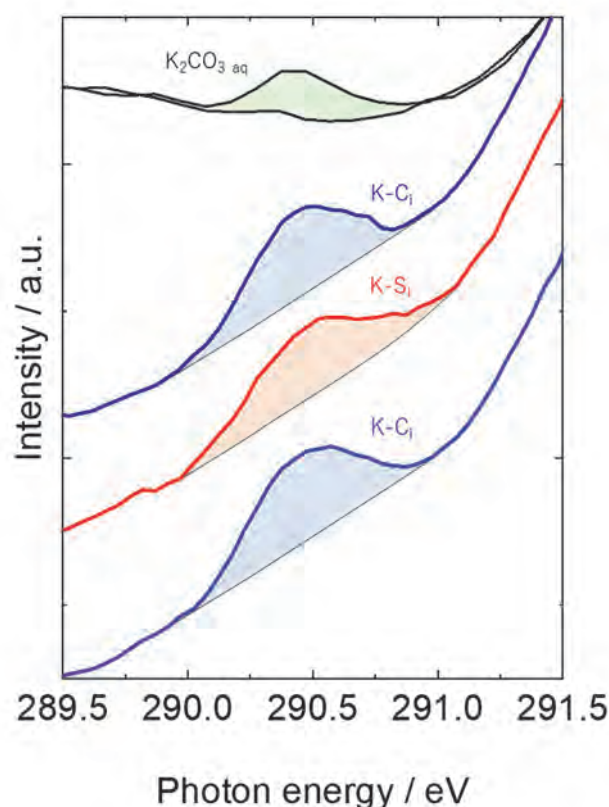


Fig. 1. Operando C-K edge XAFS spectra.

[1] W. Kanan, and D. G. Nocera, *Science* **321** (2008) 1072.

[2] A. M. Ullman, C. N. Brodsky, N. Li, S. L. Zheng, and D. G. Nocera, *J. Am. Chem. Soc.* **138** (2016) 4229.

[3] L. P. Wang, and T. Van Voorhis, *J. Phys. Chem. Lett.* **2** (2011) 2200.

[4] X. Li, and P. E. M. Siegbahn, *J. Am. Chem. Soc.* **135** (2013) 1380.

BL3B

Evaluation of Interface Between Sapphire Substrate and UV Emitting Zinc Aluminate Phosphor Thin Films

H. Kominami¹, M. Endo², T. Kawashima², N. Sonoda², K. Inoue², N. Uesugi², K. Nie², A. Adachi¹, R. Ishihara¹, Y. Kamoi¹, A. Dorokhina³ and S.Kurosawa^{4,5}

¹Graduate School of Integrated Science and Technology, Shizuoka University, Hamamatsu 432-8651, Japan

²Faculty of Engineering, Shizuoka University, Hamamatsu 432-8651, Japan

³Graduate School of Science and Technology, Shizuoka University, Hamamatsu 432-8651, Japan

⁴New Industry Creation Hatchery Center (NICHe), Tohoku University, Sendai 980-8579, Japan

⁵Faculty of science, Yamagata University, Yamagata 990-8560, Japan

The UV light is used for various applications depending on the wavelength as well as the sterilization described above. Recently, from the viewpoint of consideration to the environment, the mercury free UV emission devices have been demanded for the application of catalyst and medical situations. In our previous work, it was clarified that ZnAl₂O₄ phosphor was suitable for the UV field emission lamp because of its stability and luminescent property. It shows strong UV emission peaked around 250 nm which suitable for sterilization.

In this research, ZnAl₂O₄ thin film layer were prepared by thermal diffusion of ZnO and sapphire substrate for new UV devices. To obtain ZnAl₂O₄ thin film with high quality, we explore optimum condition of thermal annealing.

As a result of XRD of ZnAl₂O₄ annealed at 970 to 1050 °C, it was found that the peaks of (220), (311) and (333) appeared prominently, and polycrystalline ZnAl₂O₄ was formed. Figure 1 shows the full width of half maximum of diffraction peaks and these peak intensity ratio of each phase of ZnAl₂O₄ annealed at 970 to 1050 °C. Regarding the intensity ratio, the intensity ratio of each phase increased uniformly up to 990 °C, but at 1050 °C, the intensity ratio increased only in (333) and the intensity ratios of (220) and (311) decreased. From this result, it is considered that the growth is likely to occur in the orientation of (333) from a temperature exceeding a certain threshold value of 990 °C or higher.

Next, for ZnAl₂O₄ (333) that selectively grows on the c-plane sapphire substrate, the orientation of the c-plane sapphire substrate and the growth of ZnAl₂O₄ were investigated by evaluating the in-plane orientation by Φ scan measurement. Figure 2 shows a Φ scan of ZnAl₂O₄ (333) annealed at 970 to 1050 °C. Diffraction of (333) with the c-plane sapphire substrate was observed at 60° intervals. It is considered that both the c-plane sapphire substrate and (333) have the atomic arrangement of Aluminum atoms six-fold symmetric, and (333) has grown to inherit the six-fold symmetry of Aluminum of the c-plane sapphire substrate.

ZnAl₂O₄ was prepared at 970 to 1050 °C and evaluated by CL, XRD, SEM and the like. From the XRD results, it was found that the orientation of

ZnAl₂O₄ (333) facilitates growth from temperatures above a certain threshold of 990 °C or higher. From the results of the Φ scan measurement, it is considered that (333) grows so as to inherit the six-fold symmetry of the atomic arrangement of Aluminum in the c-plane sapphire substrate.

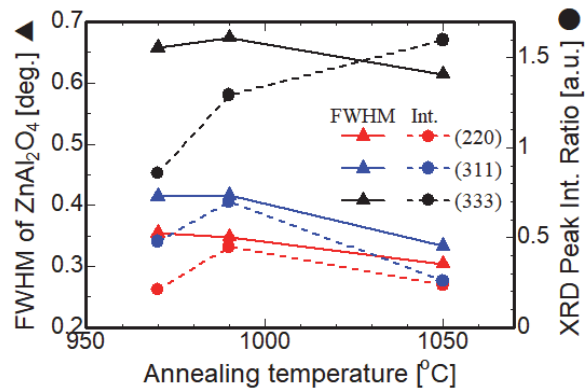


Fig. 1 dependence of FWHM and XRD Peak intensity of ZnAl₂O₄ thin films on annealing temperature.

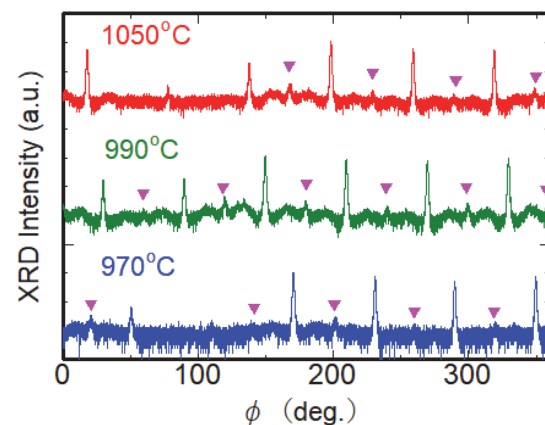


Fig. 2 Φ -scan of ZnAl₂O₄ (333) on c-plane sapphire substrate.

BL4U

Application of Atomically-thin Graphene to X-ray Astronomy: Soft X-ray Transmission Measurements

I. Mitsuishi¹, K. Kashiwakura¹, Y. Niwa¹, T. Ogawa¹, M. Hirota¹, Y. Tawara¹, R. Kitaura²,
P. Solís-Fernández³, K. Kawahara³, H. Ago³, T. Taniguchi⁴, K. Nomoto⁴, H. Kodaka⁴,
T. Ohigashi⁵, H. Yuzawa⁵ and K. Tanaka⁵

¹Graduate School of Science, Division of Particle and Astrophysical Science, Nagoya University,
Nagoya 464-8602, Japan

²Department of Chemistry, Nagoya University, Nagoya 464-8602, Japan

³Global Innovation Center, Kyushu University, Kasuga 816-8580, Japan

⁴Optical Measurement Technology Development Department, R&D Division, USHIO INC.,
Yokohama 225-0004, Japan

⁵UVSOR Synchrotron Facility, Institute for Molecular Science, Okazaki 444-8585, Japan

Thin films have been used in a variety of academic fields including astronomy. In X-ray astronomy, because X-rays are absorbed by the atmosphere of the Earth, balloons, rockets, and satellites are often used to observe X-rays from astronomical objects such as black holes, neutron stars, clusters of galaxies, and so on. Thin film devices have often been used in payloads of previous missions and playing a key role as, e.g., optical and contamination blocking filters and thermal shields [e.g., 1,2]. For such thin film devices, tolerance for severe launch and space environments and high transmission for more efficient use of limited observing time are required at the same time. Polyimide films have often been adopted because of relatively higher mechanical strength and heat tolerance in plastic materials. However, there is still room for improvement especially in transmission of a soft energy band below 1 keV. Thus, we have proposed to make use of graphene which is an atomically-thin material but has excellent mechanical and thermal properties at the same time. Our idea is to apply graphene to thin film devices in X-ray astronomy for the first time.

As a first step, we need to conduct X-ray transmission measurements to verify whether the transmission of graphene films especially in a soft energy band is actually high or not as expected because, as far as we know, no observed data is available except around 300 eV corresponding to the C K-edge structure. We prepared 5-layer free-standing graphene on a quartz substrate with a thickness of 200 μm with through holes with a diameter of 10 μm . To measure the number of X-ray photons with/without the 5-layer free-standing graphene collected by the Fresnel zone plate correctly, a taper structure with a taper angle of 30 degrees was prepared for each free-standing structure. The sample in the vacuum chamber and a close-up SEM image of the free-standing 5-layer graphene are shown in Fig. 1. Consequently, we obtained the transmission in 100, 140, 180, 220, 260, 340, 380, 420, 460, 500 eV, and the C K-edge structure between 280 and 320 eV in details successfully and confirmed that the observed transmission is very high as expected on the order of

>89% corresponding to >97% for single-layer graphene although the transmission goes down to ~80% in the C K-edge structure corresponding to ~95% for single-layer graphene as shown in Fig. 1 (Mitsuishi et al., in prep.). To investigate the impact of residual of the coated material, PMMA, on the free-standing graphene structure used in our fabrication process, we obtained transmission around the O K-edge structure even though the coated material was removed by using acetone. The observed transmission in 520—564 eV ranges from 95 to 98% and thus no strong contamination was found. To estimate the transmission more accurately, a systematic error such as a variation in the beam intensity should be taken into account in the near future.

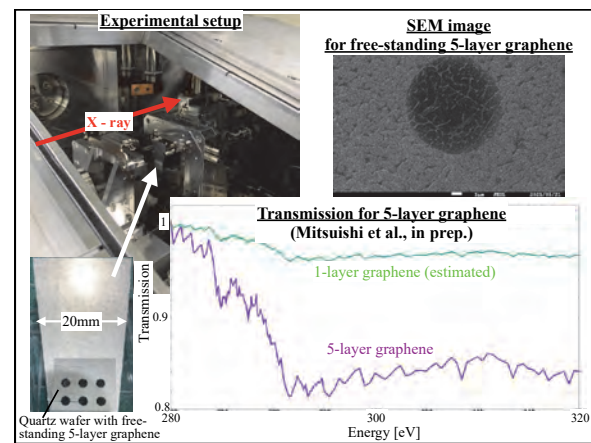


Fig. 1. Experimental setup with our sample and an example of the observed soft X-ray transmission curve.

[1] P.J. Serlemitsos *et al.*, Publ. Astron. Soc. Japan **47** (1995) 105-114.

[2] P.J. Serlemitsos *et al.*, Publ. Astron. Soc. Japan **59** (2007) S9-S21.

BL4B

Annealing Effect on the Vacuum Ultraviolet Transmission Spectrum of Amorphous Selenium

K. Hayashi

Department of Electrical, Electronic and Computer Engineering, Gifu University, Gifu 501-1193, Japan

The decrease in the photoconductivity and the dark conductivity by long exposure to bandgap light have been observed in hydrogenated amorphous silicon [1] and amorphous chalcogenide materials [2]. This effect is usually called photodegradation and is explained in the creation of light-induced metastable defects (LIMD). Many models have been proposed for LIMD creation, but details of the mechanism for LIMD creation in these materials are still not clear. Recently, we have observed changes in photoconductivity in amorphous chalcogenide materials that cannot be explained by the creation of LIMD. The x-ray diffraction and the volume change of the films before and after irradiation of bandgap light suggest that the photoinduced phenomena is due to a change of the local structure of the amorphous network. Understanding the physical mechanism underlying metastability is one of the important fundamental problems related to these materials. In the previous reports, we reported the photoinduced effects on the vacuum ultraviolet (VUV) transmission spectrum of amorphous arsenic triselenide by the irradiation of the bandgap light. In this report, we study the annealing effect on the VUV transmission spectrum of amorphous selenium.

Sample used for the measurement of the VUV transmission spectra was amorphous Se (a-Se) thin film prepared onto thin aluminum film by conventional evaporation technique. The sample thickness was about 180nm. The aluminum film of the thickness of 200 nm was used to eliminate the higher order light from the monochromator in the VUV region. These measurements were carried out at room temperature on the BL4B beam line of UVSOR. The spectrum was measured by using the silicon photodiode as a detector. Two pinholes of 1.5mm in a diameter were inserted between the monochromator and sample to remove stray light. The intensity of the VUV light was monitored by measuring the TPEY of a gold mesh. The positions of the core levels for the samples were calibrated by referencing to the 2p core level absorption of the aluminum film.

Figure 1 shows annealing effect on the VUV transmission spectra of amorphous Se thin film. The VUV transmission spectrum of amorphous As_2Se_3 is also shown on the figure for reference. Annealing effect on the VUV transmission spectrum was investigated by annealing the amorphous Se with 353 K for 1 hour. Amorphous Se is thought to crystallize (polycrystalline) at this annealing temperature. As shown in the figure, each spectrum is very broad and multiple shoulders are observed. The absorption spectrum observed in the amorphous Se is roughly consistent with the previous

report [3]. Main absorption peaks around 22nm corresponds to the 3d core level of Se atom. Although the wavelength resolutions in the spectral measurements are all the same, the spin-orbit splitting of the $3d_{5/2}$ and $3d_{3/2}$ level of Se atom is clearly resolved in amorphous As_2Se_3 , while they are not clearly resolved in as-deposited amorphous Se and annealed amorphous Se. When amorphous Se crystallizes by annealing, it can be seen that the broad peak around 20 nm was composed of about three absorption peaks. It is not clear about the origin of broad spectra and several peaks. I think that these origins are related to the local structures of the amorphous network. The detailed experiments and analysis will be done in the next step. More detailed experiments are necessary to clarify the origin of the VUV transmission spectra.

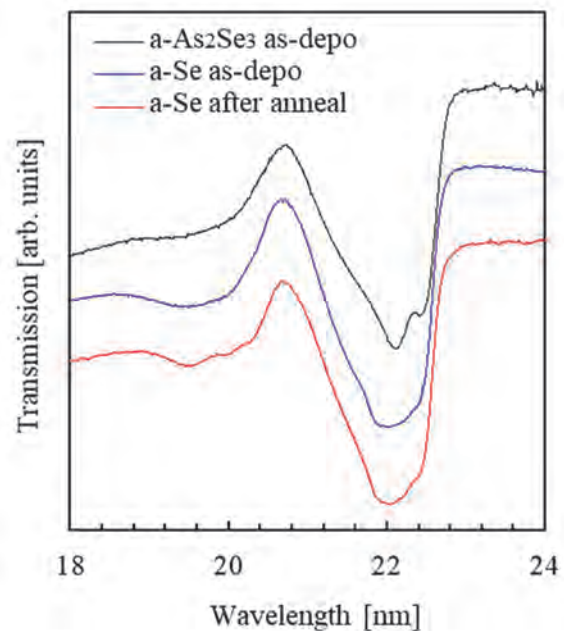


Fig. 1. Annealing effect on the VUV transmission spectra of a-Se thin film.

- [1] D. L. Staebler and C. R. Wronski, *Appl. Phys. Lett.* **31** (1977) 292.
- [2] K. Shimakawa, S. Inami, and S. R. Elliott, *Phys. Rev. B* **42** (1990) 11857.
- [3] J. Bordas and J. B. West, *Phil. Mag.* **34** (1976) 501.

BL4B

Magnetic Properties of CoPc/ γ' -Fe₄N Organic-inorganic Hybrid Interface

T. Miyamachi^{1,2}, H. Ono¹, Y. Umeda¹, K. Yamamoto^{3,4}, O. Ishiyama^{3,4}, T. Yokoyama^{3,4}
and M. Mizuguchi^{1,2}

¹Department of Materials Science and Engineering, Nagoya University, Nagoya 464-8603, Japan.

²Institute of Materials and Systems for Sustainability (IMaSS), Nagoya University, Nagoya 464-8601, Japan.

³Institute for Molecular Science, Okazaki 444-8585, Japan

⁴The Graduate University for Advanced Studies (SOKENDAI), Okazaki 444-8585, Japan

Organic materials are expected to be useful to spintronics devices due to their low spin current dissipation derived from weak spin-orbit interaction. In particular, an organic-inorganic hybrid interface has attracted much attention because its interface spin state can be controlled via the proximity effect. Spin-dependent electron transport properties of organic-inorganic hybrid system strongly depend on the domain size of organic molecular films, defect density and adsorption geometry of organic molecules. Thus, understanding structural, electronic and magnetic properties of the organic-inorganic interface on the level of single molecules is essential for realizing molecular spintronics devices. However, microscopic details of the hybrid interface have not been clarified so far.

In this study, we focus on fabricating organic-inorganic hybrid films with structurally controlled interface on the level of single molecules and investigating their intrinsic electronic and magnetic properties. For this purpose, ferromagnetic iron nitride atomic layers with γ' -Fe₄N stoichiometry were chosen as an inorganic material, which uniformly grow and show high surface quality on the atomic scale [1,2]. Molecular layers composed of planer cobalt phthalocyanine (CoPc) were chosen as an organic material. Structural, electronic and magnetic properties of the hybrid interface composed of CoPc with the thickness of 1, 2 and 3 molecular layers and a bilayer γ' -Fe₄N were investigated by scanning tunneling microscopy (STM), low energy electron diffraction (LEED) and x-ray absorption spectroscopy/magnetic circular dichroism (XAS/XMCD).

A bilayer γ' -Fe₄N was prepared by iron deposition on Cu (001) with N⁺ ion bombardment and subsequent annealing at 620 K. Then, CoPc/ γ' -Fe₄N hybrid thin films were fabricated by depositing CoPc on the γ' -Fe₄N at room temperature. In combination with results of STM and LEED, the impact of the thickness of CoPc layers on the interfacial magnetic state was investigated by XAS/XMCD.

XAS/XMCD measurements were performed at BL4B in UVSOR by total electron yield mode at B = 0 ± 5 T and T = 7.3 K. The XMCD spectra are obtained at the normal (NI: $\theta = 0^\circ$) and the grazing (GI: $\theta = 55^\circ$) geometries by detecting $\mu_+ - \mu_-$, where μ_+ (μ_-) denotes the XAS recorded at Fe and Co L adsorption edges with

the photon helicity parallel (antiparallel) to the sample magnetization. Note that θ is the angle between the sample normal and the incident x-ray [3].

We find that the Fe orbital magnetic moment of the bilayer γ' -Fe₄N evaluated by XMCD sum rule analysis changes with increasing thickness of the CoPc layer. The difference between the out-of-plane and in-plane Fe orbital magnetic moment, which is proportional to the magnetic anisotropy [4], is the largest when about one CoPc layer is deposited on the γ' -Fe₄N and it decreases with further increasing thickness of the CoPc layer. The results suggest the perpendicular magnetic anisotropy of the γ' -Fe₄N is enhanced by the magnetic coupling with CoPc molecules at the interface. STM and LEED observations reveal that the presence of the CoPc overlayers increases the surface roughness, which might in turn decrease the perpendicular magnetic anisotropy of the γ' -Fe₄N arising from the formation of the CoPc/ γ' -Fe₄N hybrid interface through the intermolecular interaction between CoPc layers.

[1] Y. Takahashi *et al.*, Phys. Rev. Lett. **116** (2016) 056802.

[2] Y. Takahashi *et al.*, Phys. Rev. B **95** (2017) 224417.

[3] S. Nakashima *et al.*, Adv. Funct. Mater. **29** (2019) 1804594.

[4] P. Bruno, Phys. Rev. B **39** (1989) 865.

BL4B

Enhancement of the Perpendicular Magnetic Anisotropy in N-surfactant Assisted FeCo Ordered Alloy Thin Films

T. Miyamachi^{1,2}, Y. Umeda¹, H. Ono¹, K. Yamamoto^{3,4}, O. Ishiyama^{3,4}, T. Yokoyama^{3,4}
and M. Mizuguchi^{1,2}

¹Department of Materials Science and Engineering, Nagoya University, Nagoya 464-8603, Japan.

²Institute of Materials and Systems for Sustainability (IMaSS), Nagoya University, Nagoya 464-8601, Japan.

³Institute for Molecular Science, Okazaki 444-8585, Japan

⁴The Graduate University for Advanced Studies (SOKENDAI), Okazaki 444-8585, Japan

Skyrmions are nano-scale magnetic vortex structures, attracting great attention as a promising candidate of next-generation information storage devices due to their expected high magnetic stability and low critical current density for motion. Skyrmions can emerge in magnetic thin film hetero structures with the ferromagnetic/heavy metal interface. Since Dzyaloshinsky–Moriya interaction induced by 3d-5d hybridization effects is the driving force of the emergence of skyrmions in this system, the strict control of structural, electronic and magnetic properties of the interface in magnetic thin film hetero structures is quite important. Recently, we have revealed that large-area and atomically uniform iron nitride atomic layers with γ' -Fe₄N stoichiometry can be grown on Cu(001) [1]. Thus, in this work, we intend to grow 5d heavy metal thin films on γ' -Fe₄N atomic layers and fabricate the high quality 3d-5d heterointerface towards developing skyrmions-based novel magnetic structures. For this purpose, we first grow a monatomic layer of Co onto bilayer γ' -Fe₄N and investigate the impact of the quality of 3d-3d heterointerface on electronic and magnetic properties of the system by low energy electron diffraction (LEED) and x-ray absorption spectroscopy/magnetic circular dichroism (XAS/XMCD).

To grow a bilayer γ' -Fe₄N, N⁺ ion bombardment was first conducted with an incident energy of 500 eV onto Cu substrate and iron was additionally deposited at room temperature in ultra-high vacuum. The bilayer γ' -Fe₄N was obtained by subsequent annealing at ~620 K. Appropriate growth conditions about the deposition amount of iron and annealing temperature were prechecked by atomically resolved surface characterizations using scanning tunneling microscopy (STM) [2]. Then, the low temperature deposition of a monatomic layer of Co at -170 K was performed to fabricate Co- γ' -Fe₄N magnetic thin film hetero structures. The sample was post-annealed at 300, 570 and 670 K and the annealing temperature dependence of electronic and magnetic properties was investigated by XAS/XMCD. XAS/XMCD measurements were performed at BL4B in UVSOR by total electron yield mode at B = 0 - ± 5 T and T = 7.9 K. The XMCD spectra are obtained at the normal (NI: $\theta = 0^\circ$) and the grazing (GI: $\theta = 55^\circ$) geometries. Note that θ is the angle between the sample normal and the incident x-ray.

Element specific magnetization curves were also recorded by plotting the L₃/L₂ Fe and Co XAS intensities as a function of the magnetic field.

The XMCD signal of the bilayer γ' -Fe₄N is greater in the GI geometry than NI geometry, which reveals its strong in-plane magnetic anisotropy as previously reported [1]. Adding one monolayer of Co activates the nitrogen surfactant effect [3,4], which leads to the formation of CoN in the topmost layer. Accordingly, we find from Fe magnetization curves that the out-of-plane magnetization of the Fe layer is relatively increased. The perpendicular magnetic anisotropy of the Fe layer is further enhanced by annealing at 570 K. However, at annealing temperature of 670 K, the decrease in the coercivity of the Fe layer is overserved. Taking the annealing temperature dependence of the LEED pattern into consideration, the enhancement of the out-of-plane magnetization could be caused by the improved ordering of the Co/Fe interface up to annealing temperatures of 570 K. At 670 K, surface N atoms start to desorb, which induces the interdiffusion of interfacial Co and Fe atoms and consequently lowers the coercivity.

[1] Y. Takahashi *et al.*, Phys. Rev. B **95** (2017) 224417.

[2] Y. Takahashi *et al.*, Phys. Rev. Lett. **116** (2016) 056802.

[3] K. Kawaguchi *et al.*, Phys. Rev. Materials **4** (2020) 054403.

[4] K. Kawaguchi *et al.*, Jpn. J. Appl. Phys. (accepted).

BL5U

ARPES from Si{111} Facet Surfaces on Three-dimensional Lined Structures on Si(001) Substrates

K. Hattori¹, L. N. Pamasi¹, Y. Sakai¹, H. Yang¹, T. Shimizu¹, Y. Ida³, W. Imayama³, S. Tanaka², A. N. Hattori², S. Suga² and K. Tanaka³

¹Nara Institute of Science and Technology, Ikoma 630-0192, Japan

²SANKEN, Osaka University, Ibaraki, 567-0047, Japan

³UVSOR Synchrotron Facility, Institute for Molecular Science, Okazaki 444-8585, Japan

Our information society has required highly densitized devices like 3D FET, which can break the restriction of miniaturizing 2D planar-type devices. To improve the specification (e.g., carrier mobility) of 3D devices, it is indispensable the control of 3D structure surfaces which are carrier passing region.

So far, our group have successfully created 3D Si surfaces by the combination of lithography and surface treatment techniques [1-7]: SEM, RHEED, LEED, or STM evaluations for lined or pyramidal structures with {111}, {110}, or {100} side/facet surfaces on (111), (110), or (001) substrates. In the beam time in 2021 FY, we focused electronic band investigations for 3D-Si surfaces, which promise side/facet-wall band engineering.

Figure 1 shows brief results for a 3D-Si lined structure (4 μm period) with {111} facet surfaces on a (001) substrate: (a) SEM image and (c) LEED pattern after the flash annealing in UHV. The LEED patterns clearly indicated 7×7 reconstruction on (111) and $(\bar{1}\bar{1}\bar{1})$ facet surfaces; the 7×7 spots move in right or left directions.

ARPES from the area including ≈ 13 $(\bar{1}\bar{1}\bar{1})$ facet-surfaces in geometry **A** (Fig. 1(d), note (111) is invisible) showed clear bulk-projected band dispersion and 7×7 surface bands: S_1 - S_3 , which guarantees well-controlled electronic states on the facet surfaces. ARPES from (111) mainly in geometry **B** ($\theta_e^c = 30^\circ$ and $\theta_i = 27.5^\circ$) showed band dispersions at $\theta_e \lesssim 35.3^\circ$ assigned from (111) and also dispersions below the (111) horizontal at $\theta_e \gtrsim 35.3^\circ$ which could be assigned from glancingly radiated $(\bar{1}\bar{1}\bar{1})$ or the edge regions.

[1] A.N. Hattori, K. Hattori *et al.*, Surf. Sci. **644** (2016) 86.

[2] A.N. Hattori, K. Hattori *et al.*, Appl. Phys. Express **9** (2016) 085501.

[3] H. Yang, A.N. Hattori, K. Hattori *et al.*, Jpn. J. Appl. Phys. **56** (2017) 111301.

[4] S. Takemoto, A.N. Hattori, K. Hattori *et al.*, Jpn. J. Appl. Phys. **57** (2018) 090303.

[5] A.N. Hattori and K. Hattori, *21st Century Surface Science* (IntechOpen, London, 2020).

[6] A. Irmikimov, A.N. Hattori, K. Hattori, *et al.*, ACS Cryst. Growth Des. **21** (2021) 946.

[7] S. Nakatsuka, T. Abukawa, A.N. Hattori, K. Hattori *et al.*, e-J. Surf. Sci. NanoTechnol. **19** (2021) 13.

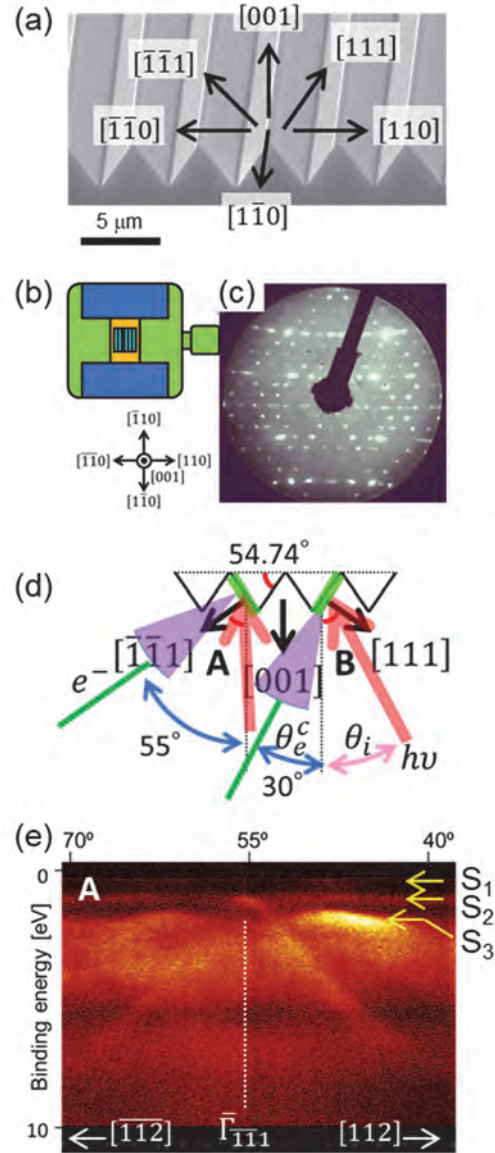


Fig. 1. (a) SEM image, (b) sample schematics on holder, (c) LEED pattern ($E_p = 80$ eV), (d) geometry of incident light (pink arrow) and electron emission (green line and fan-shaped purple) to sample, and (e) ARPES ($h\nu = 60$ eV, p -polarization; $\phi = 50$ μm , acceptance angle $\approx \pm 15^\circ$, light-analyzer angle $= 57.5^\circ$) in geometry **A** at $\theta_e^c = 55^\circ$ ($\theta_i = 2.5^\circ$), for 3D facet-lined structures with Si{111} facet surfaces on Si(001) substrates.

BL5U

Electronic Structure of K Adsorbed SmS Surface

T. Nakamura^{1,2}, T. Nakaya², H. Sugihara², K. Tanaka³,
K. Imura⁴, H. S. Suzuki⁵, N. K. Sato⁴ and S. Kimura^{1,2,3}

¹Graduate School of Frontier Biosciences, Osaka University, Suita 565-0871, Japan

²Department of Physics, Graduate School of Science, Osaka University, Toyonaka 560-0043, Japan

³Institute for Molecular Science, Okazaki 444-8585, Japan

⁴Department of Physics, Graduate School of Science, Nagoya University, Nagoya 464-8602, Japan

⁵Institute for Solid State Physics, The University of Tokyo, Kashiwa 277-8581, Japan

Samarium mono-sulfide (SmS) is a typical valence fluctuation material [1]. At ambient pressure, SmS is a semiconductor with an indirect bandgap of about 0.1 eV, and its color is black [2]. The electrical properties change to metallic above a critical pressure of 0.65 GPa. Although the pressure-induced phase transition was discovered over 50 years ago [1], the origin of the phase transition is still under debate. Recently, a phase transition like the pressure-induced one has been reported due to two different types of perturbations: light irradiation and current injection [3,4]. These perturbations are commonly expected to increase carriers, but the detailed electronic states after carrier doping have not been clarified yet.

Alkali metal adsorption on crystal surfaces is widely used as a typical method to investigate the effect of carrier injection into a material. Due to the charge transfer of the free-electron-like outermost electrons in the alkali metal to SmS, a carrier-doped SmS surface can be realized. In this work, we have studied the change of the electronic structure by potassium (K) doping on a SmS surface by synchrotron-based ARPES.

A high-quality single-crystalline SmS was grown by the vertical Bridgman method in a high-frequency

induction furnace. The clean SmS surface was obtained by cleaving in-situ in an ultra-high vacuum chamber. K atoms were evaporated from the well-degassed alkali metal dispenser (SAES-Getters) at room temperature (RT).

Figure 1(a) shows the ARPES intensity plot of the pristine-SmS along the $\bar{\Gamma} - \bar{X}$ line of the surface Brillouin zone taken with 60-eV photons. Flat $\text{Sm}^{2+} 4f^5$ multiplet structure and dispersive S 3p bands were observed. After the K deposition as shown in Fig. 1(b), the band dispersion of the Sm 4f states was changed without a higher binding energy shift due to the natural electron doping. These results suggest that the K adsorption on SmS caused a deformation of the band structure, which cannot be explained as a simple rigid band shift model due to electron doping.

[1] A. Jayaraman *et al.*, Phys. Rev. Lett. **25** (1970) 1430.

[2] K. Matsubayashi *et al.*, J. Phys. Soc. Jpn. **76** (2007) 064601.

[3] R. Kitagawa *et al.*, Appl. Phys. Lett. **82** (2003) 3641.

[4] H. Ando *et al.*, JPS Conf. Proc. **30** (2020) 011132.

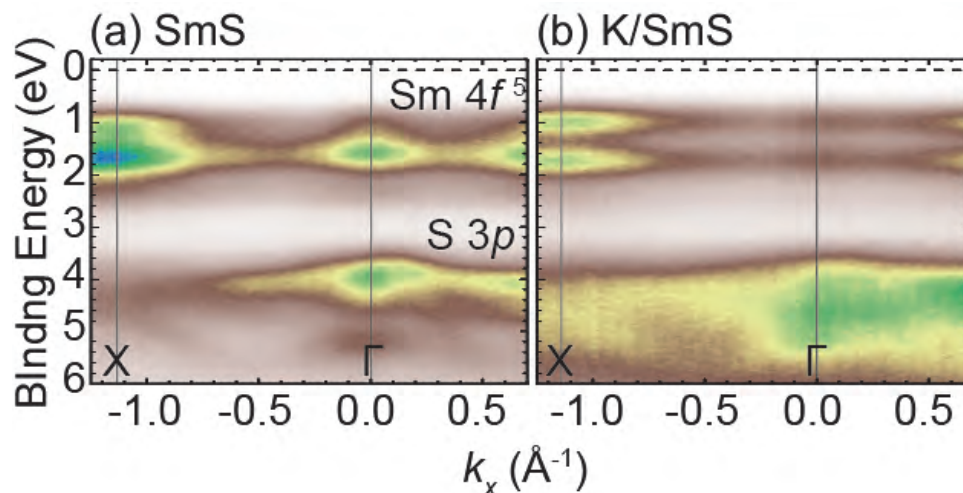


Fig. 1. ARPES intensity plots of (a) pristine SmS and (b) K-adsorbed SmS along $\bar{\Gamma} - \bar{X}$ with 60-eV photons at room temperature.

BL5U

Explorations for Spontaneously Formed Excitons in Narrow-gap Semiconductors and Semimetals

 K. Fukutani^{1,2}, M. Murakami³, C.I. Kwon^{4,5}, J. S. Kim^{4,5}, K. Tanaka^{1,2}, S. Kera^{1,2,3}
¹Institute for Molecular Science, Okazaki 444-8585, Japan

²The Graduate University for Advanced Studies (SOKENDAI), Okazaki 444-8585, Japan

³Graduate School of Science and Engineering, Chiba University, Chiba 263-8522, Japan

⁴Center for Artificial Low-Dimensional Electronic Systems, Institute for Basic Science, Pohang, Korea

⁵Pohang University of Science and Technology, Pohang, Korea

Excitons are bound pair of an electron and a hole, conventionally produced transiently by irradiation of light on semiconductors, and is one of the most fundamental quasiparticles in solids and molecular materials that play central roles in various quantum devices, such as photovoltaic cells, light emitting diodes and photodetectors.

In recent years, a new exotic phase of matter called an excitonic insulator has garnered much attentions. In the excitonic insulator phase, at sufficiently low temperature, the electrons and holes are spontaneously bound to form an excitons and undergo quantum condensation.

Among the various candidate materials for excitonic insulator, Ta_2NiSe_5 is particularly suitable for the experimental investigations as it exhibits a direct band gap and the excitonic insulator transition accompanies only a minor structural distortion, which preserves the periodicity of the material. For this relative simplicity, Ta_2NiSe_5 has been investigated extensively in the past decade by various experimental methods [1] and it is widely conceived to be a Bose-Einstein condensation (BEC)-type excitonic insulator.

Of particular interest in the BEC-type excitonic insulator is the theoretical prediction of the intermediate phase called “preformed exciton phase”, which is believed to appear between the excitonic insulator and the normal phases (see Fig. 1) [2]. In the preformed exciton phase, the magnitude of the bandgap is small enough (i.e., the free carrier screening is small enough) to allow for the bound state for the electrons and holes, yet the temperature is too high for these spontaneously formed excitons to undergo the Bose-Einstein condensation. Therefore, this particular region of the phase diagram supports the existence of finite number of excitons in equilibrium. In our recent study [3], the direct photoemission signal from these spontaneously formed excitons have been detected and long-standing theoretical prediction has been confirmed. However, the detailed formation mechanism of such excitons is still elusive due to the lack of experimental data for this particular phase of excitonic insulator materials.

Thus, in order to pin down the origin of these spontaneously formed excitons, we are performing a series of angle-resolved photoemission spectroscopy (ARPES) experiments at BL5U for the chalcogen-substituted compounds $\text{Ta}_2\text{Ni}(\text{Se}_{1-x}\text{S}_x)_5$ for various compositions x . In the experiments, the freshly cleaved

samples of $\text{Ta}_2\text{Ni}(\text{Se}_{1-x}\text{S}_x)_5$ have been measured to reveal their band structures as well as to explore for the photoemission signals from the spontaneously formed excitons as a function of temperature, photon energy as well as the light polarizations.

A representative result of the ARPES intensity plot is shown in Fig. 2. It can be seen that the photoemission signal from excitons, observed in Ta_2NiSe_5 [3] is also observed for the S-substituted compounds.

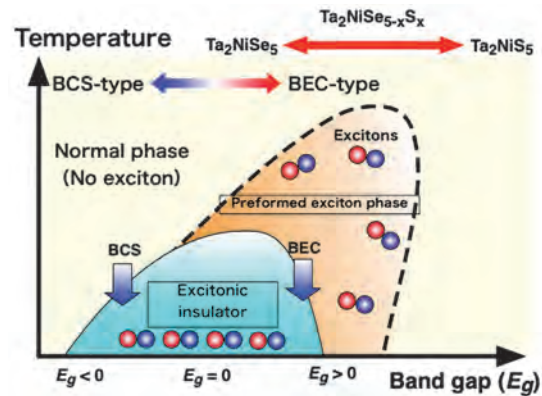


Fig. 1. Theoretical phase diagram of excitonic insulators.

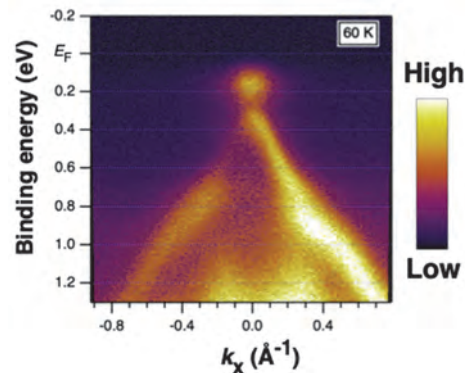


Fig. 2. ARPES intensity plot for chalcogen-substituted excitonic insulator $\text{Ta}_2\text{Ni}(\text{Se}_{1-x}\text{S}_x)_5$.

- [1] Y. Wakisaka *et al.*, Phys. Rev. Lett. **102** (2009) 026402; Y.F. Lu *et al.*, Nat. Commun. **8** (2017) 14408.
 [2] F.X. Bronold *et al.*, Phys. Rev. B **74** (2006) 165107.
 [3] K. Fukutani *et al.*, Nat. Phys. **17** (2021) 1024.

BL5B

X-ray Absorption Spectroscopy Measurements of Au/Fe/MgO Sandwich Structure Sample for Study of Soft X-ray Second Harmonic Generation

 T. Sumi¹, M. Horio¹, X. Zhang¹, T. Kato² and I. Matsuda^{1,3}
¹Institute for Solid State Physics, The University of Tokyo, Kashiwa 277-8581, Japan

²Institute of Materials and Systems for Sustainability, Nagoya University, Nagoya 464-8603, Japan

³Trans-scale Quantum Science Institute, The University of Tokyo, Tokyo 113-0033, Japan

Second harmonic generation (SHG), which is a phenomenon that occurs by the interaction between light and a system where the inversion symmetry is broken, has been used not only to convert light to higher frequencies but also to investigate electronic states of molecules at the systems in the visible region. After the construction of X-ray Free Electron Laser (XFEL) such as Pring-8 Angstrom Compact free-electron LAsER (SACLA), we have been developing SHG methods in the range of soft X ray, and applied to GaFeO₃ [1], LiNbO₃ [2], LiOsO₃ [3], and GaAs [4]. By setting the incident energy to the inner-shell core level, SHG acquires element selectivity by inner-core excitation resonance. Although this technique is useful to reveal the electronic states of the targeted atoms at surfaces/interfaces, there is no report for the interface SHG.

In this research, at UVSOR BL5B, we conducted X-ray absorption spectroscopy for a Fe film sandwiched by films of Au and MgO to grasp the possibility of the occurrence of soft X-ray SHG before observing it. We synthesized the sample by ultrahigh vacuum molecular beam epitaxy method. The sandwich structure of Au/Fe/MgO was repeated 4 times. The structure of the sample is [Au (2 nm)/Fe (2 nm)/MgO (2 nm)]₄/MgO(001, substrate) (Fig. 1). The sample was placed perpendicular to the incident beam, and the drain current was measured.

Figure 2 shows a XAS spectrum around the Fe *M*-edge. The drain current, *I*, was normalized by incident intensity, *I*₀, measured by the Au mesh. The result shows Fe *M*-edge (53 eV) absorption peak appears. This means that the Fe *M*-edge dipole transition is allowed. To investigate the transition around the SHG energy (106 eV), the drain current was measured around that energy without the Au mesh to prevent the effect of the mesh (Fig. 3). The peak appears around 106 eV. These results suggest that the dipole transitions in the SHG process starting from Fe *M*-shell are allowed.

In conclusion, we investigated the electric dipole transition for the Au/Fe/MgO sandwich structure sample by XAS and found the possibility of the SHG process starting from the Fe *M* shell (*hν* = 53 eV). It is expected that SHG originating from the interfaces is available. Furthermore, it is possible to achieve soft X-ray magnetization-induced SHG (MSHG) by applying a magnetic field to this sample because it has perpendicular magnetization anisotropy (PMA).

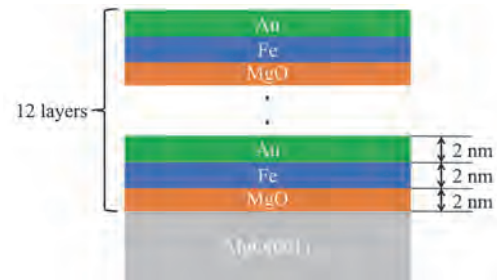


Fig. 1. Structure of the [Au/Fe/MgO]₄ / MgO(001) sandwich structure sample.

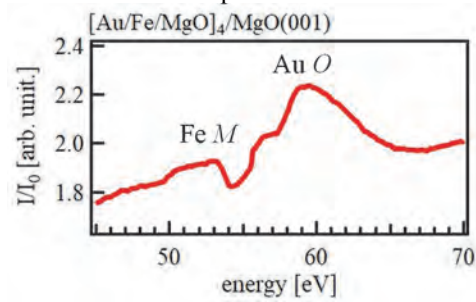


Fig. 2. XAS spectrum for the sandwich structure sample around Fe *M*-edge.

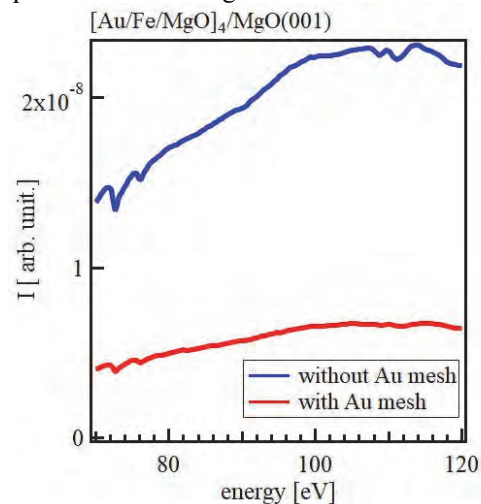


Fig. 3. Drain current of the sandwich structure sample without (blue) and with (red) the Au mesh.

[1] Sh. Yamamoto *et al.*, Phys. Rev. Lett. **120** (2018) 223902.

[2] E. Berger *et al.*, Nano Lett. **21** (2021) 6095.

[3] C. B. Uzundal *et al.*, Phys. Rev. Lett. **127** (2021) 237402.

[4] T. Sumi *et al.*, e-J. Surf. Sci. Nanotech. (2022) (accepted).

BL6U

Bromine Doping to Perylene Monolayer on Au(110): Photoelectron Momentum Microscopy

O. Endo^{1,3}, F. Matsui², S. Kera², W. -J. Chun³, M. Nakamura⁴, K. Amemiya⁵ and H. Ozaki¹¹Department of Organic and Polymer Materials Chemistry, Faculty of Engineering, Tokyo University of Agriculture and Technology, Koganei 184-8588, Japan²UVSOR Synchrotron Facility, Institute for Molecular Science, Okazaki 444-8585, Japan³Graduate School of Arts and Sciences, International Christian University, Mitaka 181-8585, Japan⁴Department of Applied Chemistry and Biotechnology, Faculty of Engineering, Chiba University, Chiba 263-8522, Japan⁵Photon Factory, High Energy Accelerator Research Organization (KEK-PF), Institute of Materials Structure Science (IMSS), Tsukuba 305-0801, Japan

Energy level alignment at organic-metal interface is one of the important topics in the field of organic electronics [1]. The HOMO and LUMO levels of organic molecules shift upon adsorption as a result of the work function change due to the formation of an interfacial dipole. This causes the change of the charge injection barrier from the metal electrode, which affects the efficiency of the organic devices. Recently, doping of organic semiconductors is re-focused to improve the conductivity [2]. The doping process in organic semiconductors is the charge transfer between the molecules, and two representative mechanisms are proposed: one is the integer charge transfer, or ionization, and the other is the formation of charge transfer complex [2]. In either case, the energy levels of the doped molecule are altered from those of the original HOMO or LUMO, because of the electrostatic effect derived from the doped charge, or the orbital re-hybridization. Therefore, the energy level alignment of the doped molecules at the metal interface is necessary to be elucidated. In this study, we have observed the electronic structure of perylene molecules on the Au(110) surface and the effect of bromine doping by angle resolved photoelectron spectroscopy (ARPES) and X-ray photoelectron spectroscopy (XPS) using momentum microscope, which has recently been introduced at BL6U.

Figure 1(a) shows the ARPES results of the perylene monolayer on the Au(110)-(1x2) surface, which was obtained at $E_b = 1.5$ eV at the surface normal direction. The photoelectron pattern simulated for the HOMO of the perylene molecule at the normal direction with respect to the molecular plane is shown in Fig. 1(c), right panel, which was obtained by the plane wave approximation. This four-fold pattern is changed to a two-fold one for the $\pm 18^\circ$ off-normal direction, as shown in Fig. 1(b). The pattern resemblance for Fig. 1(a) and 1(b) indicates that the molecular plane is tilted $\pm 18^\circ$ with respect to the surface normal. The tilted molecular orientation is in accordance with the results of X-ray absorption spectroscopy (XAS), and the scanning tunneling microscopy [3]. Figure 1(d) depicts the structural model of perylene on Au(110)-(1x2).

Bromine molecules doped to the perylene monolayer

penetrate into the monolayer and adsorbed dissociatively on the Au(110) surface. This was confirmed by the Br-3d XPS spectra. Upon bromine penetration, the orientation of the perylene molecules become random. Therefore, the characteristic ARPES pattern of the HOMO electrons disappears. The XAS results indicates that the perylene molecules are cationized upon bromine doping, because of the charge transfer from the perylene to the Au surface mediated by the bromine layer. The HOMO level exceeds the Fermi level as a result of the upward energy shift of the perylene MOs induced by the bromine layer, and hence, part of the HOMO electron is transferred. The energy shift was confirmed by the C-1s XPS spectra.

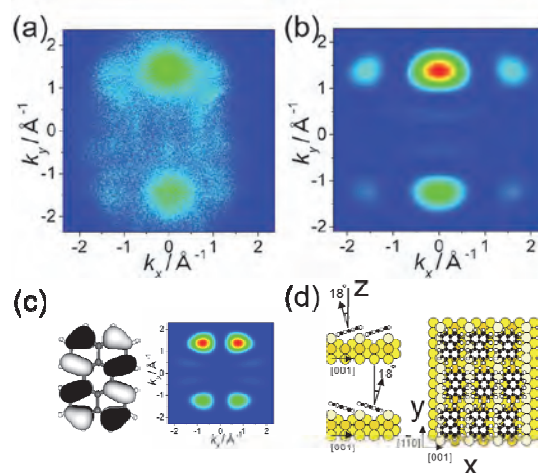


Fig. 1. (a) Momentum map of perylene/Au(110) at $E_b = 1.5$ eV. (b) Simulated photoelectron distribution for perylene molecule tilted $\pm 18^\circ$ along the short axis. (c) Orbital distribution of perylene HOMO and the simulated photoelectron distribution at the normal direction with respect to the molecular plane. (d) Structural model of perylene on Au(110).

[1] H. Ishii, *et al.*, Adv. Mater. **11** (1999) 605.

[2] I. Salzmänn, *et al.*, J Electron Spectros Relat Phenomena **204** (2015) 208.

[3] L. Gross, *et al.*, Org. Electron. **3** (2002) 1.

BL6U

High-resolution Photoelectron Momentum Microscope Study on the Electronic Structure of Charge-density-wave Material

K. Fukutani^{1,2}, S. Tanaka³, F. Matsui^{1,2} and S. Kera^{1,2,4}

¹Institute for Molecular Science, Okazaki 444-8585, Japan

²The Graduate University for Advanced Studies (SOKENDAI), Okazaki 444-8585, Japan

³Sanken, Osaka University, Ibaraki 567-0047, Japan.

⁴Graduate School of Science and Engineering, Chiba University, Chiba 263-8522, Japan

Among various critical phenomena in solids, charge density wave (CDW) is one of the widely observed phase transitions, which induces deformation of lattice periodicity as well as of the electronic density. The prototypical examples of such CDW are found in many of the transition metal dichalcogenides (TMDCs), which exhibit the wide range of periodicities upon the phase transitions, including commensurate and incommensurate CDWs [1].

On the other hand, despite the ubiquity of CDWs and the decades-long intensive research efforts, aimed for revealing their microscopic mechanisms, there is no clear consensus on their driving forces.

Recently, the roles of dimensionalities on the properties of TMDC materials and their CDWs have attracted much attentions. In particular, in the two-dimensional limit (i.e., a single monolayer), some TMDC materials are found to behave in drastically different manners, as can be seen in two-dimensional ferromagnetism of VSe₂ [2], the suppression of CDW in TaS₂ [3], and the enhancement of CDW in NbSe₂ [4], to name a few. These recent observations show that the careful studies of the dimensionality effects can provide key insights in resolving the long-standing mysteries of the origin of CDW transitions.

Among such TMDC materials, the series of titanium dichalcogenides, TiX₂ (X = S, Se, Te) present particularly interesting trends in CDW properties. While in the bulk form, only TiSe₂ exhibits CDW, in the two-dimensional limit, CDW with the same periodicity emerges for TiTe₂ [5], suggesting the role of dimensionality in the emergence of CDW.

However, it has been reported that the choice of substrate affects significantly the CDW order [6]. This is most naturally attributed to the interactions between the monolayer TiTe₂ and the substrate. In other words, while the dimensionality is a critical factor for CDW formation, the degree to which the monolayer-substrate interaction breaks the “pure” two-dimensionality of TiTe₂ is a critical issue that must be systematically investigated.

In this project, we attempt to tune the dimensionality quasi-continuously by inserting the intercalation layer with various atomic thicknesses near the surface of bulk TiTe₂, whereby gradually “lifting up” the two-dimensional layer to investigate the respective electronic structures.

For this purpose, photoelectron momentum microscope (PMM) is an ideal instrument, which can efficiently identify the periodicity and the topology of the Fermi surface structure in wide momentum range. In the first

phase of this project, we have performed the high-resolution PMM measurements on pristine TiTe₂.

Combined with the use of space-resolved mode, the surface of high crystallinity can be readily found and the example of the obtained spectra is shown in Fig. 1. The experiments were performed with photon energy as well as polarization dependence, and the obtained set of data are expected to yield detailed information on the three-dimensional (k_x, k_y, k_z) electronic structures as well as their orbital textures.

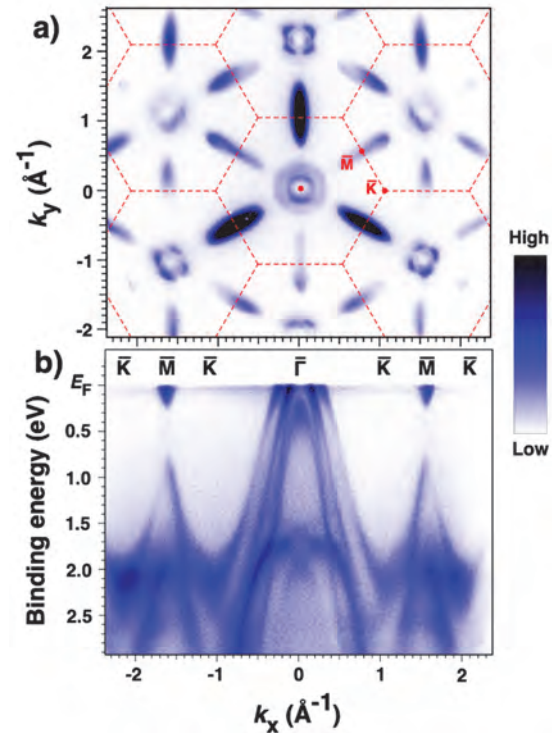


Fig. 1. (a) Fermi surface intensity image and (b) band structure mapping of TiTe₂ obtained at $h\nu = 52$ eV and $T = 50$ K with PMM at BL6U.

- [1] K. Rossnagel, J. Phys.: Condens. Matter **23** (2011) 213001.
- [2] M. Bonilla *et al.*, Nat. Nanotechnol. **13** (2018) 289.
- [3] C. E. Sanders *et al.*, Phys. Rev. B **94** (2016) 081404(R).
- [4] X. Xi *et al.*, Nat. Nanotechnol. **10** (2015) 765.
- [5] P. Chen *et al.*, Nat. Commun. **8** (2017) 516.
- [6] M.-K. Lin *et al.*, Phys. Rev. Lett. **125** (2020) 176405.

BL6U

Twin-domain Boundary and Monoatomic Step of Graphite Surface Imaged by Photoelectron Momentum Microscopy

 F. Matsui^{1,2}, Y. Okano¹, H. Matsuda¹, T. Yano¹, E. Nakamura¹, S. Kera^{1,2} and S. Suga^{3,4}
¹UVSOR Synchrotron Facility, Institute for Molecular Science, Okazaki 444-8585, Japan

²The Graduate University for Advanced Studies (SOKENDAI), Okazaki 444-8585, Japan

³SANKEN, Osaka University, Suita, Osaka 567-0047, Japan

⁴Forschungszentrum Jülich, Germany

The photoelectron momentum microscope is an instrument that combines a photoelectron microscope with a projection-type electron energy analyzer to enable both μm -scale valence band mapping and momentum-selective photoelectron microscopy [1-3]. Using these methods, we measured the local electronic structure of graphite crystal surfaces.

The cleaved graphite surface is found to have facets a few μm wide that share a twin-domain boundary in the armchair edge direction. This “armchair facet” was characterized by μm -scale VB mapping. The normal direction of the “armchair facet” differed from that of the terrace region by about 20° . The π -band splitting due to interlayer interaction was the same in the “armchair facet” and the terrace region, indicating that the interlayer distance between the two regions was identical. By transforming the photoelectron distribution of the selected momentum direction in reciprocal space to real space, a momentum-selective microscopic image can be obtained. By detecting photoelectrons of the “armchair facet” at the M symmetry point, a microscopic image in which the “armchair facet” is selectively enhanced was successfully obtained [4].

Furthermore, the k_z dispersion of graphite from the few mm region was measured using photoelectron momentum microscope (Fig. 1). The π band dispersion over the entire Brillouin zone was investigated. Note that graphite crystals with an *ABAB*...-type stacking structure are six-fold symmetric around the z axis, whereas a surface with one type of termination is three-fold symmetric. The microscope function of the PMM has a detection area sufficiently small to select only one type of graphite termination structure on the cleavage plane. We found that the π band was no longer degenerate in the ALH plane and its symmetry was reduced from C_{6v} to C_{3v} . This phenomenon is attributed to the coupling of the single-domain three-fold graphite surface π -band with the six-fold bulk k_z dispersion, which has been neglected up to now. This symmetry breaking was used to image the monoatomic steps on the graphite surface [5].

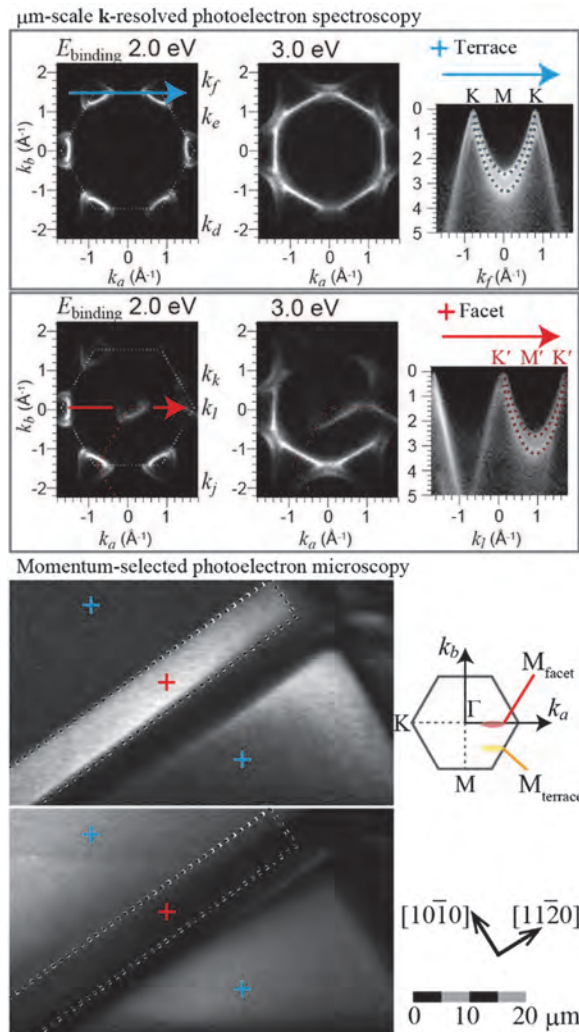


Fig. 1. μm -scale valence band mapping and momentum selective photoelectron microscopy of graphite surface.

[1] F. Matsui, S. Makita, H. Matsuda, T. Yano, E. Nakamura, K. Tanaka, S. Suga, and S. Kera, *Jpn. J. Appl. Phys.* **59** (2020) 067001.

[2] S. Makita, H. Matsuda, Y. Okano, T. Yano, E. Nakamura, Y. Hasegawa, S. Kera, S. Suga, and F. Matsui, *e-J. Surf. Sci. Nanotech.* **19** (2021) 42.

[3] F. Matsui, S. Makita, H. Matsuda, E. Nakamura, Y. Okano, T. Yano, S. Kera, and S. Suga, *J. Phys. Soc. Jpn.* **90** (2021) 124710.

[4] F. Matsui, Y. Okano, H. Matsuda, T. Yano, E. Nakamura, S. Kera, and S. Suga, submitted (2022). "Domain-resolved Photoelectron Microscopy and μm -scale Momentum-resolved Photoelectron Spectroscopy of Graphite Armchair Edge Facet".

[5] F. Matsui and S. Suga, submitted (2022) "Coupling of graphite surface π band with k_z dispersion"

BL6U

Development of the Fabrication System for the μm -scale Ultra-thin Film at BL6U

T. Nakamura^{1,2}, F. Matsui³ and S. Kimura^{1,2,4}¹Graduate School of Frontier Biosciences, Osaka University, Suita 565-0871, Japan²Department of Physics, Graduate School of Science, Osaka University, Toyonaka 560-0043, Japan³UVSOR Synchrotron Facility, Institute for Molecular Science, Okazaki 444-8585, Japan⁴Institute for Molecular Science, Okazaki 444-8585, Japan

Photoelectron spectroscopy (PES) is a powerful technique to investigate the electronic structures of materials. Recently developed at UVSOR-III BL6U, synchrotron-based photoelectron momentum microscopy (PMM) is one of the state-of-the-art PES systems [1]. On the other hand, research on unique electronic states in the microscopic region, such as edge states in topological materials and domains in inhomogeneous samples, has been intensively explored [2-4]. The combination of PMM and small-sized samples with the unique electronic state leads to fertile physics. In this work, we have developed a new thin-film deposition system in the preparation chamber at the BL6U end station.

The basic concept of this system is the selective deposition of the materials passes through the spatial mask filter from the evaporator. Figure 1(a) shows the photo of the flagship-type sample holder with two M2 holes to attach the additional filter component. Spot-welded Ta foils are used to fix a substrate. Figure 1(b) shows the mask filter. The main material is a flat Ta foil ($10 \times 10 \text{ mm}^2$) with a $\phi 2 \text{ mm}$ hole at the center. A honeycomb-type TEM grid (The hole and bar sizes on the TEM grid are $290 \mu\text{m}$ and $59 \mu\text{m}$, respectively) was used to make a pattern in the current system. A commercially available square clip ($4 \times 4 \text{ mm}^2$) is used as a handle to fix the mask on the sample. The opposite side of the clip is an M2 screw. Figure 1(c) shows the photo of the sample holder with the mask filter on a heating stage in the preparation chamber of the BL6U end station. The distance between the holder and mask filter is about 1.5 mm . When cleaning the substrate by annealing and Ar sputtering, the mask filter is removed and set to other sample holders on the sample bank.

We used the InSb(111)B substrate as a test sample. The substrate was cleaned by the cycle of Ar-ion sputtering (acceleration energy of 1 kV) and annealing up to 600 K . After checking the sharp (3×3) diffraction pattern, the 1-nm Sb layer was evaporated on the InSn(111)B substrate with the mask filter at room temperature.

Figure 2 shows a spatial-resolved In $4d$ core level intensity map. One pixel indicates the sum of the photoelectron intensity measured by the microscopy mode of PMM. The domain scale of the bright area is almost consistent with the size of the bar of the TEM grid.

As the next step, we quantitatively evaluate the spatial

resolution of selective deposition with mask filters and observe the band structure from a single micro-scale domain.

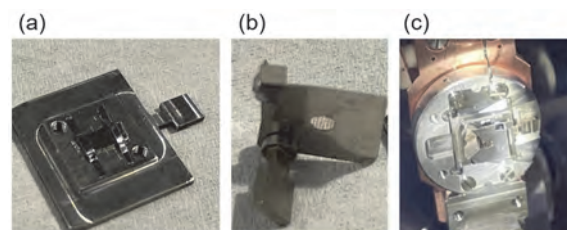


Fig. 1. Photos of the spatially selective deposition system. (a) sample holder. (b) mask filter. (c) sample holder with mask filter on a heating stage in the preparation chamber of BL6U.

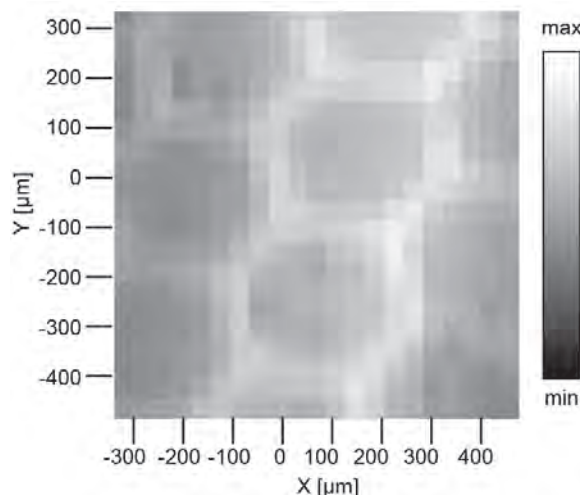


Fig. 2. Real-space image of the In $4d$ photoelectron intensity plot. The incident photon energy is 80 eV .

[1] F. Matsui *et al.*, Jpn. J. Appl. Phys. **59** (2020) 067001.

[2] K. Nakayama *et al.*, Nano Lett. **19** (2019) 3737.

[3] R. Noguchi *et al.*, Nature **566** (2019) 518.

[4] H. Iwasawa, Electron. Struct. **2** (2020) 043001.

BL7U

High-resolution Angle-resolved Photoemission Study on MnBi₂Se₄/Bi₂Se₃/MnBi₂Se₄ Sandwich Structure

R. Fukushima¹, S. Ichinokura¹, K. Tanaka² and T. Hirahara¹¹Department of Physics, Tokyo Institute of Technology, Tokyo 152-8551, Japan²UVSOR Synchrotron Facility, Institute for Molecular Science, Okazaki 444-8585, Japan

Topological insulators (TI) are extensively studied recently due to its peculiar properties [1]. The Dirac-cone surface states of TI are protected by time-reversal symmetry (TRS) and backscattering among these surface states is prohibited. But when TRS is broken by application of a magnetic field or incorporating magnetic materials, a gap opening in the Dirac cone is expected and an intriguing phase called the quantum anomalous Hall state can be realized [2]. This phase is expected to show even more exotic phenomena such as the topological magnetoelectric effect. To realize such state, two types of sample fabrication techniques have been employed up to now: (1) magnetic doping while growing the single crystal or thin film of TI [3], and (2) magnetic impurity deposition on the surface of TI [4]. While method (1) was successful and showed evidence of the TRS violation, no one has succeeded using method (2), which should be a more direct way to examine the interaction between the topological surface states and magnetism. We have previously found another novel technique to induce magnetism into TI, namely the magnetic extension effect [5]. By depositing Mn and Se on Bi₂Se₃, we found that Mn and Se are incorporated in the topmost Bi₂Se₃ layer and a novel heterostructure MnBi₂Se₄/Bi₂Se₃ is formed [5]. This heterostructure with an ordered magnetic Mn single layer showed a clear Dirac cone gap of 85 meV. From magnetic measurements utilizing high-resolution X-ray magnetic circular dichroism (XMCD) at the Mn *L* adsorption edge, it was revealed that the Curie temperature *T_c* of the system is 15-20K. However, when we fabricated a sandwich structure of MnBi₂Se₄/*n* quintuple layer (QL) Bi₂Se₃/MnBi₂Se₄, which includes two magnetic Mn layers, we found that the *T_c* was enhanced to 20-25 K for *n* = 1-7. Thus it is important to measure the electronic structure of the sandwich structure and investigate the origin of the enhancement of *T_c*.

Therefore in this study, we have measured the band dispersion of MnBi₂Se₄/7 QL Bi₂Se₃/MnBi₂Se₄ sandwich structure by angle-resolved photoemission spectroscopy (ARPES). The band dispersion measured at 10 K is shown in Fig. 1 system. It shows a band structure similar to the heterostructure with a linear dispersion [5] and a quantitative analysis of the energy dispersion curve (EDC) at the Γ point revealed that the gap size was 100 meV. This result showed that there is practically little difference between the hetero and sandwich structures. Further magnetic characterization with XMCD including measurements for nonmagnetic elements (Se or Bi)

have given new insights into the magnetic interaction of the two Mn magnetic layers for the sandwich structure. Namely it was revealed that the bulk carriers of the Bi₂Se₃ near the Fermi level mediate the magnetic interaction between the two Mn layers [6].

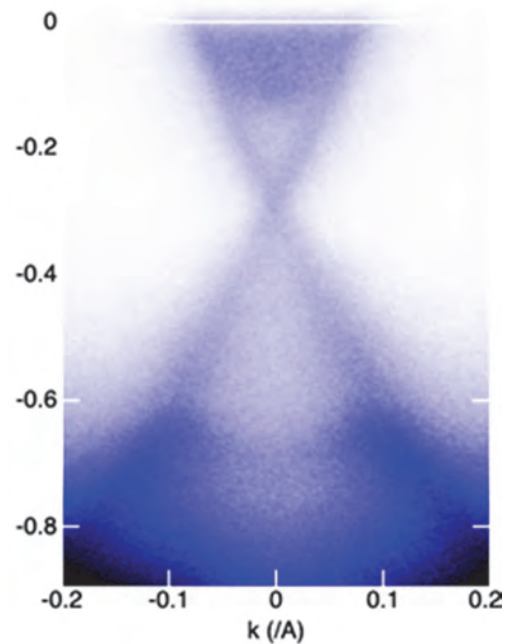


Fig. 1. Band dispersion image of the MnBi₂Se₄/7 QL Bi₂Se₃/MnBi₂Se₄ sandwich structure measured at 10 K.

- [1] M. Hasan and C. Kane, *Reviews of Modern Physics* **82** (2010) 3045.
- [2] X.-L. Qi and S.-C. Zhang, *Reviews of Modern Physics* **83** (2011) 1057.
- [3] For example, C. Z. Chang *et al.*, *Science* **340** (2013) 167.
- [4] For example, M. Ye *et al.*, *Physical Review B* **85** (2012) 205317.
- [5] T. Hirahara *et al.*, *Nano Letters* **17** (2017) 3493.
- [6] R. Fukushima *et al.*, to be published.

BL7U

Observation of Electronic Structure of YbCu₂/Cu(111) Surface Alloy

 H. Sugihara¹, T. Nakamura^{2,1}, Y. Chen¹, K. Tanaka³ and S. Kimura^{2,1,4}
¹Department of Physics, Graduate School of Science, Osaka University, Toyonaka 560-0043, Japan

²Graduate School of Frontier Biosciences, Osaka University, Suita, 565-0871, Japan

³UVSOR Synchrotron Facility, Institute for Molecular Science, Okazaki 444-8585, Japan

⁴Department of Materials Molecular Science, Institute for Molecular Science, Okazaki 444-8585, Japan

The Kondo coupling between localized f -electrons and carriers leads to exotic physical phenomena such as the formation of the heavy-fermion (HF), the emergence of a magnetic quantum critical point, and unconventional superconductivity [1]. Among them, the HF system, in which massive effective carriers appear due to the Kondo effect, has fascinated many researchers [2,3]. On the other hand, the combination of HF system and low-dimensionality strongly modulate the hybridization strength because an order parameter of these systems is much sensitive to dimensionality. In a typical bulk HF compound, CeIn₃, for instance, the suppression of the antiferromagnetism and the increase of the carrier's effective mass appear due to the reduction of the dimensionality [4]. In addition, a HF quasicrystal, which has higher dimensionality, has an unconventional quantum criticality [5]. To clarify the relation of the dimensionality to the HF character, we investigate electronic structure of low-dimensional HF materials. Here, we have studied the surface electronic structure of a HF surface alloy, YbCu₂/Cu(111), which is a new candidate for the two-dimensional HF system, measured by angle-resolved photoelectron spectroscopy (ARPES).

The clean Cu (111) substrate was prepared by the cycle of Ar⁺ sputtering and annealing up to 800 K. After checking a sharp and low-background streak electron diffraction pattern, Yb-metal was evaporated by a homemade Knudsen cell, resulting in the observation of fractional order originated from the YbCu₂ layer. ARPES measurement was carried out at UVSOR BL7U ($h\nu = 21$ eV) at temperature of 6 K.

Figure 1 shows the ARPES intensity plot of YbCu₂/Cu(111) surface along $\bar{\Gamma}-\bar{K}$ on a surface Brillouin zone of Cu(111). To see the band dispersion above the Fermi level, the ARPES spectra were divided by the Fermi-Dirac distribution function convoluted with the instrumental resolution. The flat bands with the binding energy of around 0.2 eV are attributed to the Yb²⁺ $4f_{7/2}$ final state after the photoexcitation process. Several hole bands centered on the $\bar{\Gamma}$ point were observed. The hybridizations between the hole bands and the Yb $4f$ state appears as the modulation of the shapes and intensities. In addition to the hybridization, as shown in Fig. 2, a steep peak, which seems to be a Kondo resonance peak usually observed in HF materials [6], appears near the Fermi level. These results suggest the HF formation in YbCu₂/Cu(111).

Further analysis to understand the hybridization between the Yb $4f$ orbital and conductive hole bands

and the relation to the dimensionality are in progress.

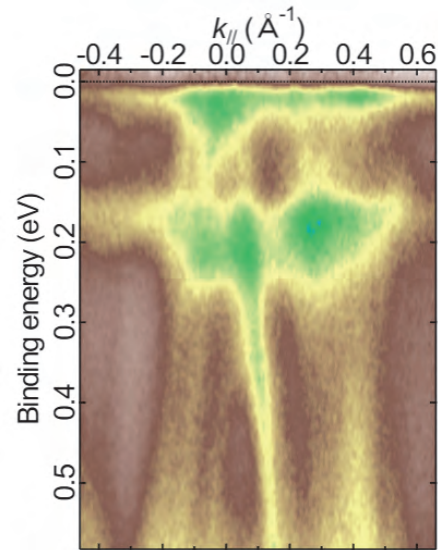


Fig. 1. ARPES band dispersion of YbCu₂/Cu(111) surface along $\bar{\Gamma}-\bar{K}$ taken at $h\nu = 21$ eV ($T = 6$ K). The photoelectron intensities were normalized by Fermi-Dirac distribution function convoluted with the instrumental resolution.

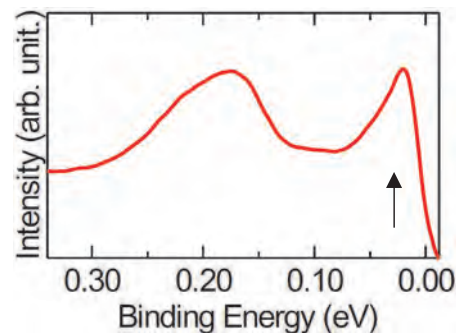


Fig. 2. Angle-integrated photoelectron spectra of YbCu₂/Cu(111). The arrow indicates the Kondo resonance peak.

- [1] C. Pfleiderer, Rev. Mod. Phys. **81** (2009) 1551.
- [2] A. C. Hewson, *The Kondo Problem to Heavy Fermions* (Cambridge Univ. Press, Cambridge, 1993).
- [3] P. Coleman *et al.*, J. Phys.: Condens. Matter **13** (2001) R723.
- [4] H. Shishido *et al.*, Science **327** (2010) 980.
- [5] K. Deguchi *et al.*, Nat. Mater. **11** (2012) 1013.
- [6] S. Chatterjee *et al.*, Nat. Commun. **8** (2017) 852.

BL7B

Electrochemical Attenuated Total Reflectance Ultraviolet (EC-ATR-UV) Spectroscopy Applied for Organic Semiconductor / Ionic Liquids Interface

I. Tanabe, Y. Hanamori and K. Fukui

Department of Materials Engineering Science, Graduate School of Engineering Science, Osaka University,
Toyonaka 560-8531, Japan

Electric double-layer organic field-effect transistors (EDL-OFETs) have attracted much attention because of their significantly low operation voltage (<1 V) compared to conventional SiO_2 -gated OFETs (>10 V). In EDL-OFETs, a high electric field is generated in the EDL that accumulates in the interfacial region between the organic semiconductor and electrolyte, resulting in a low operation voltage. Therefore, the organic semiconductor/electrolyte interface is especially important. Recently, we developed a new spectroscopic system, namely electrochemical-attenuated total reflectance (EC-ATR) ultraviolet-visible spectroscopy, which can access the interfacial area [1,2].

In this study, ionic liquid gated organic field-effect transistors (IL-gated OFETs) were fabricated on the ATR prism (Fig. 1). Two-layer single crystalline film of C_9 -DNBDT-NW was used as an organic semiconductor, and two kinds of ionic liquids ([EMIM][FSA] and [TPMA][TFSA]) were cast on the film. Au films were evaporated to a thickness as the source and drain electrodes (working electrodes) on both sides of the ATR prism, and a Pt coil and a Pt wire were placed in the ionic liquids as pseudo counter and reference (gate) electrodes, respectively. In our previous study [2], in response to the applied gate voltage, the spectral peaks of the organic semiconductor shifted and bleached. This was correlated with the drain current.

The fabricated IL-gated OFETs on the ATR prism was put on the sample chamber in BL7B at UVSOR. The light from UVSOR had one important advantage; polarization direction control. That is to say, by changing the placing direction of the ATR prism to the incident light, the polarized direction to the sample can be controlled. While our previous study used a halogen lamp as the light source, which was unpolarized, the synchrotron radiation is innately polarized. In the UV region, especially in the deep-UV (<300 nm) region, the preparation of a polarizer is difficult, and thus, the polarized light generated from the synchrotron is highly useful.

Figure 2 shows the ATR spectra of C_9 -DNBDT-NW on the sapphire prism measured in BL7B at UVSOR. While the *s*-polarized incident light gave distinct peaks in the 200-500 nm range (Fig. 2 (a)), *p*-polarized incident light did not (Fig. 2 (b)). This is because the C_9 -DNBDT-NW film on the ATR prism was well packed, and shows strong polarized dependence.

These peaks could be assigned by quantum chemical calculations, and they verified depending on the applied voltage [2]. In addition, EC-ATR-UV spectroscopy

could measure the absorbance due to the ionic liquids near the surface of the C_9 -DNBDT-NW film because of the short penetration depth (< 50 nm) and the strong ionic liquids' absorbance of the light in the UV region, which was a unique point of the new technique. Therefore, we are trying spectral measurements of both organic films and ionic liquids during device operations using the polarized light from BL7B. It will reveal orientations of interfacial ionic liquids and their behaviors under electrochemical environment. Additionally, the interactions between the organic semiconductor film and ionic liquids will be investigated, leading to the mechanism research and improvement of the high performance EDL-OFETs.

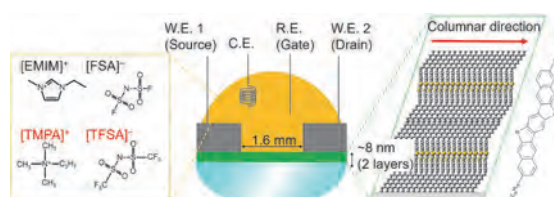


Fig. 1. Schematics of EDL-OFET fabricated on ATR prism.

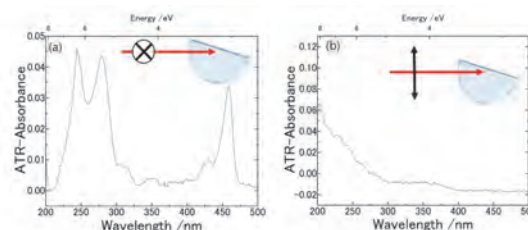
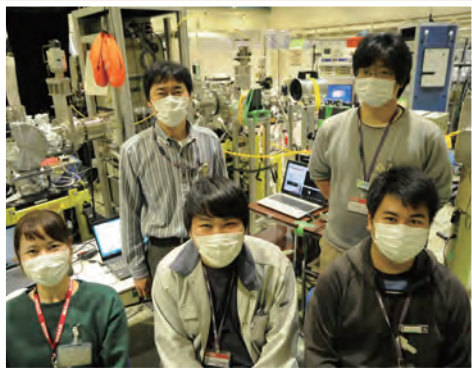
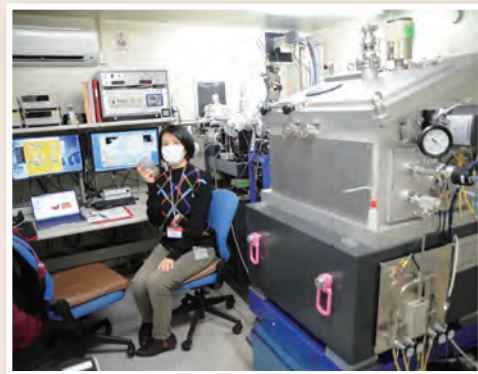
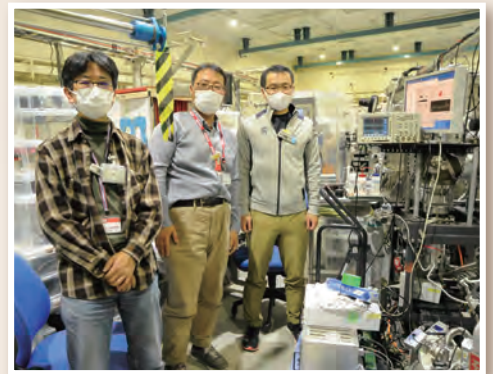
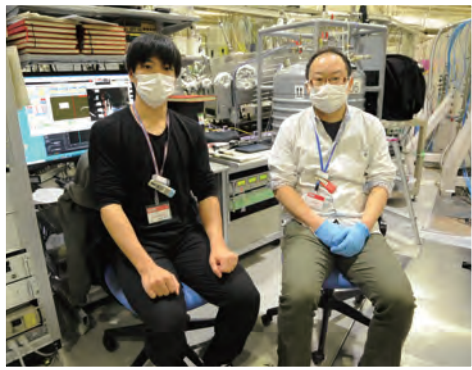
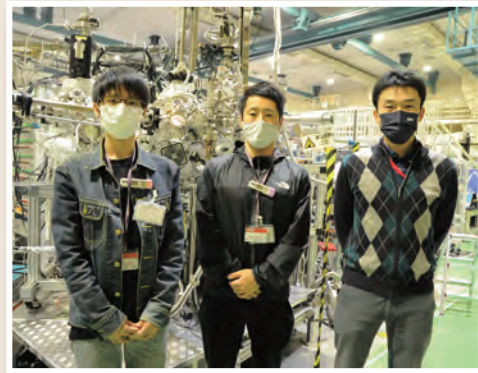
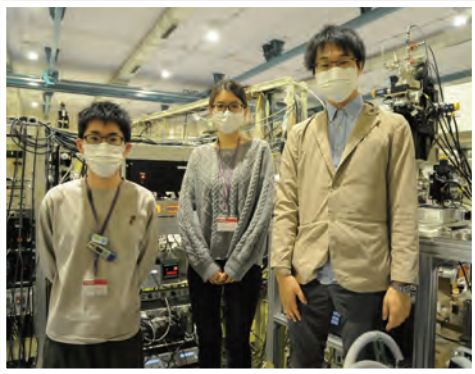


Fig. 2. Polarization dependence of ATR spectra of C_9 -DNBDT-NW on a sapphire prism.

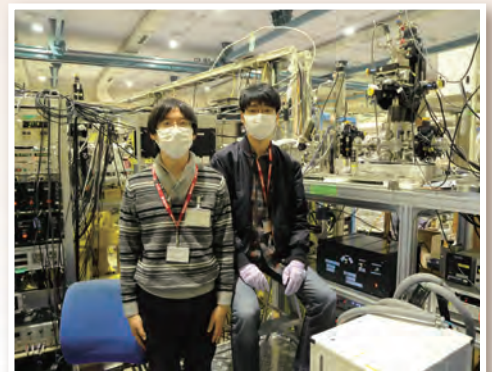
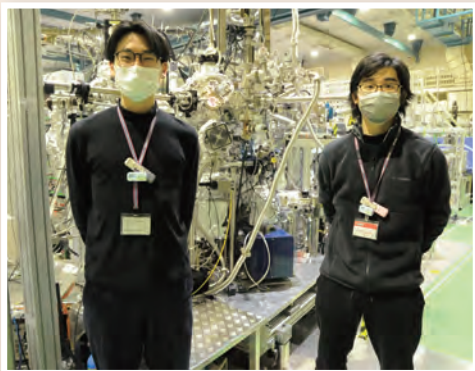
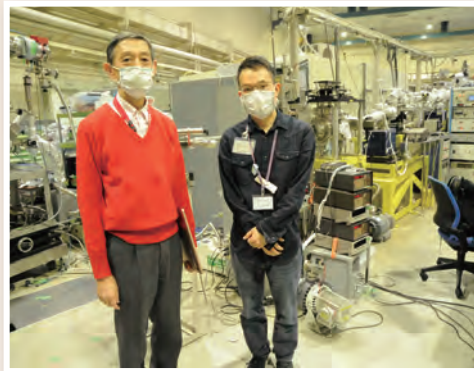
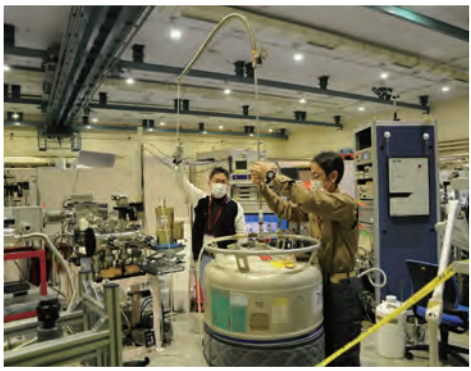
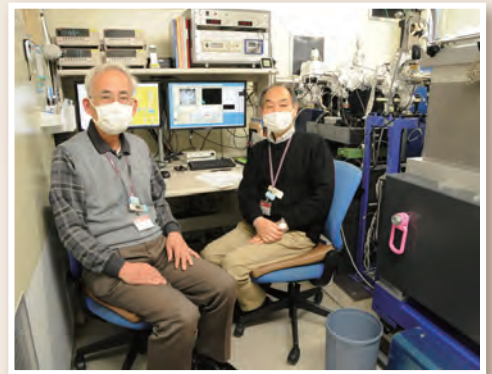
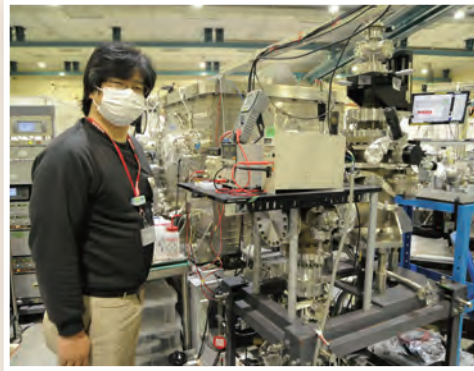
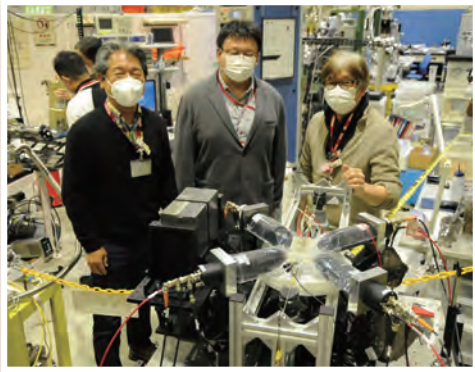
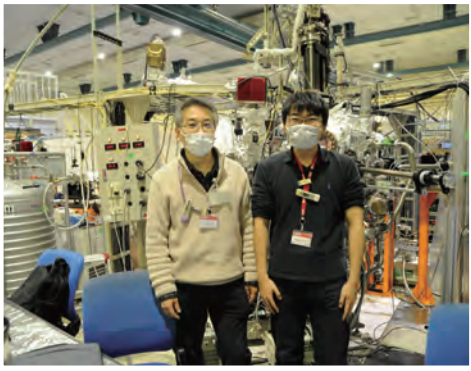
[1] I. Tanabe, A. Suyama, T. Sato and K. Fukui, *Anal. Chem.* **91** (2019) 3436.


[2] I. Tanabe, I. Imoto, D. Okaue, M. Imai, S. Kumagai, T. Makita, M. Mitani, T. Okamoto, J. Takeya and K. Fukui, *Commun. Chem.* **4** (2021) 88.

UVSOR User 6



UVSOR User 7



The background is a solid purple color with several abstract geometric elements. A large, semi-transparent circular graphic is centered on the right side, featuring concentric rings and a dotted border. Diagonal lines and a grid of small dots are also visible, creating a sense of depth and movement.

III-5

Life, Earth and
Planetary Sciences

BL4U

Hayabusa2 Returned Samples: Unique and Pristine Record of Solar System Materials from Asteroid Ryugu

M. Ito¹, N. Tomioka¹, M. Uesugi², A. Yamaguchi^{3,4}, N. Imae^{3,4}, N. Shirai⁵, T. Ohigashi^{4,6}, M. Kimura³, M.-C. Liu⁷, R.C. Greenwood⁸, K. Uesugi², A. Nakato⁹, K. Yogata⁹, H. Yuzawa⁶, Y. Kodama¹⁵, A. Tsuchiyama¹⁰, M. Yasutake², R. Findlay⁸, I.A. Franchi⁸, J.A. Malley⁸, K.A. McCain⁷, N. Matsuda⁷, K.D. McKeegan⁷, K. Hirahara¹¹, A. Takeuchi², S. Sekimoto¹², I. Sakurai¹³, I. Okada¹³, Y. Karouji¹⁴, T. Yada⁹, M. Abe⁹, T. Usui⁹, S. Watanabe¹³ and Y. Tsuda^{4,9}

¹JAMSTEC Kochi, ²JASRI/SPring-8, ³NIPR, ⁴SOKENDAI, ⁵Tokyo Met. Univ., ⁶UVSOR/IMS, ⁷UCLA, ⁸Open Univ., ⁹JAXA/ISAS, ¹⁰Ritsumeikan Univ., ¹¹Osaka Univ., ¹²Kyoto Univ., ¹³Nagoya Univ., ¹⁴JAXA/JSEC, ¹⁵Toyo Corp.

The Hayabusa2 spacecraft successfully returned surface materials from the C-type asteroid Ryugu to Earth on December 6th, 2020. The sample capsule contained a large number of small grains, collected from touchdown (TD) sites 1 and 2 on Ryugu, with a total mass of ~5.4 g [1]. After initial characterization of the grains by JAXA curation [1,2], eight Ryugu particles (~60 mg in total), four from Chamber A and four from Chamber C, were allocated to the Phase2 curation Kochi team (Ph2K). The principal goals of the research are to elucidate the nature, origin, and evolutionary history of asteroid Ryugu, and to document the similarities to and/or differences from other known extraterrestrial samples, such as chondritic meteorites, interplanetary dust particles and returned cometary samples collected by the NASA Stardust mission.

The coordinated micro-analysis work involved the use of a wide range of multi-beam instruments to acquire detailed micro-textural and chemical information about the samples at a sub-micrometer scale using a combination of FIB, STXM-NEXAFS, NanoSIMS and TEM [4,5]. In parallel, we conducted bulk systematic analysis of the samples using SEM-EDS, EPMA, XRD, large geometry type SIMS, high precision O isotopic analysis by laser fluorination and INAA [4-8].

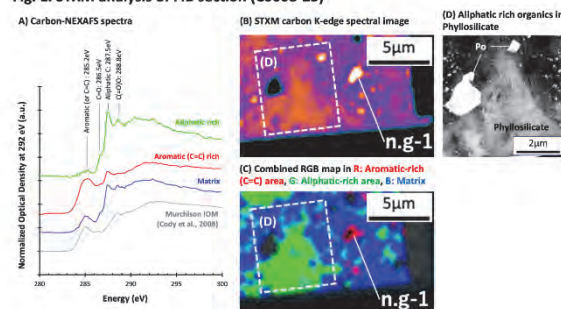
Using a combination of STXM-NEXAFS – NanoSIMS – TEM techniques, we have been able to establish the spatial distribution of organics with an aliphatic-rich carbon structure that are associated with phyllosilicates at sub-micrometer scale in the C0068-25 FIB section (Fig. 1).

C-NEXAFS spectra in the C0068-25 section show a variety of functional groups of aromatic (or C=C), C=O, C-H or aliphatic, and C(=O)O, without 1s-σ* exciton of graphene structures (Fig. 1(A)). Figure 1(B) shows the spatial distribution of carbon in the section. In Fig. 1(C), three representative areas of aromatic (or C=C)-rich organics can be seen in red, aliphatic-rich carbon is shown in green and matrix in blue. Areas with an intense aliphatic-rich carbon structure (green area in Fig. 1(C)) are present locally in coarse-grained phyllosilicates in the section (Fig. 1(D)), as well as areas with a poorly aromatic (C=C) carbon structure.

The distribution of organics with an aliphatic carbon structure may vary significantly depending on the existence of coarse-grained phyllosilicates. The C-NEXAFS revealed that the organics in the Ryugu particles are chemically distinct from the previously studied IOM of the Murchison CM chondrite [8] and show greater similarity to IDPs [9] and cometary particles obtained by the Stardust mission [10].

A question that arises is whether the unique nature of the aliphatic carbon-rich organics associated with coarse-grained phyllosilicates observed in this study is a unique feature, only found in the Ryugu asteroid. This question requires additional work. Further study is needed to fully define the nature of the organics and their relationship with the surrounding hydrous mineral phases.

Fig. 1. STXM analysis of FIB section (C0068-25)



- [1] Yada T. *et al.*, *Nature Astron* (2021) doi.org/10.1038/s41550-021-01550-6.
- [2] Pilorget, C. *et al.*, *Nature Astron* (2021) doi.org/10.1038/s41550-021-01549-z.
- [3] Uesugi M. *et al.*, *Rev. Sci. Instrum.* **91** (2020) 035107.
- [4] Ito M. *et al.*, *Nature Astron*, in revision (2022).
- [5] Tomioka N. *et al.*, 53rd LPSC (2022).
- [6] Yamaguchi A. *et al.*, 53rd LPSC (2022).
- [7] Greenwood R.C. *et al.*, 53rd LPSC (2022).
- [8] Cody, G.D. *et al.*, *Earth Planet. Sci. Lett.* **272** (2006) 446.
- [9] Keller, L.P. *et al.*, *Geochim. Cosmochim. Acta* **68** (2004) 2577.
- [10] Sandford S.A. *et al.*, *Science* **314** (2006) 1720.

BLIU

Study of Pygmy Dipole Resonance using Linearly Polarized Photon Beam

T. Shizuma¹, M. Omer², T. Hayakawa¹, K. Ali³, H. Zen³, H. Ohgaki³, S. Miyamoto⁴,
K. Sugita⁵ and Y. Taira⁵

¹National Institutes for Quantum Science and Technology, Tokai 319-1106, Japan

²Japan Atomic Energy Agency, Tokai 319-1195, Japan

³Institute of Advanced Energy, Kyoto University, Uji 611-0011, Japan

⁴Laboratory of Advanced Science and Technology for Industry, University of Hyogo, Kamigori 678-1205, Japan

⁵UVSOR Synchrotron Facility, Institute for Molecular Science, Okazaki 444-8585, Japan

The emergence of low energy dipole strength so called Pygmy Dipole Resonance (PDR) has motivated many experimental and theoretical efforts [1]. The PDR has been observed as a concentration of electromagnetic strength near the low-energy tail of the Giant Dipole Resonance (GDR). It provides useful information on fundamental properties such as the neutron-skin thickness of medium to heavy nuclei, the nuclear symmetry energy, and the properties of neutron stars. The stable lead isotopes, including ^{206}Pb , are suitable for these studies since they exhibit an appreciable amount of low-energy dipole strength.

In a previous nuclear resonance fluorescence (NRF) measurement for ^{206}Pb using unpolarized bremsstrahlung [2], extra strengths were observed at the energy region ranging from 5 to 8 MeV which could be related to the PDR. The photo-absorption cross sections in ^{208}Pb in average amount to about 60% of that in ^{206}Pb . This behavior differs from that found in the series of xenon isotopes, in which the summed dipole strength in the energy region from 6 to 9 MeV increases with the neutron numbers [3]. Possible reasons are that the strength in the quasi-continuum may not be neglected in ^{208}Pb either or that there are structural differences that interfere the effect of the neutron excess [3].

To study the PDR nature in ^{206}Pb we measured NRF γ rays using linearly polarized photon beam. The laser Compton scattering (LCS) γ rays with a maximum energy of 7.54 MeV were generated by collision of 746-MeV electrons with linearly polarized laser photons with a wavelength of 800 nm at a collision angle of 82 degrees. A lead collimator with a 18-cm thickness and 3-mm aperture was used to form a quasi-monochromatic LCS photon beam. The photon flux was measured during the NRF measurement by a large volume LaBr_3 scintillation detector. The target consisted of a metallic cylinder (8 mm in diameter) of enriched ^{206}Pb . Four high-purity germanium (HPGe) detectors were used to measure scattered photons from the target. Two of these detectors were placed in the horizontal plane at a scattering angle of 90 degrees and the others were placed in the vertical plane. The experimental setup is shown in Fig. 1. A part of the photon scattering spectra observed at a polar angle of 90 degree relative to the polarization plane of the incident photon beam is represented in Fig. 2. The measured spectra are used to determine the parities of the resonant states by extracting

the intensity asymmetry of resonantly scattered γ -rays with respect to the polarization plane of the incident photon beam.

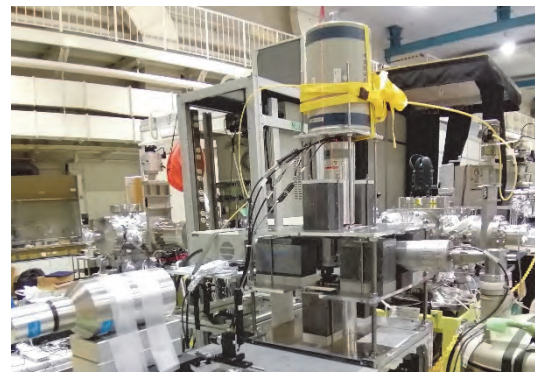


Fig. 1. Photo of the experimental setup used for NRF measurements at BLIU.

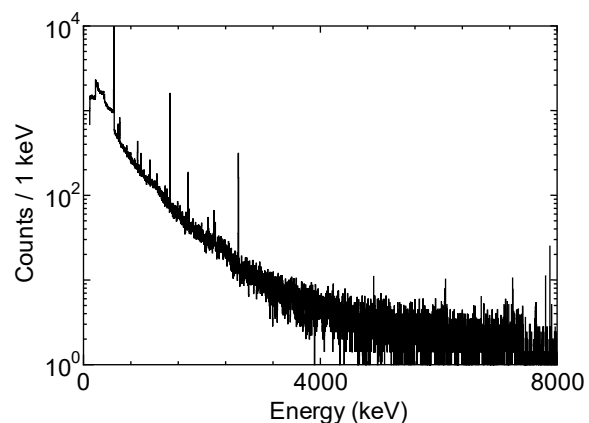


Fig. 2. Typical γ -ray spectrum observed at a polar angle of 90 degrees relative to the polarization plane of the incident photon beam.

[1] D. Savran *et al.*, Prog. Part. Nucl. Phys. **70** (2013) 210.

[2] T. Shizuma *et al.*, Phys. Rev. C **98** (2018) 064317.

[3] R. Massarczyk *et al.*, Phys. Rev. Lett. **112** (2014) 072501.

BL3U

X-ray Absorption Spectra of Lipid Bilayer Membranes in Aqueous Solutions

R. Tero¹, Yu Kinjo¹ and M. Nagasaka²¹Toyohashi University of Technology, Toyohashi 441-8580, Japan²Institute for Molecular Science, Okazaki 444-8585, Japan

The lipid bilayer is a self-assembled structure of amphiphilic lipid molecules and is the fundamental structure of biomembranes such as cell membranes. Internal structures of lipid bilayers, such as two-dimensional domains and hydrophobic thickness, and physical properties affect the transportation of materials, information, and energy through the biomembranes. All these physiological reactions proceed in the presence of ions. Ions in the aqueous solution significantly influence to these structures and properties of lipid bilayers. Phosphatidylcholine (PC) is the most abundant lipid of eukaryotic cell membranes. Cations bind to the phosphate and carbonyl groups of PC. However, affinity of cations to PC and effects of cations to molecular orientation are still controversy especially in the fields of theoretical simulations [1]. We aim to determine the binding affinity of cations to lipids in aqueous solutions experimentally, by means of X-ray absorption spectroscopy (XAS) [2,3].

Supported lipid bilayers (SLBs) of dioleoyl-PC (DOPC) were formed on the Si₃N₄ membranes of the XAS flow cell [2] by the vesicle fusion method. We prepared DOPC-SLBs with few residual vesicles as shown in Fig. 1. Fluorescence recovery after photobleaching observation showed that fluid and continuous SLB covered the whole Si₃N₄ membrane surface. O-K edge XAS spectra of the Si₃N₄ membrane before and after formation of SLB were obtained in a buffer solution (NaCl 100 mM, HEPES 25 mM/ pH 7.4 NaOH) which thickness was controlled to be less than 100 nm. The XAS spectrum of the Si₃N₄ membrane without SLB was subtracted from that with SLB.

The O-K-edge spectrum of DOPC appeared at 531 - 533 eV (Fig. 2). It is attributed to three components due to the phosphate and carbonyl groups on the PC headgroup: $1s \rightarrow \pi^*$ transitions of P=O, P-O-Na, and C=O at 531.5 eV, 532.3 eV, 532.0 eV, respectively [3]. We measured XAS spectra at different incident angle to obtain the orientation of these groups in the lipid bilayer [4]. The relative intensity of the three components varied with the incident angle (Fig. 2). The result indicates that XAS in the aqueous solution is capable to obtain information about the molecular orientation of lipids in bilayer membranes.

In conclusion, we obtained O-K edge XAS spectra of SLBs in an aqueous solution at various incident angles. We will investigate the effects of the cation concentration and species on the XAS components and their relative intensities.

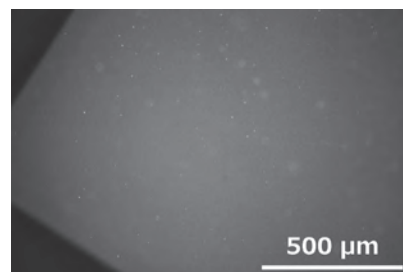


Fig. 1. Fluorescence image of DOPC-SLB on the the Si₃N₄ membranes of the XAS flow cell.

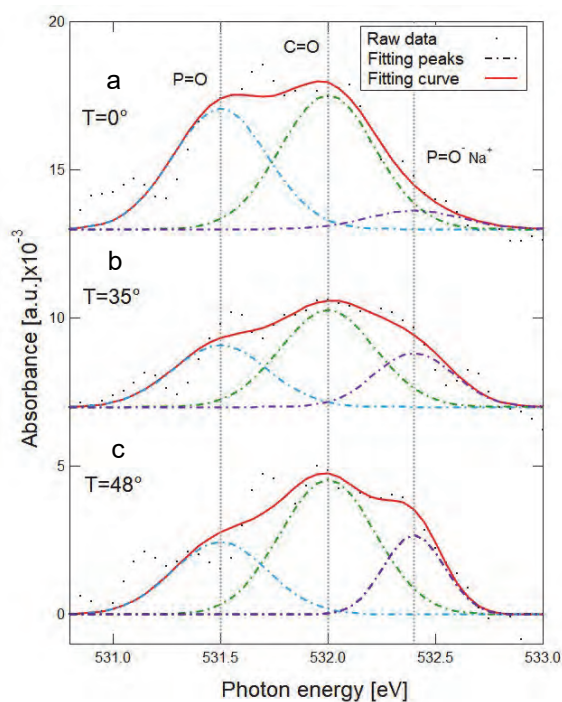


Fig. 2. O K-edge XAS spectra of DOPC-SLB obtained at various incident angle: (a) 0°, (b) 35°, and (c) 48°. Black dotted curves represent raw data. Dashed curves and red solid curves show deconvoluted components and their summation, respectively.

[1] T. B. Woolf, *Biophys. J.* **104** (2013) 746; A. Catte, *Phys. Chem. Chem. Phys.* **18** (2016) 32560.

[2] M. Nagasaka, H. Yuzawa, T. Horigome, and N. Kosugi, *J. Electron Spectros. Relat. Phenomena* **224** (2018) 93.

[3] R. Tero, W.-Z. Goh and M. Nagasaka, *UVSOR Activity Report 2020* **48** (2021) 129.

[4] H. Kondoh, F. Matsui, Y. Ehara, T. Yokoyama and T. Ohta, *Langmuir* **17** (2001) 8178.

BL4U

Evaluation of Exposure-Effects on Biomolecules for the Molecular Mapping of Biological Specimens Using STXM

A. Ito¹, K. Shinohara², A. Matsuura³, S. Toné⁴, M. Torigata¹, K. Tohya⁵, H. Yuzawa⁶
and T. Ohigashi^{6,7}

¹School of Engineering, Tokai University, Hiratsuka 259-1292, Japan

²Graduate School of Health Sciences, Fujita Health University, Toyoake 470-1192, Japan

³Research Integrity Office, Fujita Health University, Toyoake 470-1192, Japan

⁴School of Science and Engineering, Tokyo Denki University, Hatoyama 350-0394, Japan

⁵Kansai University of Health Sciences, Kumatoricho 590-0482, Japan

⁶UVSOR Synchrotron Facility, Institute for Molecular Science, Okazaki 444-8585, Japan

⁷School of Physical Sciences, The Graduate University for Advanced Studies (SOKENDAI), Okazaki 444-8585, Japan

It is well recognized that spectromicroscopy using a scanning transmission X-ray microscope (STXM) in the soft X-ray region is a powerful tool for the molecular mapping of biological specimens. We have been working on a quantitative mapping of nucleic acids (DNA and RNA) and proteins (histone and bovine serum albumin abbreviated as BSA) in chromosomes, cultured mammalian cells, and isolated apoptotic nuclei using combined NEXAFS spectra at the C, N and O-K absorption edges [1-3].

In the quantitative analysis, precise absorption spectra of constituent molecules are definitely required. However exposure of X-rays for the observation itself could induce molecular changes resulting in the spectral changes of them. Actually, we have calculated the exposure and absorption doses for biological specimens in a hydrated condition to achieve a defined spatial resolution based on the method by Sayre et al. [4], and estimated the number of DNA strand breaks generated [5]. For example to obtain 100 nm spatial resolution, the absorption dose in the order of 10^4 Gy is required, which induces about 10^5 DNA double strand breaks per cell. In the present study, we evaluated the exposure-effects on the spectra of major biological molecules such as DNA, RNA, histone and BSA as a trial.

We prepared dry thin films of DNA, RNA, histone, and BSA on SiN membrane. Each one micrometer square area in the specimens was scanned with 10×10 pixels at the energy of C, N and O-K absorption edge regions in this order with a dwell time of 6, 12 and 20 msec in addition to 2 msec for DNA. For each dwell time the scanned area was shifted to the different area.

Figure 1 shows NEXAFS of DNA at the C-K (a), N-K (b), and O-K (c) absorption edges with four kinds of dwell times. A slight but significant change was observed in the profiles of the spectra, though it was not clear whether or not that was depending on the level of exposures.

In the case of RNA and histone, similar tendency was observed. However for BSA, a clear change in the profiles was observed in a dwell time dependent manner.

At this stage of the results, we decided that spectra of the molecules observed at the same exposure condition should be chosen as the reference data for analysis,

though the repeated measurement and confirmation of the results remained.

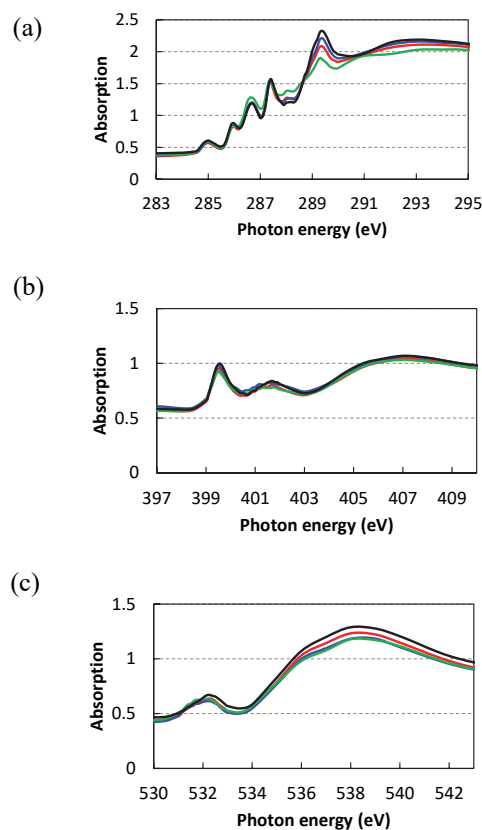


Fig. 1. NEXAFS of DNA at the C-K (a), N-K (b), and O-K (c) edges. Dwell time: 2 (black), 6 (red), 12 (blue), and 20 (green) msec.

- [1] K. Shinohara *et al.*, *Ultramicrosc.* **194** (2018) 1.
- [2] K. Shinohara *et al.*, *J. X-Ray Sci. Technol.* **26** (2018) 877.
- [3] K. Shinohara *et al.*, *Cells* **8** (2019) 8.
- [4] D. Sayre *et al.*, *Ultramicrosc.* **2** (1977) 337.
- [5] K. Shinohara and A. Ito, *J. Microsc.* **161** (1991) 463.

BL4U

Physicochemically Characterization of Dust/Salt Mixtures Originating from the Source of East Asian Dust Storms

J. Li¹, W. Liu¹, L. Li², T. Ohigashi³, M. Hallquist², S. Wang¹ and X. Kong²¹Shaanxi Key Laboratory of Earth Surface System and Environmental Carrying Capacity, Northwest University, Xi'an 710127, China²Department of Chemistry and Molecular Biology, University of Gothenburg, SE-412 96 Gothenburg, Sweden³UVSOR Synchrotron Facility, Institute for Molecular Science, Okazaki 444-8585, Japan

Mineral dust aerosols are a primary component in the atmosphere, accounting for almost half of tropospheric aerosol masses, and they can deteriorate human living conditions, endanger human health, and affect ecosystems. In the context of global climate change, the trend of warming and drying that is intensifying desertification in northern China is clear. The dominant regional geophysical feature, the neighboring Third Pole, that is the elevated region represented by the Himalayas and the Tibetan Plateau, impacts the entire planet's climate directly and via global teleconnections [1]. In this study, dust, salts and mixed samples were collected from important source regions of East Asian Dust Storms, including the Badain Jaran Desert, the Tengger Desert and the Ulan Buh Desert in northwestern China.

Scanning transmission X-ray microscopy (STXM) measurements were performed at the BL4U UVSOR-III beamline. For STXM measurements sample particles were deposited on filmed TEM grids, and data was analyzed with the aXis2000 program. Example optical images are presented in Fig. 1, where Fig. 1(a) is an image captured at 348 eV photon energy, corresponding to calcium absorption. Potassium-containing particles in the same sample are highlighted in Fig. 1(b) (297 eV) as the dark more cubic particles.

Individual particles were chemically mapped using the STXM technique. Particle images are shown in Fig. 2 and a zoomed-in view in Fig. 2(a). Figure 2(a) shows the two typically observed particle morphologies, needle-like and more cubic or polygonal. We observe distinct chemical characteristics of the two morphologies, as illustrated in Figs. 2(b)–2(d), which include the carbon K-edge and potassium L-edge spectra, the calcium L-edge spectra and the oxygen K-edge spectra.

The carbon K-edge includes the presence of a carbonate peak (at 290.2 eV) for needle particles that is minimally present for the polygonal particles [2]. Given the region around 284–290 eV is flat, these particles cannot include significant black or organic carbon components. At the potassium L-edge, a doublet at 297.2 and 299.8 eV indicates the presence of potassium in the polygonal particle [3]. In Fig. 2(c), the calcium L-edge shows the presence of calcium (at 348.8 and 352.1 eV) in the needle, suggesting the needle is likely CaCO₃ [2]. At the oxygen K-edge (Fig. 2(d)), one sharp peak is observed at 533.6 eV in the needle, which likely corresponds to the oxygen in the carbonate ions, which further supports the supposition that the needle-like particles are dominated by CO₃ and Ca. The broad

components in the oxygen K-edge spectra are associated with other oxygen species. These results show the mixing state of the CaCO₃ and K/O salts in sand samples, and these two components most likely have different solubilities, *i.e.*, CaCO₃ has low solubility in water, but the K/O salts may be highly dissolvable. The STXM results here provide unique information that cannot be accessed by other conventional methods.

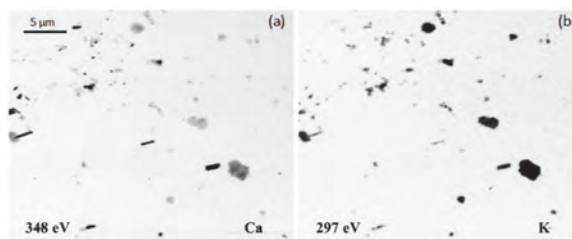


Fig. 1. STXM images shows the morphology of dust/salt mixture particles. (a,b) Snapshots measured at 348 eV and 297 eV.

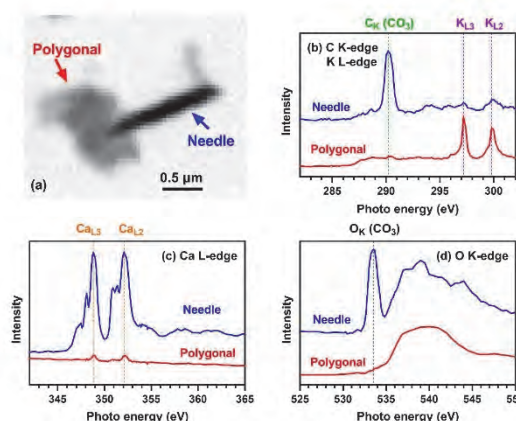


Fig. 2. STXM image and spectra of representative particles. (a) Optical image, (b) spectra scanned at C K-edge and K L-edge, (c) Ca L-edge spectra, (d) O K-edge spectra. Blue lines and red lines represent the mean spectra for needle-like particles and polygonal particles, respectively.

[1] Q. You *et al.*, *Earth-Sci. Rev.* **217** (2021) 103625.

[2] K. Benzerara *et al.*, *Geobio.* **2** (2004) 249.

[3] R. C. Moffet *et al.*, *Atmo. Chem. Phys.* **13** (2013) 10445.

BL5B

Development of Multilayer-coated Mirrors for the Next Generation of the Inner Magnetospheric Imaging

K. Inoue¹, A. Tomioka¹, J. Yang², H. Lin², K. Yoshioka^{1,2} and I. Yoshikawa^{1,2}

¹Department of Earth and Planetary Science, Graduate School of Science, The University of Tokyo, Tokyo 113-0033, Japan

²Department of Complexity Science and Engineering, Graduate School of Frontier Sciences, The University of Tokyo, Chiba 277-8561, Japan

Inner magnetospheric imaging at 30.4 nm, which is a resonantly scattered emission line by singly-ionized helium, contributed to our present understandings of plasmasphere formation, emerges of fine structures and solar wind interaction. RemFigote-sensing technique in this spectral region has become known as a promising tool in geophysics.

We have still strong motive in extension of the inner magnetospheric imaging since instrument developments on Kaguya, Nozomi, International Space Station. A multilayer coated mirror reflecting the EUV radiation at the normal incidence has been providing solutions to overcome the technical difficulties, i.e., existing optics has less effective collection of EUV photons. Therefore, multilayer coated mirrors have been employed for solar physics and astrophysics as well. The multilayer coating consisting of alternating layers of typically molybdenum and silicon (Mo/Si) achieved the highest and stable reflectivity (approximately 20 %) at 30.4 nm, and therefore it has been most often employed in the space missions. The thickness of each layer should be determined by the trade-off as follows: it maximizes the constructive interference of the incidence reflected at each interface and it minimizes the total absorption to enable more interfaces to contribute to the absolute reflectance increase.

Recently, we have shown the performance of the new multilayer coated mirror, consisting of 40 pairs of Mg and SiC. Its peak reflectivity achieved 30 % or higher. However, we had to realize that the Mg/SiC multilayer mirror has decisive disadvantage. The degradation of the reflectivity occurred under the condition of high temperature and/or high humidity. The interface between two materials became unstable, the thickness of the layer changes due to interfacial tension, and then the reflectance decreased dramatically (diffusion problem). As a result, we were forced to use a conventional multilayer mirror.

Space mission payloads have to survive hot and/or humidity environments before the launch as well as very cold condition in space. The development of robust instruments against environmental changes is mandatory for us.

More recently, we have designed a new multilayer coating, (B₄C/MgSi). We use the metal alloys of MgSi instead of using bulk of Mg to solve diffusion problems. Figure 1 shows the reflectivity of the coating for S- and P- polarizations. For both polarizations, the measured

reflectivities are relatively ~ 25 % lower than those of the expectations by calculations (We have an ordinary way using optical constants [1] to calculate the reflectivity). We will have some modification on the manufacturing process (e.g., Mg/Si ratio) to increase up to the expectations.

On the other hand, for non-polarization radiation (that is our target in planetary science), we expect that we have achieved higher reflectivity (average over S- and P-polarizations, about 30 %) than that of a conventional Mo/Si coating. The development will be progress next year.

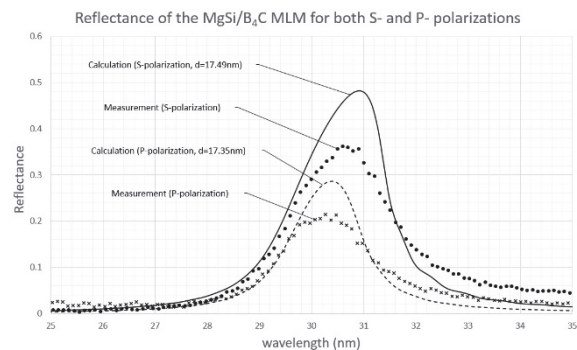


Fig. 1. Reflectivity of the multilayer coating of B₄C/MgSi. We have measured the reflectivity for both S and P polarizations. Predictions by the calculations are also shown.

[1] Eric Gullikson. The Center for X-Ray Optics. Retrieved March 27, 2022, from https://henke.lbl.gov/optical_constants/

BL5B

Performance Evaluation of an Optical Filter Aiming for Observation of Atmosphere of Comets

Y. Sasaki¹, Y. Suzuki², K. Yoshioka^{1,2}, M. Taguchi³, M. Kuwabara³, H. Akadama², T. Kosugi¹, H. Lin¹ and J. Yang¹

¹*Department of Complexity Science and Engineering, Graduate School of Frontier Sciences, The University of Tokyo, Chiba 277-8561, Japan*

²*Department of Earth and Planetary Science, Graduate School of Science, The University of Tokyo, Tokyo 113-0033, Japan*

³*Department of Physics, Graduate School of Science, Rikkyo University, Tokyo 171-8501, Japan*

Investigating the hydrogen isotope (D/H) ratio of emitted gases from comets is important to understand the water-related history of the solar system. Here, we are developing a Lyman-alpha line absorption cell that can distinguish the emission line of D and H, by utilizing the resonance absorption of the hydrogen atoms. To evaluate its performance, accurate calibration of the wavelength for the monochromator is required. However, the BL5B facility is known to have a drift-like tendency. Therefore, we examined the temporal shift of the wavelength using the known absorption line of the Krypton (Kr).

We evaluated the wavelength shift by irradiating the EUV light to the absorption cell filled with Kr gas (Fig. 1). The measurements were conducted three times. For all measurements, the scanned wavelength was from 122.6 nm to 124.6 nm, and the scan step was 0.01 nm. The slit width was 0.01 mm. The pin hole diameter was 1 mm, and the grating and the mirror were set as “G3M5”. The gas pressure of the Kr gas was 1000 Pa.

The result is shown in Fig. 2. The absorption wavelength by Kr is 123.58 nm in literature [1]. However, the figure shows two primary absorptions, 123.50 nm and 123.80 nm. We have two hypotheses for this result.

The one is that the absorption near the wavelength of 123.50 nm might be the absorption by Kr, since its wavelength is near that of Kr in literature [1]. Based on this hypothesis, the other absorption, which is around 123.80 nm, should be an effect of other substances. A possible substance is water molecules. They absorb light near the wavelength of 122.00 nm, 123.85 nm, and 124.10 nm. It is difficult to completely prevent water molecules from entering the cell, so some water molecules remaining in the cell might absorb the light near 123.80 nm. However, if this hypothesis is correct, an absorption near 124.10 nm also should appear. As the future work, we plan to dry the Kr cell completely by baking enough and confirm whether the absorption around 123.80 nm is derived from water molecules.

The other hypothesis is that both two absorption lines are caused by water molecules. It means that the wavelength adjustment by approximately +0.30 nm is needed. Based on this hypothesis, we have to consider the possibility that the absorption by Kr is too faint to observe. The future work for this case is the same as mentioned above, since if both absorptions are effects of water molecules, both absorptions would disappear

by drying the cell. Moreover, we also should find out appropriate Kr gas pressure.

As a supplementary experiment, we also evaluated the upper limit of absorption rate by hydrogen by filling the cell with hydrogen gas. It can be derived by calculating the ratio of the standard deviation to the average direct count, using the hydrogen-filled cell. We call it “relative error”.

The measurement was conducted 10 sets. Each measurement set has three trials. The scanned wavelength was from 119.6 nm to 123.6 nm, and the scan step was 0.02 nm. The slit width was 0.01 mm. The pin hole diameter was 1 mm, and the grating and the mirror were set as “G3M5”. The hydrogen gas pressure was 200 Pa. Electric energy applied to the filament in the cell was changed from (1.05 W, 2002 K) to (2.60 W, 2740 K).

As a result, the average “relative error” was 2.31%. This means that if the absorption for hydrogen Lyman-alpha is less than 2.31%, we cannot find it out. Therefore, we have to adjust the power for the filament so that the absorption exceeds the ratio.

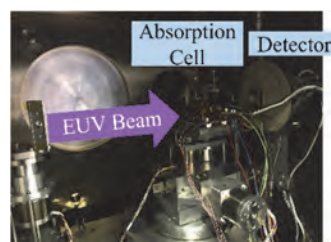


Fig. 1. The setup of experimental instruments.

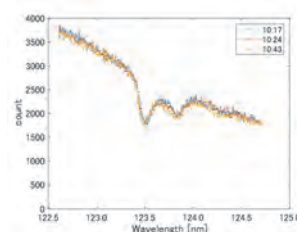


Fig. 2. The absorption spectrum of Kr. It shows primary absorptions at 123.50 nm and 123.80 nm.

[1] National Institute of Standards and Technology, *NIST Atomic Spectra Database Lines Data*, https://physics.nist.gov/PhysRefData/ASD/lines_form.html. Accessed March 2, 2022.

BL5B

Performance Evaluation of UV Absorption Filter Onboard Spacecraft

Y. Suzuki¹, M. Kuwabara², M. Taguchi², K. Yoshioka^{1,3}, T. Katsumata², M. Tateyama², K. Goda⁴,
A. Yamazaki⁴, K. Inoue⁴ and A. Tomioka⁴

¹Department of Earth and Planetary Science, Graduate School of Science, The University of Tokyo, Tokyo 113-0033, Japan

²Department of Physics, College of Science, Rikkyo University, Tokyo 171-8501, Japan

³Department of Complexity Science and Engineering, Graduate School of Frontier Sciences, The University of Tokyo, Chiba 277-8561, Japan

⁴Department of Earth and Planetary Physics, Faculty of Science, The University of Tokyo, Tokyo 113-0033, Japan

In the planetary science, deuterium-hydrogen (D/H) isotope ratio of comets is emphasized to know the origin of water on Earth. We develop an imager onboard the Comet Interceptor spacecraft to observe this. However, small spectrometers have too low wavelength resolution to distinguish emission lines of H and D, whose wavelength are different only by 33 pm. To overcome this difficulty, we use gas filters named Hydrogen Absorption Cell. This is a small glass cell filled with hydrogen molecules, in which filaments are set. By applying voltage to this filament, hydrogen molecules dissociate into atoms resulting in absorption of Ly- α . It is noted that Ly- α of deuterium is not absorbed. Therefore, we can evaluate D/H ratio from the difference of the brightness of the observation target when the voltage is applied (called “on”) and not applied (called “off”) to the filament.

Our experiments aim to understand appropriate pressure of filled hydrogen for the future comet exploration. We obtained transmittance spectra with several pressure conditions through the comparison of “on” and “off” data. Then, absorption width and depth are evaluated using Gaussian fitting. Wavelength scanning was performed using the G3M4 grating system with the range of 121.5-122.5 nm, 0.02 nm steps and summing 20 times. The higher hydrogen pressure

is, the more difficultly the filament temperature rises, since hydrogen molecules take away the heat of the filament. Thus, experiments were conducted under three conditions –temperature of the filament is fixed, power applied to the filament is fixed, and applied voltage is fixed.

The results are shown in Fig. 1. When power or voltage are fixed, the temperature of the filament decreases and absorption gets shallower with higher pressure. On the other hand, when filament’s temperature is fixed to 1800 K, absorption gets deeper. However, power consumption also increases. Although it seems that intermediate pressure (from 200 to 400 Pa) is the best so far, we need to precisely discuss it in terms of lifetime of filaments and available power onboard the spacecraft.

When voltage is applied, filaments are expected to glow like light bulbs, which causes the contamination of observation data. To verify this fact, we measured the brightness with shutters closed. As we expected, the filament gets brighter as its temperature rises. Besides, at constant temperature, higher hydrogen pressure is found to suppress the brightness. Utilizing this knowledge, we will soon estimate the expected S/N ratio of the instrument mounted on the spacecraft.

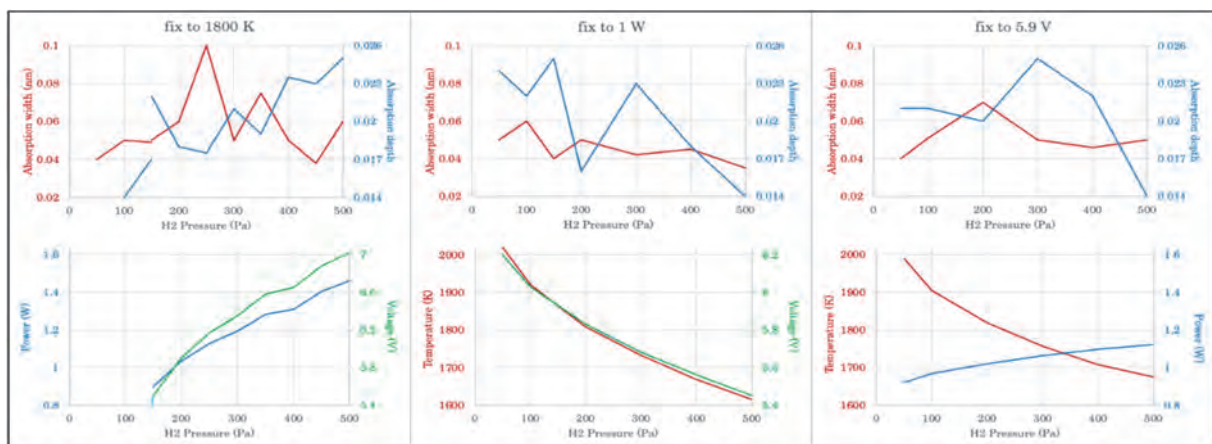


Fig. 1. Dependence of absorption width and depth on the pressure of filled hydrogen in the cell.

BL7B

The Effect of Space Weathering on The PAH Wavelength of Interstellar Dust Organic Matter

J. Yang¹, H. Lin¹, K. Inoue², A. Tomioka², K. Yoshioka^{1,2} and I. Yoshikawa^{1,2}

¹Department of Complexity Science and Engineering, Graduate School of Frontier Sciences, The University of Tokyo, Chiba 277-8561, Japan

²Department of Earth and Planetary Science, Graduate School of Science, The University of Tokyo, Tokyo 113-0033, Japan

In astronomy, extinction is the absorption and scattering of electromagnetic radiation by dust and gas between the emitting astronomical object and the observer. Interstellar extinction was first recorded in 1930 by Robert Julius Trumpler. However, its effects were already noticed by Friedrich Georg Wilhelm von Struve in 1847, and its influence on stellar colors was observed by many, but they did not link it to the prevalence of galactic dust.

Polycyclic aromatic hydrocarbons (PAH) are a prevalent component of space organics and are present in interstellar dust. They play an important role in a variety of astronomical observations in the ultraviolet and far-infrared ranges, covering a wide range of objects and environments from meteorites and interplanetary dust particles to the outer solar system [1].

A prominent feature in the measured extinction curves of many objects in the Milky Way is a broad "bulge" at about 2175 Å, right into the ultraviolet region of the electromagnetic spectrum. This feature was first observed in the 1960s, but its origin remains unclear. Several models have been proposed to explain the bulge, including graphite particles containing a mixture of PAH molecules. Studies of embedded interplanetary dust particles (IDPs) have observed this feature and identified the presence of carriers of organic carbon and amorphous silicates in the particles.

The PAH present on Earth have an absorption band with a wavelength of about 210 nm. And due to the weathering of the universe, PAH may increase the wavelength range of the UV absorption band in the universe.

Therefore, it is assumed that the reflection band of PAH on Earth has a wavelength of about 210 nm, which may correspond to the absorption band of 217.5 nm that appears in the interstellar darkening curve (the curve describing the absorption spectrum of interstellar dust).

This experiment was conducted to observe and analyze the effect of space weathering on the light absorption properties of PAH. We prepared PAH samples Fig. 1) synthesized in the laboratory for comparison experiments with PAH samples exposed on the International Space Station (ISS) (exposed samples) and similar samples synthesized and stored in the laboratory (unexposed samples), both exposed and unexposed samples were made of PAH only and not mixtures. We divided the reflectance properties of these samples into three parts with the non-exposed

samples in the wavelength range of 100-300 nm for the experiments and compared the reflectance properties.

The reflectance properties of the Coronene samples showed a significant decrease near 270 nm wavelengths and a trend in the 210-280 nm wavelength range where the attenuation of reflected light was more pronounced in the longer wavelength range (Fig. 2).

This trend suggests that the wavelength corresponding to the bottom of the depression may shift to longer wavelengths due to space weathering.

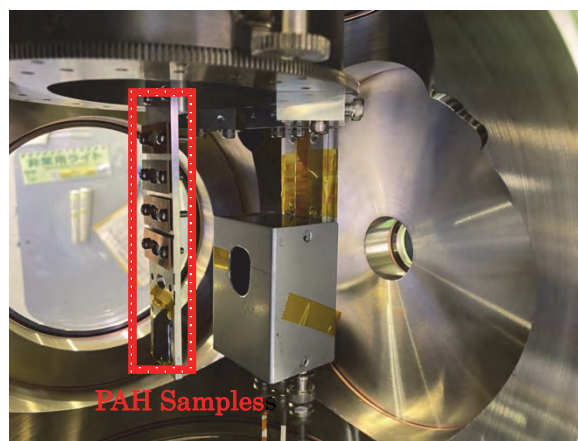


Fig. 1. PAH samples installation diagram.

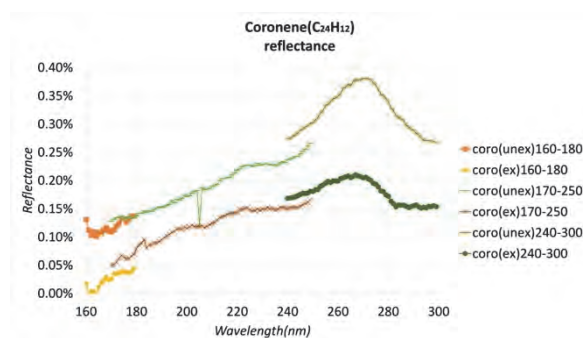


Fig. 2. The reflection characteristics of coronene samples in the wavelength range of 160-300 nm.

[1] Salama, Farid. (2008). PAHs in astronomy - A review. Proceedings of The International Astronomical Union. 251. 10.1017/S1743921308021960.

BL7B

A study on Space weathering of Carbonaceous Meteorites by Far-ultraviolet Spectroscopy

H. Akadama¹, Y. Suzuki¹, J. Yang² and K. Yoshioka^{1,2}

¹Department of Earth and Planetary Science, Graduate School of Science, The University of Tokyo, Tokyo 113-0033, Japan

²Department of Complexity Science and Engineering, Graduate School of Frontier Sciences, The University of Tokyo, Chiba 277-8561, Japan

We study space weathering in Carbon-complex asteroids by measuring the spectral shifts of carbonaceous meteorites due to weathering, focusing on the far-ultraviolet (FUV; 50-200 nm). The feature of the meteorite materials on this spectral area has not been much examined well.

Asteroids are believed to be well preserved in primitive state since they have been left out of the planetary formation process. Accordingly, they have been the focus of much attention as a clue to the nature of the early solar system. However, to analogize the past state from the present observations, it is necessary to understand the process of transformation such as space weathering.

Space weathering is the dominant transformation process on the surface of celestial bodies with thin atmospheres, such as asteroids. This process is caused by solar photons, charged particles like energetic electrons, and impacts by micrometeorites. The physical properties of such asteroid surfaces have been understood mainly through spectroscopic observations in the visible and infrared regions. However, the spectra in these regions of Carbon-complex asteroids are generally flat and have little characteristic shape [1]. On the other hand, the UV spectra of organic compounds vary remarkably with the degree of carbonization, suggesting that the UV region may be suitable for evaluating space weathering effects on Carbon-complex asteroids.

In this study, four types of carbonaceous chondrites included in the meteorites were irradiated with FUV light from the UVSOR BL7B, and the FUV spectra before and after the irradiation were compared (Fig. 1). To compare reflectance before and after UV irradiation, relative reflectance with respect to a specific wavelength was used.

As a result, bluing of the spectrum was observed in the wavelength range of 50~200 nm (Fig. 2). This change was the opposite of that observed for hydrocarbons using polystyrene, and like that observed for bodies with little or no organic matter, such as the lunar surface [2]. Since carbonaceous chondrites contain about 20 wt% of Fe, it is possible that a process of coating with Fe of several hundred nm in size occurred by the UV-irradiated surface, like that in the lunar surface.

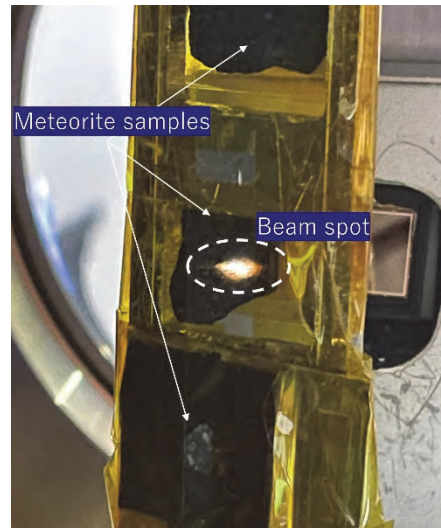


Fig. 1. Light irradiation of a meteorite sample.

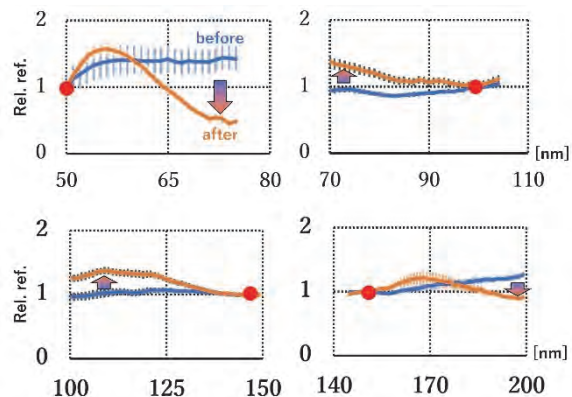


Fig. 2. Relative reflectance variation in a certain carbonaceous meteorite (“Aguas Zarcas”). (The horizontal axis is wavelength [nm] and the vertical axis is relative reflectance (normalized at red spots). Blue and orange lines correspond to before and after irradiation, respectively.)

[1] S.J. Bus & R.P. Binzel, *Icarus*, **158** (2002) 146.

[2] A. Hendrix *et al.*, *Journal of Geophysical Research*, **117** (2012) E12

The background is a vibrant red color with a complex geometric design. It features several overlapping circular and linear patterns. A prominent feature is a large, semi-transparent circular graphic on the right side, composed of concentric rings and a dotted border. Diagonal lines and bands of varying shades of red sweep across the page, creating a sense of movement and depth. The overall aesthetic is modern and technical.

IV

List of Publications

List of Publications (2021)

D. Akazawa, T. Sasaki, M. Nagasaka and M. Shiga

“X-ray Absorption Spectra of Aqueous Cellobiose: Experiment and Theory”, J. Chem. Phys., **156** (2022) 044202.

K. Ali, H. Zen, H. Ohgaki, T. Kii, T. Hayakawa, T. Shizuma, H. Toyokawa, M. Fujimoto, Y. Taira and M. Katoh

“Three-Dimensional Nondestructive Isotope-Selective Tomographic Imaging of 208Pb Distribution via Nuclear Resonance Fluorescence”, Applied Sciences, **11** (2021) 3415.

D. Céolin¹, H. Yuzawa, T. Saisopa, K. Klaiphet, J. Borsup, P. Songsiriritthigul and N. Kosugi

“Substituent effects in aqueous solutions of carboxylate salts studied by x-ray absorption spectroscopy at the oxygen K-edge”, J. Chem. Phys. **155**, (2021) 014306.

O. Endo, F. Matsui, W. J. Chun, M. Nakamura, K. Amemiya and H. Ozaki

“Nanographene growth from benzene on Pt(111)”, Surf.Sci., **711** (2021) 121874.

G. Germer, T. Ohigashi, H. Yuzawa, N. Kosugi, R. Flesch, F. Rancan, A. Vogt and E. Rühl

“Improved Skin Permeability after Topical Treatment with Serine Protease: Probing the Penetration of Rapamycin by Scanning Transmission Xray Microscopy”, ACS Omega, **6** (2021) 12213.

K. Hagiwara, M. Ishikado, M. Horio, K. Koshiishi, S. Nakata, S. Ideta, K. Tanaka, K. Horiba, K. Ono, H. Kumigashira, T. Yoshida, S. Ishida, H. Eisaki, S. Shamoto and A. Fujimori

“Superconducting Gap and Pseudogap in the Surface States of the Iron-based Superconductor PrFeAsO_{1-y} Studied by Angle-resolved Photoemission Spectroscopy”, Phys. Rev. Research **3**, (2021) 043151.

Y. Hikosaka

“Multi-Electron–Ion Coincidence Spectrometer with a High-Efficiency Microchannel Plate Detector”, J. Electron Spectrosc. Relat. Phenom., **255** (2022) 147158.

Y. Hikosaka, T. Kaneyasu, M. Fujimoto, H. Iwayama and M. Katoh

“Reply to ‘Comment on “Coherent Control in the Extreme Ultraviolet and Attosecond Regime by Synchrotron Radiation”’, Nature Commun., **12** (2021) 3782.

T. Hirai, T. Kawai, Y. Harada and N. Ohno

“Formation of Cs₃Cu₂I₅ Microcrystals in CsI Crystals through the Aggregation of Cu⁺ Ions”, Jpn. J. Appl. Phys. **60** (2021) 075501.

S. Ideta, S. Johnston, T. Yoshida, K. Tanaka, M. Mori, H. Anzai, A. Ino, M. Arita, H. Namatame, M. Taniguchi, S. Ishida, K. Takashima, K. M. Kojima, T. P. Devereaux, S. Uchida and A. Fujimori

“Hybridization of Bogoliubov Quasiparticles between Adjacent CuO₂ Layers in the Triple-Layer Cuprate Bi₂Sr₂Ca₂Cu₃O_{10+δ} Studied by Angle-Resolved Photoemission Spectroscopy”, Phys. Rev. Lett. **127** (2021) 217004.

G. Ito, H. Kimura, D. Shiratori, K. Hashimoto, D. Nakauchi, M. Koshimizu, T. Kato, N. Kawaguchi and T. Yanagida

“Evaluation of Photoluminescence and Scintillation Properties of Eu-doped 20CsCl-20BaCl₂-60ZnCl₂ glasses by a melt quenching method”, J. Mater. Sci. Electron. **32** (2021) 8725.

M. Iwasawa, S. Kobayashi, M. Sasaki, Y. Hasegawa, H. Ishii, F. Matsui, S. Kera and Y. Yamada

“Photoemission Tomography of a One-Dimensional Row Structure of a Flat-Lying Picene Multilayer on Ag(110)”, J. Phys. Chem. Lett. (2022) 1512.

T. Kanomata, T. Awano and T. Ito

“Optical Properties of the Antiferromagnetic Heusler Alloy Ru₂CrGe”, Solid State Commun, **340** (2021) 114525.

P. Kantuptim, H. Fukushima, H. Kimura, D. Nakauchi, T. Kato, M. Koshimizu, N. Kawaguchi and T. Yanagida

“VUV- and X-ray-Induced Properties of Lu₂Si₂O₇, Y₂Si₂O₇, and Gd₂Si₂O₇ Single Crystals”, Sensors and Mater. **33** (2021) 2195.

Y. Kebukawa, M. E. Zolensky, C. A. Goodrich, M. Ito, N. O. Ogawa, Y. Takano, N. Ohkouchi, K. Kiryu, M. Igisu, T. Shibuya, M. A. Marcus, T. Ohigashi, J. Martinez, Y. Kodama, M. H. Shaddad and P. Jenniskens
“Organic matter in carbonaceous chondrite lithologies of Almahata Sitta: Incorporation of previously unsampled carbonaceous chondrite lithologies into ureilitic regolith”, Meteoritics & Planetary Science **56**, Nr 7, (2021) 1311.

Y. Kezuka, H. Murata, M. Yoshida, K. Eguchi, A. Nakahira and M. Tajika

“Effects of Trace Si Impurities in Water on the Growth of Calcite Nanoparticles”, CrystEngComm, **24** (2022) 747.

S. Makita, H. Matsuda, Y. Okano, T. Yano, E. Nakamura, Y. Hasegawa, S. Kera, S. Suga and F. Matsui
“Contrast Inversion of Photoelectron Spectro-microscopy Image”, e-J. Surf. Sci. Nanotechnol., **19** (2021) 42.

F. Matsui and H. Matsuda

“Projection-type electron-spectroscopy collimator analyzer for charged particles and X-ray detections”, Rev. Sci. Instrum., **92**, (2021) 073301.

F. Matsui, S. Makita, H. Matsuda, E. Nakamura, Y. Okano, T. Yano, S. Kera and S. Suga

“Valence Band Dispersion Embedded in Resonant Auger Electrons”, J. Phys. Soc. Jpn., **90**, (2021) 124710.

S. Mitsunobu, Y. Ohashi, H. Makita, Y. Suzuki, T. Nozaki, T. Ohigashi, T. Ina and Y. Takaki

“One-Year In Situ Incubation of Pyrite at the Deep Seafloor and Its Microbiological and Biogeochemical Characterizations”, Applied and Environmental Microbiolog, **87** (2021) e00977-21.

M. Nagasaka and N. Kosugi

“Soft X-ray Absorption Spectroscopy for Observing Element-specific Intermolecular Interaction in Solution Chemistry”, Chem. Lett. **50** (2021) 956.

S. Nakata, M. Horio, K. Koshiishi, K. Hagiwara, C. Lin, M. Suzuki, S. Ideta, K. Tanaka, D. Song, Y. Yoshida, H. Eisaki, and A. Fujimori

“Nematicity in a cuprate superconductor revealed by angle-resolved photoemission spectroscopy under uniaxial strain”, npj Quantum Mater. **6** (2021)86

Y. Nakayama, K. Sudo, N. Ohashi, S. Kera and Y. Watanabe

“Interface electronic structure and valence band dispersion of bis(1,2,5-thiadiazolo)-p-quinobis(1,3-dithiole) on polycrystalline Au electrodes”, Electron. Struct. **3** (2021) 024006.

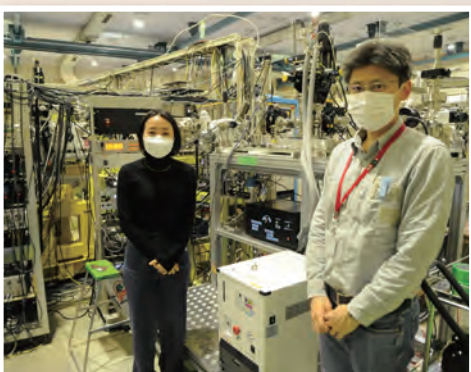
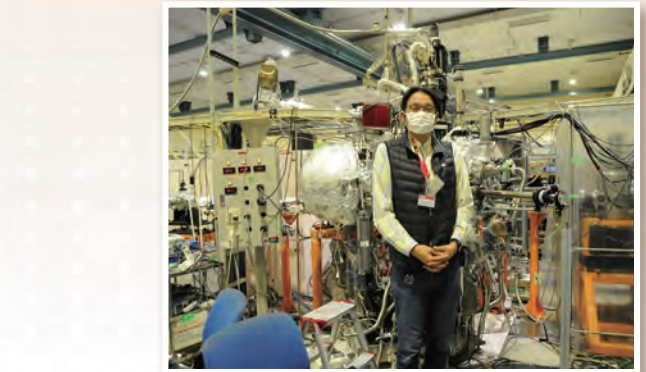
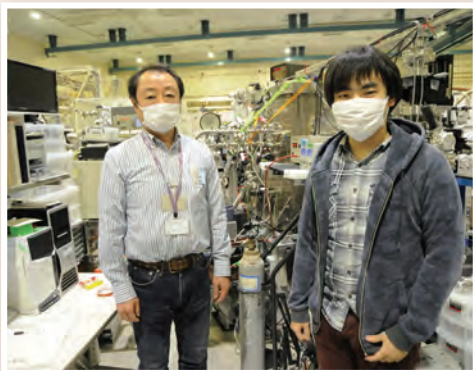
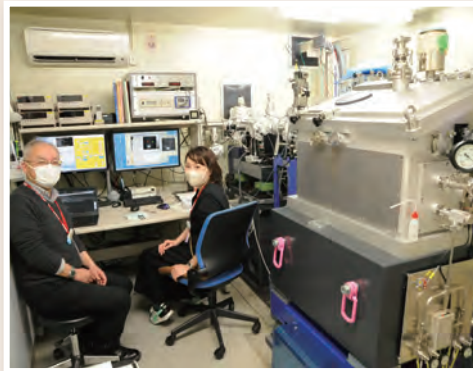
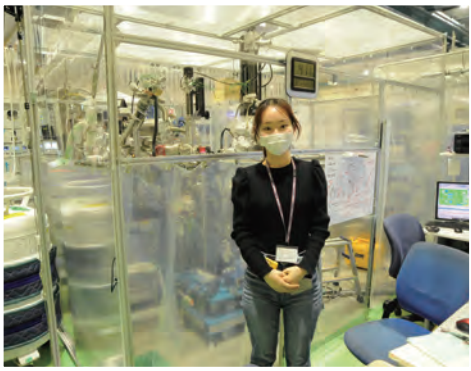
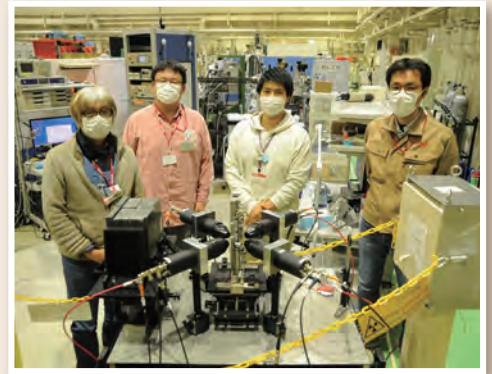
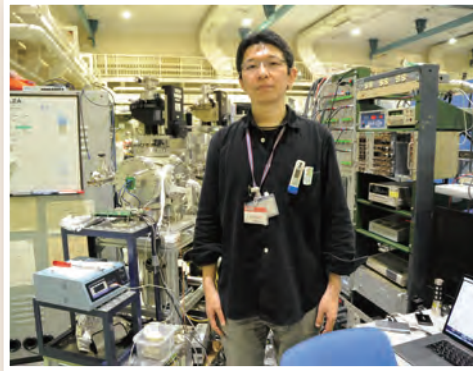
J. Rodriguez, T. Ohigashi, C. Lee, M. Tsai, C. Yang, C. Wang, C. Chen, W. Pong, H. Chiu and C. Chuang
“Modulating chemical composition and work function of suspended reduced graphene oxide membranes through electrochemical reduction”, Carbon **185**, (2021) 410.

E. Salehi and M. Katoh

“Spatial structure and angular momentum of electro-magnetic wave radiated from a relativistic electron moving on a spiral orbit”, J. Adv. Simulat. Sci Eng., **8** (2021) 87.

- H. Suga, K. Suzuki, T. Usui, A. Yamaguchi, O. Sekizawa, K. Nitta, Y. Takeichi, T. Ohigashi and Y. Takahashi
“A New Constraint on the Physicochemical Condition of Mars Surface during the Amazonian Epoch Based on Chemical Speciation for Secondary Minerals in Martian Nakhilites”, *Minerals*, **11** (2021) 514.
- I. Suzuki, Z. Lin, S. Kawanishi, K. Tanaka, Y. Nose, T. Omata and S. Tanaka
“Direct Evaluation of Hole Effective Mass of SnS–SnSe Solid Solutions with ARPES Measurement”, *Phys. Chem. Chem. Phys.* **24** (2022) 634.
- S. Tsuru, B. Sharma, M. Nagasaka and C. Hättig
“Solvent Effects in the Ultraviolet and X-ray Absorption Spectra of Pyridazine in Aqueous Solution”, *J. Phys. Chem. A*, **125** (2021) 7198.
- J. V. Vélez, Y. Chinc, M. Tsaid, O. J. Burtone, R. Wange, S. Hofmanne, W. Hsuf, T. Ohigashig, W. Pongd and C. Chuang
“Evidence of synergistic electrocatalysis at a cobalt oxide–graphene interface through nanochemical mapping of scanning transmission X-ray microscopy”, *Chinese Journal of Physics* **76** (2022) 135.
- H. Wang, J. Chiou, K. Chen, A. R. Shelke, C. Dong, C. Lai, P. Yeh, C. Du, C. Lai, K. Asokan, S. Hsieh, H. Shiu, C. Pao, H. Tsai, J. Yang, J. Wu, T. Ohigashi and W. Pong
“Role of Interfacial Defects in Photoelectrochemical Properties of BiVO₄ Coated on ZnO Nanodendrites: Xray Spectroscopic and Microscopic Investigation”, *ACS Appl. Mater. Interfaces* **13**, (2021) 41524.
- S. Yamasuso and T. Kawai
“Electronic states and relaxation dynamics of Au— centers in RbCl crystals”, *J. Lumin.* **236** (2021) 118094.
- M. Yoshida, M. Miyahara, H. Suga, A. Yamaguchi, N. Tomioka, T. Sakai, H. Ohfuji, F. Maeda, I. Ohira, E. Ohtani, S. Kamada, T. Ohigashi, Y. Inagaki, Y. Kodama and N. Hirao
“Elucidation of impact event recorded in the lherzolic shergottite NWA 7397”, *Meteoritics & Planetary Science* (2021) 1.

UVSOR User 8



A large, stylized white letter 'V' is centered within a circular graphic element. The background of the entire page is a warm, light brown color with abstract, flowing lines and a pattern of small dots at the bottom.

Workshops

UVSOR Symposium 2021

Date: November 5, 2021

Place: Zoom Conference

November 5th (Fri.)

10:35 – 10:40 Opening Remark

<Session 1, Chair: **T. Ohgashi** (UVSOR)>

10:40 – 11:00 Development of Multilayer Coated Mirror for the Next Earth Mission

L. Huiyang (Univ. of Tokyo)

11:00 – 11:20 Current-Induced Insulator-to-Metal Transition of SmS

S. Tatsukawa (Osaka Univ.)

11:20 – 11:40 Title of the Presentation (gothic, 11pt)

K. Yamanoi (Osaka Univ.)

11:40 – 12:00 Development of Reflection XMCD Measurement Setup for the Investigation of Inner Structures of Magnetic Thin Films at UVSOR BL4B

K. Yamamoto (IMS)

12:00 – 13:00 Lunch Break

<Session 2, Chair: **K. Tanaka** (UVSOR)>

13:00 – 13:20 Electronic States of Novel Dirac Semimetals Studied by High-Resolution ARPES

K. Nakayama (Tohoku Univ.)

13:20 – 13:40 The Topological Electronic Structure of the Interface Between α -Sn and InSb

T. Nakaya (Osaka Univ.)

13:40 – 14:00 The Photoelectron Momentum Mapping of Highly Oriented Organic Thin Films

M. Iwasawa (Univ. of Tsukuba)

14:00 – 14:20 Measurement of the Electronic State of η -Mo₄O₁₁ Using a Momentum Microscope

T. Kobayashi (Osaka Univ.)

14:20 – 14:30 Break

<Session 3, Chair: **Y. Taira** (UVSOR)>

14:30 – 14:50 LCS Gamma-Ray Beams Utilization for the Isotope Selective NRF-CT Imaging in UVSOR-III

K. Ali (Kyoto Univ.)

14:50 – 15:10 Charge Distribution in Delithiated LiCoO₂ Particles Visualized by Soft X-Ray Spectromicroscopy

W. Zhang (Univ. of Tokyo)

15:10 – 15:30 Mesoscopic Structure Analysis by Resonant Soft X-Ray Scattering

H. Iwayama (IMS)

15:30 – 15:50 Time-Resolved Spectroscopy of Fast Scintillators with VUV Excitation

M. Koshimizu (Tohoku Univ.)

16:00 – 17:00 Discussion and Closing Remark

S. Kimura (Osaka Univ.)

17:00 – 19:00 Poster Session

Poster Session

- P01 Photoelectron Wave Packet Interference Using a Tandem Undulator
T. Kaneyasu (SAGA- LS)
- P02 Photon Counting Experiments of Young's Double-Slit Interference Using Undulator Vortex Radiation
S. Wada (Hiroshima Univ.)
- P03 Energy-Dependence of Photoelectron Circular Dichroism of Chiral Molecules
H. Kohguchi (Hiroshima Univ.)
- P04 Photoluminescence Properties and luminescence Mechanism of $\text{Cs}_2\text{Hf}(\text{Br}, \text{X})_6$
C. Fujiwara (Tohoku Univ.)
- P05 Operando XAFS Observation of Water Splitting Electrocatalysts at UVSOR BL3U
M. Yoshida (Yamaguchi Univ.)
- P06 Elucidation of the Function of Carbonate Ions on the Cobalt Carbonate Catalysts Using Operando Observations
K. Harada (Yamaguchi Univ.)
- P07 Operando Observation of Active Site for the Nickel Carbonate Water Splitting Catalyst Induced by the Electrolyte Adsorption Ions
Z. Li (Yamaguchi Univ.)
- P08 The Structure Analysis of Soft Matter by Resonant Soft X-Ray Scattering
Y. Takanishi (Kyoto Univ.)
- P09 Solvent-Induced Transition of Polymorphological Chiral Supermolecular Architectures in a Bent-Core Liquid Crystal Dimer
F. Araoka (RIKEN)
- P10 XAS Measurements of Sugar Molecules in Liquid Phase: Interaction Between Sugar Molecules and Solvent
D. Akazawa (Univ. of Tokyo)
- P11 Intermolecular Interactions of the Acetone-Water Binary System Studied by Soft X-Ray Absorption Spectroscopy
C. Sugahara (Hiroshima Univ.)
- P12 Efficient Multielectron-Ion Coincidence Measurement with a Magnetic Bottle Electron Spectrometer
Y. Hikosaka (Toyama Univ.)
- P13 Efforts to Reduce the Photon Energy Drift at BL5B
H. Zen (Kyoto Univ.)
- P14 Local Valence Transition of SmS Induced by Alkali Metal Adsorption
T. Nakamura (Osaka univ.)
- P15 Angle-Resolved Photoemission Study of Solid Electrolytes $\text{Li}_x\text{La}_{(1-x)/3}\text{NbO}_3$ Bulk Single Crystal
R. Yamamoto (Nagoya Univ.)

- P16 Development of Photocathodes for Accelerator Beam Source by Coating with Atomically Thin Two-Dimensional Nanomaterials
K. Kouyama (Nagoya Univ.)
- P17 Angle-Resolved Photoemission Study of TPP[FePc(CN)₂]₂
T. Hoshina (Nagoya Univ.)
- P18 Operando Measurements of THz, Infrared and Visible Reflectance Spectra of SmS Under Current and Light Irradiation
H. Watanabe (Osaka Univ.)
- P19 Momentum-Resolved Resonant Photoemission Spectroscopy of TiSe₂
S. Tanaka (Osaka Univ.)
- P20 Resonant Photoemission Spectroscopy of Highly Oriented Coronene Monolayer Using Photoelectron Momentum Microscope
Y. Hasegawa (Ritsumeikan Univ.)
- P21 Measurement of Complex Reflective Index of Diamond Substrate
M. Horiba (Fukui Univ.)
- P22 Impact of Weak Interaction on the Electronic Structure at the Pentacene/Graphite Interface
Y. Hasegawa (Ritsumeikan Univ.)
- P23 Angle-Resolved Photoemission Study of Antiferromagnetic *i* - MAX Phase Compound (Mo_{2/3}Dy_{1/3})₂AlC
T. Sugimoto (Nagoya Univ.)
- P24 Investigations on the Band Structures and Anisotropic Couplings of Electrons with Molecular Vibrations in Organic Single Crystal Rubrene
K. Fukutani (IMS)
- P25 Lattice Design Study of UVSOR-IV
E. Salehi (IMS)

The 4th workshop on prospects and construction plan of the next generation synchrotron radiation facility

Date: November 4, 2021

Place: Zoom Conference

November 4th (Thu.)

- | | |
|---------------|--|
| 9:30 – 9:35 | Greetings from Guest
Section Chief from MEXT, A. Watanabe |
| 9:35 – 10:15 | Opening Remark
UVSOR Director, S. Kera |
| 10:15 – 10:20 | Break |
| 10:20 – 12:00 | Beamline Conception ①
Present Status and Future Plan of Soft X-Ray Absorption and Scattering at BL3U
M. Nagasaka (IMS)
Future Prospects for Soft X-Ray Absorption and Scattering
J. Miyawaki (QST)
Current Status and Prospects of Infrared Microscopy Using Infrared Synchrotron Radiation
Y. Ikemoto (JASRI)
Current Status and Development of Irradiation (BL1U)
Y. Taira (UVSOR)
Prospects of Irradiation and FEL
I. Matsuda (Univ. of Tokyo) |
| 12:00 – 13:30 | Lunch Break |
| 13:30 – 15:50 | Beamline Conception ②
Present Status and Future of VUV Spectroscopy in UVSOR
M. Kitaura (Yamagata Univ.)
Present and Future of Photoelectron Momentum Microscope + Spin
F. Matsui (UVSOR)
Future Prospect of Spin-Resolved Photoemission Electron Microscopy and Spectroscopy
K. Yaji (NIMS)
Current Status and Developments of ARPES at UVSOR
K. Tanaka (UVSOR)
Future of ARPES: Putting More Information on ARPES
K. Kuroda (Hiroshima Univ.)
Current Status and Future of Soft X-Ray Imaging
T. Ohigashi (UVSOR)
Future of Soft X-Ray Imaging
Y. Takahashi (Tohoku Univ.) |
| 15:50 – 16:00 | Break |
| 16:00 – 16:20 | Latest Results from Design Study on New Light Source
M. Katoh (UVSOR) |

16:20 – 17:00 Panel Discussion
 “Requests for the Construction Plan”
(Panelist : **J. Okabayashi, M. Katoh, M. Kitaura, S. Kimura, Y. Hikosaka and
H. Yamane**)

2021 IMS Open House Event

IMS is open to the public once every three years in rotation with the other two Okazaki institutes of National Institutes of Natural Sciences. It was held online on October 23, 2021.

Details can be seen in the following web site:

<https://www.ims.ac.jp/koukai2021/>.



The livestreamed video can be seen at

<https://www.youtube.com/watch?v=24JmaV8Fbgo>,

which spans about 6 hours, including a molecular science forum and virtual tours of facilities and laboratories.



For the UVSOR tour (which is included in the above video),

see <https://www.youtube.com/watch?v=WqIFnMnKBTc&t=360s>.



The presentation of the forum was given by Dr. Takuji Ohigashi about Hayabusa2 returned sample analysis:

see

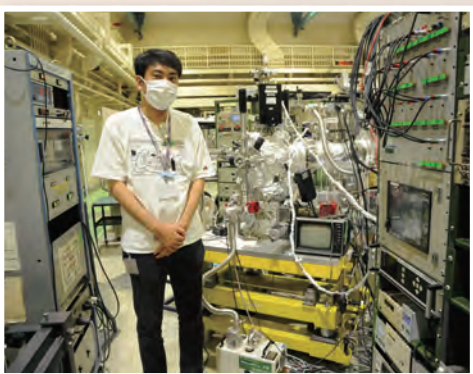
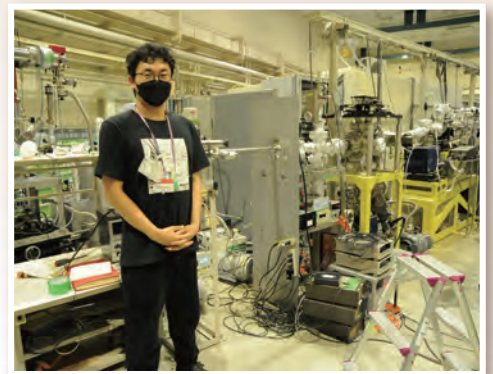
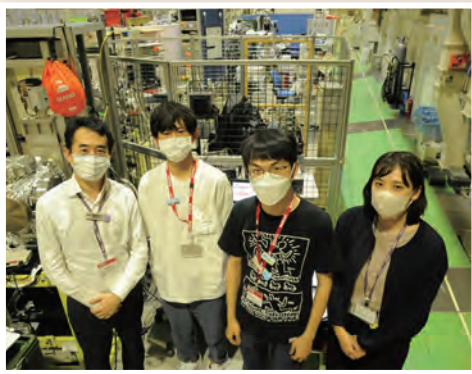
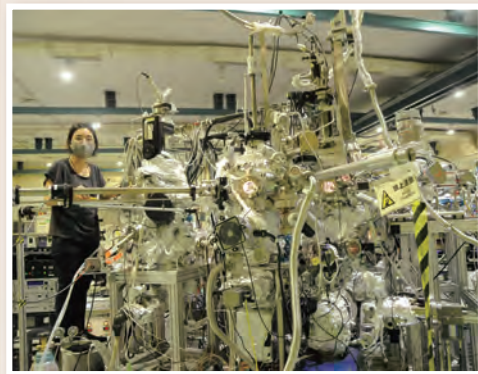
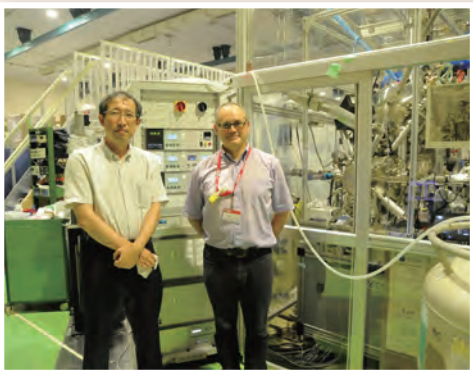
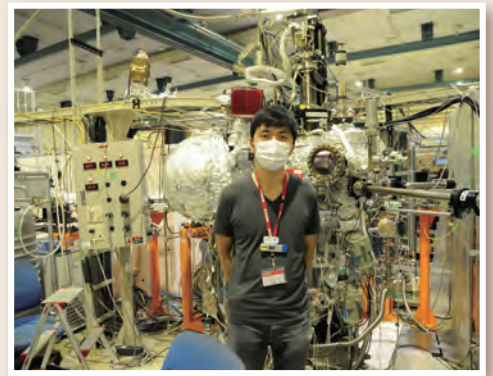
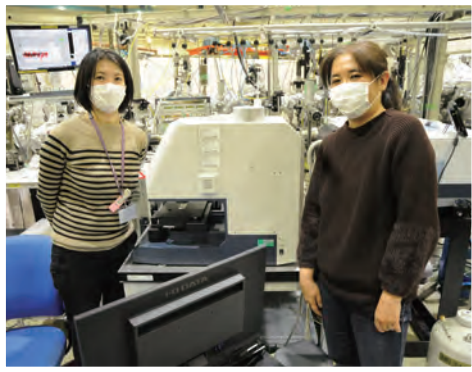
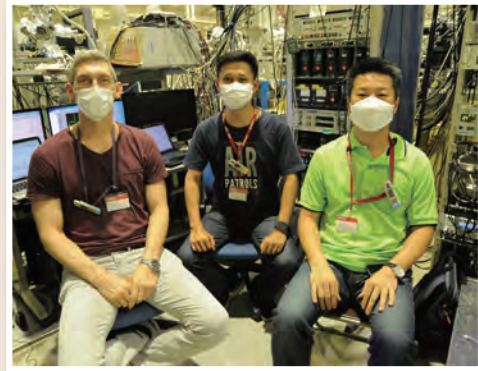
<https://www.ims.ac.jp/koukai2021/info/#micro>

and

<https://www.youtube.com/watch?v=AnchMBTwHBw>.



UVSOR User 9







Editorial Board : H. Matsuda K. Tanaka M. Sakai M. Ishihara

**Institute for Molecular Science
National Institutes of Natural Sciences
Okazaki 444-8585, Japan**

Tel: +81-564-55-7402

Fax: +81-564-54-7079

<http://www.uvsor.ims.ac.jp>



ISSN 0911-5730